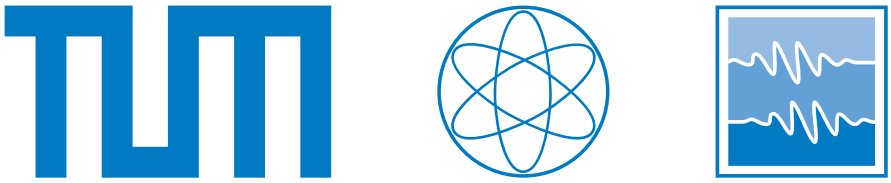

Time-Frequency-Resolved Absolute Time Delay of the Photoelectric Effect

Dissertation

von

Johann Emmeram Riemensberger

Fakultät für Physik
Lehrstuhl für Laser- und Röntgentechnik

Time-Frequency-Resolved Absolute Time Delay of the Photoelectric Effect

Johann Emmeram Riemensberger

Vollständiger Abdruck der von der Fakultät für Physik der Technischen Universität München zur Erlangung des akademischen Grades eines
Doktors der Naturwissenschaften
genehmigten Dissertation.

Vorsitzender: Prof. Dr. Michael Knap
Prüfer der Dissertation:
1. Prof. Dr. Reinhard Kienberger
2. Prof. Jonathan Finley, Ph.D.

Die Dissertation wurde am 09.04.2018 bei der Technischen Universität München eingereicht und durch die Fakultät für Physik am 28.09.2018 angenommen.

Zusammenfassung

In dieser Promotionsschrift werden Experimente und numerische Rechnungen vorgestellt, welche die Beobachtung, Analyse und quantitative Diskussion der mikroskopischen Mechanismen, welche zur Zeitverzögerung des photoelektrischen Effektes beitragen, ermöglichen. Hierbei verlässt das angeregte Elektron die untersuchte metallische Probe mit einer Zeitverzögerung von 10-100 as ($1\,\text{as} = 10^{-18}\,\text{s}$) nachdem der anregende extrem-ultraviolette Lichtpuls auf der Probe auftrifft. Die vorgestellten Experimente repräsentieren eine Vereinigung von experimentellen Techniken der Hohen-Harmonischen-Erzeugung, der Filterung einzelner Attosekundenpulse, der Photoelektronenspektroskopie und der Präparation von metallischen Einkristalloberflächen in Ultrahoch Vakuumumgebungen. Photoelektronen werden durch hochenergetische extrem-ultraviolette Strahlung in der metallischen Probe angeregt und beim Übergang über die Metall-Vakuum Grenzfläche wird ihr kinematischer Impuls durch die Wechselwirkung mit dem Nahinfrarotfeld moduliert. Bis zuletzt waren zeitaufgelöste Photoemissionsexperimente auf die Beobachtung und die numerische Analyse der relativen Zeitverzögerungen von Elektronenwellenpaketen, welche von bzw. in spektroskopisch unterscheidbare Anfangs- bzw. Endzustände emittiert werden, beschränkt. Mittels adsorbierten Atomen und hochauflösender Photoelektronenspektroskopie ist es uns möglich, die Zeitverzögerung von Elektronen welche vom Adsorbat emittiert werden, zu ermitteln und dadurch die absolute Photoemissionszeit von Metallzuständen zu bestimmen. Attosekundenspektroskopie mit isolierten Pulsen war ausserdem bisher auf einzelne Photonenenergien beschränkt. Wir wiederholen die Experimente bei einer Reihe von Photonenenergien und entwickeln die sogenannte Streakingspektroskopie hin zu einer energieauflösenden Messmethode weiter.

Indem wir Messungen der energieabhängigen und absoluten Photoemissionszeitverzögerung verbinden, können wir ein quantitatives Verständnis der einzelnen mikroskopischen Verzögerungsmechanismen und ihren Beitrag zur beobachteten absoluten Photoemissionszeit erhalten. Hierzu wurden klassische und semiklassische Modelle mit Eingangsinformationen aus hochauflösender Photoelektronenspektroskopie und (zeitabhängiger) Dichtefunktionaltheorie erstellt, berechnet und analysiert. Die dabei getroffenen Vorhersagen stimmen mit den experimentellen Beobachtungen überein, und erlauben uns die Unterscheidung der einzelnen mikroskopischen Beiträge der elastischen und inelastischen Streuung, der komplexen Bandstruktur und des ballistischen Transportes, welche bisher nur einzeln und beispielhaft anhand geeigneter Systeme diskutiert werden konnten.

Abstract

This thesis reports experiments and numerical calculations aiming at the observation, analysis and quantitative dissection of the microscopic mechanisms contributing to the temporal delays observed in time-resolved measurements of the attosecond photoelectric effect, i.e. the delayed appearance of the photoelectron in vacuum after excitation of metallic samples with extreme-ultraviolet (XUV) radiation. We combine the experimental techniques of high-harmonic generation, isolated attosecond pulse filtering and XUV photoemission spectroscopy in an ultra-high vacuum environment to release and probe photoelectrons emerging from the metal surface and their respective time delays with temporal resolution and accuracy on the 10 as time scale (1 as $= 10^{-18}$ s). Upon traversing the metal-vacuum interface, the photoelectron momentum is modulated by interaction with a phase-controlled few-cycle laser pulse, wherein the time of surface traversal is encoded in the momentum deflection of the outgoing electron.

Until recently, the measurement of photoemission time delays was limited to the observation, analysis and numerical modelling of relative time delays, i.e. the retardation of photoelectrons emerging from or through spectroscopically distinguishable initial or final states. By using surface adsorbates and high-resolution photoemission spectroscopy, we can gauge the release of photoelectrons from atomic adsorbate states located outside the crystal and use this knowledge to determine the absolute photoemission time delay from electronic states located inside the crystal. Furthermore, the extension of attosecond streaking spectroscopy from single frequency measurements towards broadband, energy-dependent spectroscopy is reported. This is accomplished in the simplest of manners, through lengthy repetition of the experiment at different central photon energies using different configurations of the attosecond pulse filtering stage and clean tungsten surface and adsorbate configurations.

Combining the measurement of the absolute time delay and broadband attosecond chronoscopy, we can quantitatively model the individual microscopic retardation mechanisms and their respective contribution to the observed release time of the photoelectrons. To this end, classical and semiclassical models including inputs from high-resolution photoemission experiments carried out with narrowband synchrotron radiation and (time-dependent) density functional theory are constructed and calculated. Their predictions match the observed photoemission time delays and allow the disentanglement and dissection of the observed relative and absolute time delays down to the individual microscopic contributions of the (intra-atomic) elastic and inelastic scattering and the complex band structure, which influence the electron trajectory, and hitherto have only been discussed individually.

List of Publications

Directly related to this thesis

Time-Frequency resolved absolute photoemission time delays from condensed matter
J. Riemensberger, M. Ossiander, M. Jobst, M. Schnitzenbaumer, A. Kim, D. Potamianos, M. Schäffer, M. Gerl, M. Mittermair, A. Guggenmos, D. Lizzit and L. Bignardi, U. Kleineberg, S. Lizzit, F. Allegretti, W. Helml, R. Ernstdorfer, A. Cavalieri, D. Menzel, J. Barth, E.E. Krasovskii, P. Feulner, S. Neppl and R. Kienberger

in preparation

Attosecond chronoscopy of soft x-ray photoemission from resonant sp-band excitation
J. Riemensberger, S. Neppl, D. Potamianos, M. Schäffer, M. Schnitzenbaumer, M. Ossiander, A. Guggenmos, U. Kleineberg, P.M. Echenique, F. Allegretti, D. Menzel, J. Barth, A.G. Borisov, A.K. Kazansky, R. Kienberger and P. Feulner

in preparation

Absolute Timing of the Photoelectric Effect
M. Ossiander, J. Riemensberger, S. Neppl, M. Mittermair, M. Schäffer, A. Duensing, M. Wagner, R. Heider, M. Wurzer, M. Gerl, M. Schnitzenbaumer, J.V. Barth, F. Libisch, C. Lemell, J. Burgdörfer, P. Feulner and R. Kienberger

Nature 561, pp.374 (2018)

Chromium/Scandium multilayer mirrors for attosecond pulses at 145 eV
A. Guggenmos, M. Jobst, M. Ossiander, S. Radünz, J. Riemensberger, M. Schäffer, A. Akil, C. Jakubeit, P. Böhm, S. Noever, B. Nickel, R. Kienberger, F. Krausz and U. Kleineberg

Optics Letters 40, 12, pp.2846 (2015)

Other

Attosecond-streaking spectroscopy on a liquid-water microjet
A. Jain, R. Heider, M. Wagner, A. Duensing, T. Gaumnitz, I. Jordan, J. Ma, J. Riemensberger, M. Mittermair, W. Helml, R. Kienberger, H.J. Wörner

in preparation

Enantiospecific desorption with circular polarized light
F. Mohateb, K. Oberhofer, J. Riemensberger, R. Kienberger, U .Heiz, H. Iglev, A. Kartouzian

in preparation

Few-Femtosecond Wave Packet Revivals in Ozone
T. Latka, V. Shirvanyan, M. Ossiander, O. Razskazovskaya, A. Guggenmos, M. Jobst, M. Fieß, S. Holzner, A. Sommer, M. Schultze, C. Jakubeit, J. Riemensberger, B. Bernhardt, W. Helml, F. Gatti, B. Lasorne, D. Lauvergnat, P. Decleva, G.J. Halász, Á. Vibók and R. Kienberger

submitted

Ultrafast quantum control of ionization dynamics in krypton
K. Hütten, M. Mittermair, S. O. Stock, R. Beerwerth, V. Shirvanyan, J. Riemensberger, A. Duensing, R. Heider, M.S. Wagner, A. Guggenmos, S. Fritzsche, N.M. Kabachnik, R. Kienberger and B. Bernhardt

Nature Communications 9, pp.719 (2017)

Dispersion engineering of thick high-Q silicon nitride ring-resonators via atomic layer deposition
J. Riemensberger, K. Hartinger, T. Herr, V. Brasch, R. Holzwarth and T.J. Kippenberg

Optics Express 20, 25, pp.27661 (2012)

Universal formation dynamics and noise of Kerr-frequency combs in microresonators
T. Herr, K. Hartinger, J. Riemensberger, C.Y. Wang, E. Gavartin, R. Holzwarth, M.L. Gorodetsky and T.J. Kippenberg

Nature Photonics 6, pp.480 (2012)

List of presented conference and invited seminar talks

Directly related to this thesis

Band structure influence in high-energy attosecond photoemission spectroscopy
J. Riemensberger, M. Schäffer, M. Schnitzenbaumer, D. Potamianos, M. Ossiander, J. Barth, S. Neppl, R. Kienberger and P. Feulner

ATTO 2017 Xi'An - 14.7.2017

Energy dependent photoemission delays from the (0001) surface of Magnesium
J. Riemensberger, M. Schäffer, M. Schnitzenbaumer, D. Potamianos, M. Ossiander, J. Barth, S. Neppl, R. Kienberger and P. Feulner

Ultrafast Surface Dynamics 10, Inzell - 16.6.2017

Excitation energy dependent attosecond photoemission timing in tungsten
M. Jobst, S. Neppl, J. Riemensberger, M. Ossiander, M. Schäffer, E. Bothschafter, M. Gerl, A. Kim, J. Barth, F. Krausz, P. Feulner and R. Kienberger

2015 Conference on Lasers and Electro Optics (CLEO), San Jose - 15.5.2015

Attosecond Photoemission Spectroscopy on Surfaces and Interfaces
J. Riemensberger, M. Jobst, A.Schiffrin, S. Neppl, M. Ossiander, M. Schäffer, E. Bothschafter, M. Gerl, A. Kim, J. Barth, F. Krausz, P. Feulner and R. Kienberger

Invited talk, Condensed Matter Seminar, UBC Vancouver - 23.4.2015

Other

Photoactive metal-organic nanoarchitectures on surfaces: Probing ultrafast intramolecular charge dynamics

J. Riemensberger, A. Schiffrin, M. Jobst, M. Gerl, M. Schäffer, M. Ossiander, A. Guggenmoos, N. Karpowicz, J.V. Barth, P. Feulner, S. Burke, F. Krausz and R. Kienberger

2013 Workshop on Quantum Materials, Stuttgart - 13.12.2013

Phase noise and dispersion in integrated silicon nitride based Kerr-Comb generators

J. Riemensberger, K. Hartinger, T. Herr, E. Gavartin, R. Holzwarth and T.J. Kippenberg

2012 Conference on Lasers and Electro Optics (CLEO), San Jose - 11.6.2012

Contents

List of Figures

List of Tables

List of Abbreviations

XUV	extreme-ultraviolet
UHV	ultra-high vacuum
HHG	high-harmonic generation
NIR	near-infrared
(TD-)DFT	(time-dependent) density-functional theory
RABITT	reconstruction of attosecond bursts by interference of two-photon transitions
FWHM	full width at half maximum
CEP	carrier-envelope-phase
SFA	strong-field approximation
SAE	single-active electron approximation
CMA	central-momentum approximation
TOF	time-of-flight
ARPES	angle-resolved photoelectron spectroscopy
LEED	low-energy electron diffraction
FLAPW	full-potential linearised augmented plane wave
CPA	chirped-pulse amplification
RWA	rotating-wave approximation
CTT	classical-transport-theory

Part I

Introduction

Introduction

The photoelectric effect, which is the release of electrons from matter upon irradiation with ultraviolet light, was first described independently by Heinrich Hertz [1] and Wilhelm Hallwachs [2] in 1887 and 1888, respectively. The most peculiar observation of the existence of a minimum optical frequency for the exciting radiation and the independence of the electron energy from the intensity of the irradiating light observed by Phillip Lenard [3] was explained by Albert Einstein [4] in 1905. This work, for which he was awarded the Nobel Prize in 1921, confirmed the quantization hypothesis of light introduced empirically by Max Planck [5] in order to explain the optical spectrum of black-body radiation and thereby laying the groundwork for the quantum revolution of experimental and theoretical physics in the 20th century.

Experimental advancements over the last 100 years allowed photoemission spectroscopy to become a powerful tool for the investigation of solid, liquid and gaseous samples. However, time-resolved information about the photoemission process and the relaxation of photoexcited carriers in solids could only be obtained after the advent of ultrashort femtosecond [6, 7] and attosecond [8, 9, 10] laser pulses very recently. The time delay between the absorption of the photon and the subsequent release of the electron is on the attosecond time scale. The ultrafast inelastic scattering of the electrons inside the solid, mediated by the strong Lorentz force of electron-electron and electron-ion interactions, limits the extraction depth to few atomic layers. The recent development of the attosecond streaking technique [11, 12, 13] allows to measure these time delays with few attosecond precision and to investigate this most fundamental process of light-matter interaction with unprecedented insight. The measurement of photoemission time delays is deemed ”attosecond chronoscopy” [14].

The time-resolved observation of the photoelectric effect is a challenging experimental task. Time-resolved measurements in general rely on the observation of a change of a sample observable, such as absorption strength [15, 16, 17] or photoelectron/-ion yield [18, 19] or kinetic energy [11, 13], upon previous excitation of the sample with a light pulse shorter than the electric or vibrational processes ongoing in the sample under investigation.

Attosecond chronoscopy experiments can be carried out on samples in gas [13, 20, 21], liquid [22, 23] and solid states [12, 24, 25, 26, 27, 28, 29] using attosecond pulse trains (reconstruction of attosecond bursts by interference of two-photon transitions (RABITT)) or isolated attosecond pulses (Attosecond streaking spectroscopy). Trains and isolated attosecond pulses are generated by means of high-harmonic generation (HHG) of intense few-cycle near-infrared laser fields routinely generated in modern laboratories. The resulting high-frequency radiation is in the extreme ultra-violet (XUV) spectral range beyond the photoionization potential of all neutral matter and photoelectrons are directly generated upon irradiation of the sample. In both

cases the underlying time axis for determination of the photoemission time delay is provided by cross-correlation with a synchronized near-infrared (NIR) femtosecond laser pulse, the spatio-temporal field distribution of which defines the characteristic clock of the experiment. A most peculiar case are metals, where the p-polarized external NIR field is all but fully screened outside the surface atomic layer by the highly mobile conduction band electrons [30, 31, 25]. Hence, the interaction between the released electron and the clocking NIR field begins at a well defined spatial position above the crystal deemed the jellium edge. The relative delay in photoemission measured in attosecond chronoscopy thus can be interpreted as the relative arrival time of the center-of-mass of the excited photoelectron wavepackets at the jellium edge. Hence, these concepts paved the path to the observation of electron movements in solids on their natural attosecond time scale. The time duration of the photoelectric effect in solids can be estimated by the mean free escape depth and the group velocity of the excited electrons inside the solid. For excitation with XUV light above photon energies of 20 eV, photoemission times of 100 as up to 300 as are estimated and observed [12, 25, 28].

Three particular recent experimental results stand out. First the measurements of Neppl et al. [25], who investigated photoemission time delays between tungsten 4f and magnesium 2p electrons excited from a system of few atomic layers of magnesium over a tungsten single crystal surface at 117.5 eV. Systematic variation of layer thickness not only allowed to verify the theoretical result of screening of the infrared field on the sub-atomic scale, but also to assign a ballistic velocity equal to the free electron velocity, within the margin of error to the propagation inside the magnesium layers. A second series of studies by Tao et al. [28, 29] measured the time delay between the doublet of 3d states from nickel and copper valence bands using the RABITT technique with $20 - 30$ eV photons. The observed photoemission time delays are assigned to the lifetime of the final state of the electron corresponding to the bandwidth of resonant enhancement. Furthermore, Siek et al. [32] observed that effects of intra-atomic electron-electron interaction and angular momentum of the localized initial state contribute to the photoemission time delay not only in atomic physics, but do need to be accounted for also in dissecting observed photoemission time delays in solid-state attosecond chronoscopy, especially for heavy elements.

One of the main results of this work is the observation of band structure related photoemission time delays at high photon energies in excess of 120 eV, which is presented in detail in chapter III. Herein, the relative time delay between the emission from localized 2p core orbitals and delocalized conduction band states in magnesium is measured for a range of photon energies. Comparing experimental results, both attosecond time-resolved as well as high-resolution photoemission, with a range of contemporary theories of the photoemission time delay is performed to gain insight into the time dependence of bulk and surface photoemission processes from simple metals.

Hitherto attosecond chronoscopy experiments relied on an internal reference and could only provide relative time delays between photoemission events from two discernible bound states. An absolute and precise calibration of the attosecond streaking clock to the absorption of the XUV photon is still lacking. Two approaches have been developed in recent years. The first approach is using a separate gas phase target for an additional attosecond chronoscopy experiment [26, 33]. This ex-situ approach has severe limitations in terms of the measurement precision because of the difficulty of Gouy-phase calibration [34], where one attosecond systematic error corresponds to 2.5 mrad Gouy-phase mismatch. The second approach is to use helium as an internal reference, for which the time delay of the 1s level is known from experiment and extensive studies of all-electron ab-initio theory. Using helium as a reference in solid state photoemission chronoscopy is possible, but very challenging as it necessitates sub-4 Kelvin cryogenic operation and very low NIR light flux to avoid desorption. A more feasible approach is presented in this thesis and makes use of adsorbed heavy atoms, which feature well-localized weakly bound core orbitals, as clock atoms on top of a metallic crystal and within or above the jellium edge [35]. Herein, it is necessary to calibrate both the atomic time delay of photoemission as well as the influence of the adsorbate layer on the electronic scattering and dielectric screening of the combined system. In chapter IV a method is presented to achieve the latter using a sub-monolayer iodine coverage on a tungsten single crystal. To this end, utilizing a combination of two adsorbate systems, iodine and oxygen, and two different radiation sources, table-top HHG attosecond XUV pulses and monochromatized undulator radiation from the ELETTRA synchrotron facility in Trieste, Italy, we measure time delays of the valence band and the 4f core level of the tungsten (110) surface on unprecedented spectral bandwidth of 90 eV to 145 eV with 10 as level accuracy. Using extensive numerical calculations, which combine a semiclassical model of the time-dependent photoemission with inputs from contemporary (time-dependent) density functional theory ((TD)-DFT), we unravel and dissect the individual microscopic mechanisms of attosecond time delay and provide quantitative comparison between theory and experiment. Furthermore, broadband information about the absolute time delay of photoemission for core levels as well as valence bands is obtained, which allows to shed the ambiguities that have complicated the interpretation of attosecond chronoscopy of solid samples for such a long time. We thus finally solve the twelve year old question posted by A. Cavalieri in their seminal paper about the time delay of the tungsten 4f core level. The extension of attosecond chronoscopy beyond the measurement of relative and the guessing of absolute time delays bears profound consequence in extending time resolved photoemission spectroscopies beyond the investigation of gas phase atomic and simple crystals into complicated systems such as 2d layered systems, i.e. perovskites, cuprates or topological insulators, and the liquid phase.

Part II

Attosecond solid state photoemission chronoscopy

Attosecond solid state photoemission chronoscopy

2.1. Introduction

In this chapter the fundamentals of attosecond pulse generation and chronoscopy as well as solid state (angle-resolved) photoemission are presented and reviewed to the extent necessary to understand the performed experiments and analysis.

Performing attosecond chronoscopy measurements on solid targets requires the combination of two experimentally challenging techniques. First the generation of isolated attosecond extreme ultraviolet (XUV) pulses or pulse trains through high harmonic generation (HHG) from intense sub-two cycle near-infrared (NIR) laser pulses. The NIR laser field $\vec{E}_L(t)$ propagates along the x-direction and the z-axis is aligned with its linear polarization

$$\vec{E}_L(t) = \Re\left\{E_{0,L}(t)\cdot\vec{e}_z\cdot e^{-iw_L\cdot t-\frac{i}{2}\beta_L\cdot t^2+\phi_{CE}}\right\}. \tag{2.1}$$

Herein ω_L denotes the central angular frequency and $k_L = 2\pi/\lambda_L$ the wavenumber of the infrared field with central wavelength λ_L. The Gaussian function $E_{0,L}(t) = E_{0,L}\cdot e^{-4ln(2)t^2/\tau_L^2}$, represents the envelope of the laser field with full width at half maximum (FWHM) τ_L. The quadratic chirp of the laser field is denoted β_L, and ϕ_{CE} represents the carrier-envelope-phase (CEP), which is the phase delay between the respective maxima of $\vec{E}_L(t)$ and $E_0(t)$. Similarly, the isolated attosecond XUV pulse is parametrized as with a Gaussian temporal envelope and is always polarized parallel to the generation NIR field

$$\vec{E}_{0,X}(t) = \Re\left\{E_{0,X}(t)\cdot\vec{e}_z\cdot e^{-iw_X\cdot t-\frac{i}{2}\beta_X\cdot t^2}\right\}, \tag{2.2}$$

with the envelope function $E_{0,X}(t) = e^{-4ln(2)t^2/\tau_X^2}$. The envelope of the XUV field is normalized, because the inefficiency of HHG negates the possibility of driving and resolving nonlinear optical interactions driven by the XUV field in our experimental setup. Isolated attosecond pulse generation relies on the availability of CEP-stable intense NIR driver fields. Although commercial titanium sapphire lasers delivering sub-mJ energy, sub-two cycle pulses can be considered state of the art nowadays, a short description of the different laser systems driving the experiments is given in section 2.6.1 for the sake of completeness. It is crucial for attosecond chronoscopy of metal surfaces to prepare and characterize clean single crystal surfaces in an ultra-high vacuum (UHV) system. A concise description of the utilized UHV beamline will be given in section 2.6.2.

Attosecond chronoscopy experiments rely on the cross-correlation of a sub-femtosecond XUV light pulse with a rapidly varying electric field to modulate the kinetic energy spectrum of the released photoelectrons [36]. The NIR laser field, often also called the streaking field, exerts a periodic change of the released electron momentum via the Lorentz force and is conveniently provided by the driving laser field. The last requirement is the attosecond level synchronization of the two fields in the experiment, which is intrinsic to the non-perturbative and phase-sensitive HHG process [10]. All the experiments presented in this thesis have been carried out using attosecond streaking spectroscopy with isolated attosecond pulses, however recently also the technique of RABITT utilizing attosecond pulse trains emerged as a viable and complementary technique for attosecond chronoscopy on solid state targets. Both techniques and their respective advantages and disadvantages and range of applicability are described and compared in section 2.4.

2.2. Interaction of intense laser pulses with matter

The foundation of the field of attosecond physics are nonperturbative optics and strong field physics, wherein the perturbative approximation of the optical polarization response $\vec{P}$ in relation to the strong laser field $\vec{E}$

$$\vec{P}(\vec{E}) = \epsilon_0 \chi_1 \cdot \vec{E} + \epsilon_0 \chi^{\langle 2 \rangle} \cdot \vec{E} \cdot \vec{E} + ... + \epsilon_0 \chi^{\langle n \rangle} \cdot \vec{E} \cdot ... \cdot \vec{E}, \tag{2.3}$$

with

$$|\chi_n| \approx \alpha \, |\chi_{n-1}| \,, \;\; \alpha \ll 1,$$

breaks down. This situation is formally equal to the strength of the laser field reaching the level of the strong microscopic intra-atomic electrostatic field binding the outermost electrons, which for hydrogen is given by the Hartree field $5.1 \cdot 10^9$ V/cm. These extreme conditions can be technically realized nowadays using high-energy ultrashort pico- and femtosecond laser pulses. During each half-cycle of the electric field a significant fraction of the neutral atoms are ionized. In general, three dominant mechanisms of ionization in strong low frequency laser fields are distinguished (see figure 1) by the so-called Keldysh parameter γ_K of the atom and the laser field [37]

$$\gamma_K = \sqrt{\frac{I_p}{2U_P}}, \tag{2.4}$$

wherein I_P denotes the first ionization potential of the atom and U_P denotes the ponderomotive energy, i.e. the cycle-averaged quiver energy of the laser field

$$U_P = \frac{e^2 \cdot max\left\{|E_0(t)|^2\right\}}{4 m_e \omega_L^2}, \tag{2.5}$$

where e and m_e are the charge and mass of the electron respectively. The main achievement of Keldysh theory is the use of a laser-dressed continuum as final states of strong-field ionization, which allows the unification of all three ionization processes into a single theoretical description, neglecting the influence of the electrostatic Coulomb potential of the parent ion on the final state of the electron after ionization. This approximation is deemed the strong-field approximation (SFA) [38].

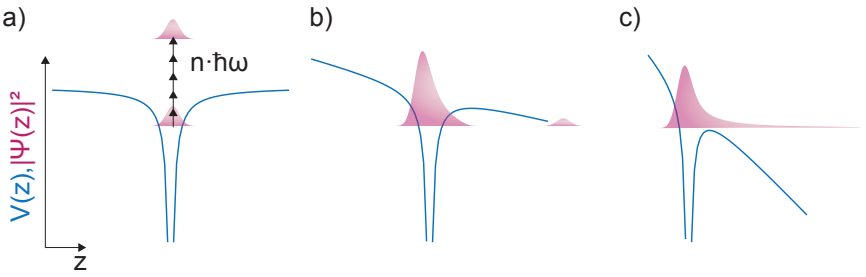

Figure 1 Illustration of ionization mechanisms in strong-field physics. a) Multiphoton ionization. b) Tunnel ionization. c) Above-threshold ionization

The first mechanism is multiphoton ionization (see figure 1 a), wherein a single electron absorbs an integer number of photons and in turn is excited above the vacuum level of the atom. The probability of sequential multiphoton ionization P_I can be described perturbatively by an exponential scaling law

$$P_I(t) \propto \left|E_L(t)^2\right|^n, \tag{2.6}$$

with

$$n = \frac{I_P}{\hbar\omega_L}.$$

Multiphoton ionization is the predominant ionization mechanism at high Keldysh parameters $\gamma_K > 1$. For high intensities of the NIR streaking field, perturbative multiphoton ionization processes contribute considerably to the photoelectron spectrum at low kinetic energy in attosecond chronoscopy experiments. HHG on the other hand is nonperturbative and cannot be expressed correctly in the multiphoton picture. The second process is tunnel ionization (see figure 1 b), which is the dominant ionization mechanism for Keldysh parameters in the range of $0.1 < \gamma < 1$. The strong laser field distorts the symmetrical Coulomb potential around the atom to an extent, which facilitates quantum mechanical tunneling between the bound electron wavefunction and the laser-dressed continuum. Most importantly however, tunnel ionization constitutes the first step in HHG (see section 2.3.1). The tunnel ionization rate can be calculated for example using the PPT formalism [39] or the ADK formalism [40]. The cycle averaged ionization rate in the ADK formalism for the hydrogen atom W_{ADK} can be expressed as

$$W_{ADK} \propto I_P \cdot e^{-\frac{2\,(2I_P)^{3/2}}{3E_0}}. \tag{2.7}$$

A non-adiabatic correction for the ADK formalism is found in [41]. The ionization probability for a

single atom at an instance in time w.r.t to the driving laser pulse $E(t)$ follows as

$$P_I(t) = 1 - e^{\int_{-\infty}^{t'} W(t')\,\mathrm{d}t'}. \tag{2.8}$$

The third mechanism is deemed above-threshold ionization, which is dominant for small Keldysh parameters $\gamma_K \ll 1$ and is depicted in figure 1c. The ground state wavefunction of the valence electrons in the absence of external fields is no longer a bound state in the presence of the strong laser field and can freely propagate outside of the influence of the ionic potential. Complete ionization and generation of higher charged states of the neutral atoms occurs.

2.3. High harmonic generation

The term high harmonic generation denotes the process of radiation oscillating at very high (up to 5000) [42] integer multiples of the carrier frequency of the visible or infrared field, which drives the nonlinear process. First observation of the HHG process is attributed to Burnett et al. [43] in reflection from solids and McPherson et al. [44] in gases. The nonperturbative nature of the process, i.e. the observation of a plateau of harmonics with non-diminishing radiation intensity for increasing harmonic order was first recognized in a series of ground breaking experiments using picosecond Nd:Yag lasers by A. Huillier et al. [45, 46].

2.3.1. Single atom response

Early theoretical assessments of HHG relied on numerical solutions of the full time-dependent Schrödinger equation, which could explain the formation of nonperturbative plateau harmonics but failed to provide an intuitive physical insight into the microscopic single atom response underlying HHG [47, 48]. This was only managed later by P. Corkum and the development of the so called three-step-model [49], which is illustrated in figure 2.

The main achievement of the three-step model is to break up the complex quantum mechanical electron trajectories into three distinctive steps, which can much more easily be calculated, and relating the center-of-mass movement of the electron wavepacket in the laser field, pivotal to all non-perturbative optics, to a classical trajectory through the Ehrenfest theorem [49]. This provides an intuitive understanding of the microscopic mechanism of HHG. Further refinement was provided by Lewenstein [50] who replaced the classical trajectory calculation with a quantum mechanical integration in the strong field approximation. The equations are then exactly solvable within the saddle-point approximation of the path integral of the quantum mechanical trajectory.

1. Tunnel ionization of a valence electron

   The distortion of the Coulomb potential by the strong laser field facilitates the tunneling of

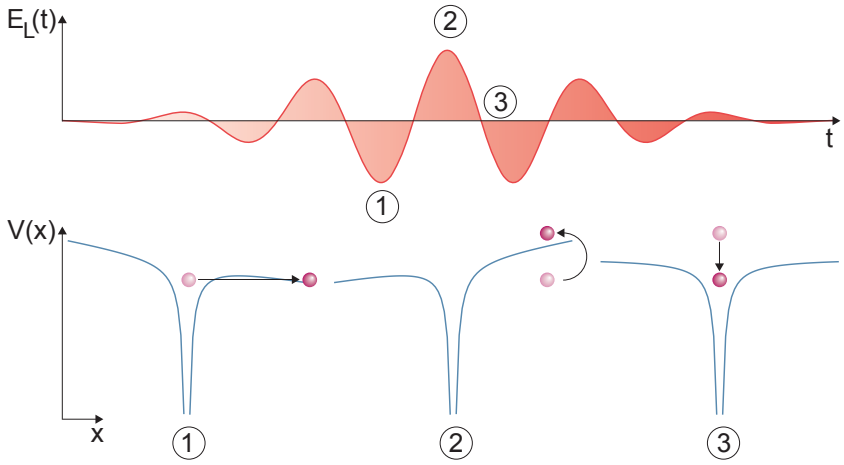

Figure 2 Illustration of the three step model of high harmonic generation for the Coulomb potential $V(x)$. (1) Tunnel ionization of the atom at the crest of the intense laser field $E_L(t)$. (2) Acceleration of the electron away from the parent ion to the reversal point, acceleration back towards the ion. (3) Recombination with the parent ion. All energy is released into a single XUV photon.

valence electrons through the now finite-width potential barrier, as illustrated in figure 1. Because of the exponential dependence of the ionization rate on the field strength (ref. eq. 2.7), ionization events are localized in time around the individual half-cycle maxima and minima of the electric field. In the Lewenstein model, the electron is assumed to be at rest ($E_{kin} = 0$) after tunnel ionization.

2. Acceleration in the laser field

   The ionized electron is subsequently accelerated by the strong laser field away from the parent ion. The Coulomb potential of the parent ion is neglected in the numerical propagation, greatly reducing the numerical effort. After a quarter cycle the sign of the laser field is inverted and the electron decelerated. For linear and almost linear polarization of the laser field, the electron trajectory traverses the parent ion again after approximately three quarters of the optical cycle. The maximum kinetic energy transferred to the electron is $3.17U_P$ and corresponds to electrons ionized $17°$ after the electric field crest of the previous half-cycle. Most electrons do not recombine with the parent ion and undergo another cycle of deceleration and acceleration in the periodic electric field of the driving laser pulse.

3. Radiative recombination with the parent ion

   A small fraction of electrons upon traversing through the vicinity of the parent ion recombines, releasing all its energy into a single XUV photon.

$$E_{max} = I_P + 3.17U_P \tag{2.9}$$

The quantum mechanical probability for recombination is given by the dispersive spreading of the electron wavepacket along its trajectory [51] and the size of the photoemission

matrix element. Radiative recombination is the time-reversed process of single-photon photo-emission. Hence, the magnitude of the photoemission matrix element is crucial for the efficient generation of high-harmonic radiation [52]. For electrons ionized in a laser field of elliptical or circular polarization, no spatial overlap with the parent ion is generated during propagation. Thus, recombination and HHG are strongly suppressed in elliptical fields [53, 54, 55]. Circularly polarized one [56] and two-colour fields [57] however can be combined and adjusted for single attosecond pulse generation or XUV pulse generation with circular polarization [58].

The maximum attainable photon energy is thus tightly linked to the parameters of the laser under use. Most importantly, the cut-off energy scales as $E_{max} \propto \lambda^2$. A drawback is the fact that both the photoemission matrix element $\propto E_{max}^{-1/2}$ as well as the quantum mechanical spreading of the wavepacket $\propto \lambda^{-2}$ scale unfavourably with the laser wavelength. Intricate numerical calculations [59, 60], indicate an even more atrocious scaling of the harmonic emission of $\propto \lambda^{-5.5\pm0.5}$ for the cut-off harmonics, which has been experimentally confirmed by Shiner et al. [51].

The HHG process is symmetric with respect to the sign of the driving NIR laser field. Thus, two attosecond radiation bursts are created within a single cycle of the laser field. This implies that for sufficiently long pulses only odd harmonics of the laser frequency are created. A similar argument can be derived from the isotropic symmetry of the nonlinear medium, usually a noble gas. The generation of an attosecond pulse train from high harmonic generation was proposed by Farkas and Tóth [61] and experimentally confirmed by Paul et al. [8].

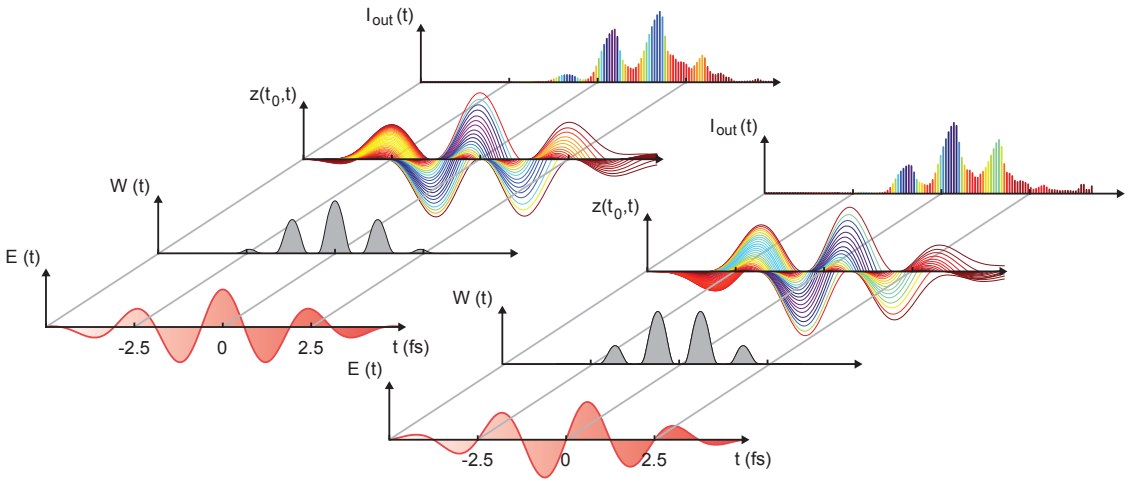

Figure 3 Illustration of the generation of complex time-energy profiles in HHG according to the three step model as a function of the CEP of NIR two-cycle pulses. (Top left: Cos-pulse, Bottom right: Sine-pulse). The ionization rate $W(t)$ is as function of the NIR electric field E(t) and is localized in time around the crests of the field half cycles. The excursion of the electron $z(t_0, t)$ from the atom as function of the release time t_0 is plotted in the third pane. The kinetic energy of the electron upon recollision is colour coded with purple shading representative of the highest energy electrons and dark red colour indicating the lower kinetic energies. The time-energy distribution of recollision energies $I_{out}(t)$ is plotted in the uppermost panel. We find that the cut-off radiation is distributed over two consecutive half-cycle field crests for the Sine-pulse. For Cos-pulses, the highest energies are contained within a single attosecond burst.

The trajectories and quantum phases corresponding to the emission of individual harmonics can be traced out using advanced two-colour [62, 63] or elliptical polarization gating mechanisms [64]. The single atom response to NIR fields of different CEP and the trajectories of the released electrons are illustrated in figure 3. Two types of trajectories, the so-called short and long trajectories, wherein the spatial excursion is smaller or larger than in the cut-off trajectory respectively, are distinguished [65] within a single cycle of the electric field. They differ in terms of their phase-matching properties, which will be outlined in section 2.3.2. The highly nonlinear ionization probability (grey area) is localized in time around the half-cycle field crests, and the classical equations of motion of the electron in the laser field, neglecting the Coulomb potential of the parent ion, are straightforwardly integrated to reveal the characteristic trajectories of HHG. It is noted that only trajectories, which return to the position of the parent ion within a single cycle of the laser pulses are plotted in figure 3. The non-recombining fraction of ionized electrons is re-accelerated along the next half-cycle of the driving laser field and again may collide with the parent ion. However, radiative recombination is strongly suppressed due to dispersive spreading of the quantum mechanical wavepacket over the prolonged propagation time of the trajectory.

2.3.2. Ensemble response and phase matching

Efficient nonlinear frequency conversion relies on coherent in phase emission of generated radiation over the full volume of the nonlinear medium. This condition is formally equivalent to the requirement of momentum conservation between the generating NIR photons and the radiated XUV photon. The requirement of photon energy conservation of course is implied, because the electron is subject to purely conservative forces along the trajectory and both tunnel ionization as well as radiative recombination are non-dissipative processes.

$$\begin{aligned} \vec{k}_X - n \cdot \vec{k}_L &= 0 \\ \hbar\omega_X - m \cdot \hbar\omega_L &= 0. \end{aligned} \tag{2.10}$$

Detailed studies of phase-matching in HHG including the extreme cases of very tight focusing and waveguiding in hollow-core fibers can be found in [66, 67, 68, 69]. In short, four main contributions to phase mismatch along the propagation direction Δk_z,

$$\Delta k_z = \Delta k_q + \Delta k_g + \Delta k_n + \Delta k_p \stackrel{!}{=} 0, \tag{2.11}$$

are distinguished.

1. Neutral gas dispersion Δk_n

   Both the NIR and XUV fields are non-resonant with the atomic transitions of the generating medium, however they are influenced by the polarization response of the noble gas medium. The NIR field has lower frequency than the lowest atomic transitions in all noble gases, therefore retardation of the phase is observed. The XUV field is always of higher

frequency compared to the atomic transitions because the bound-continuum transition of radiative recombination is always higher in energy than the bound-bound transitions dominating the polarization response of the medium. Hence, advancement of the XUV field phase is observed and the overall phase mismatch contribution $\Delta k_n > 0$ of the neutral gas atoms is in general positive.

2. Plasma dispersion Δk_p

   The second contribution to the refractive index of the medium is the polarization response of the ionized atoms and free electrons. The plasma frequency

$$w_p = \sqrt{\frac{n_e \cdot e^2}{m_e \cdot \epsilon_0}} \tag{2.12}$$

   of free electron densities n_e corresponding to diluted noble gas plasma at pressure 200 mbar and neutral gas ionization fraction of 1%, is around 2 THz, which is far below the frequency of the NIR and XUV fields. Hence, the refractive index is smaller than unity and the phase of both XUV and NIR fields is advanced, stronger so in case of the NIR field. The resulting phase mismatch contribution of the plasma $\Delta k_p < 0$ is always negative.

3. Gouy phase shift Δk_g

   A focused Gaussian laser pulse experiences a position-dependent phase shift along the propagation direction, which along the optical axis is given by

$$\Delta\Phi = -tan^{-1}\left(\frac{z}{z_R}\right), \tag{2.13}$$

   wherein $z_R = \frac{\pi \cdot w_0^2}{\lambda_L}$ denotes the Rayleigh length of the Gaussian laser focus, with the focussed beam waist w_0 and the laser wavelength λ_L. The Gouy phase shift [70] was initially predicted by Louis Gouy in 1890, but could only be experimentally confirmed in the THz spectral region by Ruffin et al. 102 years later [71]. Recently Hoff et al. [72] succeeded in performing a three dimensional characterization of the spatial phase shifts in a tight focus of a few cycle laser through near-field enhanced multiphoton photoemission from a tungsten nanotip, revealing a more intricate phase dependence in tight laser foci of few-cycle laser pulses.

   The resulting contribution to the phase mismatch can be interpreted as the equivalence of the derivative of the Gouy-phase shift along the propagation direction to an effective wavevector [67, 65]

$$k_g = \frac{\partial}{\partial z}\Delta\Phi. \tag{2.14}$$

   Because the Rayleigh length is much larger and the divergence angle $\phi_X = \phi_L/\sqrt{m}$ for the generated XUV radiation of harmonic order m, compared to the driving NIR laser pulse, the Gouy phase gradient of the generated XUV field is strongly reduced. Hence, a

net contribution to phase mismatch arises $\Delta k_g < 0$, which is always negative.

4. Atomic dipole phase shift Δk_a

The last contribution to phase mismatch arises from the HHG process itself and can intuitively be understood in context of the three-step model. As can bee seen from figure 3 a, an XUV photon energy-dependent time delay between the zero-crossing of the laser field and the time instance of radiative recombination exists. This time delay corresponds to a phase delay and is intensity-dependent [73, 67]. Because the NIR intensity decreases both along as well as perpendicular to the direction of propagation away from the focus, a contribution to the phase mismatch arises similar to the Gouy phase shift

$$\Delta k_q = -\alpha \cdot \frac{\partial}{\partial z} I(z). \tag{2.15}$$

The proportionality constant α is always positive and much larger for long trajectories compared to short trajectories. Hence, the high-frequency photon emission from electrons traversing along short trajectories can be isolated using suitable focusing optics and gas pressure [74].

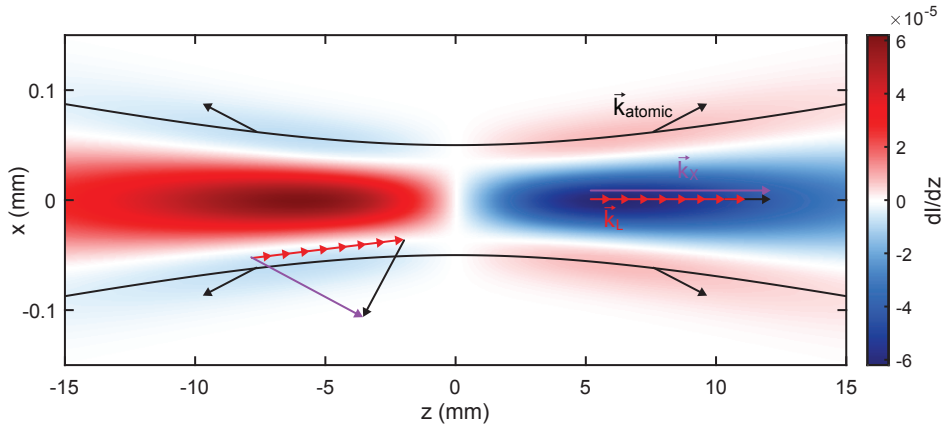

Figure 4 Illustration of HHG phase matching of Gaussian laser focus. The axial intensity gradient is colour coded. The resulting atomic phase wavevector is indicated as black arrows. The wavevectors of the XUV and NIR beams are indicated as violet and red arrows, respectively. The solid grey lines mark the Gaussian beam waist. The region in front of the focus is favourable for phase matching of noncollinear long trajectory HHG. The region after the focus is suitable for phase matching of collinear short trajectory harmonics, which are necessary for the attosecond experiments.

Furthermore, it should be noted that the short-trajectory phase-matching cut-off of few-cycle to single-cycle pulses extend to higher energy and the temporal structure of the harmonic emission becomes shorter [75], ultimately permitting the generation of single attosecond pulses. Regardless, it is paramount to the efficient generation of XUV radiation to carefully choose the focusing conditions, laser intensity and gas target pressure and geometry in order to obtain a long coherence length $l_{coh} = 2\pi/\Delta k$ between the NIR driver laser and the generated XUV radiation [76, 77]. The most efficient nonlinear frequency conversion is obtained if the coherence length exceeds the absorption length l_{abs}. This argument indicates that the highest conversion efficiency for high harmonic generation can surprisingly be obtained for long wavelength driving pulses

and very high energy X-ray emission [78, 42]. However, limitations to the long wavelength/high pressure scaling of HHG is expected due to the absorption of the IR driver laser in the generated high-density plasma (ref. eq. 2.12).

Recently, universal scaling laws of nonperturbative optics in the gas phase were derived by Heyl et al. [79], in turn heavily simplifying the design process of new HHG beamlines, because existing knowledge can be transferred between laser systems rigorously. These scaling laws can be applied in the experimental practice for example, if photoelectron count rates become too high for the detection electronics and saturation occurs. Reduction of the XUV flux, while retaining the shape of the spectrum can be achieved by reducing the diameter of the iris aperture and the gas pressure concurrently.

2.3.3. Isolation of a single attosecond pulse

Isolated attosecond pulses can be generated by a variety of means through HHG, the most successful of which is deemed amplitude gating and spectral filtering [9, 11], which will be described in this section. Further methods of isolated attosecond pulse generation include polarization gating [56] or double optical gating [57], which rely on the superposition of two laser fields with different polarization and/or different colour spoiling HHG in all but a single half-cycle of the laser field. Lastly, ionization gating [80, 81] relies on the fact that the phase matching condition of high harmonic generation can only be fulfilled for a certain fraction of neutral gas ionization, which can be constrained to a single half-cycle on the rising edge of strong driving laser fields. Hence, only one attosecond pulse spike experiences a coherent build-up of radiation intensity in the far-field.

The concept of amplitude gating and spectral filtering is illustrated in figure 5. Two prerequisites for isolated attosecond pulse generation are identified. First, the availability of few-cycle laser pulses, which provide significant intensity contrast between the central and adjacent half-cycle field crests. This is generally realized by the use of Titanium Saphhire (Ti:Sa) lasers spectrally broadened in hollow core fibers filled with noble gases [82, 83] (see section 2.6.1), or broadband optical parametric amplifiers. Second, the possibility to stabilize the CEP of the NIR laser in order to isolate a single set of short trajectories contributing to cut-off harmonic generation [84]. Such a NIR waveform is usually called cosine-pulse (see figure 5 d,f). In contrast, a sine-pulse (see figure 5 e,h) supports two equally strong half-cycle field crests and cut-off radiation will be created at two instances during each cycle of the laser field. The possibility of CEP measurement, control and stabilization through nonlinear interferometry is closely linked to the advent of frequency comb metrology [85, 86, 87], for which the Nobel prize was awarded in 2005.

For NIR pulses approaching the single-cycle regime ($T_L = 2.5$ fs) strong deviations from the sine-cosine behaviour is observed, and isolated attosecond pulses can be generated over a

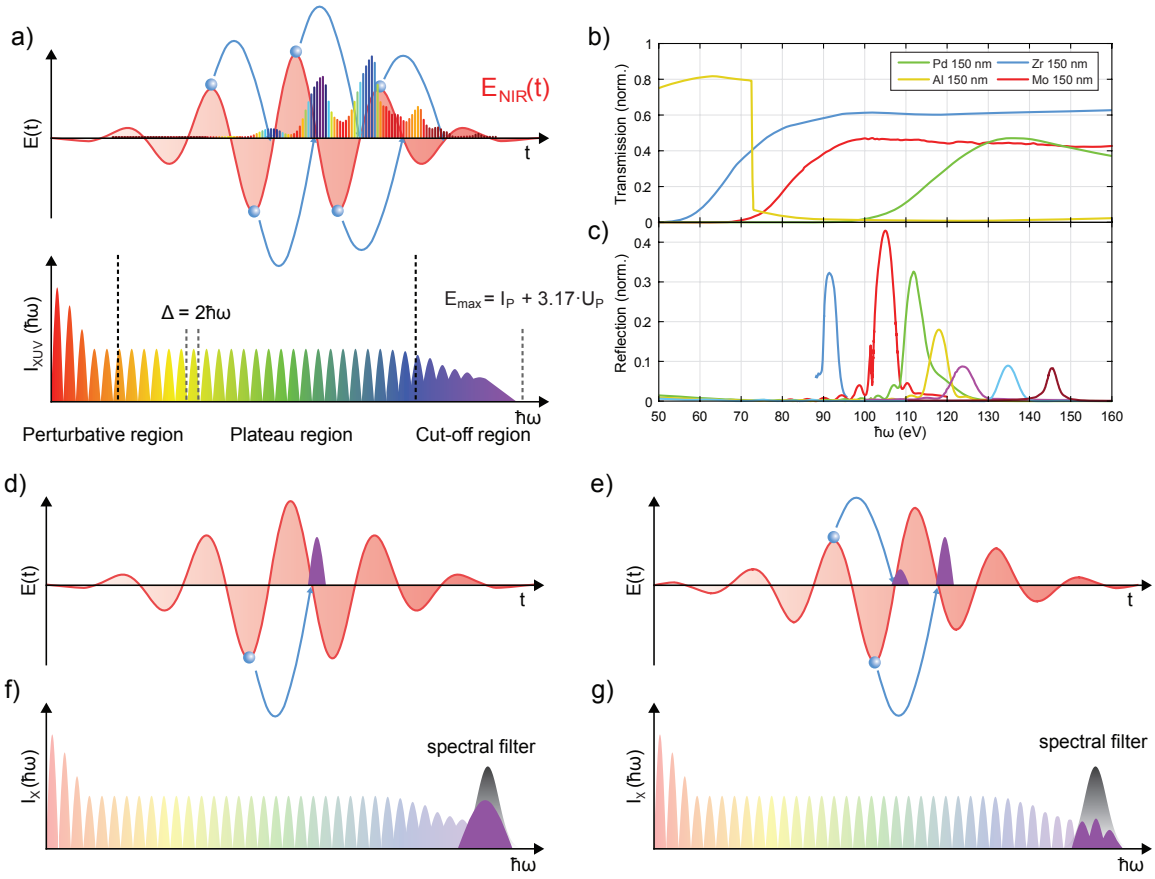

Figure 5 a) Illustration of attosecond pulse train and XUV spectrum of HHG. The colour coding is similar to figure 3. Spectral filtering curve is indicated as grey shaded area. b) Transmission of metal filters used to block low order harmonics in the experiment. c) Reflectivity of XUV multilayer mirrors utilized in the experiment to filter isolated attosecond pulses from the cut-off region of HHG and define the central energy of the attosecond chronoscopy experiment. d,e) Attosecond pulse generation from a cosine-(sine-)type NIR driver pulse. Envelope of pulse is indicated as grey shaded area. Temporal structure of XUV pulses is indicated in purple. f,g) Corresponding XUV spectra to d,e) with filtered cut-off spectrum indicated in purple.

wide range of CEP values [74]. Under certain laser conditions HHG from a sine-pulse might even be advantageous for broadband high-flux isolated attosecond pulse generation [88, 16]. Further shortening of the driver pulse towards the attosecond domain even suppresses HHG because of the insufficient ionization in the half-cycle field crest leading up to the most intense half-cycle of the NIR transient waveform [89, 90].

Spectral filtering is performed by transmission through a thin metal filter, which also blocks the generating NIR driver pulse, as well as reflection from a tailored XUV multilayer mirror designed for Gaussian reflection curves at the desired central photon energy for the experiment. The transmission and reflection curves for the filters [91] and mirrors [92] are reproduced in figure 5 b,c, respectively. Recent advances in thin film coating technology allow the extension of attosecond chronoscopy up to photon energies of 145 eV and beyond [93], as well as the preparation of attosecond pulses with controlled quadratic chirp [94].

2.4. Photoemission time delay measurements

Early measurements on time-resolved two-photon photoemission aimed at the investigation of the femtosecond relaxation of so called hot electrons, i.e. electrons excited into higher conduction band states up to several eV above the Fermi energy [95, 7]. Only the advent of attosecond pulses allowed the time-resolved investigation of the photoelectric effect itself, which takes place on the attosecond time scale [12]. The pioneering experimental result by Cavalieri et al. [12], who measured the photoemission from 4f core levels to be delayed w.r.t. the conduction band and valence band electrons from the (110) surface of tungsten, spurred a manifold of theoretical and numerical approaches to the solid state photoelectric effect including references [12, 96, 97, 98, 99, 100, 101]. This is in spite of the fact that photoemission as a physical problem is considered to be numerically tractable for long XUV and X-ray pulses since the formulation of the so called one-step theory by Pendry in 1970 [102, 103]. It furthermore inspired new experiments extending attosecond chronoscopy to atoms and molecules in the gas phase [13, 21, 20] and recently even liquid phase targets [104]. The experiments are performed by pump-probe cross-correlation of the XUV radiation generated in HHG with a second field whose half-cycle period is longer than the XUV pulse duration. Very conveniently, this condition is fulfilled in-situ by the temporal localization and attosecond synchronization of the tunnel ionization and radiative recombination steps in HHG. Hence, the NIR laser field driving the HHG is also used as clocking field in the attosecond chronoscopy measurements. The time delay Δt between the XUV and NIR pulses has to be varied with attosecond level precision and stability, which necessitates nanometer interferometric stability of the pump-probe apparatus. In general only relative time delays $\Delta\tau$ between photoelectron wavepackets originating from different bound states can be assessed. One notable difference is the chronoscopy of atomic helium in the gas phase, wherein through extensive measurements and numerical multilevel ab-initio calculations an absolute calibration of attosecond chronoscopy was possible [14, 20]. For more complex systems, a fully ab-initio solution of the many-electron wavefunction cannot be obtained within reasonable computation time.

The interpretation of the measurement observable, i.e. the relative streaking time delay $\Delta\tau$, is quite different depending on the electronic response of the target to the NIR streaking field and the propagating high energy electron and illustrated in figure 6. All attosecond chronoscopy experiments are performed within the limit of weak excitation, i.e. only a linear response of the medium w.r.t. the XUV and NIR fields is expected. For dilute gases, no screening of the NIR field is expected (see figure 6 d). Only few electrons are scattered during propagation in the dilute sample. Attosecond chronoscopy therefore measures the so-called atomic group delay of the photoelectron wavepacket, i.e. its retardation and acceleration as it interacts with the parent ion along its outward trajectory. For solid and especially metallic targets the situation is remarkably different. The NIR streaking field is strongly refracted and screened at the solid-vacuum interface on an atomic scale by the highly mobile conduction band electrons. The streaking field thus only

acts on the photo-excited electron outside the image charge plane, or jellium edge of the crystal, which is indicated as black dashed line in figure 6 f). Attosecond chronoscopy thus clocks the time between absorption of the XUV photon and the center-of-mass of the photo-excited electron traversing the jellium edge [25]. Hence, real time observation and clocking of the photoelectric effect becomes possible.

Liquid phase photoelectron spectroscopy and chronoscopy was facilitated by the invention of in-vacuo liquid microjets [105, 106]. The liquid-vacuum interface is not yet well understood, especially the size and strength of the density-gradient perpendicular to the interface is subject of ongoing investigations [107, 108] (see figure 6 e). Furthermore, existing models and experimental results for the inelastic scattering cross section and the mean-free path length of photoelectrons in the liquid micro-jet and across the liquid-vacuum interface are varying strongly. Attosecond chronoscopy can provide valuable insight into the density and structure of the interface through the correlation of observed photoelectron transport times with theoretical models accounting for elastic and inelastic scattering of the photoelectrons and the dielectric response of the liquid-vacuum interface [22] (see figure 6 b,e).

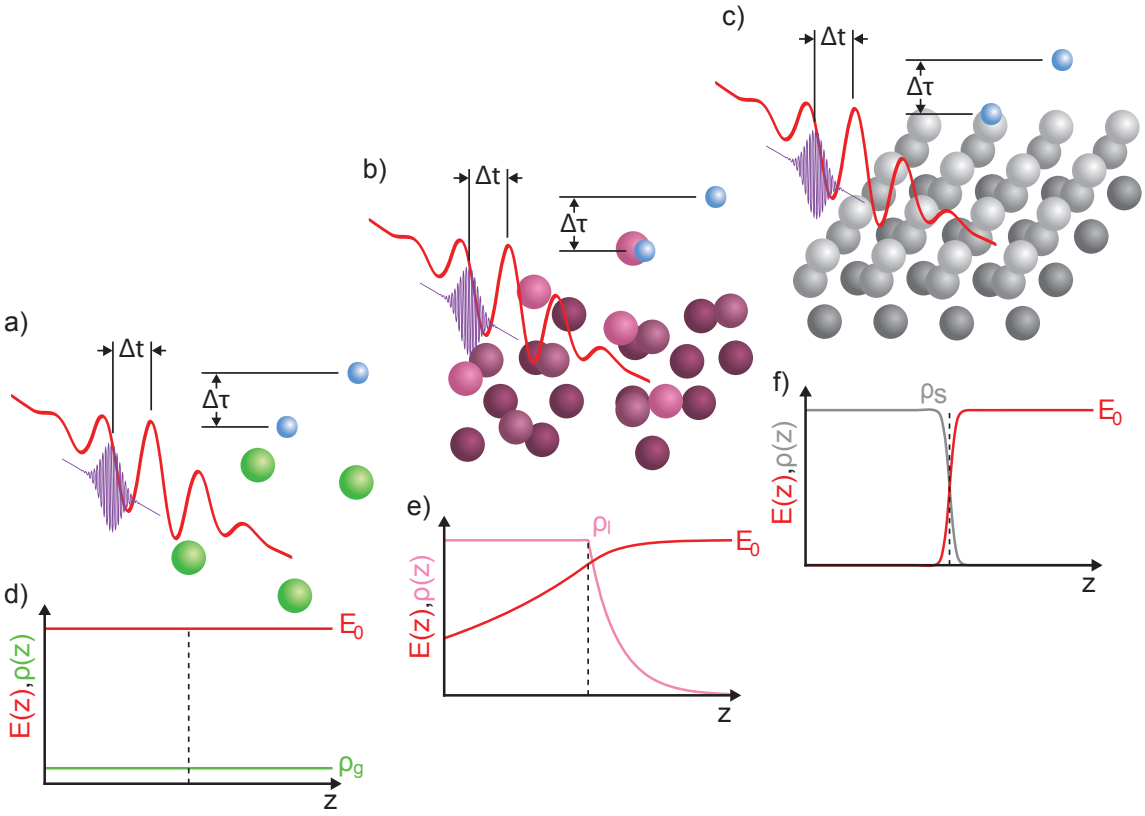

Figure 6 Illustration of the attosecond chronoscopy concept and the respective interpretation of the attosecond time delay for gas, liquid and solid state matter. a,b,c) XUV (purple) and NIR (red) light pulses impinging on gaseous (green), liquid (purple) and solid metallic samples (grey), respectively. Shading of spheres encodes atoms and their respective depth beneath the sample surface. The time delay between the XUV and NIR pulses is denoted Δt. The relative photoemission time delay between the different electronic states under investigation is denoted $\Delta\tau$. d,e,f) Corresponding sample densities $\rho(z)$ (coloured same as a) in the interaction region. Qualitative illustrations of atomic scale screening of the NIR streaking field $E(z)$ (red) for solid, liquid and gaseous samples.

2.5. Photoemission Spectroscopy

Photoemission spectroscopy is a powerful tool of condensed matter physics, as it provides a most direct pathway towards the observation and investigation of the electronic structure and phase transitions of solids and solid interfaces [109, 110, 111]. A solid-state photoemission spectroscopy experiment consists of a light source, either a narrowband UV lamp or synchrotron radiation or a laser based source of high energy radiation exceeding the work function of the sample, a vacuum apparatus to prevent contamination of the sample surface and recombination of the photoemitted electrons with ambient air molecules, an electron kinetic energy analyser and an electron detector. If the radiation source is emitting short pulses, as in the case of HHG with femtosecond laser pulses, the velocity dispersion of inertial flight of the mass-bearing electrons in vacuum can be used to temporally disperse electrons of different kinetic energy. Charged particle spectrometers operating on this principle are referred to as time-of-flight (TOF) spectrometers. If continuous emission sources are utilized, such as X-ray tubes, electrons are spatially separated usually by electrostatic fields of hemispherical or cylindrical geometry.

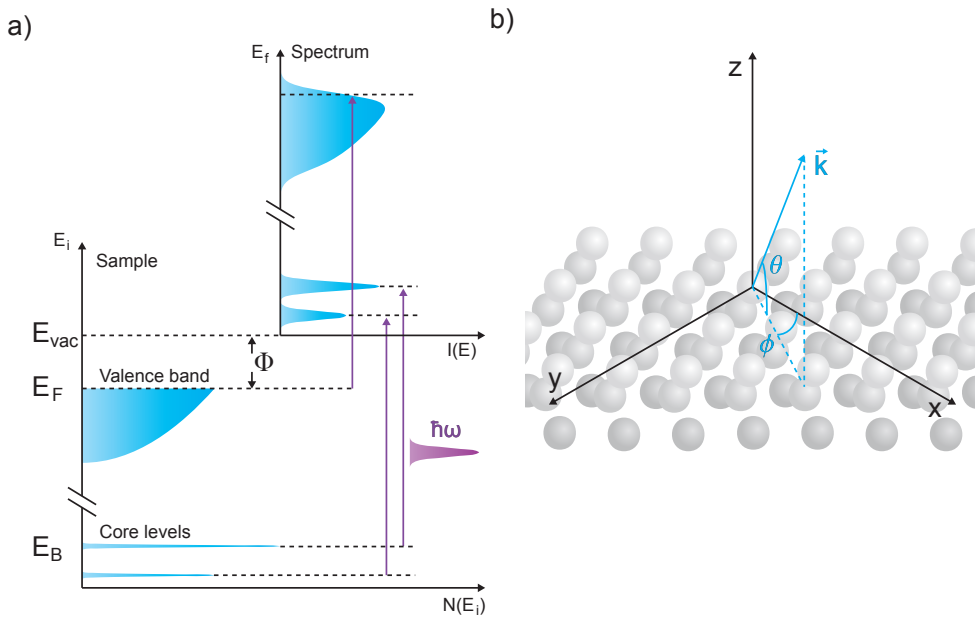

Figure 7 a) Energetics of the photoemission process. The kinetic energy distribution of electrons (blue top) measured in the analyser and recorded on the detector is produced by the bandwidth of the incoming photons (purple) and by the spectral function of the sample (blue bottom) at binding energy E_B. The work function Φ denotes the minimal energy for single photon ionization of the solid. Adapted from [109] b) Definition of emission angles θ and ϕ in ARPES.

The energy balance of the photoemission process is sketched in figure 7. Photoelectrons are observed at kinetic energies E_f corresponding to the difference between the XUV photon energy and the binding energy E_B of the core or valence atomic state under investigation and the minimum photon energy necessary to liberate electrons from the surface called the material work function Φ. For the high photon energies utilized in attosecond streaking experiments both electrons from weakly bound and delocalized valence states as well as from shallow atomic

inner-shell (core) orbitals are ejected from the solid

$$E_f = \hbar\omega - E_B - \Phi, \tag{2.16}$$

wherein Φ denotes not the work function of the sample, but of the electron detector because of the contact potential between sample and detector [112] additionally retarding or accelerating the photoelectrons. For high-resolution photoemission experiments, a determination of the sample work function via fitting of the Fermi-edge spectrum or known narrowband core level emission can be performed. The broad bandwidth of isolated attosecond pulses however precludes determination of the sample work function. Calibration of the photon energy has to be performed either by direct characterization of the multilayer optics or by fitting the known kinetic energies of the Auger electrons from noble gases. Calibration of the central photon energy and FWHM bandwidth was performed using either direct reflectometry with narrowband synchrotron radiation [93] or the emission of NOO-Auger electrons of xenon in the gas phase [113]. The results of the calibration process are compiled in appendix A.

Because of the strong electron-electron and electron-ion scattering mediated by the Coulomb repulsion, high-energy electrons travel only short times on the order of 100 attoseconds between subsequent elastic or inelastic scattering events. This limits the escape of photoexcited electrons at energies around 100 eV from solids to few atomic layers below the surface. Thus, photoemission is a highly surface sensitive process and the disentanglement of surface and bulk related excitations is a major challenge in almost all photoemission studies. The energy dependence of the inelastic mean-free path λ of the high-energy electron bears striking similarity for all condensed matter systems. This general trend is described with the so-called universal curve, which is depicted in figure 8a.

Analytic forms and parameters of the universal curve are found in [115, 116, 117] for a wide range of materials. The strength and energy dependence of the universal curve also has profound consequences for time-resolved photoemission from condensed targets. As seen in figure 8 b, the mean escape time for electrons from solid targets is on the order of 100 as for all photon energies between 50 eV and 1 keV, rendering sub-femtosecond XUV pulses a necessity for its investigation. The mean escape time of photoelectrons is linked to the lifetime of the high-energy Bloch states inside the solid [28]. Photoexcited electrons not inelastically scattered inside the solid are referred to as primary photoelectrons. The relative probability of energy transfer from the primary photoelectron to the many-electron system or vice versa is obtained from the detailed balance ($\propto e^{\hbar\Delta E/kT}$). At the high energy of primary XUV photoelectrons it is equal to one. Thus, inelastic scattering is associated with energy loss of the primary photoelectron and the generation of secondary photoelectrons at lower kinetic energy.

Further insight into the electronic structure of solids is obtained by angle-resolved photoemission spectroscopy (ARPES), which can provide high-resolution snapshots of the electronic band

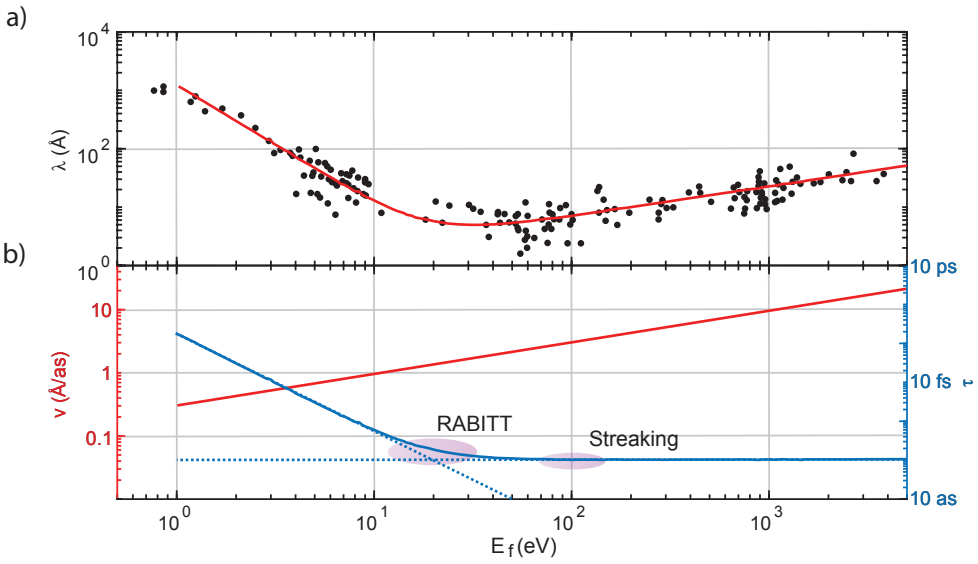

Figure 8 a) Universal curve (red) of inelastic mean free path λ of electrons in condensed matter. Black dots are measurements tabulated in [114] b) Free electron velocities v (red) and corresponding photoemission times τ (blue). Dotted lines are extrapolations of the low-energy regime, which is probed by the RABITT technique and high-energy regime, which is probed by the streaking technique, respectively.

structure [110]. The electronic band structure of solids is synonymous with the dispersion relation of the periodic Bloch states

$$E = E_n\left(k_x, k_y, k_z\right), \tag{2.17}$$

with the band index n and the wavenumber k. The material band structure describes the momentum-dependent eigenvalues of the stationary many-body Schrödingers equation

$$H\Psi_n^{\vec{k}} = E_n(\vec{k})\Psi_n^{\vec{k}}, \tag{2.18}$$

of the a periodic electrostatic potential of the crystal. The XUV photons $(\hbar\omega < 150\mathrm{eV})$ carry only little momentum $\vec{q}$ and the momentum of the photoexcited electron is $\vec{K} = \vec{k} + \vec{q}$ similar to the initial state momentum, ignoring Umklapp processes, which are of little relevance in high energy photoemission. This approximation allows the direct mapping of the electronic band structure of the occupied valence states from ARPES measurements. Because of translational symmetry, the momentum components parallel to the crystal are conserved upon transmission of the photoexcited electron and the electron momentum can directly be inferred from the polar emission angle θ and the azimuthal emission angle ϕ and the kinetic energy of the photoemitted electron E_{kin}

$$\begin{aligned} k_x &= \frac{\sqrt{2m_e E_{kin}}}{\hbar} \cdot sin\theta \cdot cos\phi, \\ k_y &= \frac{\sqrt{2m_e E_{kin}}}{\hbar} \cdot sin\theta \cdot sin\phi. \end{aligned} \tag{2.19}$$

The determination of the normal component of the electron momentum k_z is more difficult,

because the translational symmetry is broken at the surface. The normal component of the momentum is modified according to

$$k_z = \frac{1}{\hbar} \cdot \sqrt{2m_e \left(E_{kin} \cdot cos^2\theta + V_0\right)}, \tag{2.20}$$

wherein V_0 denotes the so-called inner potential, which corresponds to the energy difference between the bottom of the valence band and the vacuum level. The exact determination of V_0 from experiments is impossible. However, for nearly-free electron metals a good approximation can be obtained from matching the experimental data with theoretical calculations of the parabolic band dispersion [118].

2.5.1. Theoretical background of solid state photoemission

In the following section, a short introduction into photoemission theory is given and the most commonly utilized theoretical descriptions, namely the three-step model and the one-step model, are introduced. The comparison and interpretation of photoemission experiments based on these models has become a "longstanding and increasingly confusing issue" [119]. Attosecond photoemission chronoscopy is expected to be able to resolve these questions by unravelling and disentangling the interplay between the photoexcitation and photoelectron transport effects directly in the time domain. The Hamiltonian of solid state photoemission is written as [111]

$$H = -\frac{1}{2}\sum_{n=1}^{N}\left(\vec{p}_i - e\vec{A}_X\right)^2 + \sum_{n=1}^{N}\sum_{k=1}^{K}\frac{1}{4\pi\epsilon_0}\frac{Ze^2}{\left|\vec{r}_n - \vec{R}_k\right|} + \frac{1}{2}\sum_{n=1}^{N}\sum_{m\neq n}^{N}\frac{1}{4\pi\epsilon_0}\frac{Ze^2}{|\vec{r}_n - \vec{r}_m|}, \tag{2.21}$$

wherein N is the number of electrons and K the number of atomic cores with atomic number Z. Ignoring nonlinear effects, like multiphoton ionization, the weak attosecond XUV field (vector potential A_X) can be treated perturbatively

$$H_{int} = -\frac{e}{2m_e}\left(\vec{p}\cdot\vec{A}_X + \vec{A}_X\cdot\vec{p}\right) = -\frac{e}{m_e}\vec{A}_X\cdot\vec{p}. \tag{2.22}$$

The photocurrent can be calculated via the transition probability $\Gamma^{\vec{k}}_{i\to f}$ from Fermi's Golden rule

$$\Gamma^{\vec{k}}_{i\to f} = \frac{2\pi}{\hbar}\left|\left\langle\Psi^{\vec{k}}_f\right| H_{int}\left|\Psi^{\vec{k}}_i\right\rangle\right|^2 \delta\left(\hbar\omega_X - E_f - E_i\right), \tag{2.23}$$

wherein the energies of initial and final states $E_{i,f}$ are referenced to the vacuum level $(E_{vac} = 0)$, as the incoherent sum over all occupied states

$$P(\vec{k}, E_f) = \sum_i \Gamma^{\vec{k}}_{i\to f}. \tag{2.24}$$

The initial and final states are complicated eigenstates of the many-body Hamiltonian. The so-called sudden approximation, commonly used in many-body physics, strongly simplifies the problem by assuming the instantaneous transition of the electron from the initial to the final state

and the discontinuous change of the effective non-local potential of the solid at that instant [111]

$$\Psi_{i,f}^{\vec{k}} = \mathrm{A}\psi_{\vec{k}_{i,f}}\Psi_{i,f}^{N-1}. \tag{2.25}$$

Herein, $\psi_{k_{i,f}}$ denotes the one-electron wavefunction, $\Psi_{i,f}^{N-1}$ the (N-1)-electron wavefunction of the solid after photoemission and the operator A ensures the proper exchange symmetry of the N-fermion wavefunction. The transition matrix element can now be split into the one-electron dipole matrix element $M_{f,i}^{k}$ and the (N-1)-electron overlap matrix element $c_{i,f}$

$$\left\langle \Psi_f^{\vec{k}} \right| H_{int} \left| \Psi_i^{\vec{k}} \right\rangle = \left\langle \psi_{\vec{k}_f} \right| H_{int} \left| \psi_{\vec{k}_f} \right\rangle \langle \Psi_f^{N-1} | \Psi_i^{N-1} \rangle = M_{f,i}^{\vec{k}} \cdot c_{i,f}. \tag{2.26}$$

In the noninteracting electron picture the latter can be neglected [111].

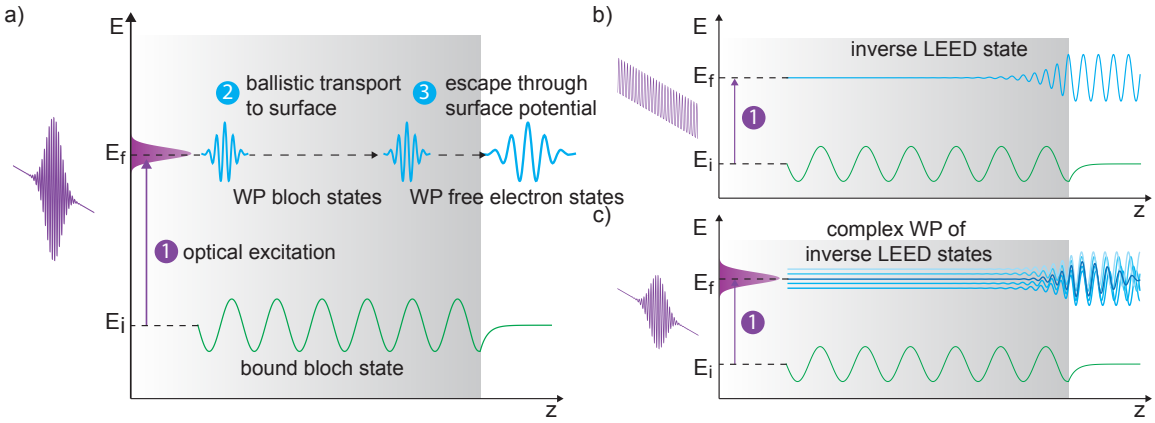

Figure 9 Illustration of common photoemission models and theories. a) Three step model of photoemission. (1) The XUV photon (purple) excites the electron between Bloch states above (blue) and below (green) the vacuum energy of the solid. The electron propagates to the surface subject to elastic and inelastic scattering. (3) The electron traverses the surface potential barrier. b) One-step theory of photoemission. (1) The propagation, scattering and transport is taken into account via the construction of the inverse LEED state. The photocurrent is calculated directly via the matrix element between the initial and inverse LEED states. Generally one-step theory is only applied for long excitation pulses. c) Superposition of inverse LEED states forming the attosecond electron wavepacket.

Three-step model

The three-step model of photoemission was originally proposed by Berglund and Spicer [120, 121] in 1964. The photoemission process is split up into three separate steps similar to the description of HHG (see Figure 9 a).

1. Photoexcitation
   The process of photoemission is started by excitation of an electron from a bound Bloch state below the Fermi energy to an unbound Bloch state above the vacuum level. The transition probability can be calculated by Fermi's golden rule (see equation 2.23).

2. Propagation in the solid
   The propagation of the electron inside the solid is governed by the group velocity of the

high-energy Bloch state

$$\vec{v_g} = \frac{1}{\hbar}\frac{\partial E_n(\vec{k})}{\partial \vec{k}}, \tag{2.27}$$

as well as elastic and inelastic scattering with the ionic cores (phonon excitations) and remaining electrons (plasmon and electron-hole excitations). High-energy electrons investigated in attosecond streaking experiments are often approximated as quasi-free electrons and their propagation velocity accordingly follows as function of the detected kinetic energy in vacuum

$$v_g = \sqrt{\frac{2}{m_e}(E_{kin} + V_0)}. \tag{2.28}$$

3. Transmission through the surface
   Traversing the surface, the electron loses kinetic according to the energy of interaction between the delocalized electron and the positive background charge in the solid, and the attractive force between the electron and its own image charge. The kinetic energy loss corresponds exactly to the inner potential V_0. This surface gradient force acts only on the normal component of the electron momentum. Hence, the parallel component of the momentum is conserved. One-to-one correspondence to optical refraction is noted, wherein the inner potential of the surface corresponds to the increased refractive index in the Fresnel equations. Electrons with insufficient energy to overcome this effective surface potential are subject to total internal reflection and remain bound.

One-step model

The three-step model is entirely empirically constructed. A more accurate description of photoemission can be obtained within the so-called one-step model, first introduced by Mahan [102]. This model treats the photoexcitation, propagation, scattering, and surface refraction processes in a single coherent quantum mechanical process. This implies that one can no longer just use the Bloch wavefunctions, which solve the bulk Hamiltonian to construct the final state of the photoemission process. Also evanescent states corresponding to imaginary wavevectors as well as surface states and surface resonances have to be considered in the construction of the final state of photoemission. This final state is approximated by means of the time-reversed LEED state [103]. In low-energy electron diffraction (LEED) experiments a single incoming electron beam enters the solid, is scattered elastically and inelastically inside the solid and thus multiple beams exit the solid. Time-reversal of the LEED state provides a suitable outgoing electron wave with the correct interaction with the surface potential, as well as the coherent treatment of all elastic scattering and propagation effects and is an eigenfunction of the energy and angle resolving detector. The transition rate from the initial states into the inverse LEED state are thus proportional to the detected photocurrent. The inelastic scattering, i.e. the transfer of energy between the photoexcited electron is commonly simplified by introduction of an imaginary valued optical potential V_i. This approximation retains the correct surface sensitivity and photoelectron escape depths, but does not include the generation of secondary electrons,

and was very successfully applied to high-resolution photoemission [110].

The time-reversed LEED state, sometimes called the inverse LEED state, is calculated via state-of-the-art DFT codes. One such example is the full-potential linearised augmented plane wave method (FLAPW), which was extended to the semi-infinite crystal in the works of Krasovskii and Schattke [122, 123].

2.5.2. Attosecond streaking spectroscopy

In a conventional streak camera, used i.e. for the measurement of picosecond to nanosecond fluorescence lifetimes, the light pulse under investigation releases electrons from a photocathode via the photoelectric effect. These electrons are accelerated towards a phosphor screen and the luminescence is detected on a conventional camera. A fast rising electrostatic field E_{AC}, which is synchronized to the laser pulse, is applied to the electrodes of a plate condensator oriented perpendicular to the drift direction of the electrons, thus mapping the photoemission time of the electron to the spatial deflection of its trajectory due to the Lorentz force

$$F(t) = \frac{dp(t)}{dt} = -e \cdot E_{AC}(t). \tag{2.29}$$

In order to resolve the attosecond photoelectric effect itself a much faster streaking field must be applied, which needs to be synchronized to the XUV pump field initiating the photoemission on an attosecond time scale. Both requirements are fulfilled by the XUV and NIR fields generated in and driving HHG, respectively. The so-called attosecond streak camera was proposed by Itatani et al. [124] and realized experimentally by Kienberger et al. [11].

In the following a concise description of the semi-classical and quantum-mechanical formalism of attosecond streaking, following the outline in [36], will be provided. In both cases, two approximations need to be applied in order to obtain an analytic solution. First, the action of the electrostatic potential of the residual ion on the ionized electron is neglected. This is commonly referred to as strong field approximation (SFA). Second, we assume that no rearrangement of the electronic charge density in the residual ion takes place, which is referred to as single active electron approximation (SAE).

Semi-classical formalism

In the semi-classical formalism of streaking, sometimes deemed two-step model, the single-photon ionization and the undulation of the electrons in the NIR streaking are separated. The motion of the electron in the laser field is treated as classical trajectory. This approach is a good approximation for XUV pulses much shorter than the half-cycle period of the laser field [125, 124].

Single photon ionization of the sample in the XUV field $\vec{E}_X(t)$ initiates the streaking process. The

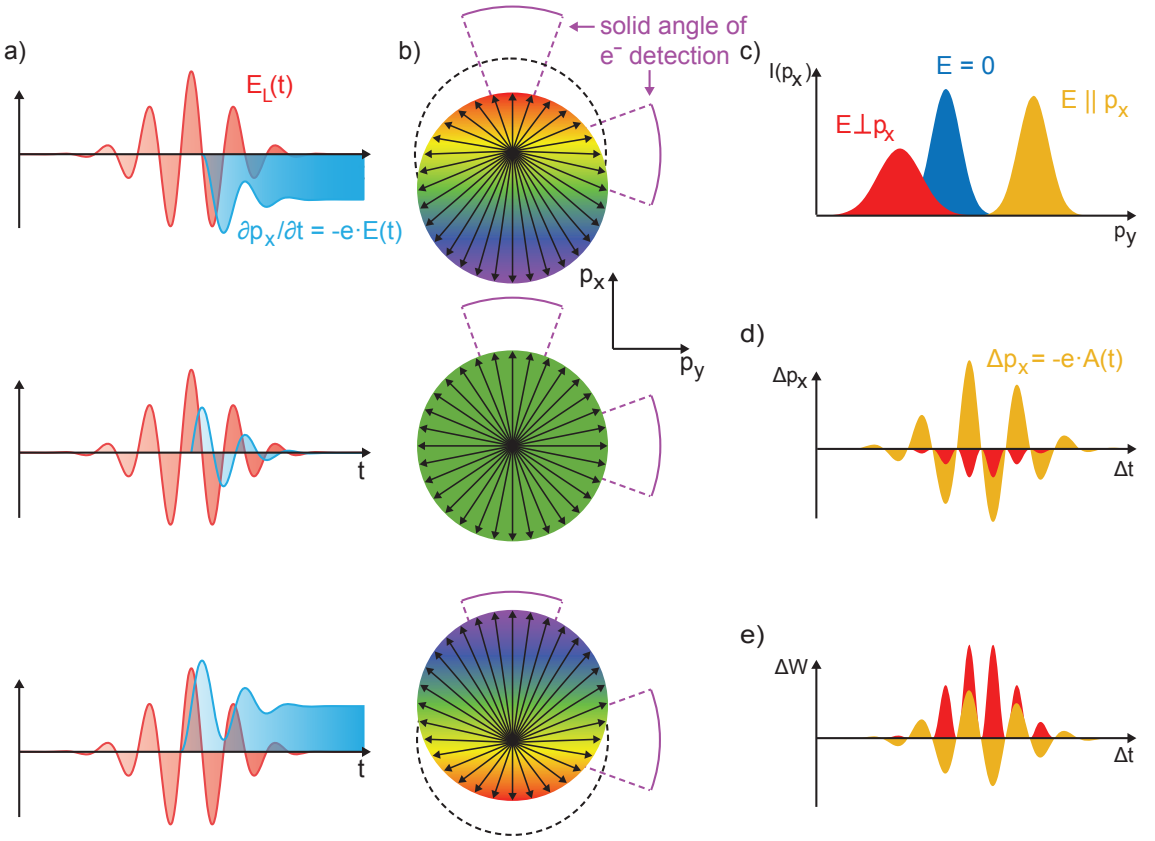

Figure 10 Classical trajectory analysis of attosecond streaking. a) Electron trajectories in are modulated in momentum space depending on the time of ionization. b) Colour coded 2D representation of final momentum. Solid angle of detection for parallel and perpendicular photoemission w.r.t. the laser polarization are indicated in purple. c) Distortions of the electron spectrum due to the laser field for parallel (yellow) and perpendicular (red) polarization at the time of maximum net acceleration. d) Central momentum shift of photoelectron wavepacket as function of XUV-NIR delay Δt. Colour code same as in d). e) Same as c), but for spectral width of electron wavepacket.

transition amplitude between the bound and excited states can be calculated with Fermi's golden rule in first order perturbation theory (see equation 2.23). The photoelectron is excited from the initial bound state with binding energy E_{bin} and appears in the continuum with momentum $p_0 = \sqrt{2m_e\left(\hbar\omega_X - E_{bin} - \Phi\right)}$ at the time $-\Delta t + \tau$ w.r.t. to the NIR streaking field ($\beta_L = 0$) and is subsequently accelerated therein (see figure 10a)

$$\frac{d\vec{p}(t)}{dt} = -e \cdot \vec{E}_L(t) = -e \cdot \vec{e}_z E_0(t) \cdot cos(w_L t + \phi_{CE}). \tag{2.30}$$

The final momentum shift of the electron follows as

$$\Delta\vec{p} = -\int_{-\Delta t+\tau}^{\infty} dt\, e \cdot \vec{E}_L(t) = -e \cdot \vec{A}_L(t), \tag{2.31}$$

and is parallel to the polarization of the laser field. The final kinetic energy, which is measured in the electron analyser, thus depends not only on the timing and strength of the NIR streaking field but also on the alignment angle θ of its polarization w.r.t. the axis of the electron analyser

(see figure 10b)

$$p^2 = p_0^2 - \Delta p^2 + 2\,|p_0| \cdot |\Delta p|\, cos\,\theta. \tag{2.32}$$

The kinetic energy E_f recorded in the electron spectrometer follows directly as

$$E_f(\tau) = E_{0,f} + 2U_p(\tau) \cdot cos\,2\theta \cdot \sin^2(w_L\tau + \phi_{CE}) + \sqrt{8E_0U_P(\tau)} \cdot cos\,\theta \cdot \sin(w_L\tau + \phi_{CE}) \tag{2.33}$$

For parallel polarization $cos\,\theta = cos\,2\theta = 1$ and for weak streaking fields $E_0 >> U_P$, kinetic energy modulation proportional to the amplitude of the vector potential of the NIR streaking field is observed. For perpendicular polarization $cos\,\theta = 0, cos\,2\theta = 1$, the electrons are mostly retarded by the streaking field. The spectral position and bandwidth of the photoemission is modulated at twice the laser frequency (see figure 10 c,d,e) because of the symmetry of the streaking field w.r.t. to the detector axis.

Quantum-mechanical formalism

In the quantum mechanical formalism both the XUV and NIR fields contribute to the transition matrix element from an initial bound state i with binding energy $E_i < 0$ to a free-electron final state of momentum p, directly. The Hamiltonian describing the attosecond streaking experiment performed on isolated hydrogen atoms is formulated as follows [126]

$$i\hbar\frac{\partial}{\partial t}\Psi(\vec{r},t) = -\left(\frac{\hbar^2}{2m_e}\nabla^2 + \frac{e^2}{4\pi\epsilon_0}\frac{1}{r}\right)\Psi(\vec{r},t) + \vec{r}\cdot\left(E_L(\vec{r},t;\tau) + E_X(\vec{r},t)\right)\Psi(\vec{r},t) \tag{2.34}$$

Applying the SFA and neglecting the interaction of the electron with the parent ion allows the continuum of scattering final-states to be replaced by their laser-dressed plane-wave counterparts, referred to as Volkov states. Time-dependent quantum-mechanical transition amplitudes are calculated directly [126, 127, 128]

$$a_i(p,\tau) = \frac{1}{i\hbar}\int_{-\infty}^{\infty} dt\, d(p - eA_L(t)) \cdot E_X(t-\tau) \cdot e^{-i\Phi_V(t;p)}, \tag{2.35}$$

wherein $d(p - eA_L(t)) = \langle p - eA_L(t)|\,\hat{x}\,|i\rangle$ denotes the dipole transition matrix element between the initial state and the Volkov state. The Volkov phase $\Phi_V(t;p)$ carrying the interaction of the free electron with the laser field is calculated as

$$\Phi_V(t;p) = \frac{1}{2m_e\hbar}\int_t^{\infty} dt'\left(p - eA_L(t')\right)^2. \tag{2.36}$$

The photocurrent follows as $I(p,\tau) = \sum_i |a_i(p,\tau)|^2$ for fully incoherent emission and $I(p,\tau) = |\sum_i a_i(p,\tau)|^2$ for fully coherent emission from overlapping initial states i. Example spectrograms for different values of the pulse duration τ_X and XUV chirp β_X are depicted in figure 11 for atomic hydrogen. Finite chirp of the XUV pulse imparts a modulation of the energy width of the detected electrons at the NIR fundamental frequency during temporal overlap, due to the parallel and anti-parallel alignment of the time-dependent XUV frequency and the NIR induced

momentum shift.

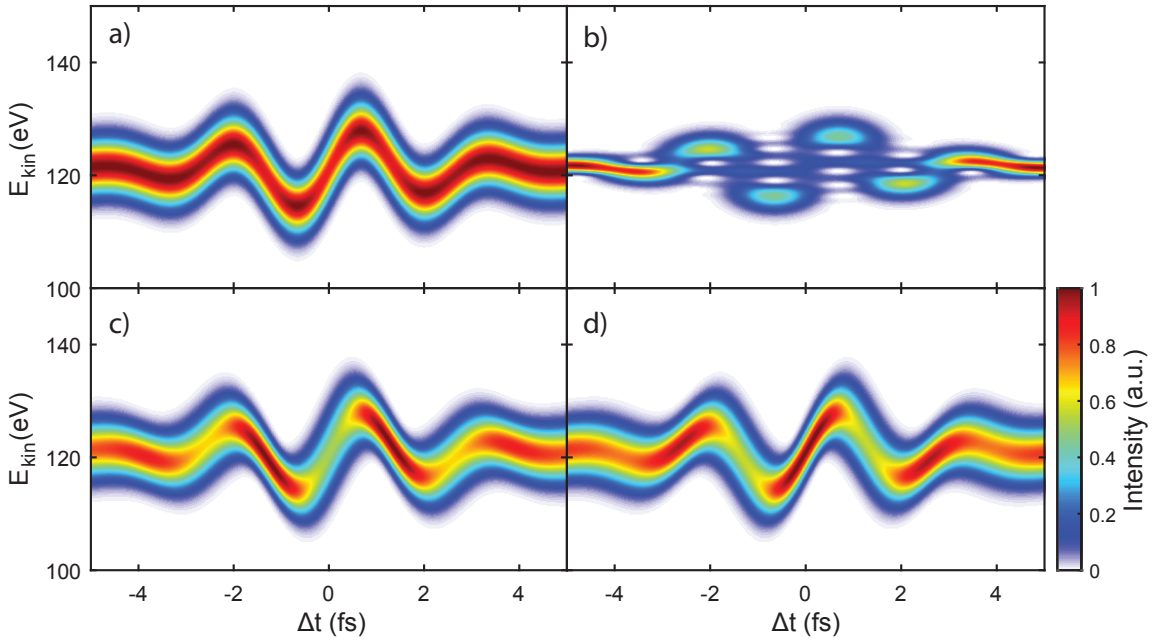

Figure 11 Streaking spectrograms calculated with the quantum mechanical formalism (no CMA) for the hydrogen atom for different XUV pulses with central energy 135 eV. a) Spectral FWHM $\Delta\omega = 5$ eV, spectral chirp $\beta_\omega = 0$ as/eV, b) $\Delta\omega = 1.25$ eV, $\beta_\omega = 0$ as/eV, c) $\Delta\omega = 5$ eV, $\beta_\omega = 10$ as/eV d) $\Delta\omega = 5$ eV, $\beta_\omega = -10$ as/eV.

2.5.3. Reconstruction of attosecond bursts by interference of two-photon transitions

Recently, it came to fruition that not only isolated attosecond pulses but also attosecond pulse trains [8, 129, 130] are viable options for attosecond chronoscopy measurements [21, 26]. The measurement method is dubbed reconstruction of attosecond bursts by interference of two photon transitions (RABITT) and is schematically outlined in figure 12. As in attosecond streaking the time-delay τ between the XUV pulse train and the generating NIR driver field is scanned and stabilized with attosecond precision. During temporal overlap of the XUV and NIR fields, sidebands at the position of even-order harmonics appear in the photoelectron spectrum, which are absent in the XUV spectrum. These sidebands originate from the coherent superposition of two-photon transitions from neighbouring harmonics including absorption or emission of one NIR photon. The sidebands are modulated at twice the laser frequency and the photoemission time-delay can be extracted from the phase of these modulations using a suitable reference [131].

The most prominent advantage of RABITT is the gain in spectral resolution upon utilization of long trains of attosecond pulses (see figure 12 c,d) generated by long IR driver pulses in suitable phase-matching conditions. This allows to use closely spaced spectral lines as references in attosecond chronoscopy experiments [28, 132, 133, 134, 135]. The advantage of the streaking scheme on the other side is the availability of high-energy isolated attosecond pulses (≈ 100 eV)

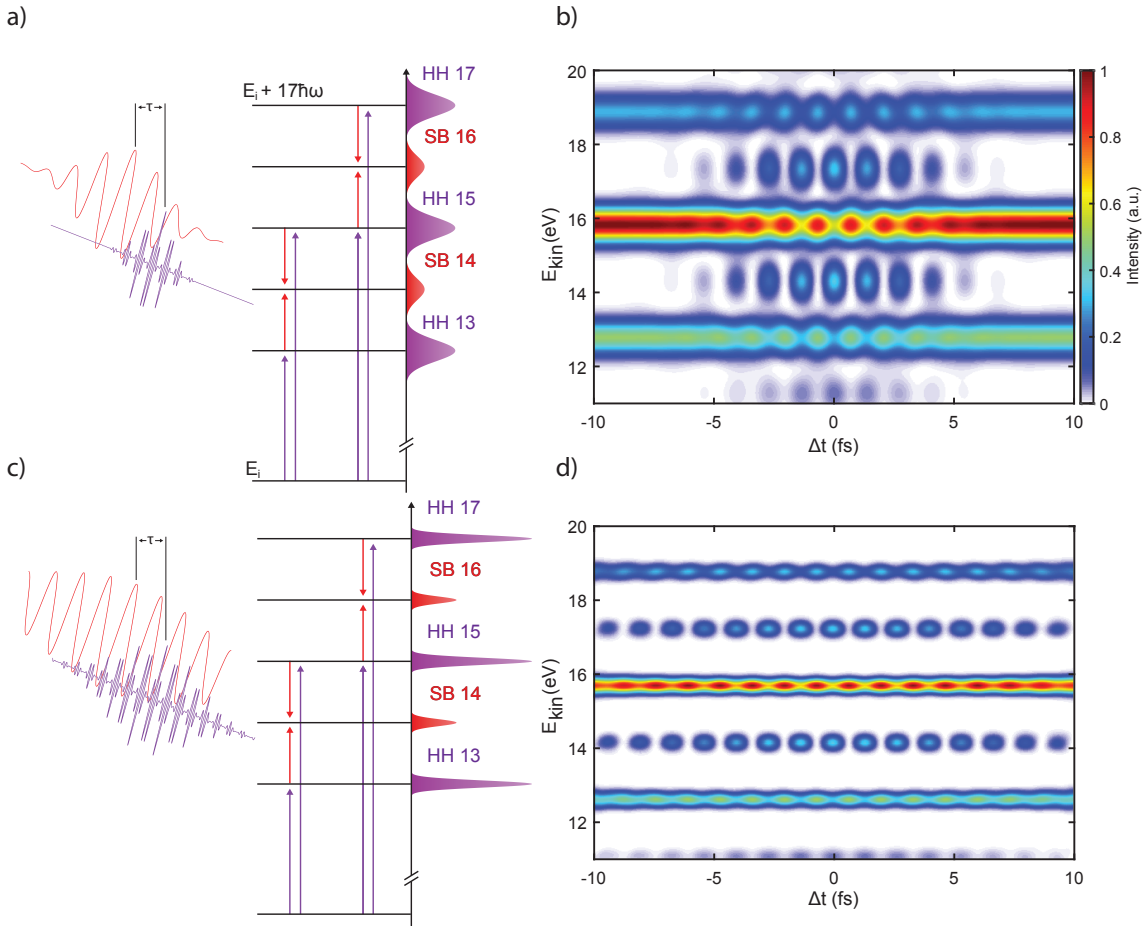

Figure 12 Schematic representation of the RABITT technique (a,c) and RABITT spectrograms calculated with the quantum mechanical formalism for the hydrogen atom (b,d) for 8 fs NIR laser pulses (a,b) and 25 fs NIR laser pulses (c,d).

as compared to typical experiments with attosecond pulse trains (< 50 eV). Hence, it is possible to use core level photoemission [12, 24] as references for attosecond chronoscopy and achieve element-specific attosecond chronoscopy [35, 25]. Moreover, the maximum spectral bandwidth of investigated features is limited in RABITT by the distance between adjacent harmonics and evaluation of the photoelectron spectrum can be challenging, i.e. in liquid water [22]. The two methods must thus be regarded as complementary in their respective applicability in condensed-matter attosecond chronoscopy.

2.6. Experimental setup

The solid-state attosecond chronoscopy experiments rely on the combination of high-harmonic generation and attosecond pulse generation, an attosecond interferometer and an ultra-high vacuum (UHV) surface science end-station for sample preparation. As to avoid possible contamination of the surface, which could falsify the observed attosecond delays [35], the pressure should be kept below 10^{-10} mbar during measurements. An overview schematic of

the attosecond chronoscopy experiment is depicted in figure 13.

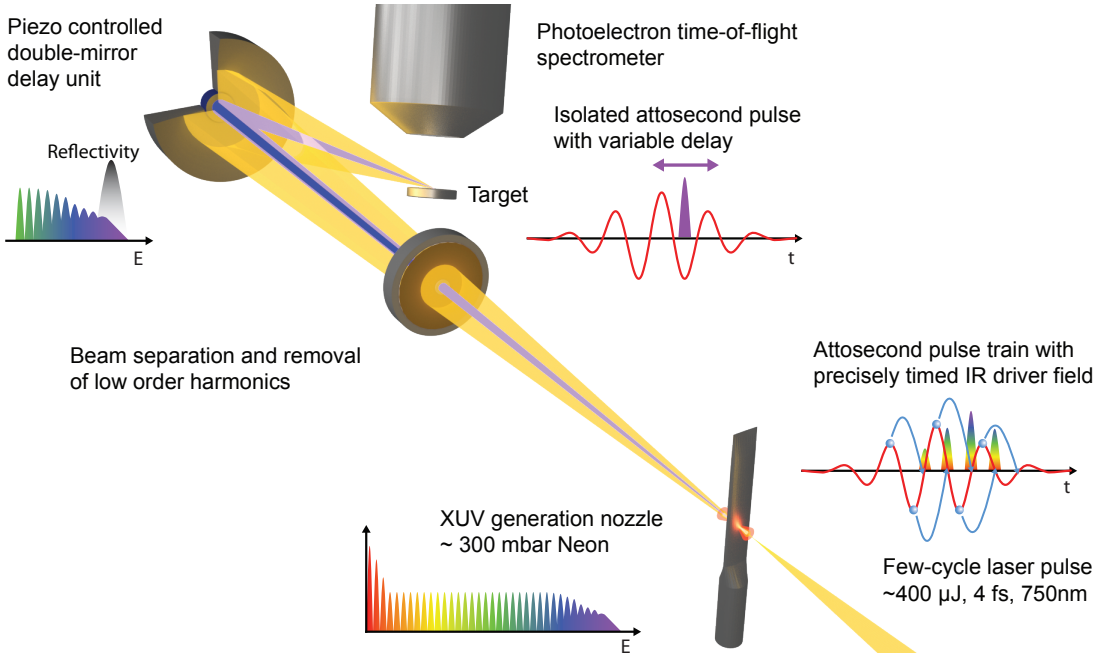

Figure 13 Overview schematics of a solid state attosecond streaking experiment.

2.6.1. Laser systems

The generation of single isolated attosecond pulses necessitates the generation of intense sub-two cycle NIR laser pulses. This challenging task is most readily achieved utilizing a combination of Ti:Sa lasers and the techniques of chirped-pulse amplification (CPA) [136] and spectral broadening in a gas filled capillary [82, 83]. The experiments presented in this thesis have been performed on three different laser systems henceforth referred to as FP2old, FP2new and FP3.

Front-end of laser system

The front-end of the laser systems is depicted in figure 14. The laser-system is driven by a commercial passively modelocked Ti:Sa oscillator (Femtolasers Rainbow) capable of generating 6 fs, 6 nJ light pulses at a repetition rate f_{rep} of 73 MHz (FP2Old) or 78 MHz (FP3, FP2New) [137, 138]. The spectrum of the oscillator spans from 650 nm to 950 nm at 10% maximum intensity. The laser output is focused into a magnesium-oxide doped periodically-poled lithium-niobate crystal (PPLN) for difference frequency generation and spectral broadening. A dichroic beamsplitter isolates the infrared part of this broadened spectrum, which is further bandpass filtered and focused onto an avalanche photodiode for measurement of the carrier-envelope-offset frequency f_{ceo}. In order to avoid detrimental nonlinear optical effects as well as optical damage, the oscillator pulses are subsequently stretched by chromatic dispersion in a SF57 glass block to about 15 ps. Higher orders of the dispersion are adjusted for either by specially designed

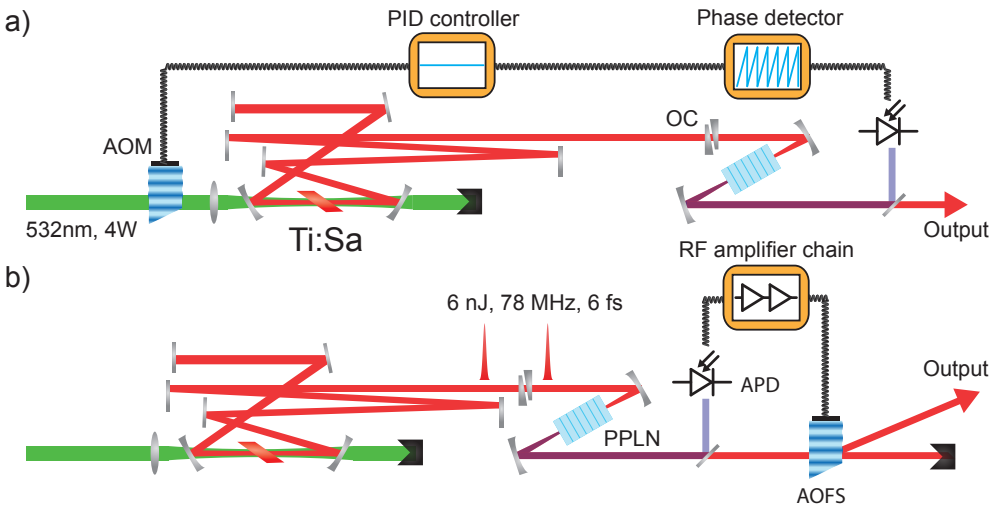

Figure 14 a) Laser system front end of FP2old and FP3 system with CEP feedback stabilization scheme. b) Front-end of FP2new laser system with feed-forward stabilization scheme.

chirped mirrors (TOD) (FP2old) [139, 12] or via insertion of an acousto-optic programmable dispersive filter (AOPDF) [140] into the beam path after the first 4 passes through the amplifier crystal (FP2new, FP3). A Faraday isolator in the beampath prevents spurious back-reflections of amplified pulses into the oscillator.

The pulse energy delivered by the oscillator is insufficient for XUV attosecond generation, but is amplified by several orders of magnitude in a subsequent multipass amplifier (Femtopower HR compact Pro) [141, 142] pumped by a neodymium-doped yttrium lithium fluoride (Nd:YLF) laser at 527nm and 20W average power in dual pass geometry. The pump energy is released in form of 150 ns pulses with a repetition rate of 3 kHz (FP2old, FP2new) or 4 kHz, respectively. A second Ti:Sa crystal is cooled to $-70°$C in a vacuum chamber for more efficient heat extraction and prevention of thermal lensing effects. After four passes through the amplifier medium the pulse repetition rate is reduced from 78 MHz to $3(4)$ kHz (FP3) by means of a pulse-picker (PC). The pulse picker is electronically synchronized to the oscillator pulse repetition rate. The isolated pulse is further amplified by five more passes through the amplifier medium. The spectral bandwidth is reduced during amplification due to the gain narrowing effect, wherein the spectral bandwidth of the signal is reduced by repeated multiplication with the peaked gain profile of the amplifier medium [143]. The reduction in bandwidth is inexplicably linked to an increase in best achievable pulse duration. The gain narrowing is partially compensated via dielectric filters (FP2old) [144, 141] or the AOPDF [145] (FP2new, FP3), respectively.

In the FP3 system, further pulse energy enhancement is provided by a second multipass amplifier operated at $-210°$C and pumped with 50 W from a frequency doubled Nd:YAG laser at 532 nm in single pass geometry [146].

The pulses are subsequently compressed close to their respective Fourier-limit of 21 fs by

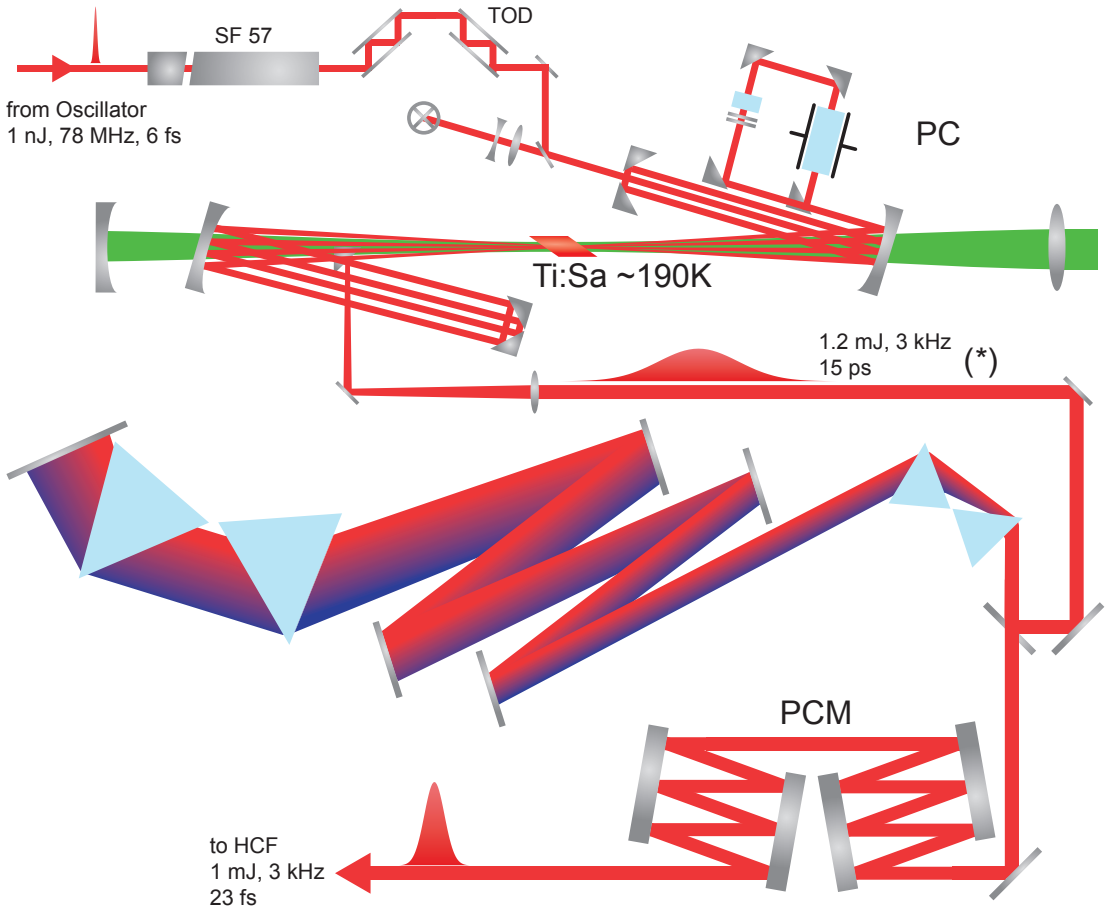

Figure 15 Schematics of the FP2 chirped pulse amplifier system. Top: Multipass amplifier with pockels cell (PC). Bottom: Hybrid compressor with fused silica prisms and positive dispersive mirrors (PCM). (*) Up to this point the FP3 system and the FP2 system are setup similar.

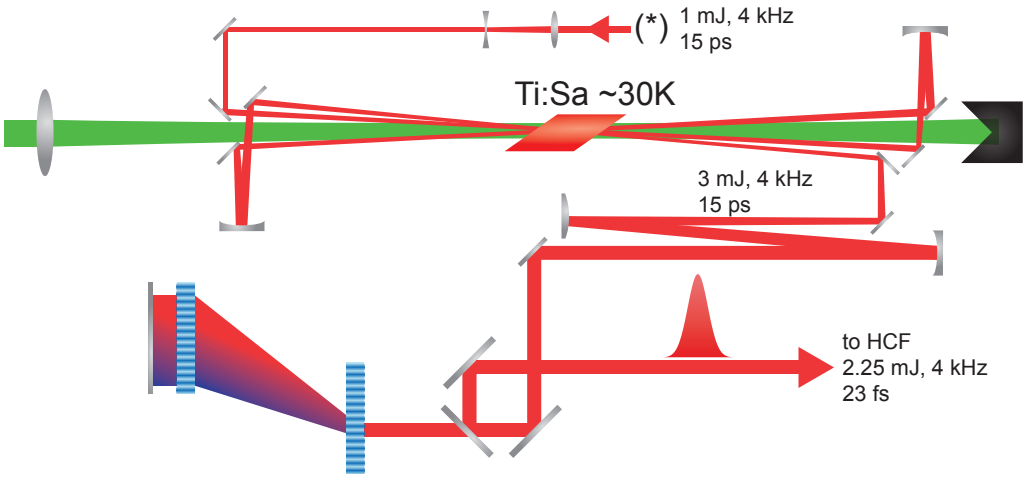

Figure 16 Sketch of the second amplifier, reflective periscope and transmission grating compressor stages of the FP3 laser system. (*) Up to this point the FP3 system and the FP2old system are set up similar.

means of an prism-chirped mirror hybrid compressor [147, 12] (FP2old) or a transmission grating compressor [148] (FP2new, FP3). The final pulse energies after compression are 1.2 mJ

(FP2old, FP2new) and 3 mJ (FP3), respectively. The temporal properties of the laser pulse compression are monitored by SHG-FROG, which is depicted in figure 17 (see appendix D) for the case of the FP2old system. The retrieved full-width half-maximum (FWHM) pulse duration is 25 fs.

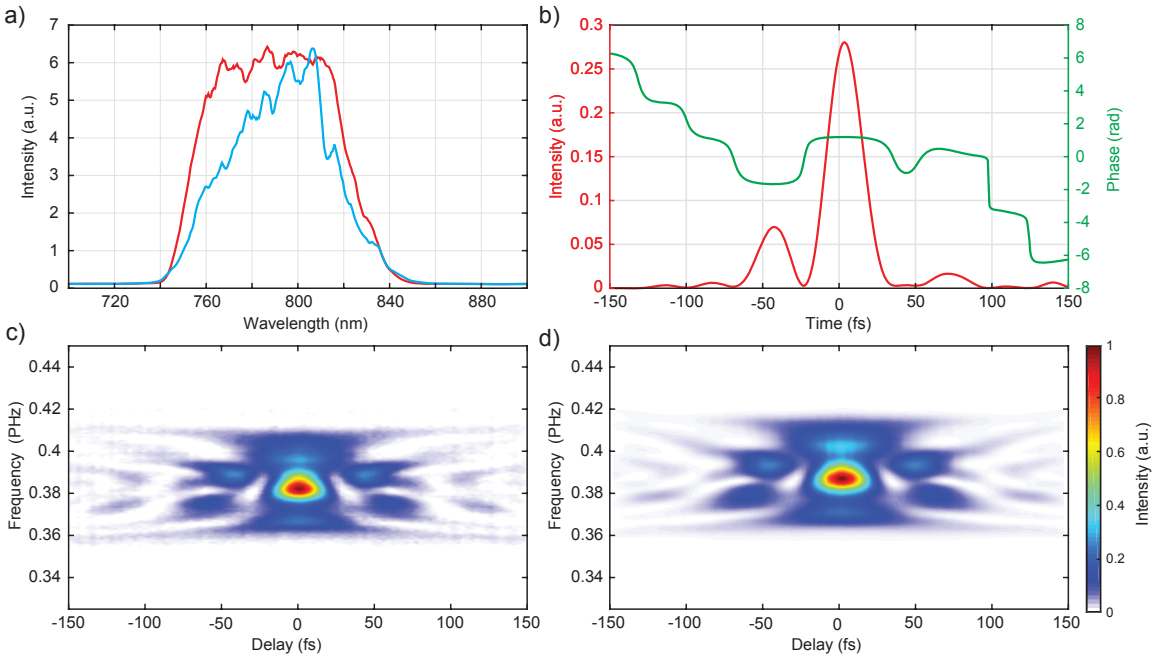

Figure 17 a) Spectrum of Femtopower CPA without dielectric filter (blue) and with dielectric filter (red) to counter gain narrowing effect. b) Pulse envelope intensity $E_0(t)$ (red) and temporal phase $\phi(t)$(green) retrieved with the iPIE algorithm. c) Measured SHG FROG spectrogram. d) Reconstructed SHG FROG spectrogram.

Hollow core fiber and chirped mirror compression

The state-of-the-art spectral bandwidth and pulse duration of Ti:Sa multipass systems are insufficient for isolated attosecond pulse generation. Hence, external spectral broadening and compression must be achieved if few-cycle light pulses are to be generated. The most established technique in the field of attosecond science is the spectral broadening by means of self-phase modulation and self-steepening of the laser pulse in a neon gas-filled glass capillary [82, 83]. The instantaneous third-order nonlinear electronic response of the gas, called the Kerr-effect

$$\vec{P}(\vec{E}) = \epsilon_0 \chi_1 \cdot \vec{E} + \epsilon_0 \chi^{\langle 3 \rangle} \cdot \vec{E} \cdot \vec{E} \cdot \vec{E}, \tag{2.37}$$

wherein $\chi^{\langle 3 \rangle}(\omega) = 4/3 \cdot \epsilon_0 c n_0^2 n_2$ denotes the nonlinear susceptibility and n_0 and n_2 denote the linear and nonlinear refractive indices [149] of the medium, respectively. Optical waveguiding in the hollow-core glass capillary [150] increases the nonlinear interaction length by three orders of magnitude. The hollow core fiber is encased in a vacuum tube, which is filled with neon gas and the beam enters and exits the tube through thin fused silica windows, mounted at Brewster's angle. For higher input pulse energies, such as the FP3 system, it is advantageous to implement a dual differential pumping scheme, wherein gas is supplied through a small opening in the middle of the fiber and removed from both ends of the fiber. Detrimental optical filamentation at

both the fiber input and exit apertures is thus avoided altogether.

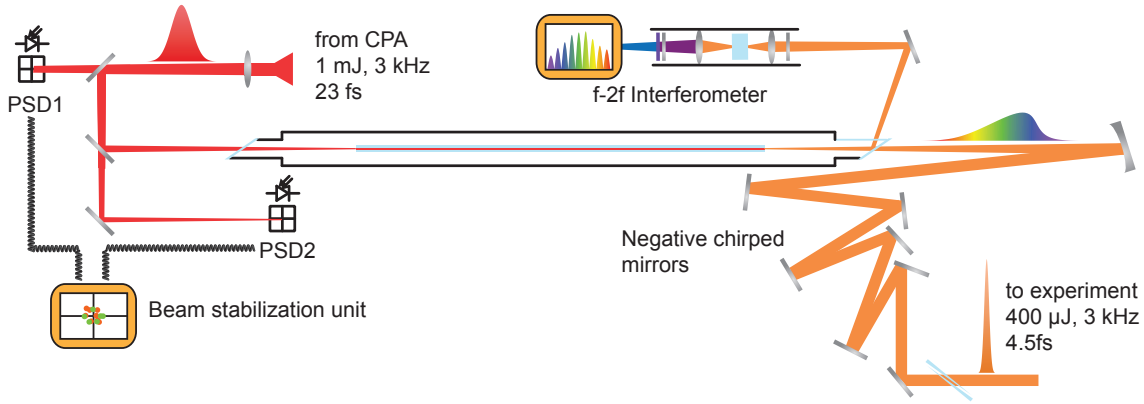

Figure 18 Sketch of the spectral broadening and temporal compression stages. The laser pulse is coupled into the hollow core fiber controlled and stabilized by commercial beam stabilization unit utilizing position sensitive four-quadrant diodes (PSD). New spectral components are created via SPM and self-steepening resulting in a sharkfin-like pulse envelope. The broadened spectrum is compressed in a double-angle negative chirped mirror compressor.

The positive dispersion of the neon, air and fused silica in the beam path are subsequently compensated for in a broadband negative chirped-mirror compressor [142]. The final compression is achieved in a pair of fused silica wedges mounted in vacuum on a motorized translation stage. The temporal structure of the pulses is measured using TG-FROG (see appendix D) and depicted in figure 19, revealing a FWHM pulse duration of 3.4 fs, which corresponds to less than 1.5 cycles of the optical carrier wave.

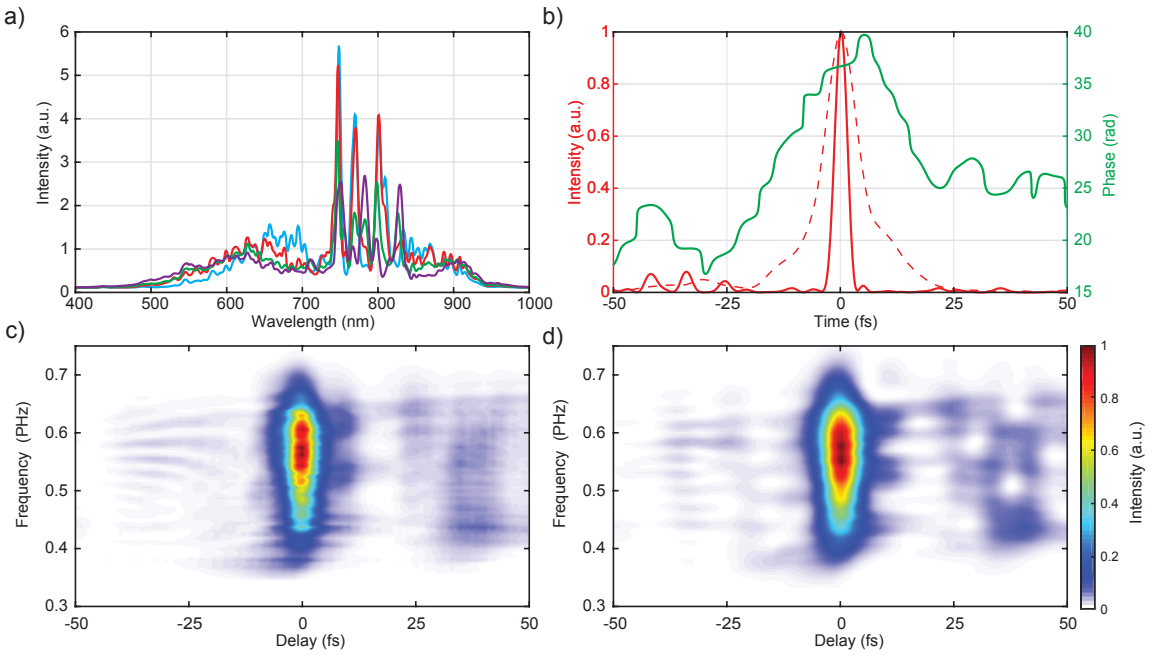

Figure 19 a) Output spectra from the hollow core fiber filled with 1.6 bar (blue), 1.8 bar (red), 2.0 bar (green) and 2.2 bar (purple) Neon gas. b) b) Pulse envelope intensity $E_0(t)$ (solid red), gate $G(t)$ (dashed red) and temporal phase $\phi(t)$ (green) retrieved with the iPIE algorithm. c) Measured TG FROG spectrogram. d) Reconstructed TG-FROG spectrogram.

Carrier-envelope phase stabilization

The periodic pulse train emitted by the mode-locked femtosecond oscillator in the time domain constitutes a so-called optical frequency comb in the frequency domain [87, 151]. The spectral properties of an optical frequency comb can be found by Fourier transformation of the electric field emitted by the mode-locked oscillator

$$E_L(t) = \frac{1}{2} \sum_{n=-\infty}^{\infty} E_0(t - nT) \cdot e^{-i\omega_L(t-nT) - in\Delta\phi_{CE}} + c.c., \tag{2.38}$$

wherein E_0 denotes the real envelope function of a single few-cycle pulse and T denotes the 12.8 fs period between two consecutive pulses. Because of the mismatch of the group-velocity $v_g = (\partial k/\partial\omega)^{-1}$ and the phase-velocity $v_c = k/\omega$ during one round-trip of the pulse inside the oscillator, the phase of the electric field of consecutive pulses is shifted w.r.t. to its envelope by (see figure 20)

$$\Delta\phi_{CE} = \frac{2\pi}{\omega_L} \int_0^{L_{cav}} \frac{1}{v_g(z)} - \frac{1}{v_p(z)} \, \mathrm{d}z, \tag{2.39}$$

wherein L_{cav} denotes the length of the cavity [152]. The spectral representation of the oscillator field follows as

$$\begin{aligned} \tilde{E}_L(\omega) &= \frac{1}{2} \sum_{n=-\infty}^{\infty} e^{-in(\omega T + \Delta\phi_{CE})} \int dt \, E_0(t) e^{-i(\omega+\omega_L)t} + c.c \\ &= \frac{1}{2} \sum_{n=-\infty}^{\infty} e^{-in(\omega T + \Delta\phi_{CE})} \left[\tilde{E}_0(\omega - \omega_L) + \tilde{E}_0(\omega + \omega_L) \right], \end{aligned} \tag{2.40}$$

wherein $\tilde{E}_0(\omega)$ denotes the Fourier transform of the envelope function of a single few-cycle pulse. Finally, through application of the definition of the Dirac delta-function via the complex-exponential, the frequency comb is unravelled

$$\tilde{E}_L(\omega) = \frac{1}{2} \sum_{n=-\infty}^{\infty} \delta\left(\omega - n \cdot \frac{2\pi}{T} + \frac{\Delta\phi_{CE}}{T} \right) \left[\tilde{E}_0(\omega - \omega_L) + \tilde{E}_0(\omega + \omega_L) \right]. \tag{2.41}$$

The frequency comb consists of equally spaced and narrow linewidth laser lines at the comb frequencies $f = n \cdot f_{rep} + f_{ceo}$, with the repetition rate $f_{rep} = 1/T$ and the carrier-envelope offset frequency $f_{ceo} = \Delta\phi \cdot f_{rep}/2\pi$, which both lie in the radio-frequency domain for state of the art solid state laser oscillators. In practice, the linewidth of the individual comb lines is limited by the technical noise of the laser as well as the so-called Schawlow-Townes linewidth. However the finite broadening of each comb line does not influence the comb line spacing [153].

The measurement of f_{ceo} and ϕ_{CE} can be performed using perturbative or non-perturbative nonlinear optics. In the former case parametric, i.e. energy-conserving, low-order optical nonlinearities [85, 154] are utilized to create new frequency combs with differing integer or fractional multiples of f_{ceo}. The case for second harmonic generation [86] (SHG) $f_{ceo(2\omega)} =$

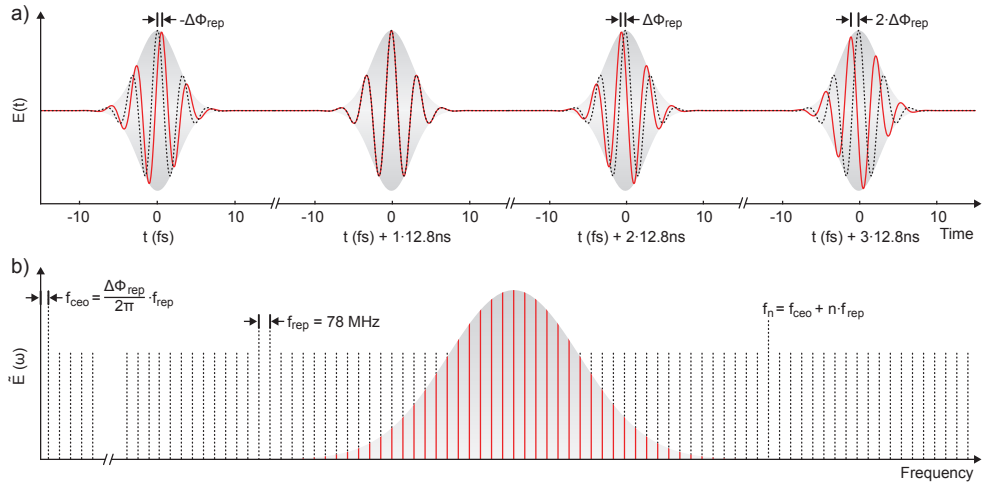

Figure 20 a) Femtosecond pulse train emitted by the mode-locked oscillator at repetition rate $f_{rep} = 78$ MHz, corresponding to a pulse period of 12.8 ns. The periodic phase slippage between the electric field (red line) and the pulse envelope (red shading) is $\Delta\phi_{CE}$ is closely linked with the carrier-envelope-offset frequency f_{ceo}. The dotted line represents the electric field for $f_{ceo} = 0$. b) Corresponding frequency spectrum of single femtosecond pulse (gray) and femtosecond pulse train emitted by the oscillator (red). The dotted lines represent the underlying frequency comb and its continuation to the radio-frequency domain. Only the positive frequency side of the spectrum is depicted.

$2 \cdot f_{ceo}$ and difference-frequency generation [155] (DFG) $f_{ceo(0\omega)} = 0 \cdot f_{ceo}$ is illustrated in figure 21. The use of the DFG scheme has several advantages, as the spectral broadening process necessary to achieve spectral overlap between the fundamental and DFG spectra takes place in the same PPLN crystal as the DFG. This allows a rugged common-path interferometer design [155] and is used in all laser systems utilized for the experiments presented in this thesis. Furthermore, measurement of the CEP can be achieved using directional multiphoton ionization from isolated atoms [156, 157] or nonperturbative photocurrent generation from solid-state targets [158, 159].

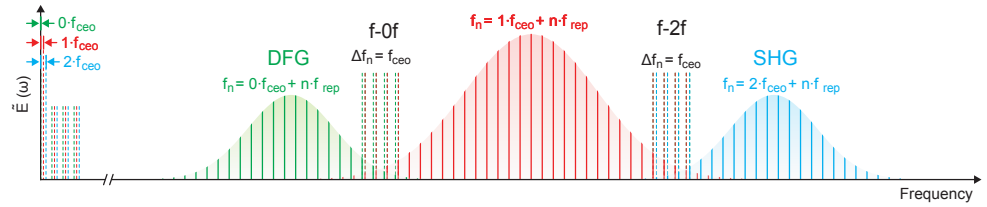

Figure 21 Schematics of CEP measurements using the f-0·f and f-2·f interferometer techniques.

Three schemes for stabilization of f_{ceo} exist. First and foremost is the feedback-stabilization scheme [160], wherein the measured f_{ceo} is compared to an integer fraction of f_{rep} in a digital phase-detector and the generated error signal is stabilized by control of the oscillator pump power or the Ti:Sa crystal temperature (FP2old,FP3). The pulse-picker inside the amplifier chain is synchronized to select pulses with an integer multiple of the ratio f_{rep}/f_{ceo} in order to output a pulse train with $\Delta\phi_{CE} = 0$. The second possibility is to directly use the $f_{ceo(0\omega)} = 0 \cdot f_{ceo}$ frequency comb generated in DFG for seeding of the amplifier [161]. This scheme however is impractical for Ti:Sa lasers, because the stabilized output has a different frequency than the

amplification gain spectrum. The third method is the so-called feed-forward stabilization scheme [162, 163], wherein an acousto-optical crystal is excited by a strong radio frequency signal at f_{ceo}. A beam with $f_{ceo} = 0$ emerges at the diffraction order -1 and is used to seed the amplifier chain (FP3).

Furthermore, slow drifts of the CEP that accumulate during propagation of the beam through the amplification, compression and nonlinear broadening stages [84, 164] need to be compensated. This stabilization is achieved with a collinear f-2f interferometer, the precise setup of which is described in [165]. The generated error signal is fed back to a piezoelectric translation stage below either the second prism in the prism compressor (FP2old), or one of the SF57 glass blocks in the pulse stretcher (FP2new, FP3).

2.6.2. Ultrahigh-vacuum beamline

The low absorption length of XUV radiation (few mm) as well as released photoelectrons in air (few μm), necessitates a vacuum enclosure for the whole attosecond beamline from the XUV generation to the sample surface. The main difficulty arises in removal of the gas used for HHG, which enters the vacuum apparatus at pressures around 200 mbar. To this end, a sophisticated multi-stage differential pumping scheme utilizing multiple turbomolecular drag pumps is implemented in the attosecond beamline, allowing for a 13 orders-of-magnitude reduction in pressure between the HHG volume and the sample surface. Maintaining UHV conditions at the sample position is key in preventing contamination of the surface, which could falsify the measured attosecond delays [35]. Furthermore, a bake-out of the UHV chambers is necessary to remove adsorbed gasses (H_2O, CO, CO_2,C_xH_y) from the stainless steel chamber walls. To this end, the experimental and preparation chambers are heated to $150°$C for 4 days.

A schematic of the vacuum enclosure as well as the NIR and XUV beam paths is depicted in figure 22. A detailed description of the beamline and UHV apparatus as well as the alignment procedure can be found in [166, 167] and [168, 35], respectively.

High harmonic generation chamber

The NIR beam enters the attosecond beamline through a fused silica window mounted at Brewster's angle to avoid reflection loss. A pair of fused silica wedges, with one mounted on a stepper motor controlled linear translation stage, is traversed by the beam and utilized for final temporal compression of the pulse. Mounting the final compression stage as close as possible to the HHG target avoids radiation damage of the beam steering mirrors due to self focusing [169]. The beam size and power are adjusted with an iris aperture and the beam is subsequently focused into the HHG target. The folding and focusing mirrors are installed to minimize the angle of incidence on the curved mirror in order to minimize astigmatism in the laser focus, which is detrimental to both the achievable XUV flux and cut-off energies.

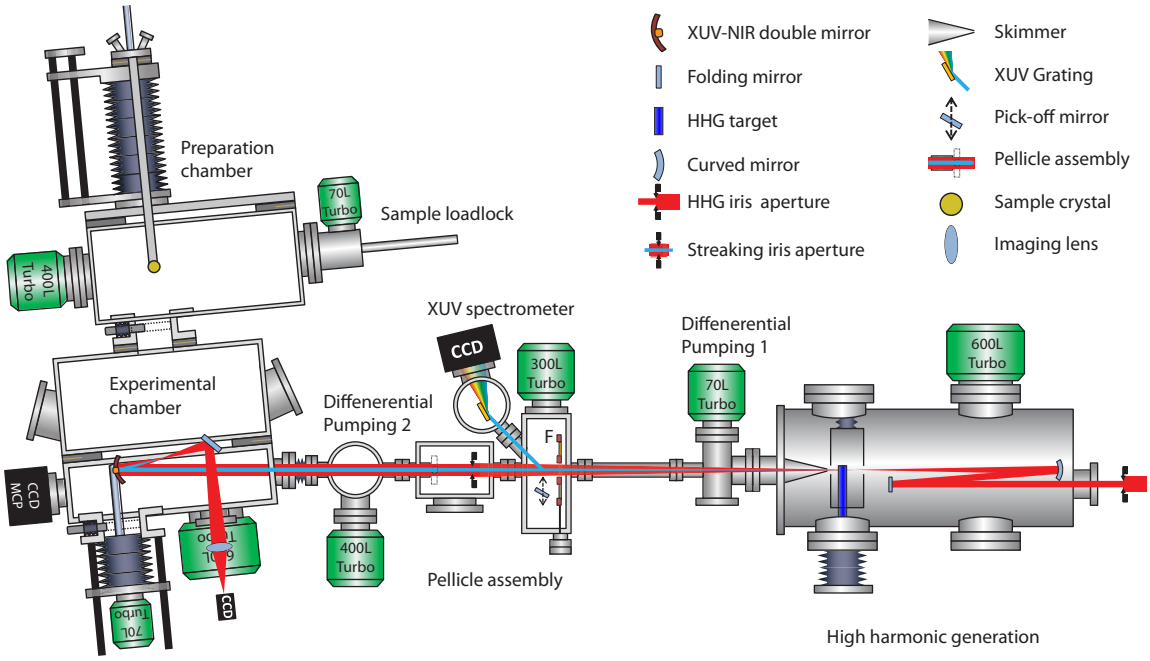

Figure 22 a) Schematic illustration of the vacuum apparatus and the laser beam path in the UHV attosecond beamline. Adapted from [35].

The HHG target is a gas-filled ceramic or stainless steel tube and mounted perpendicular to the beam and the end is either pinched off (stainless steel) or sealed with vacuum epoxy (ceramics). Pre-drilled holes allow the seamless transmission of the beam. The target is filled with neon gas at pressures of $100 - 300$ mbar, to achieve phase-matching of the creation of XUV radiation at photon energies between 90 eV and 150 eV. The neon gas is continuously supplied through the target and evacuated from the HHG chamber with a 600 l/s turbomolecular drag pump. Furthermore, the chamber is outfitted for concurrent UV/XUV generation through third harmonic generation in a second gas target [170]. However this functionality was not used in the experiments presented in this thesis. To avoid excessive noble gas transmission into the beamline and re-absorption of the XUV, a skimmer is placed approximately 30 mm behind the target. The first differential pumping stage is placed directly behind the skimmer and is evacuated with a 70 l/s turbomolecular drag pump.

Spectral and spatial filtering, XUV spectrometer

The first beamsplitter of the Mach-Zehnder type collinear interferometer is a circular thin metal filter with radius 3.5 mm, which is aligned to the center of the copropgating NIR and XUV beams. The filter material and thickness is chosen to transmit the radiation in the cut-off region of the XUV spectrum (see section 2.3.3) and reflect and absorb the NIR field and low-order UV and XUV harmonics, respectively. Typical filter thickness range from 150 nm to 1μm. For photon energies below 115 eV most commonly a zirconium filter is used, whereas for higher energies a palladium filter is preferable in order to create Gaussian pulses with vanishing low-energy pedestals. The pellicle filter is glued on top of a nitrocellulose membrane or suspended from thin tungsten wires

mounted on top of a 20μm thin glass plate with a central hole for transmission of the XUV. The pellicle assembly is implemented to physically separate UHV part of the experimental apparatus from the beamline.

Furthermore, a set of interchangeable filters are mounted on a magnetically coupled translation feedthrough. Zr and Pd filters allow the blocking of the NIR beam during imaging and spectral characterization of the XUV mode. Aluminium (Al) and silicon (Si) filters are introduced for their sharp L_2 absorption edges at 72.8 eV and 100 eV, which can be used for calibration of the energy scale. An additional 500 nm Zr foil can be introduced in the beam path to prevent damaging of the Si filter as well as further reduce XUV flux for calibration. The transmission curves of the filter foils are depicted in figure 5 b. The filters also introduce negative chirp into the XUV beam and compensate for the positive chirp of short-trajectory harmonics [130, 74, 171].

A gold pick-off mirror can be inserted at grazing incidence to reflect the beam onto a gold-coated flat-field grating [172, 173], which disperses the beam onto a backside-polished charge-coupled-device camera (CCD), which is sensitive to the XUV radiation and vacuum-sealed, for spectroscopic analysis of the generated XUV radiation. Lastly, a second differential pumping stage consisting of a small vacuum chamber and a 400 l/s turbomolecular drag pump is used to pump residual gas passing past the pellicle assembly.

Experimental chamber

The beam-combiner of the collinear interferometer is a concentric two-component focusing mirror, which is cut from a single super-polished mirror substrate with radius of curvature -25 cm. The inner part of this mirror has a diameter of 5 mm and is coated with a multilayer coating optimized for XUV reflection. The design of the multilayer is adjusted to the central energy and bandwidth required in the chronoscopy experiments [93, 174]. The outer mirror is either coated with a silver coating $(R = 96\%)$ for maximum NIR intensity in the experiment, or with a thin boron carbide layer $(R = 10\%)$ for reduced NIR intensity on samples prone to radiation induced damage and ablation. The mirrors are mounted on a double mirror mount, which allows independent beam steering for both mirrors. The distance between the mirror front faces is adjusted with a piezo delay stage with active capacitance feedback stabilization for attosecond control of the relative XUV-NIR time delay Δt. The whole double mirror assembly is mounted on a CF 250 flange, which is retractable from the experimental chamber and can be separated from the vacuum system with a gate valve. Thus the double mirror can be extracted from the chamber for exchange and bake-out of the temperature sensitive XUV multilayer coatings and piezo stages.

For photoelectron detection a commercial time-of-flight (TOF) spectrometer with differential pumping is installed, allowing both gas-phase as well as solid state experiments to be performed. All attosecond photoelectron spectroscopy measurements presented in this thesis are performed

with the TOF spectrometer and the conversion from electron flight times to kinetic energies is explained in some detail in appendix A. Furthermore, a hemisperical electron analyser for angle-resolved photoemission experiments is installed. Both electron spectrometers are mounted on a rotational section of the experimental chamber in order to adjust the angle between the XUV beam and the electron spectrometer as well as to interchange the TOF and hemispherical analysers depending on the experimental requirements. A mass spectrometer allows residual gas analysis and quick in-situ leak detection. For gas phase streaking experiments a small gas nozzle is mounted to the fixed part of the experimental chamber. The gas nozzle is made from a glass capillary, which is coated with graphite to avoid electrostatic charging.

A dual-anode X-ray source for generation of Mg K_α (1253 eV) and Al K_α (1486 eV) radiation, which in conjunction with the hemispherical can be used for chemical analysis of samples and surfaces through core-level photoemission spectroscopy (ESCA). Especially the 1s core levels of oxygen (532 eV) nitrogen (400 eV) and carbon (285 eV) are analysed to determine surface contamination.

Lastly, an assembly consisting of a double micro-channel-plate (MCP) in chevron geometry with a caesium iodide coating for enhanced XUV sensitivity, and a phosphor screen on the rear side of the detector, is installed for detection of the XUV flux and mode. The spatial distribution of the XUV radiation is converted into electrons in the MCP, which in turn excite green light fluorescence on the phosphor screen to be detected with a CCD camera positioned outside vacuum.

Preparation chamber

The preparation of well defined single crystal surfaces is performed in a designated cylindrical vacuum vessel connected to the main experimental chamber via an all-metal gate valve. The front flange is again a rotational flange with the sample mounted on top of a helium continuous flow cryostat capable of cooling down to about 20 K. Furthermore, an electron bombardment heating system is installed on the sample holder allowing heating of single crystals to beyond 2400 K. The sample temperature is monitored by a thermocouple directly spot welded to the edge of the crystal. C-type thermocouples are used for tungsten crystals, K-type thermocouples otherwise.

The sample manipulator is mounted off-center on the front flange so the sample can be brought in front of the different preparation instruments located on the mantle of the chamber. Furthermore, the manipulator can be translated in all three axes with stepper motors located outside of the vacuum and the sample arm can be rotated around its axis with a DC motor. The positions of all stepper motors are read out with position retaining linear scales with 5μm precision. A separately pumped load-lock system allows fast sample exchange.

For sputtering and oxygen cycling a commercial sputter gun and a gas dosing valve are attached to the chamber. Furthermore, thin films can be grown on top of the sample with several thermal evaporators, which can be attached to the camber via two designated UHV gate valves. A second mass spectrometer is installed in the preparation chamber for residual gas analysis.

Lastly, an commercial low-energy electron diffraction (LEED) system is installed in the preparation chamber, which allows to investigate the crystal symmetry and surface flatness of the prepared surfaces.

Part III

Attosecond chronoscopy of simple metals

Attosecond chronoscopy of simple metals

3.1. Introduction and statement of contributions

As already outlined in the introduction, the technique of photoemission chronoscopy was first introduced in a seminal paper by Cavalieri et al. [12], who performed attosecond streaking spectroscopy and showed the photoemission at 91 eV from tungsten 4f core levels to be delayed by 110 ± 70 as w.r.t. the photoemission from valence and conduction bands. This result inspired a plethora of theoretical and numerical studies proposing different microscopical mechanisms for the aforementioned time delay [96, 97, 98, 99, 175, 176, 101, 177, 178]. However, systematic investigations of the applicability of such models were not possible at the time because of the limited availability of further experimental data. One difficulty recognized early was the complexity of the electronic structure of the transition metal tungsten, which is composed of 74 electrons per atom. Thus, experiments of the much simpler alkaline earth metal magnesium (Mg), which is only contributing 12 electrons per atom and unit cell, were conducted at photon energy 117.5 eV, which revealed a very small time delay of 5 ± 20 as between the photoemission from valence and conduction band electrons and 2p core levels [24].

More recently, much interest has been given to the question of the relationship of photoemission from surface and bulk electronic states and their respective mean depth of origin within the crystal. Using the RABITT technique, Tao et al. [28] measured photoemission time delays up to 240 as between the 3d sub-levels of the valence band from transition metals and attributed this observation to different lifetimes of the high-energy conduction band states constituting the photoemission final-state. These lifetimes effectively represent the different inelastic scattering cross-sections of electrons in high-energy conduction band states [29]. However, they could not conclusively solve the question whether and how the ballistic transport and mean-escape path are affected from the photoemission resonance. Progress in this direction has been reported by L. Kasmi et al. [33], who investigated low-energy time delays of the copper d-band against an external argon reference and found time delays greater than the time delay expected from free electron propagation for some but not all photon energies, which was attributed to the high-energy band structure with a model based on the bulk band structure of copper. Such models however exclude surfaces states and surface resonances altogether and are incapable of accounting for the transition matrix elements between the initial and final states and inelastic and elastic scattering.

In this chapter energy-dependent attosecond streaking spectroscopy is demonstrated on the Mg(0001) surface to show the profound interplay between the electronic structure of the material and the observed attosecond delay. The experimental results are compared to semi-classical

and quantum-mechanical modelling. The attosecond streaking spectroscopy and angle-resolved photoemission experiments presented in this chapter have been performed in collaboration with Martin Schäffer, Maximilian Schnitzenbaumer, Dionysios Potamianos and Marcus Ossiander. The experiments were supervised by Prof. Reinhard Kienberger and Prof. Peter Feulner and carried out at the AS-3 beamline at Max-Plank Institute for Quantum Optics. The Gaussian fitting algorithm used for delay and chirp retrieval of both the experimental and numerical streaking spectrograms was implemented by Marcus Ossiander and adjusted for the magnesium experimental and numerical data by the author. The synchrotron measurements have been performed by Dr. Stefan Neppl and Prof. Peter Feulner at Bessy in 2010. They have been re-evaluated by the author and are included in this thesis in order to give a complete picture of the resonant and non-resonant photoemission experiment. Data evaluation and semiclassical calculations were performed by the author in part using projected inverse LEED states provided by Prof. Eugene Krasovskii from the Universidad del Pais Vasco/Eusakal Herriko Unibertsitaetea in San Sebastian. The implementation of the Full-Penn algorithm, necessary for determination of the inelastic mean free path was done by Christian Schröder. The quantum-mechanical calculations were performed by Prof. Andrey Kazansky also from the Universidad del Pais Vasco/Eusakal Herriko Unibertsitaetea with input from the semiclassical simulations.

3.2. The Magnesium (0001) surface, properties and preparation

The alkaline earth metal magnesium with atomic number 12, crystallizes in the hexagonal-close packed (hcp) geometry (see figure 23 a). The lattice vectors are $|\vec{a}_1| = |\vec{a}_2| = 3.21\,\text{Å}$ and $|\vec{a}_3| = 5.21\,\text{Å}$, respectively. The (0001) surface of the crystal is oriented parallel to $\vec{a}_3$ and perpendicular to the hexagonal planes. The corresponding surface Brillouin zone is similar to the $\Gamma - M - K$ plane of the volume Brilloin zone (see figure 23 b).

Pristine single crystalline surfaces of magnesium crystals for photoemission experiments can be produced by cutting, polishing and cleaning of large single crystal samples [179, 118]. This option is traditionally employed for noble and transition metals, which can be heated to high-temperatures in order to evaporate residual adsorbates from the surface. However, the process requires several hours and cycles of sputtering and thermal annealing. A preparation procedure more suitable towards the repetitive task of measuring attosecond streaking spectrograms with combined statistics in the 10 as range, is the thermal evaporation of magnesium thin films on tungsten host crystals [180]. The low relative lattice mismatch $(a_{\text{Mg}} - a_{\text{W}})\,/a_{\text{Mg}} = 1.4\,\%$ between the Mg(0001) plane of and the W(110) surface leads to smooth layer-by-layer growth without formation of three dimensional islands [181] even for film thickness beyond 60 monolayers [180].

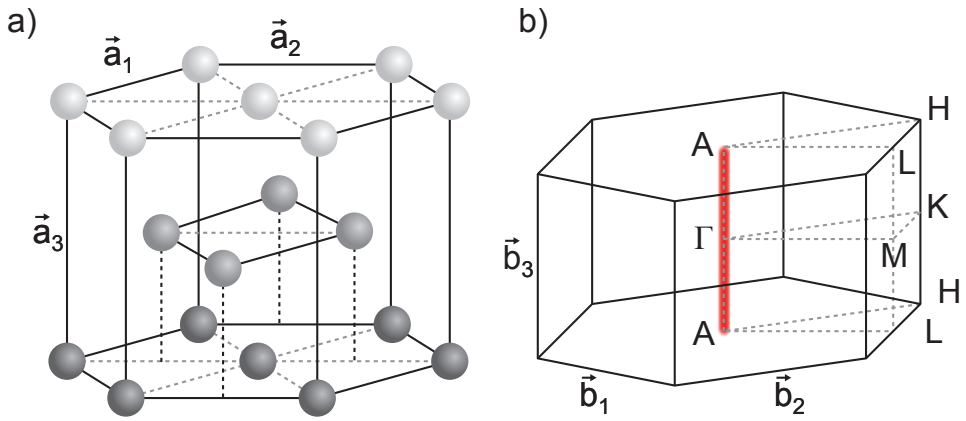

Figure 23 a) Real space magnesium crystal structure. Grey balls represent individual magnesium atoms. $\vec{a}_{1,2,3}$ are the lattice vectors spanning the unit cell of the hcp grid. b) First Brillouin Zone of the reciprocal lattice of the magnesium crystal. $\vec{b}_{1,2,3}$ are reciprocal lattice vectors. The red line marks the Γ-A direction, which corresponds to normal emission from the (0001) surface. The surface Brillouin zone associated with the (0001) surface is constructed from the $\Gamma - M$ and the $\Gamma - K$ vectors.

The preparation of the tungsten host crystal is presented in section 4.2. The magnesium film is evaporated from a well-outgassed tantalum crucible at a temperature of $400°$C for at least five minutes. The approximate growth speed is 7 layers per minute. The sample is held at room temperature during the evaporation. Subsequently, the film is annealed at about $200°$C for 3 minutes while the sample is transferred from the preparation chamber to the experimental chamber. The surface structure is monitored with LEED (see figure 24 b,c,d). The annealing step greatly improves the surface quality of the sample. The final thickness of the film is about 30 atomic layers, which is enough to describe both the core levels, as well as the valence and conduction band states as bulk magnesium-like [181, 180].

Figure 24 a) shows an X-ray photoemission spectrum (Bessy 2010) of magnesium recorded with synchrotron radiation tuned to 700 eV photon energy. The absence of 1s core-level photoemission from oxygen (532 eV) and carbon (285 eV) shows the high degree of surface cleanliness achieved with this preparation technique [35]. The surface cleanliness is sustained by frequent re-preparation of the magnesium thin film at least every 90 minutes during attosecond streaking and high-resolution photoemission measurements. The underlying tungsten surface is cleaned and prepared according to the process described in section 4.2 once at the beginning of each day of measurements.

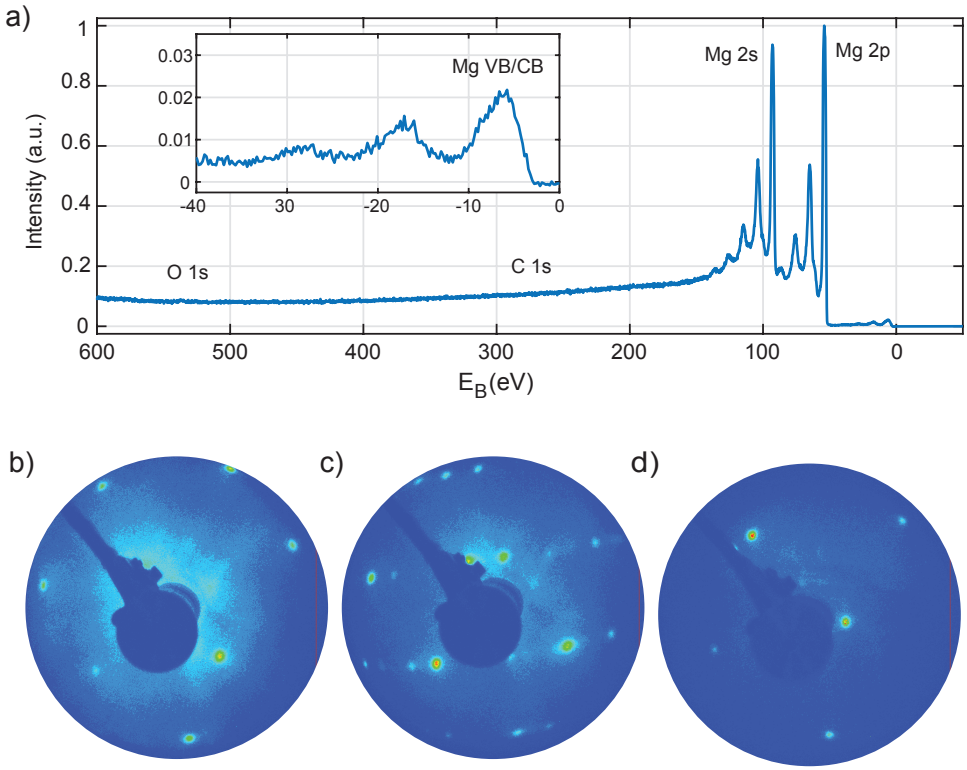

Figure 24 a) XPS of the Mg(0001) surface grown on top of W(110) with synchrotron radiation at 700 eV. The inset highlights the valence and conduction band region. Adapted from [35]. b) LEED pattern of the Mg(0001) surface measured directly after evaporation. Hexagonal LEED pattern is superimposed with amorphous background diffraction from the rough surface. Adapted from [35]. c) LEED pattern after annealing to $250°$C. A superstructure indicative of the formation of stripe superstructure for ultrathin magnesium films on W(110) is observed due to excessive evaporation of magnesium during thermal annealing process. d) LEED pattern after annealing to $200°$C. The sharp hexagonal diffraction pattern implies high degree of and surface flatness and regularity.

3.3. Energy-, angle-, and time-resolved photoemission from Mg(0001)

The band structure of the Mg(0001) surface has been extensively studied both theoretically [182, 183, 184] and experimentally [118, 180]. Measurements of the photoelectron spectrum of the Mg(0001) surface have been performed by Bartynski et al. [118] up to photon energies of 115 eV, revealing a peculiar resonant enhancement of the surface state photoemission at 45 eV and parabolic resonant emission bands centered at photon energies 20 eV and 95 eV. Further surface state resonances and parabolic bands have been observed for the (111) surface of the free-electron metal aluminium up to photon energies of 700 eV [185] and thus are expected for the Mg(0001) surface as well. Around the Γ-point, the band structure is dominated by parabolic free-electron states characteristic of simple metals such as light alkali and earth alkali metals. For the Mg(0001) surface the parabolic dispersion is isotropic around the Γ-point, because of the perfect hexagonal symmetry of the (0001) surface of the hcp crystal lattice.

In order to investigate the influence of the band structure on the photoemission process, the study of energy-dependent and time-resolved photoemission is performed. The attosecond streaking technique utilized for photoelectron chronoscopy notoriously suffers from poor spectral-energy resolution because of the multi-eV bandwidth of isolated attosecond pulses. Further detail on the spectrum of initial states and photoemission matrix elements can be found from high-resolution synchrotron photoelectron spectroscopy measurements, which can be correlated with attosecond photoemission time delays to disentangle the complicated photoemission process. Motorized grating monochromators allow the smooth variation and precise selection of narrowband XUV and soft X-ray radiation from a broadband undulator source. The first resonance of the surface state photoemission at 45 eV eludes the attosecond streaking technique, because a reference core level for photoemission delay comparison is lacking at such low energies. A suitable workaround would be the adsorption of monolayers of Neon or Helium, but at the cost of the added complexity of generating isolated attosecond pulses at lower energy [57, 186]. The second surface resonance at 135 eV, however is suitable for relative delay measurement w.r.t. the photoemission from the Mg 2p core level. To this end, photoemission experiments with synchrotron radiation have been performed at the undulator beamline U49/2-PGM1 at BESSY-II [35, 187] up to photon energies of 500 eV in order to characterize higher order resonances of the surface state photoemission (see figure 25).

Consecutive resonant photoemission from the surface state and Fermi edge states is observed at photon energies of 135 eV, 265 eV and 450 eV along with the characteristic parabolic resonant enhancement bands spanning the whole valence band. The synchrotron photoemission spectrogram can be well understood in the framework of the one-step photoemission theory [188]. However, the one-step theory of photoemission was developed for long excitation pulses and is generally believed to not be applicable for attosecond photoemission chronoscopy at high energies. A direct integration of the Kohn-Sham equations in three dimensions for short excitation pulses and a multitude of time delays for each numerical calculation of an attosecond streaking is hitherto not computationally feasible.

A graphic representation of the attosecond chronoscopy principle and the investigated electronic structure of the combined valence and conduction band and the Mg 2p core level is depicted in figure 26 a. The geometry of sample, electron TOF spectrometer and XUV and NIR beams in the streaking measurement setting is drawn in figure 26 c. The copropagating NIR and XUV beams impinge on the sample at $75°$ angle-of-incidence and generated photoelectrons are detected along the surface normal.

In order to investigate the manifestation of the material band structure for photoemission with isolated attosecond pulses, angle and excitation energy-dependent measurements of the photoemission in the valence band region of Mg(0001) have been performed. The emission angle was systematically varied by rotating the sample under the TOF spectrometer. Each

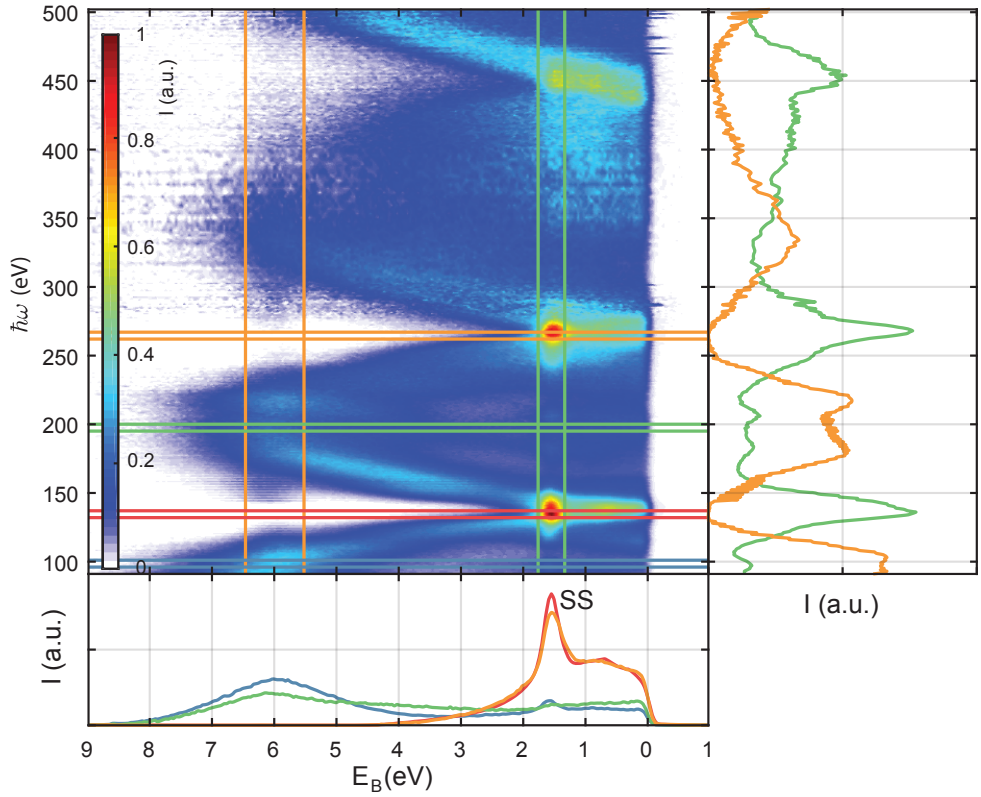

Figure 25 Left: Photoemission intensity from Mg(0001) in normal emission after Shirley background subtraction. Coloured lines mark energy ranges of lineouts along the photon energy (vertical) and binding energy (horizontal) axes. The parabolic bands correspond to higher orders of resonant bulk photoemission. Enhancement at binding energy $E_B = -1.7$ eV corresponds to emission from the Shockley-type surface state (SS) of Mg(0001). The total valence band photocurrent is normalized at each photon energy. Right: Fraction of photocurrent originating from surface states (green) and bottom of valence band states (orange). Bottom: Photoelectron spectra at photon energy $E_{\hbar\omega} = 99$ eV (blue), 135 eV (red), 199 eV (green), 265 eV (orange).

valence band spectrum is divided by the total photocurrent of its respective 2p core level spectrogram, in order to cancel the geometric increase of the photocurrent with increasingly grazing incidence of the XUV radiation on the surface. No background subtraction has been applied. The valence band spectra resulting from this normalization procedure for normal emission and for photon energies of 110.1 eV, 124.4 eV and 133.7 eV are depicted in figure 27.

The fitted positions of the surface normal are $250.3°$, $249.3°$ and $247.8°$ for photon energies 133.7 eV, 124.4 eV and 110.1 eV, respectively. The Γ-point of the surface Brillouin zone can be clearly identified at all three photon energies. Both an increase of the photocurrent and its enhancement around the Γ-point ($k_{||} = 0$) is observed as the excitation energy approaches the 2nd resonance at 135 eV. For comparison, ARPES with synchrotron radiation was performed to confirm the dispersion of the Γ_4 surface state (see Figure 27). The obtained dispersion curve is

$$E_B(\Gamma_4) = -1.65\,\text{eV} + k_{||}^2 \cdot 3.7\,\text{Å}^2 \cdot \text{eV} \tag{3.1}$$

in agreement with [180]. Furthermore, the spectral weight in the valence band region is shifted

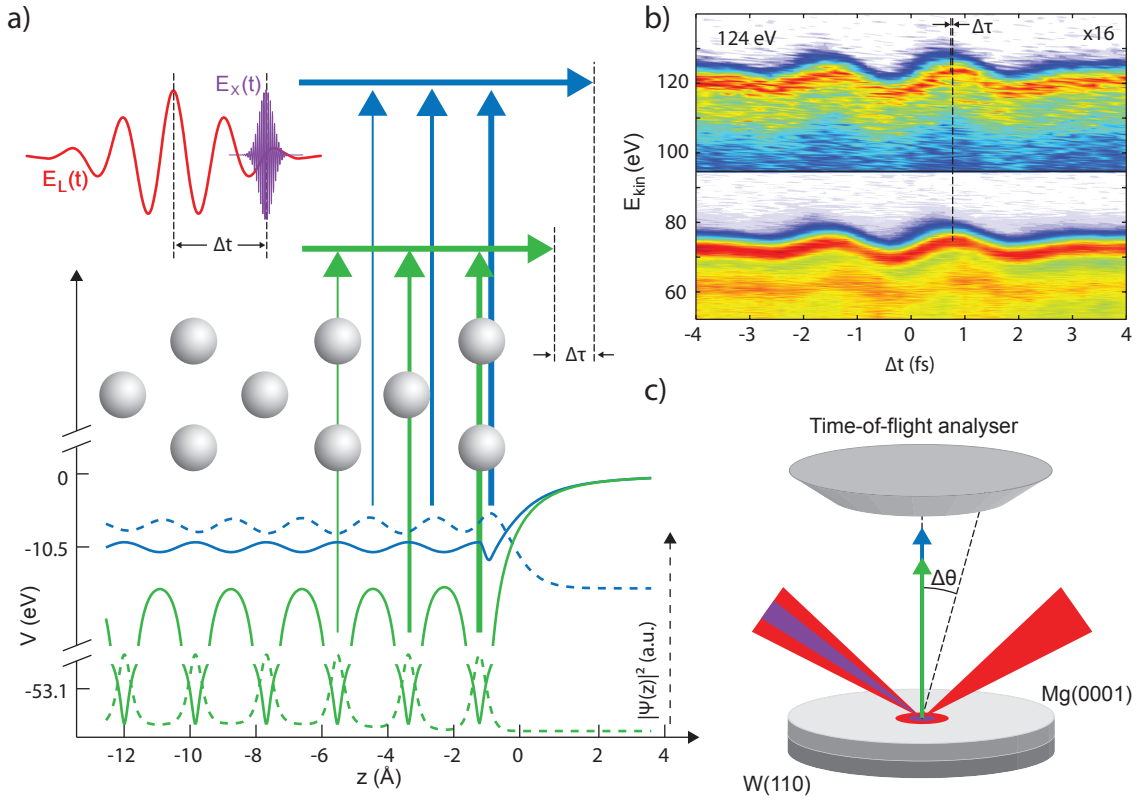

Figure 26 a) Schematics of the attosecond chronoscopy experiment on Mg(0001). Effective one-electron potentials (solid lines) and charge densities (dotted lines) of valence band (blue) and 2p core level (green). Arrows denote photoexcitation into the photoemission final state. b) Streaking spectrogram from Mg(0001) recorded with isolated attosecond pulse centered at 124.4 eV. The photoemission from the Mg 2p core level and the Mg VB are observed at kinetic energies 72.5 eV and 120 eV, respectively. The relative time delay of photoemission $\Delta\tau$ is extracted from the spectrogram. c) Geometry of the sample and XUV (purple) and NIR (red) beams. $\Delta\theta$ denotes the cone angle of acceptance of the TOF spectrometer.

towards the Fermi energy in accordance with the synchrotron result (see Figure 25). This result clearly demonstrates the strong influence of the material band structure on the high energy photoemission process even with attosecond pulses. Because only one of the two angles between the surface normal and the TOF axis can be smoothly rotated inside the experimental chamber, the second angle of the surface normal w.r.t. the TOF spectrometer is aligned visually by approaching the sample to the spectrometer entrance aperture very close without touching it. A flexible TOF mount allows tilting of both angles of the connecting flange around the TOF axis up to $\pm 2°$. The resulting angular deviation from surface normal is estimated to be below $0.5°$, which is much smaller than the cone angle of acceptance of the TOF spectrometer. The geometric acceptance cone angle of the electron detection of the TOF spectrometer is $\pm 2°$. The precision of the orientation of the crystal axis w.r.t to the polished surface is specified by the manufacturer to be better than $\pm 0.5°$.

After determination of the surface normal, attosecond streaking spectrograms are recorded by superimposing both the XUV and NIR beams on the Mg(0001) surfaces. Typical spectrograms are recorded with 100-200 as equidistant resolution on a 7-10 fs temporal range. It shall

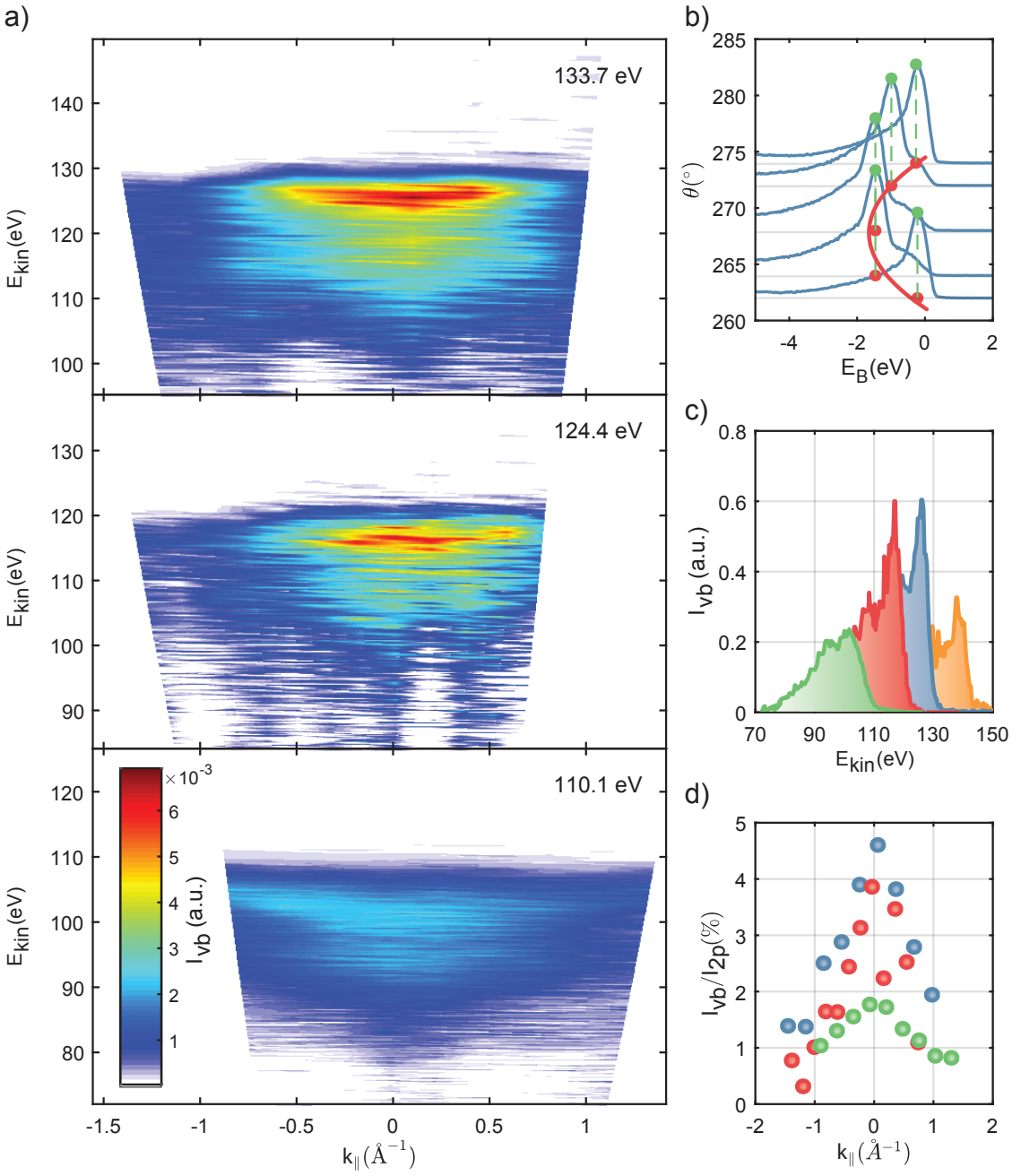

Figure 27 Angle-dependent photoemission from Mg(0001) surfaces measured with attosecond pulses at central photon energies 110.1 eV (green), $124.4eV$ (red), $133.7eV$ (blue) and 145 eV (orange). a) Photoemission spectra recorded for different angles and normalized to the respective photoemission strength from the 2p core level ignoring the plasmon satellites. The angles are converted to corresponding surface-parallel momenta $k_{||}$ (see equation 2.19). b) Surface state dispersion from ARPES with synchrotron radiation at 130 eV c) Photoemission spectra for normal photoemission $k_{\|} = 0$. d) Momentum-dependent integrated photocurrents from a).

be noted that the determination of attosecond delay times does not necessitate a temporal range exceeding the pulse duration, because the interaction of the released electron and the field is similar for both the core level photoelectron and the valence band electron. Example spectrograms at all relevant central photon energies are depicted in figure 28 for the case of narrow cone photoemission ($\pm 2°$).

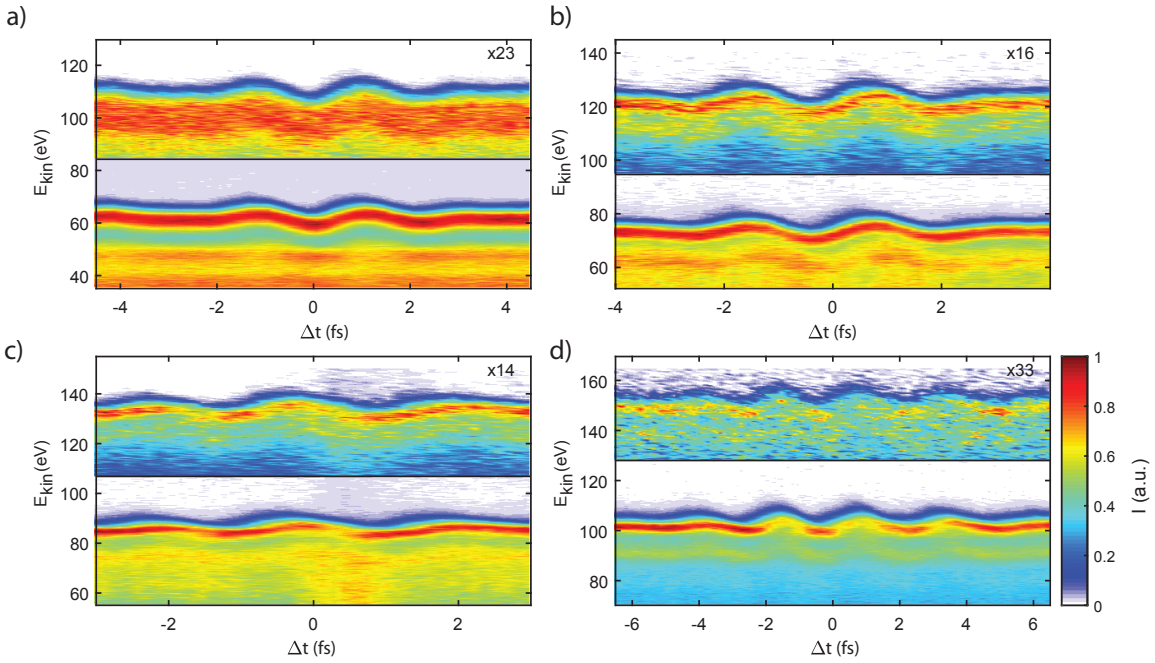

Figure 28 Attosecond streaking spectrograms of narrow cone photoemission measured at central photon energies 110.1 eV (a), 124.4 eV (b), 133.7 eV (c), 145.0 eV (d) . Valence band sections amplified for clarity. Amplification factor noted in top right of spectrogram.

Furthermore, a second set of streaking spectrograms with activated electrostatic Einzel lens was recorded and example spectrograms are depicted in figure 29. The activation of the electrostatic lens increases the acceptance cone angle of the detection electronics up to $\pm 22°$, which corresponds to the surface parallel momentum of the Γ-point in the second Brillouin zone [180]. Thus, photoemission from initial states along the full first-order Brillouin zone is expected to contribute to the spectral intensity and attosecond time delays.

Because photoemission time delays are somewhat susceptible to the introduction of systematic errors, a multitude of photoemission time delay retrieval algorithms and background subtraction methods were used in the evaluations of the obtained time-resolved photoemission spectrograms. The corresponding algorithms are explained in detail in appendix E. The algorithms denoted TDSE and DIFF, rely on the strong-field solution of the time-dependent Schrödinger equation and incoherent superposition of Gaussian wavepackets [13, 24] with a parametrization of both the NIR and XUV laser fields. These techniques necessitate the definition of a set of initial states with corresponding binding energies and photoemission cross-section. The dominant feature of the photoemission spectrograms is the Mg 2p core level photoemission, which is actually comprised by a quadruplet of photoemission lines with spin-orbit splitting 280 meV and surface-bulk splitting 140 meV spanning binding energies between 49.5 and 49.9 eV [189, 24]. For valence band photoemission, a set or artificial initial states is chosen to match the photoemission profile after splitted Shirley background subtraction. The static photoemission spectra before and after background subtraction as well as the static TDSE fitting model (see Equation E.2) are depicted in figure 30.

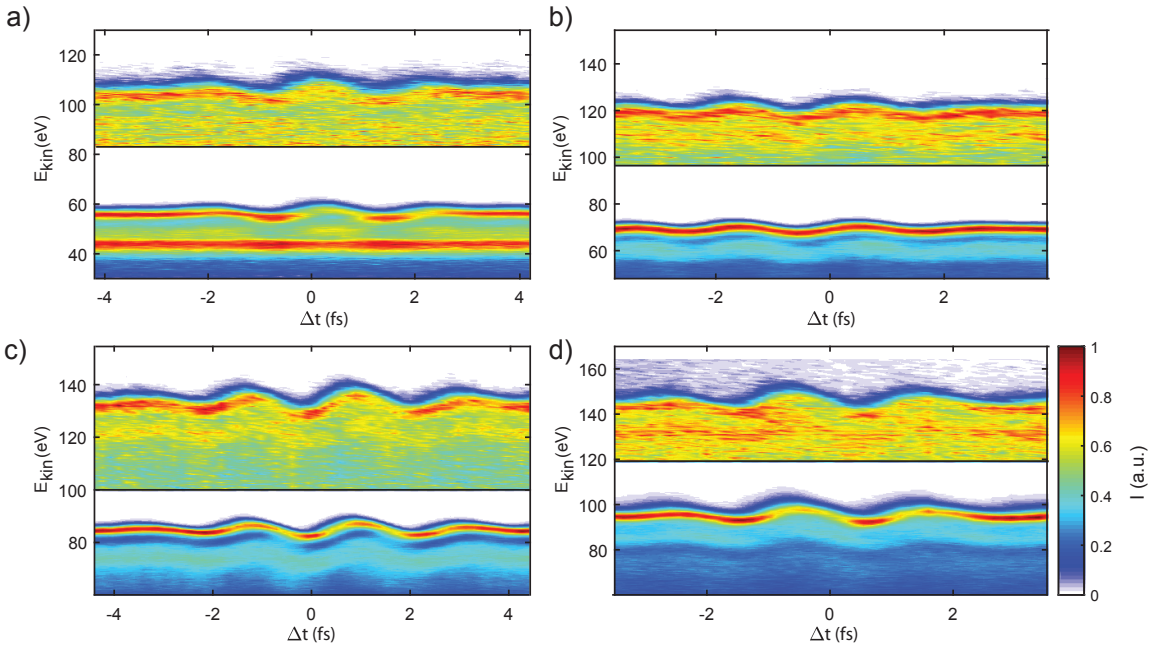

Figure 29 Attosecond streaking spectrograms of wide cone photoemission measured at central photon energies 110.1 eV (a), 124.4 eV (b), 133.7 eV (c), 145.0 eV (d). All spectra are taken with the lens-switching technique outlined in appendix A.

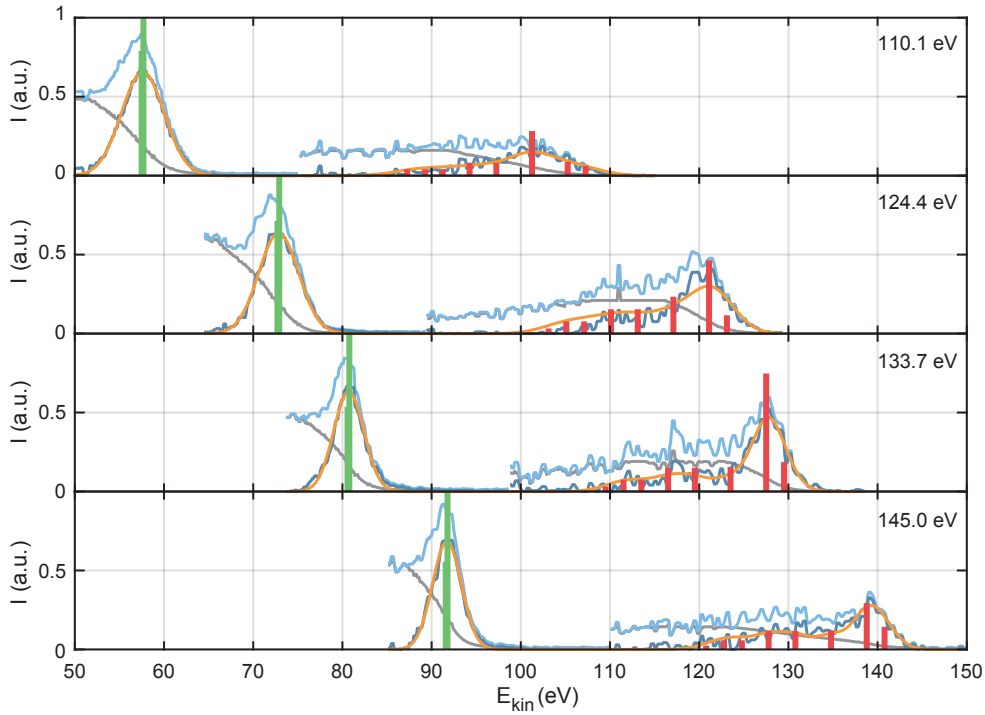

Figure 30 Definition of electronic bound initial states for the TDSE retrieval algorithm for relevant photon energies. Spectral region of Mg 2p core level and valence band photoemission before (light blue) and after (dark blue) splitted Shirley background (grey) substraction. Static photoemission spectra are modelled as incoherent sum of Gaussian wavepackets (see equation E.2) with binding energies and cross sections indicated by stick graphs ($2p^{3/2}$ and $2p^{1/2}$ green and VB/CB red). The corresponding Gaussian fit is indicated in orange. All spectra have been acquired without the electrostatic Einzel lens. The XUV pulse was delayed 300 fs w.r.t. the NIR pulse.

The resulting average delay values are depicted in figure 32 alongside the synchrotron spectrogram in the relevant photon energy range. Indifferent of delay extraction method and

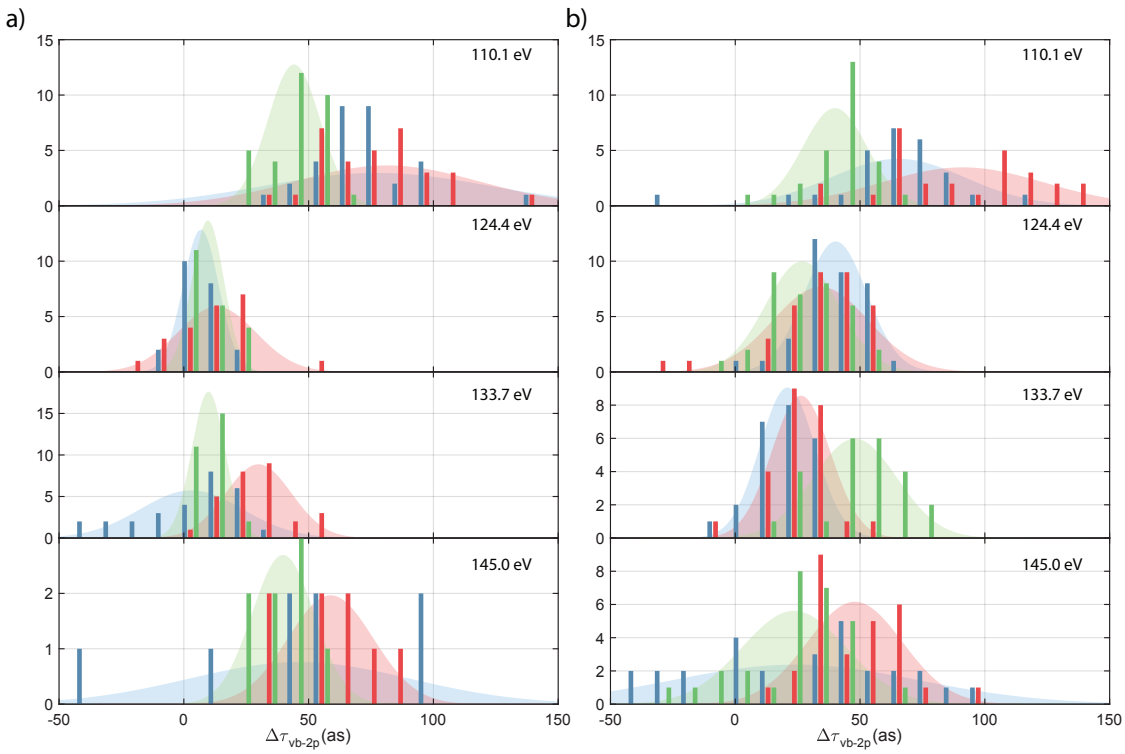

Figure 31 Statistical distribution of relative photoemission time delay of Mg 2p core level w.r.t the Mg valence band extracted from repeated attosecond streaking measurements. The different colours encode the evaluation methods (see figure 32) and central photon energies are marked in the top right of each plot. a) Narrow cone emission $\pm 2°$ b) Wide cone emission $\pm 22°$.

cone-angle of detection, a pronounced minimum of relative photoemission time delay between the delocalized valence band and 2p core level is observed close to the resonance photon energy of 135 eV. All delay extraction results from different methods are averaged and their mutual weights are adjusted to represent the correct observation frequencies of the Student-T distribution. The demonstrated error bars represent the 95% confidence interval of the mean of the distribution. The resulting averages are plotted in figure 32 d, and compiled in table 1.

$\hbar\omega$ (eV)	110.1	124.4	133.7	145.0
$\pm 2°$ (as)	63.6 ± 10.2	12.8 ± 8.6	15.7 ± 8.3	52.4 ± 33.1
$\pm 22°$ (as)	65.9 ± 13.6	16.2 ± 8.5	19.5 ± 12.3	48.8 ± 10.7

Table 1 Relative retardation of the Mg 2p core level photoelectron wavepacket w.r.t. the delocalized valence band $\Delta\tau_{2p-vb}$ (see figure 32).

A. Borisov et al. [100] attributed the photoemission time delay dependence for relative photoemission time delay of the Mg 2p core level to the distinguishable contributions of resonant and nonresonant photoexcitation initiating the photoemission process, and their link to the structure of the effective periodic crystal potential. The increase in photoemission time delay of the valence band in this model is not linked to reduced group velocity, but to the effective depth profile of the photoexcitation [176, 100]. Nonresonant transitions occur at the metal-vacuum interface surface only, regardless of the nature of the initial state being a bulk or surface state [100]. The

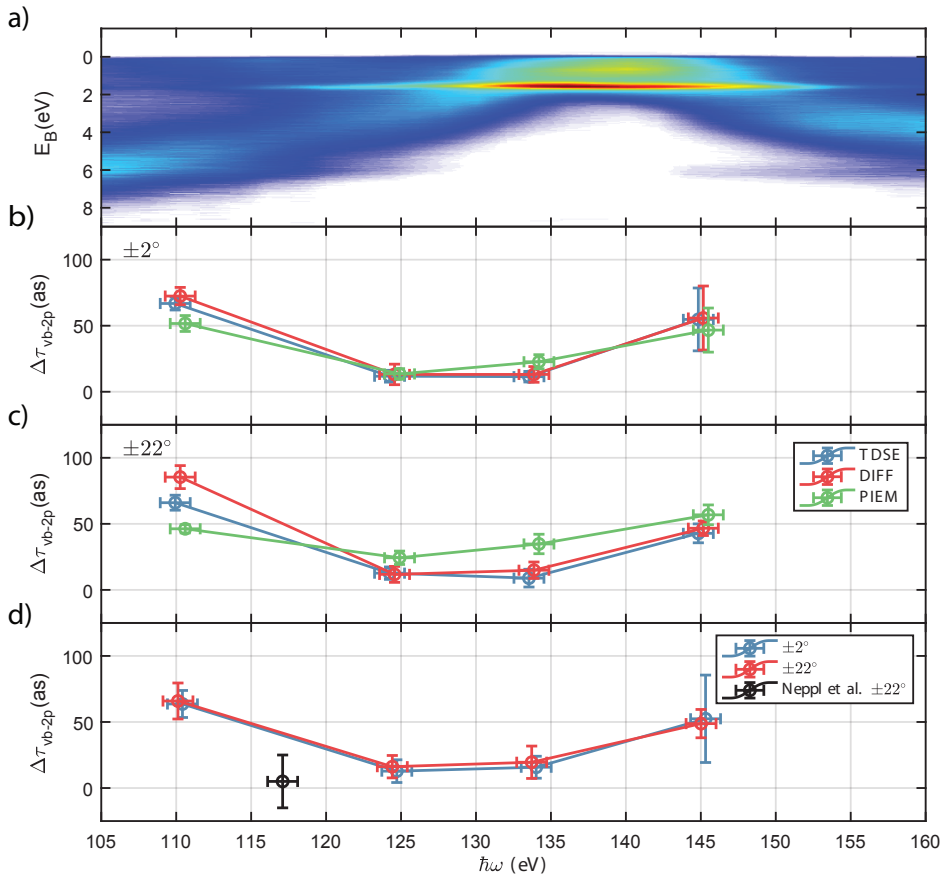

Figure 32 a) Photoemission intensity from Mg(0001) in direction of the surface normal after Shirley background subtraction. b) Relative time delay of Mg 2p photoelectron wavepacket $\Delta\tau$ w.r.t. to valence band photoelectron wavepacket as function of central energy of XUV pulse for measurements performed with narrow cone detection $\pm 2°$ (see figure 28). Error bars denote 95% confidence intervals. c) Same as b), but for wide cone emission $\pm 22°$ (see figure 29). d) Weighted average retrieved time delay $\Delta\tau_{vb-2p}$ for narrow cone (blue) and wide cone (red) detection of photoemission. Error bars represent weighted confidence intervals. Result of Neppl et al. [24] marked in black for comparison.

semi-classical and quantum-mechanical versions of the resonant excitation model are presented in section 3.4 and compared to the experimental result alongside further considerations of possible contributions to the photoemission time delay in section 3.4. Neppl et al. performed attosecond streaking experiments on the Mg(0001) surface in 2010 at photon energy 117.5 eV. They obtained a relative delay of the Mg 2p core states of 5 ± 20 as standard error, which is slightly lower than the interpolated wide-angle $\pm 22°$ results in the new study, but is still commensurable with the new results at 124.4 eV.

3.4. Discussion

3.4.1. Intra-atomic scattering phase shifts

Very recently, Siek et al. [32] discovered that the angular momentum-dependent Eisenbud-Wigner-Smith scattering phase shift $\delta\phi_w$ (EWS) must be taken into account, when modelling

time-dependent photoemission from solids in a very much similar manner as in gas phase attosecond chronoscopy [13, 21, 131]. The temporal delay in photoemission is linked to the retardation of the outgoing photoelectron wavepacket via

$$\Delta\tau_{EWS} = \hbar\frac{\partial}{\partial E}\delta\phi_w. \tag{3.2}$$

The EWS of the 2p core level is calculated numerically with the ePolyScat software package, which is an implementation of the method of partial-wave-decomposition in an all-electron model [190, 191] and depicted in figure 33. One problem arising in the calculation of the scattering delay is that the scattering phase shift diverges for long-range Coulomb potentials and the potential is separated into a Coulomb part and a short range part. The scattering phase shift of the Coulomb potential is called Coulomb-laser-coupling (CLC) and can be calculated analytically [14]

$$\Delta\tau_{CLC} = \frac{\hbar^3 Z}{a_0^3(2m_e E_{kin})^{3/2}} \cdot \left(2 - \ln\frac{2\pi E_{kin}}{\hbar\omega_L}\right), \tag{3.3}$$

with Z denoting the integer charge of the ionic core. In the case of solid-state photoemission, the core hole is screened by the remaining electrons in the solid and no long-range potential is associated. However, as the photoelectron traverses the solid-vacuum interface, an image charge is formed on the surface, with asymptotic behaviour [192, 193]

$$V(z) \propto \frac{1}{4z}, \tag{3.4}$$

which is equivalent to the Coulomb potential with $Z = 1/4$. The CLC time delay of the image charge potential is depicted in figure 33.

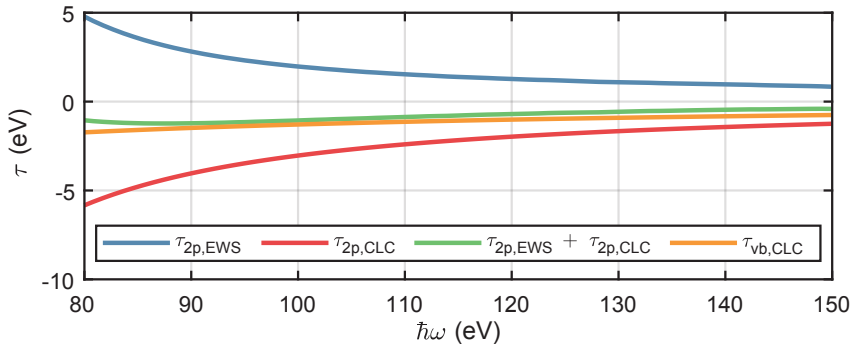

Figure 33 Eisenbund-Wigner-Smith (EWS) and Coulomb-laser-coupling (CLC) attosecond time delays for the Mg 2p core level and valence band. The CLC is referenced to the image potential of the outgoing electron on the magnesium crystal surface and has Coulomb asymptotic behaviour with $Z = 1/4$. The EWS delay for the delocalized valence band is zero because no localized hole-potential is assumed [32].

For the photon energy region of interest of this study, the atomic contributions to the attosecond time delay are limited to 2 as. Furthermore, tracking the resulting net contribution (see figure 33 orange and green lines) to the relative photoemission time delay as recorded in the experiments, we find the total atomic photoemission time delay to be less than 0.5 as for Mg 2p. Hence, the atomic contribution can be safely neglected in the discussion of the experimental results on

Mg(0001).

3.4.2. Classical transport model

The most simple and intuitive model for the prediction of attosecond photoemission time delays is the ballistic transport model assuming free-electron like propagation of the photoexcited wavepacket to the surface. The group velocity of the electron wavepacket is given by equation 2.28 and the time delay follows as

$$\tau = \frac{\bar{d}}{v_g}, \tag{3.5}$$

with the mean electron escape depth $\bar{d}$ w.r.t to the jellium edge. The energy and depth distribution I(z,E) of the photoexcited electron density in the solid is calculated via the following Gaussian model

$$I(z,E) = \sum_{q}^{Q}\sum_{l}^{L} a_q^2 e^{-\ln 2\frac{(z-z_l)^2}{r_q^2}} \cdot e^{-4\ln 2\frac{(E-E_q+\hbar\omega_X)^2}{\hbar^2\Delta\omega_X^2}}, \tag{3.6}$$

wherein the index q denotes the different atomic orbitals (Mg 2p, Mg 3s) with FWHM radius r_q of the charge density and photoemission cross section a_q^2 and l denotes the individual layers of Mg atoms inside the crystal. The XUV photon energy is denoted $\hbar\omega$ with FWHM $\hbar\Delta\omega = 5$ eV. The binding energy of the 2p state is fixed at 49.5 eV and the binding energy of the valence band is determined by averaging the synchrotron spectra (see figure 25) after background subtraction. The average escape depth is calculated by weighting the energy depth distribution with the exponential damping due to inelastic scattering, calculated as the IMFP λ either with the TPP2M-formula [117] or with the Full-Penn-Algorithm [194] from existing measurements of surface reflectivity [195] or electron inelastic scattering [196].

$$\bar{d_q} = \frac{\int_{E_{q,1}}^{E_{q,2}} dE \int dz\, I(z,E) \cdot \left(\theta(-z)e^{\frac{z}{\lambda}} + \theta(z)\right)}{\int_{E_{q,1}}^{E_{q,2}} dE \int dz\, I(z,E)}, \tag{3.7}$$

wherein $z = 0$ locates the image charge plane, at which the amplitude of the NIR streaking field decreases by half w.r.t to the field strength in vacuum. The integration limits are chosen to separate the core and valence emission. The predicted time delay variations for the photon energies of interest are depicted in figure 34 and compared to the experimental values. The simple ballistic model is essentially similar to the case of fully-resonant bulk photoemission as described by Borisov et al. [100]. From figure 34 b, it is obvious that the pronounced minimum of the relative photoemission time delay cannot be explained simply within the simple ballistic transport model, which was very successfully applied in the description of the core level photoemission time delay in case of the Mg/W hybrid systems [25]. Only through extensive measurements over a much increased spectral region and the evaluation of valence band photoemission time delays does the interplay of resonant and non-resonant photoemission beyond the simple transport models become apparent.

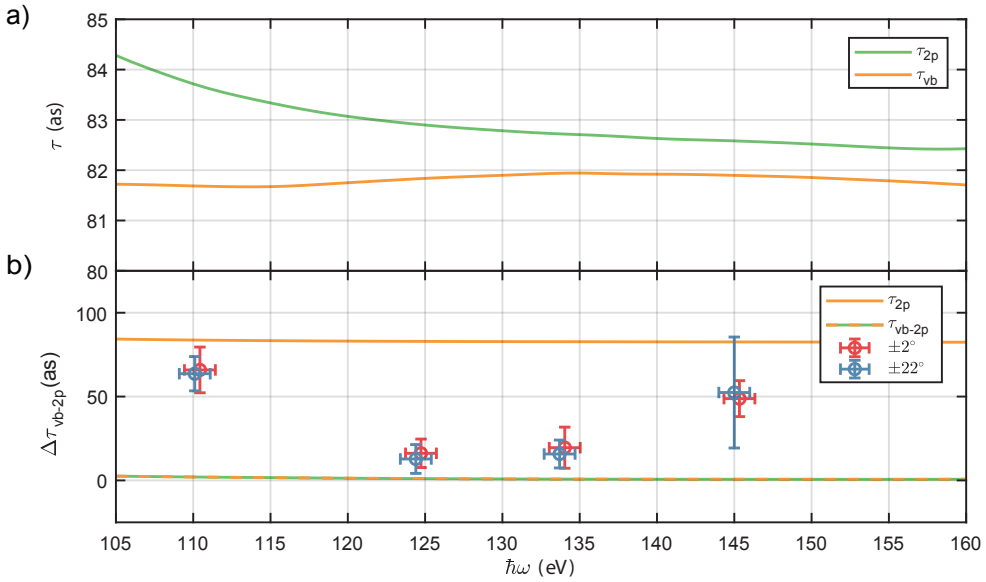

Figure 34 a) Photoemission time delays of Mg 2p (green) and delocalized valence band (orange) calculated with the simple ballistic transport model and free-electron like group velocity in the crystal. b) Comparison of experimental data (see Figure 32) with the simple ballistic transport model. The orange and orange-green lines represent the fully non-resonant ($\tau_{vb} = 0$) and fully resonant cases of Mg valence band photoemission, respectively.

3.4.3. Hamiltonian of 1D time-resolved photoemission

The time-dependent Schrödinger equation (TDSE) of the one-dimensional (1D) attosecond photoemission chronoscopy experiment can be written down in the single active electron approximation (SAE) as in reference [197]

$$i\frac{\partial}{\partial t}\Psi(z,t) = \left[-\frac{\hbar^2}{2m_e}\frac{\partial^2}{\partial z^2} + V(z) + V_h(z,t) - iV_i(z,E) + z\cdot E_L(r,t,\tau) + z\cdot E_X(t)\right]\cdot\Psi(z,t). \tag{3.8}$$

The terms $V(z)$, $V_h(z,t)$ and $V_i(z,E)$ describe the local effective potential of the photoelectron, the attractive potential of the screened core-hole, which according to the sudden approximation is switched on instantaneously after photoexcitation inside the solid, and the imaginary optical potential, which is implemented to model the electron wavepacket damping due to inelastic scattering inside the crystal for electron states above the vacuum level, respectively. The TDSE of these one-dimensional model systems can be solved numerically to high accuracy. Common approaches include time propagation of the Hamiltonian in the spectral basis [198, 99] or application of the rotating wave approximation in the pseudospectral basis [197, 178, 100]. The initial state, from which the electron is ejected is

$$\Psi_i(z,t) = \psi(z)\cdot e^{-i\omega t}, \tag{3.9}$$

for $t \to -\infty$. The initial state wavefunctions $\psi_i(z)$ are the solution of the unperturbed hamiltonian

$$\left[-\frac{\hbar^2}{2m_e}\frac{\partial^2}{\partial z^2} + V(z)\right]\psi_i(z) = E_i\psi_i(z). \tag{3.10}$$

The integration is performed for all initial states individually. However, the explicit time integration of the Hamiltonian for every delay step τ in attosecond chronoscopy experiments is computationally rather expensive and thus for comparative studies further simplifications are desirable.

3.4.4. Semi-classical model

One such simplification is the application of the 1D semi-classical 3-step photoemission model based on the strong-field approximation (SFA). The model was first introduced by Zhang et al. [175, 176, 199] and refined by Liao et al. [101, 177, 200]. In this work, it is expanded using higher order terms of the periodic potential inside the crystal, an idea which was first explored by Borisov et al. [100], who combined Chulkov potentials [184] with additional Gaussian terms modelling a repulsive potential experienced by the valence band electrons due to the Pauli principle with the core electrons. Furthermore, using initial and/or final states generated with modern state-of-the-art density-functional-theory (DFT) codes, we can extend the semiclassical formalism well beyond the limitations of simple one-electron model potentials.

Here, the initial state of photoemission is obtained by evaluation of the stationary Schrödinger equation of a one-dimensional model potential that is adjusted to replicate the band structure, bandgap and surface state energies of the real solid. The contribution of photoemission excited from initial state i into final state f, with energies E_i and E_f defined w.r.t to the vacuum energy, to the total photocurrent as function of the XUV-NIR pulse delay τ is calculated via the photoemission transition dipole matrix element $T_{i,f}$ in the velocity gauge

$$T_{i,f}(E_f,\tau) = -\frac{i}{\hbar}\int dt\, \frac{e}{m_e} A_X(t)\, \langle \Psi_f(\vec{r},t,\tau)|\, \hat{p}\, |\Psi_i(\vec{r},t)\rangle\,, \tag{3.11}$$

wherein $\Psi_i(\vec{r},t)$ and $\Psi_f(\vec{r},t)$ denote the initial and final state wavefunctions, respectively. The photoelectron spectrum $P(E_f,\tau)$ finally follows as

$$P(E_f,\tau) = \sum_i |T_{i,f}(E_f,\tau)|^2\,. \tag{3.12}$$

Neglecting the infrared streaking field and treating the weak XUV field in first order perturbation theory, the time-dependence of the initial and final states can be trivially derived via separation of variables in Schrödinger's equation

$$\Psi_{i,f}(\vec{r},t) = e^{-i\frac{E_{i,f}}{\hbar}t}\cdot\psi_{i,f}(z). \tag{3.13}$$

Strong-field approximation and Volkov states

In the presence of the streaking field the final states in the semi-classical model are replaced by their laser dressed counterparts, the so called Volkov states

$$\Psi_f(\vec{r}, t, \tau) = e^{-i\Phi_V(z_0,t_0;p)} \cdot \psi_f(z), \tag{3.14}$$

with the XUV-NIR pulse delay τ and the Volkov-phase $\Phi_V(z_0, t_0; p)$. Because of the space-time coupling induced by the streaking field, which is screened inside the metal, the integral in the Volkov phase calculation (see equation 2.36) cannot be solved easily, but must be integrated along the electron trajectory. The propagation of the electron is solved classically using a Velocity-Verlet algorithm [201, 202] for all possible initial starting positions of the electron inside the crystal z_0 and all possible initial starting times t_0

$$\begin{aligned} z(t) &= z(z_0, t_0; t) \\ p_z(t) &= p_z(z_0, t_0; t), \end{aligned} \tag{3.15}$$

wherein z and p_z denote the electron position and momentum, respectively. One iteration time step dt of the classical propagation is applied via the following equations

$$\begin{aligned} t_{n+1} &= t_n + dt, \\ z(t_{n+1}) &= z(t_n) + p_z(t_n) \cdot dt - \frac{1}{2} E_L(z(t_n), t_n) \cdot dt^2, \\ p_z(t_{n+1}) &= p_z(t_n) - \frac{1}{2} \left(E_L(z(t_{n+1}), t_{n+1}) + E_L(z(t_n), t_n) \right) \cdot dt. \end{aligned} \tag{3.16}$$

The Velocity-Verlet algorithm has three advantages: First, the momentum is recorded at every time-step, which is the quantity that enters the calculation of the Volkov-phase. Second, its second order accurate, i.e. the propagation error is $O(t^3)$. Third, the Velocity-Verlet method constitutes a symplectic integrator of Newton's equation of motion, i.e. the total energy of the electron is contained and oscillates in a small range around the true value. The complicated spatial dependence of the electric field at the metal-vacuum interface due to the response of the mobile conduction band electrons is found from 1D-TDDFT calculations (see figure 35) published already in [25] for tungsten and magnesium.

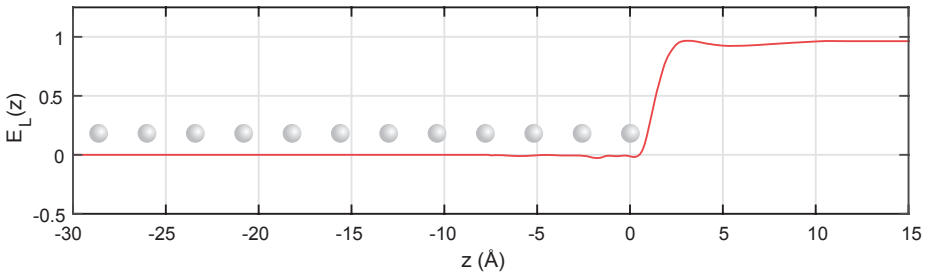

Figure 35 Electric field distribution $E_L(z)$ at the metal vacuum interface (red). Grey balls indicate the position of the magnesium atomic layers in the 1D slab.

The electrostatic crystal and surface potentials V are taken into account only for the case of non-plane-waves via a separate force term, which is calculated via conservation of energy after each step of the propagation

$$\begin{aligned} E_{kin}(t_{n+1}) &= \frac{p_z(t_{n+1})^2}{2m_e} \\ E_{kin}(t_{n+1}) &= E_{kin}(t_{n+1}) + (V(z(t_{n+1})) - V(z(t_n)) \\ p_z(t_{n+1}) &= \sqrt{2m_e E_{kin}(t_{n+1})}. \end{aligned} \tag{3.17}$$

This is formally equivalent to calculation of the conservative force $F(z) = -\frac{\partial}{\partial z}V(z)$ in the secant approximation, which is more convenient as the potential is known analytically anyways, and the introduction of errors via the differentiation, interpolation and subsequent integration of the electrostatic potential is avoided. Furthermore, the correct final kinetic energy at the end of the propagation even for long range attractive potentials, such as the Coulomb-like potential of the image charge, is ensured.

Finally, the Volkov-phase of the propagated electron is calculated by time integration of the resulting canonical momentum

$$\Phi_V(z_0, t_0; p_z) = -\frac{1}{2m_e\hbar}\int_{t0}^{\infty} dt'\, p_z(z_0, t'; t_n)^2, \tag{3.18}$$

and the photoemission matrix element as

$$\begin{aligned} T_{i,f}(E_f, \tau) = -\frac{i\sqrt{2\pi}e}{\hbar m_e}\int dt_0\, A_X(t_0 - \tau)\cdot e^{-iE_i t_0/\hbar} \\ \cdot \int dz_0\, e^{-i\Phi_V(z_0,t_0;p_z)}\psi_f^\dagger(z_0)\cdot\left(-i\hbar\frac{\partial}{\partial z}\right)\cdot\psi_i(z_0), \end{aligned} \tag{3.19}$$

wherein the integration runs over all possible start times and positions. This implementation has the advantage that the trajectory integration needs only to be performed once per final state f, because the different sets of initial states and the delay dependence is introduced via the XUV field in the matrix element calculations. For the calculation of high-resolution photoemission spectra, the classical trajectory integration is not necessary and the Volkov phase simplifies to the final state energy term $\Phi_V(z_0, t_0; p_z) = -E_f \cdot t$.

Chulkov model potentials of Mg(0001)

The spatial dependence of the initial state wave functions $\psi_{i,k}(z)$ are found by direct diagonalization of the stationary Hamiltonian in the absence of the laser field E_L and XUV field E_X

$$\left(-\frac{\hbar^2}{2m_e}\frac{\partial^2}{\partial z^2} + V(z)\right)\psi_i(z) = E_i\cdot\psi_i(z), \tag{3.20}$$

wherein the crystal and surface potential $V(z)$ are modelled with the so-called Chulkov potential. Chulkov potentials [184] are one-dimensional model potentials originally developed to describe and model surface and image-potential states [193] of simple metals. The latter describes electron states, whose wavefunctions are located outside the crystal, but are nevertheless bound by the attractive potential of the image charge formed by the remaining electrons screening the electric field of the outside electron on the metal surface. The original formulation of the Chulkov potential is only a good approximation of the effective local potential for electrons with energies close to the vacuum level. Hence, an extension of the Chulkov potential towards higher order components of the cosine series of the periodic crystal potential [100] is performed. This model potential is referred to as extended Chulkov potential V_C and can be written down as

$$V_C(z) = \begin{cases} A_{10} + \sum_{k=1}^{N} A_k \cdot cos\left(\frac{2\pi k}{a_s} \cdot z\right) & \text{, if } \; |z| \leq z_0 \\ A_{20} + \frac{1}{2}\sum_{k=2}^{N} A_k & \\ \quad + \left(A_{21} + \frac{1}{2}\sum_{k=2}^{N} A_k\right) \cdot cos(\beta\,(z - z_0)) & \text{, if } \; |z| \leq z_0 + z_1 \;\; \wedge \;\; |z| > z_0 \\ A_{30} \cdot e^{-\alpha(z - z_1)} & \text{, if } \; |z| \leq z_0 + z_{im} \wedge \;\; |z| > z_0 + z_1 \\ E_H \cdot \dfrac{e^{-\gamma(z - z_{im})} - 1}{z - z_{im}} & \text{, if } \; |z| > z_0 + z_{im}, \end{cases} \tag{3.21}$$

wherein z_0 denotes the position of the outermost atomic layer of the slab with crystal periodicity a_s and $E_H = 27.2$ eV denotes the Hartree unit of energy. Only $4 + N$ free parameters, $A_{10} = -10.55$ eV, $A_{21} = 1.26$ eV, $\beta = 8.94\,\text{Å}^{-1}$, $z_{im} = z_0 + 1.83\,\text{Å}$ and A_k, define the shape of the effective valence band potential of the Mg(0001) surface [193]. The other parameters are fixed by the conditions of the continuity of the logarithmic derivative of V_C via the following system of equations

$$\begin{aligned} z_1 &= z_0 + \frac{5\pi}{4\beta} \\ A_{20} &= A_{10} - A_{21} + A_1 \\ A_{30} &= A_{20} - \frac{A_{21}}{\sqrt{2}} \\ \alpha &= -\frac{\beta \cdot A_{21}}{\sqrt{2} \cdot A_{30}} \\ \lambda &= -4 \cdot A_{30} \cdot e^{-\alpha(z_{im} - z_1)}. \end{aligned} \tag{3.22}$$

The restriction of the Fourier series to cosine terms is motivated by the symmetry of the potential around each ionic core. Positive A_k indicate a repulsive core potential similar to [100].

The model potential of the core states is found by combination of the Chulkov potential ($A_k = 0 \; \forall \, i > 1$) and a periodic screened Coulomb potential at all the core positions, deemed

Chulkov-Yukawa potential

$$V_{core} = V_C + \frac{e^2}{4\pi\epsilon_0} \sum_{j=0}^{N_{layers}} \frac{e^{-(z-z_0-j\cdot a_s)/\zeta}}{\sqrt{(z-z_0-j\cdot a_s)^2 + a_y^2}}. \tag{3.23}$$

The free parameters $\zeta = 1.59$ Å and $a_y = 0.156$ Å of the potential are fitted by comparison with the bulk and surface binding energies of the Mg 2p level of 49.6 eV and 49.46 eV [189, 100], respectively. The Chulkov and Chulkov-Yukawa potentials for a 31 layer single crystal cut along the (0001) direction is depicted in figure 36 a,b along typical eigenfunctions and the integrated charge densities.

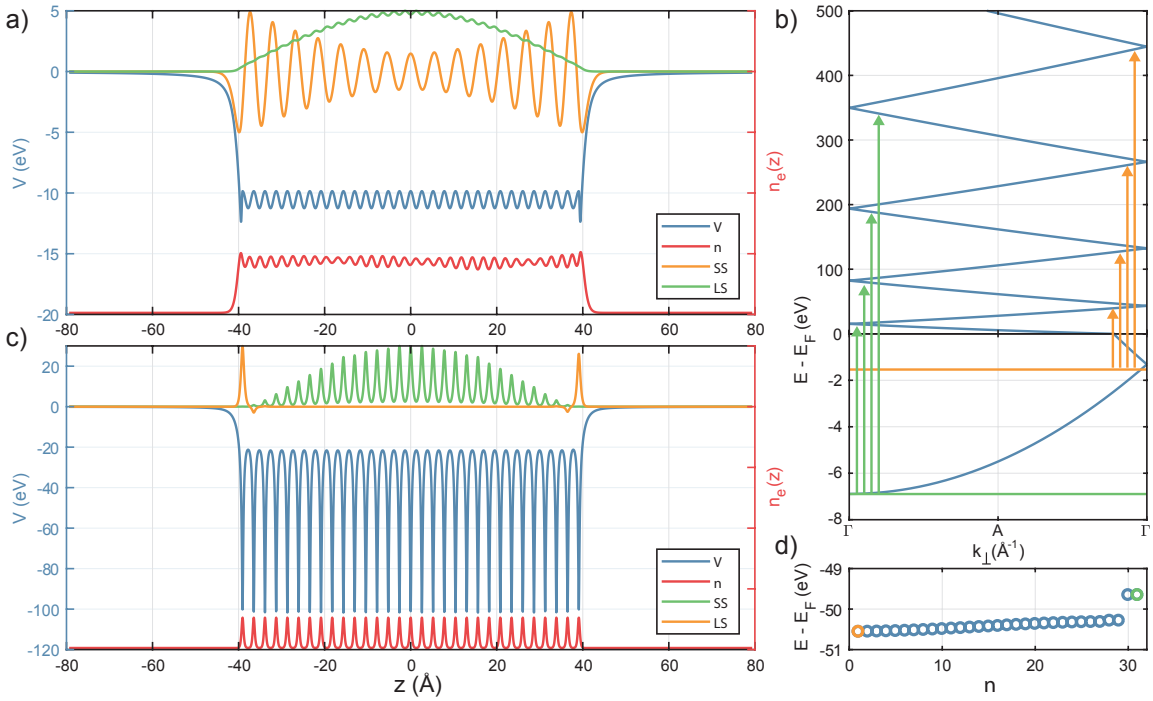

Figure 36 a) Chulkov potential (blue) and wavefunctions corresponding to the symmetrical surface state (orange) and the lowest energy valence band state (green) of the 31 layer magnesium slab utilized to model the (0001) surface of the single crystal. The integrated charge density $\rho = \sum_i |\psi_i(z)|^2$ (red) is indicative of a nearly free electron behaviour of the valence and conduction band electrons. b) Free electron band structure along the z-direction of the magnesium crystal (see figure 23) in the reduced zone scheme along the Γ-A direction. The energy axis is referenced w.r.t to the Fermi energy of the Mg(0001) surface. The horizontal green and red lines mark the energy of the valence band minimum and surface states, respectively. The arrows mark photon energies corresponding to resonant photoemission processes [100]. c) Same as a) for the Chulkov-Yukawa model potential utilized for the description of the 2p core level. d) Core level spectrum of the Mg slab.

Example calculations for $A_1 = 0.7$ eV and $A_i = 0.5$ eV and $A_{j\neq i} = 0$ for $i = 2..5$ are depicted in figure 37 alongside the experimental spectrogram. Immediately we can associate each higher order component of the Cosine series of the extended Chulkov potential with a single parabolic branch of resonant transitions in the Mg crystal. This model directly links the strength of the resonant transition band to the periodicity of the effective one-electron potential V_C, most strongly the $A_{2,3}$ components of the extended Chulkov potential.

Plane wave-like final states

The spatial dependence of the propagating final state is modelled by an electron wave of momentum $p_z(z)$, which is damped inside the crystal,

$$\psi_f(z) = \frac{1}{\sqrt{2\pi}} \cdot e^{ip_z(z)(z-z_0)} \cdot e^{-(z-z_1)/(2\lambda)}, \tag{3.24}$$

wherein λ denotes the inelastic mean-free path (IFMP) of the highly excited electron in the solid. The IMFP can be found from tabulated measured values, or calculated with algorithms such as the Full-Penn algorithm [194] using model dielectric functions [203, 204]. For the latter method, we can find material specific fits to simple analytical formulas in the literature [205, 116, 117]. The asymmetric damping of the final state wavefunction ensures unidirectional photoemission from the symmetric crystal slab.

In the work of Zhang and Liao [175, 176, 177], plane wave final states with momentum equal to the outgoing free electron were assumed $p_z(z) = \sqrt{2m_e E_f}$. While this is a reasonable approximation to gauge the dependence of attosecond streaking delays on the IMFP and the dielectric screening of the NIR streaking field, it fails to reproduce the correct energies of the resonant parabolic bands in the synchrotron photoemission spectrogram of magnesium. Taking into account the inner potential of the solid and the retardation of the electron upon traverse of the surface potential barrier, a more realistic plane wave momentum $p_z(z)$ is constructed. It is equal to the inner potential everywhere inside the solid and matched to the Coulomb tail of the surface potential

$$p_z(z) = \sqrt{2m_e(E_f - V_{inner})}, \tag{3.25}$$

with

$$V_{inner} = \begin{cases} A_{10} \cdot & \text{, if } \; z \leq z_x \\ V_C & \text{, if } \; z > z_x \end{cases} \tag{3.26}$$

and z_x the outermost root of the equation $V_C(z) = A_{10}$.

It is noted that the simulated resonance energies of the surface state are approximately 3 eV lower than observed experimentally, which can be explained terms of the self-energy shift of the final states, which is on the order of 4 eV in case of aluminium around 100 eV [188]. This self-energy shift is a many-body effect observed in ab-initio photoemission calculations using density-functional theory approaches. Although the eigenstates of Chulkov's potential are not true Kohn-Sham quasiparticles as in case of [188], similar behaviour with regard to the omission of the many-body interaction of the outgoing electron with the valence band hole can be expected. We attribute the narrow linewidth at high binding energies to the negligence of the decreasing lifetime of the valence band hole far away from the Fermi edge.

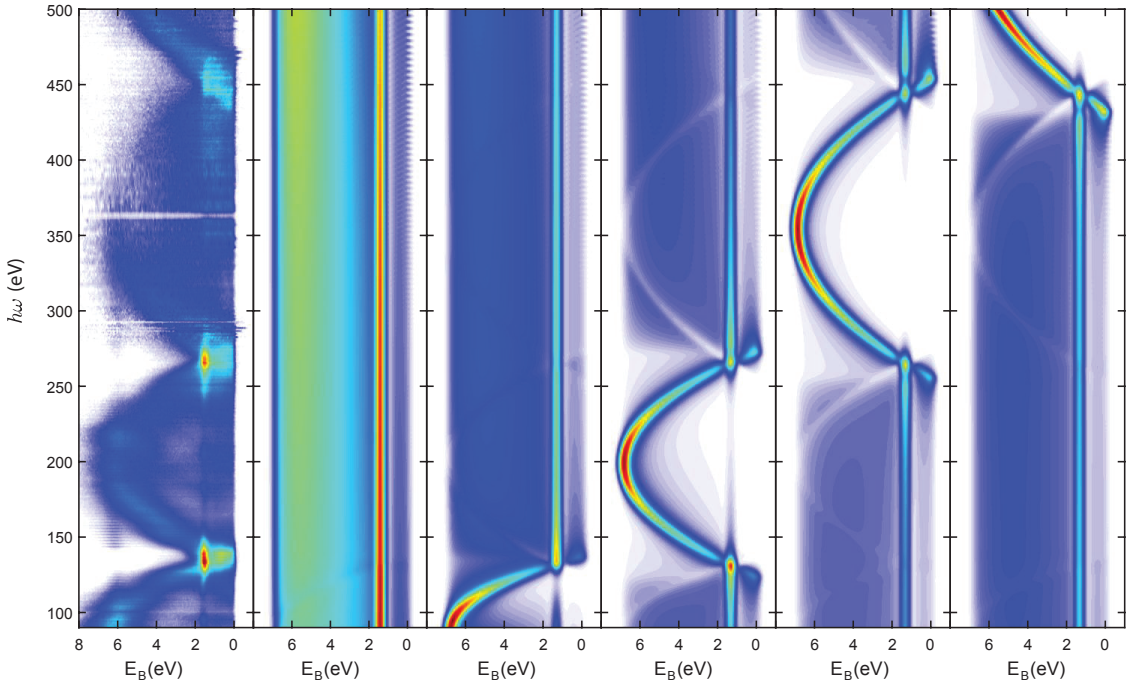

Figure 37 Comparison of experimental data (left) with calculated synchrotron photoemission spectrograms for different non-zero components of the extended Chulkov potential cosine-series. From left to right $A_{2..5} = 0$, $A_2 > 0$, $A_3 > 0$, $A_4 > 0$, $A_5 > 0$. A one-to-one correspondence between the resonant enhancement parabolas and the higher-order periodicity of the effective one-dimensional model potential is observed.

Using our semiclassical model, we have established the link between the higher-orders of the crystal periodicity of the effective one-electron potential and the parabolic bands of resonant photoemission. Borisov et al. used a repulsive Gaussian function to model the exchange-correlation interaction of the valence and core electrons of magnesium. We approximate this potential with the following quotients of the Cosine series $A_2 = 0.6$ eV, $A_3 = 0.4$ eV and $A_4 = 0.2$ eV. We calculate both the high-resolution photoemission spectrogram as well as the energy-dependent photoemission time-delays for five potentials gradually increasing the strength of $A_{2,3,4}$ and the results are depicted in figure 38.

Clearly, the connection between both the strength of the parabolic band and the relative time delay of the Mg 2p core level and the fast oscillations of the effective potential, which is alluded to by Borisov et al. [100], is observed within the semiclassical model, too. The shaded area in figure 38 c,d marks the deviation of the retrieved time delay obtained from the different delay extraction algorithms (DIFF, TDSE, PIE).

Z-projected inverse LEED states

Calculations of the inverse LEED state of the Mg(0001) surface in terms of the high-energy complex band structure of the magnesium single crystal have been performed by Krasovskii et al. [99]. The $\vec{G}_{||} = 0$ component of the $\vec{k}_{||} = 0$ inverse LEED wavefunction is a suitable final state wavefunction to be implemented in the semiclassical model. This ansatz was carried out to

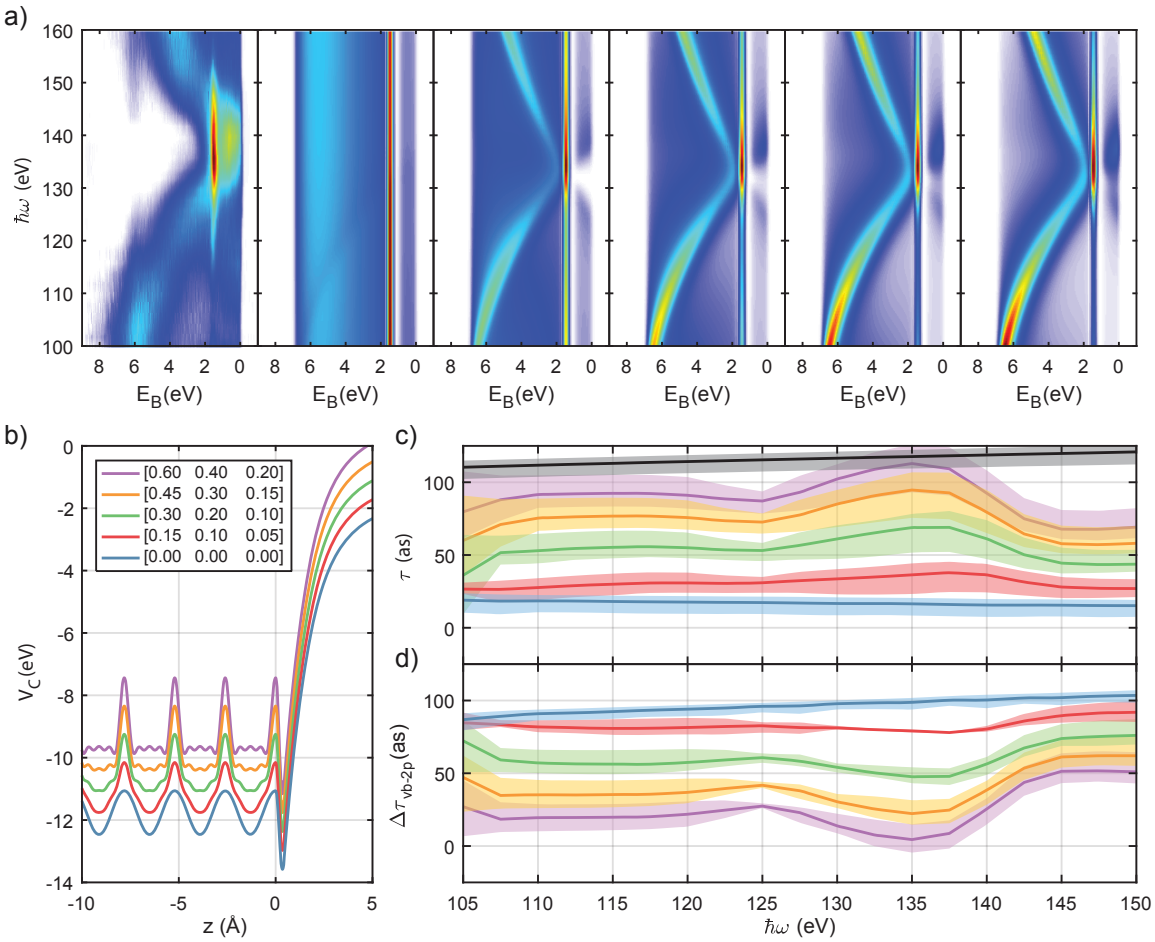

Figure 38 a) Comparison of experimental data (left) with calculated synchrotron photoemission spectrograms for increasing strength of $A_{2,3,4}$ according to the legend in panel b). b) Extended Chulkov potentials gradually increasing in strength of higher cosine terms. The three columns in the legend mark $A_{2,3,4}$ in units of eV, respectively. c) Absolute time delay of the Mg 2p core level τ_{2p} (black) and the combined valence and conduction bands τ_{vb} (colored) extracted from the semiclassical simulations. The shaded areas mark the range of delay values extracted with the different algorithms also utilized in the experiment. d) Relative time delays τ_{vb-2p}.

investigate to which extent the simple semiclassical model can be modified towards the inclusion of modern state-of-the-art photoemission theory. The inverse LEED wavefunction can be written in the so-called Laue representation [122]

$$\psi_f(z,\rho;\vec{k}_{\|},E) = \sum_{\vec{G}} u_{\vec{G}}(z)\cdot e^{i\cdot(\vec{k}_{\|}+\vec{G})\cdot\vec{\rho}}, \tag{3.27}$$

with $\vec{G}$ denoting the surface reciprocal lattice vectors and $\vec{\rho}$ the spatial coordinates in the surface plane. In the one-dimensional model $\vec{k}_{\|} = \vec{G} = 0$ is assumed by construction. This approximation is well justified in the case for some of the measurements on Mg(0001), which were recorded without the electrostatic lens of the TOF spectrometer and thus the angle between detected electrons and the (0001) surface normal is limited to $\pm 2°$. The obtained wavefunctions were calculated assuming an optical potential of 0.45 eV, which is unrealistically weak. The proper optical potential can be obtained, assuming free-electron like propagation, from the IMFP

of the solid

$$V_i = \frac{\Gamma}{2} = \frac{\lambda}{2v_g}, \tag{3.28}$$

where Γ denotes the final-state lifetime [28]. The inverse LEED wavefunctions were calculated assuming only small imaginary potentials. Because the increased contributions from deep inside the bulk material would falsify the extracted photoemission time delay, we adjust wavefunctions empirically using the inelastic mean free path extracted from [205]

$$\psi_f(z; E_f) = \Psi_f(z, 0; 0, E_f) \cdot e^{-(z-z_1)/(2\lambda)}. \tag{3.29}$$

Streaking spectrograms are calculated according to equation 3.19 and depicted in figure 39 for XUV excitation with Fourier-limited attosecond pulses of FWHM duration 480 as and central photon energies between 90 eV and 150 eV in steps of 2.5 eV. The time-dependent spectra are convoluted with a 4.5 eV Gaussian prior to evaluation to account for the significant lifetime broadening of the final states at realistic values of the optical potential.

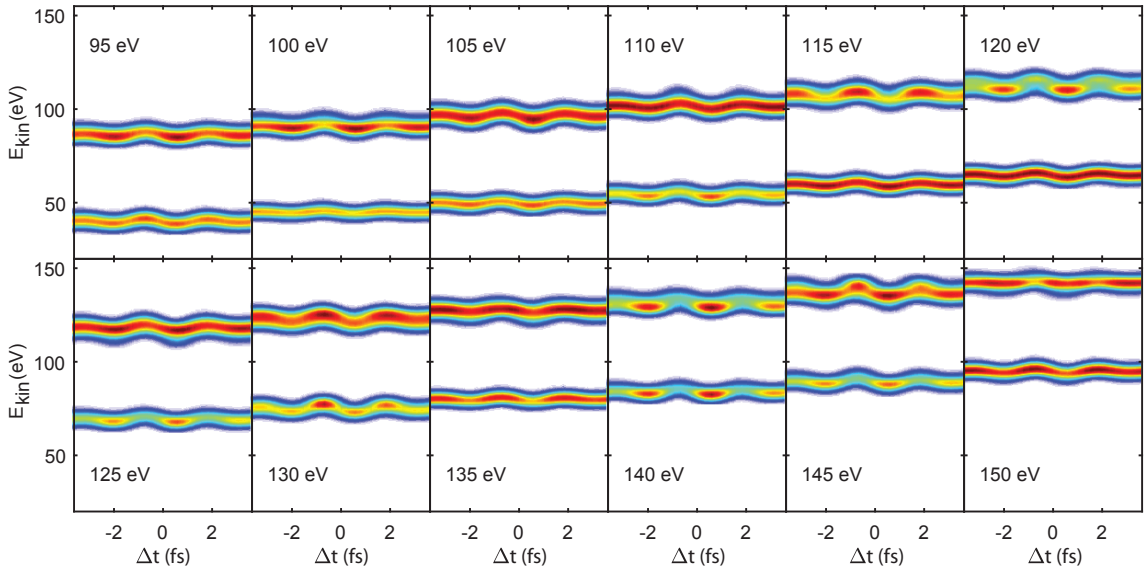

Figure 39 Photoemission streaking spectrograms calculated with the semi-classical model 3.19 using the $\vec{G}_{\parallel} = 0$ component of the $\vec{k}_{\parallel} = 0$ inverse LEED wavefunction [99] of the Mg(0001) surface at photon energies between 95 eV and 150 eV

.

The modulations of the delay-dependent photocurrent, which is most pronounced at photon energies 100 eV and 140 eV, are reminiscent of the Volkov approximation, i.e. the delay-dependent modulation of the final-state energies E_f, which leads to different final states fulfilling energy conversation at different XUV-NIR delay. Although some modulation is also observed in the experimental data, quantitative analysis requires precise knowledge of the time-energy structure of the electron energy-loss function, which goes beyond the scope of this study. The simulated attosecond streaking spectrograms are evaluated with the same delay retrieval algorithms implemented for the experimental data (see section E) and the result is depicted in figure 40 alongside the simulated and measured synchrotron spectrum. The shaded region

represents the minimum and maximum values obtained from the different delay retrieval methods, which does not surpass a range of ± 10 as.

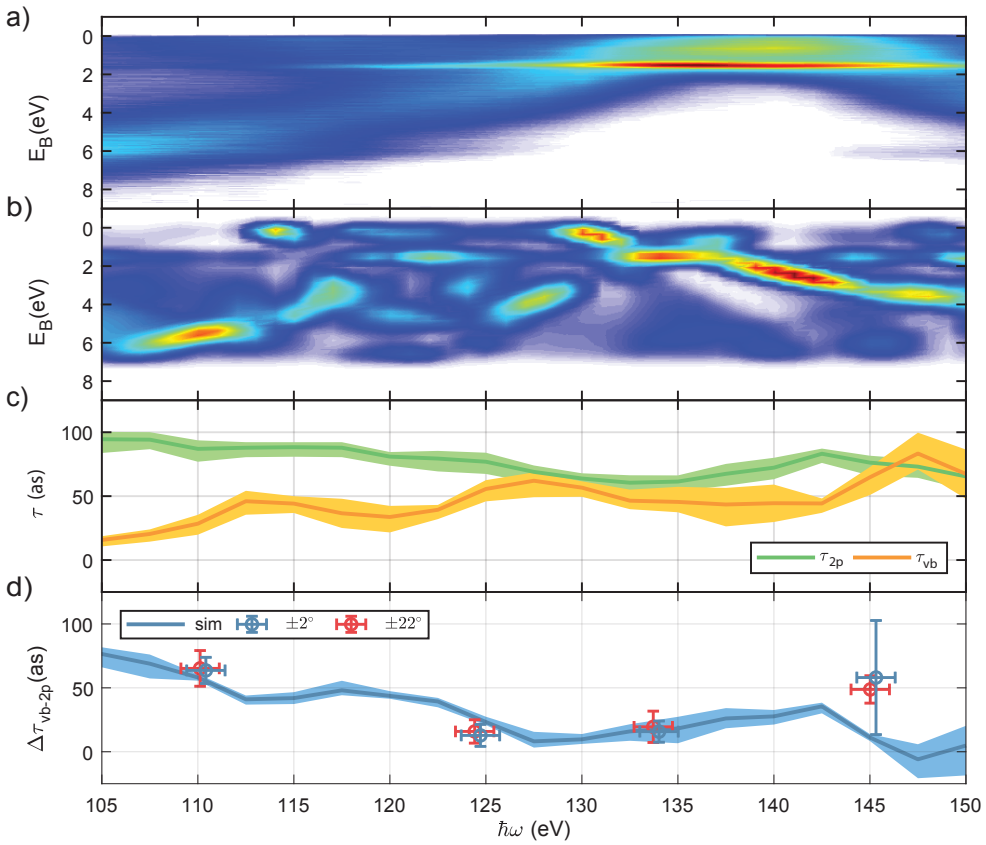

Figure 40 a) Experimental synchrotron photoemission spectrogram. b) Corresponding synchrotron spectrogram calculated with the semi-classical model (see equation 3.11) using the $\vec{G}_{\parallel} = 0$ component of the $\vec{k}^{\parallel} = 0$ inverse LEED wavefunction. c) Absolute time delays τ for Mg 2p (green) and valence band (blue), extracted from simulated attosecond streaking spectrograms (see figure 39. d) Same as c), but for relative time delay (orange). Shaded error marks deviations obtained from different delay extraction algorithms (see appendix E). Experimental data plotted for comparison (see figure 32).

The minimum of the experimentally determined τ_{vb-2p} is also observed in the simulations with about 10 as of additional retardation of the 2p core level observed in the experiment. The position of the minimum of the relative time delay coincides well with the prediction from the numerical calculation. This semiclassical calculation was carried out using the original Chulkov potential.

3.4.5. Quantum-mechanical model

A computationally efficient direct integration of the 1D TDSE (see Eq. 3.8) can be performed through application of the rotating-wave approximation (RWA) on the propagating electron wavepacket [100, 32]. The total wavefunction is written as

$$\Psi(z,t) = e^{-i\frac{E_i}{\hbar}t}\psi_i(z) + e^{-i\frac{E_f}{\hbar}t}\psi_f(z,t). \tag{3.30}$$

The calculation is furthermore strongly simplified by the approximation that the weak XUV field only interacts with the initial state, the depletion of which is neglected, and the NIR pulse only modulates the energy of the propagating electron wavepacket. The complicated energy-dependent treatment of the absorbing optical potential as well as the time dependence of the hole potential can be dropped by applying the RWA and restricting the equation of motion to the propagating electron wavepacket in the final state. The equation of motion of the electron wavepacket follows as

$$i\hbar\frac{\partial}{\partial t}\psi_f(z,t) = -\frac{\hbar^2}{2m_e}\frac{\partial^2}{\partial z^2}\psi_f(z,t) + \left(V_C(z) + V_h(z) - iV_i(z) + U_L(z)\cdot E_L(t,\tau) - E_f\right)\psi_f(z,t) + i\frac{\hbar e}{2m_e}\sum_n A_X(t)\frac{\partial}{\partial z}\psi_{i,n}(z), \tag{3.31}$$

wherein $V_C(z)$, $V_h(z)$ and $V_i(z)$ denote the Chulkov potential (see equation 3.21), the Yukawa potential of the core hole (see equation 3.23) and the optical potential, respectively. For the calculation of valence band photoemission, no localized hole potential is assumed. The initial states are calculated from the Chulkov potential of a 31 layer magnesium slab (see figure 36). The initial states of 2p core photoemission are calculated from a model potential $V(z) = V_C(z) + V_h(z + k\cdot a)$ for each layer k individually. In both cases the integration is performed for each individual initial state and the spectrogram is calculated by incoherent addition of the individual initial state spectra. The computational details of the simulations can be found in [100]. We note that while the XUV excitation is treated in the velocity gauge, the NIR streaking is treated in the Coulomb length gauge to facilitate the numerical effort of including the inhomogeneous NIR field distribution in the calculations.

Calculations of the energy-dependent relative photoemission time delays of the Mg(0001) surface with the quantum-mechanical model have been conducted using an modified Chulkov model potential.

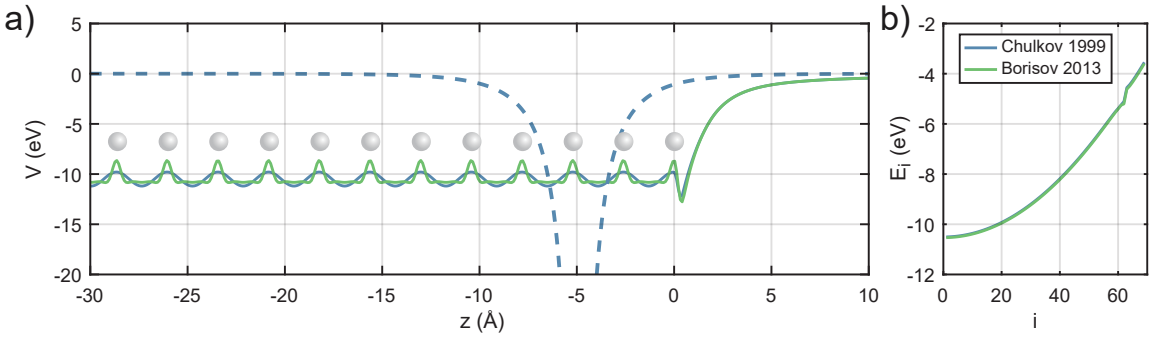

Figure 41 a) Extended Chulkov potential (green) investigated with the quantum mechanical model and its comparison to the original Chulkov potential (blue). The blue dashed line respresents the hole potential of core level photoemission from the third layer. Grey balls indicate the position of the magnesium atomic layers in the 1D slab.b) Initial state energies of occupied orbitals relative to the vacuum energy level for both potentials are all but indistinguishable.

The initial states of both potentials are all but indistinguishable with constant energy photoemission spectroscopy. The numerical results of high-resolution photoemission and time-dependent

photoemission along the surface normal are depicted in figure 42.

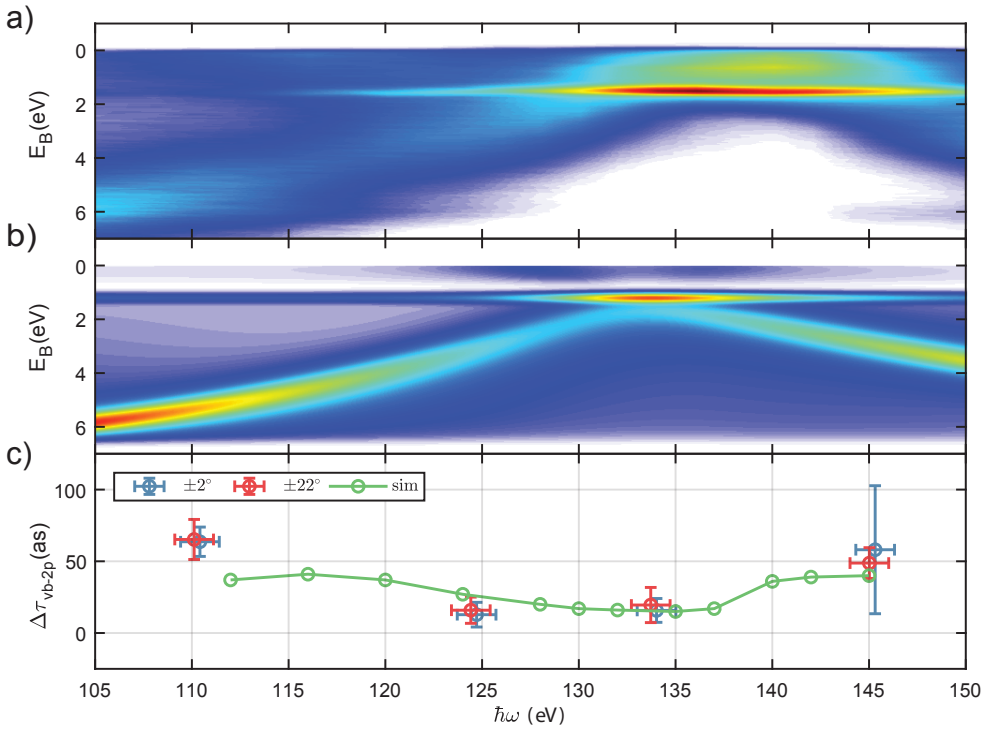

Figure 42 a) Measured synchrotron streaking spectrogram. b) Corresponding synchrotron spectrogram calculated with the quantum-mechanical model using the extended Chulkov model potential. c) Time delays extracted from simulated attosecond streaking spectrograms (green). Experimental data plotted for comparison (see figure 32).

Qualitative agreement between numerical and experimental data is noted in both cases. The pronounced minimum indeed is related to the interplay of non-resonant surface and resonant bulk-like photoemission and observed in both the quantum mechanical model and the semiclassical models. The comparison of results from the semiclassical model to this direct integration of the 1D-TDSE, which is much more profoundly motivated from fundamental principles of quantum mechanics, allows to investigate the range of applicability of the Volkov laser-dressing of the final-state of photoemission, which resides at the very base of the semiclassical formulation of photoemission chronoscopy as discussed in section 3.4.4.

3.5. Conclusion

The results are interpreted in the context of surface and bulk photoemission due to the mechanism of resonant and non-resonant photoexcitation of the initial states in the photoemission process. They can ultimately be traced back to the electronic band structure and the underlying crystal potential, and suggest photoelectrons from Mg(0001) to emerge faster than expected from the free electron-like ballistic propagation. Our results show that for high-photon energies, the valence band photoemission from the sp-band of the simple free-electron like metal magnesium can proceed faster than expected from the free electron model, which is linked to non-resonant

photoexcitation at the surface of the metal. Nonresonant excitation leads to a broadband photoemission continuum in the band and thus is best resolved using the attosecond streaking technique. Our energy-dependent study thus guides the way to the investigation and evaluation of the interplay between the electronic structure and the complex band structure on the observed time delay of the photoelectric effect.

Part IV

Broadband measurements of absolute photoemission time delays

Broadband measurements of absolute photoemission time delays

4.1. Introduction and statement of contributions

In this chapter energy-dependent attosecond streaking and high-resolution photoemission spectroscopies are demonstrated on the clean and adsorbate covered W(110) and W(100) surfaces. As subject of investigation of the seminal first paper on attosecond photoemission time delays [12], the W(110) surface holds special weight in the discussion of the physics of time-resolved photoemission, because most theoretical assessments of the attosecond photoemission problem were performed on this system [96, 97] or derived model systems [175, 176, 176, 178, 98, 99]. The restriction of the attosecond chronoscopy towards the measurement of relative photoemission time delays further complicates the comparison of the results of theoretical models and numerical calculations with the experiments. Further data points for comparison between theory and experiment can only be generated either by adding different atoms to the tungsten surface with additional shallow core levels, which can be photoionized with contemporary attosecond pulses [32] or by systematic variation of the photon energy, which is routinely performed in RABITT experiments [28, 29, 33], but has not been shown on streaking experiments beyond the gas phase [206]. Here we show, how a combination of all aforementioned approaches, i.e. systematic investigation of clean and adsorbate covered tungsten surfaces as well as variation of the photon energy, allows us to determine absolute time delays over an extensive spectral bandwidth from 90 eV up to 145 eV. Furthermore, a simple semi-classical model is constructed with inputs from advanced density-functional-theory codes, which facilitates the dissection of the different contributions to the attosecond time delay in tungsten.

We perform systematic variation of the sub-monolayer coverages of atomic iodine on the W(110) surface and demonstrate the possibility of using surface adsorbates as time-zero indicator for the determination of absolute photoemission times, i.e. the time between the arrival of the photon at the surface and the subsequent release of the photoelectron from the surface. This time marks the fundamental speed limit for light-induced charge-separation and -transfer across material surfaces and interfaces. The study of iodine adsorbate adlayers at coverages far smaller than one monolayer relies heavily on the high photoelectric cross section at the so-called giant dipole resonance, which limits the applicability of the iodine chronoscopy technique to a small energy window around photon energies of 100 eV. Using saturated monolayers of oxygen on W(110), atomistic calculations of photoemission time delays, theoretical modelling and high-resolution photoemission data, we can show the transferability of the absolute photoemission timing

experiment to a wider range of photon energies up to 145 eV. Furthermore, determination of the absolute photoemission time delay we study for the first time the importance of the high-energy complex band structure on localized and delocalized photoemission timing systematically. Lastly, we combine our semiclassical model of time-resolved photoemission with numerical and empirical corrections induced by the intra-atomic interaction [32] and the inelastic scattering [97, 207] to quantitatively dissect all microscopic mechanisms and their respective contributions to the unambiguously measured absolute time delays.

The tungsten project in the Attosecond Dynamics research group of Prof. Reinhard Kienberger at the Max Plank Institute for Quantum optics was a long running project with many people involved, who contributed to measurements at different photon energies and the overall extent of the presented data set, including more than 1300 individual streaking spectrograms. The streaking measurements at 92 eV were performed by Dr. Stefan Neppl, Dr. Andreas Kim, Dr. Florian Blobner and Konrad Hütten. The measurements at 105 eV were performed by Dr. Stefan Neppl and Michael Gerl. The measurements at 112 eV were performed by Dr. Michael Jobst, Marcus Ossiander, Matrin Schäffer, Ayman Akil and Sebastian Jarosch. The measurements at 118 eV were performed by Dr. Stefan Neppl, Dr. Ralph Ernstdorfer, Dr. Adrian Cavalieri, Dr. Wolfram Helml and Dr. Elisabeth Bothschafter. Additional measurements were performed by the author and Dionysios Potamianos with a new XUV multilayer mirror, including the whole dataset of W(100). The measurements at 124 eV were performed by the author and Dionysios Potamianos. The measurements at 135 eV were performed by the author, Maximilian Schnitzenbaumer, Martin Schäffer and Dionysios Potamianos. The measurements at 145 eV were performed by the author, Michael Jobst, Marcus Ossiander, Martin Schäffer and Ayman Akil. Special acknowledgement is given to Prof. Thomas Uphues, Dr. Ralph Ernstdorfer, Dr. Elisabeth Magerl, Michael Stanislawski, Dr. Stefan Neppl and Prof. Peter Feulner, who designed the AS-3 beamline and UHV systems. Data evaluation, classical and semi-classical calculations were performed by the author in part using projected inverse LEED states provided by Prof. Eugene Krasovskii from the Universidad del Pais Vasco/Eusakal Herriko Unibertsitaetea in San Sebastian. Furthermore, high-resolution photoemission experiments were performed at the SuperESCA beamline at the Elettra synchrotron in Trieste in collaboration with Dr. Silvano Lizzit, Dr. Daniel Lizzit and Dr. Luca Bignardi from Elettra Sincrotrone Trieste. The iodine sub-monolayer experiment was performed in collaboration with Marcus Ossiander, Dr. Stefan Neppl, Michel Gerl, Martin Schäffer and Michael Mittermair. All chronoscopy results presented here were evaluated by the author using the Gaussian fitting algorithm implemented by Marcus Ossiander and the PIE algorithm implemented by the author.

4.2. The W(110) and W(100) surfaces, properties and preparation

Tungsten served as the poster-child of attosecond photoemission timing spectroscopy ever since its prominent investigation in the seminal paper of A. Cavalieri et al. [12]. The original reason of choosing tungsten for the proof-of-principle experiment was twofold. First, the extraordinary heat resistance and hardness of tungsten simplifies the preparation process significantly over most other metal surfaces. Second, its electronic structure is especially favourable for investigation with the attosecond streaking technique, because the strong photoemission of the 4f core level with binding energies around 32 eV is easily distinguishable from the valence band photoemission and thus provides the essential reference for photoemission chronoscopy.

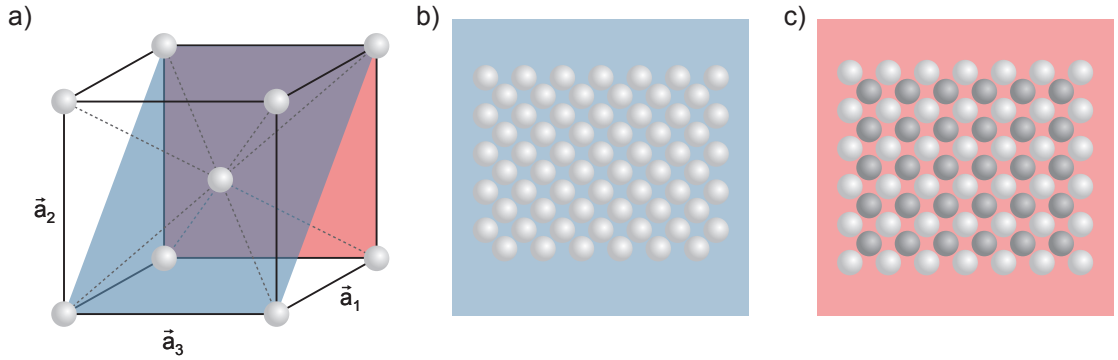

Figure 43 a) Real space tungsten crystal structure. Grey balls represent individual tungsten atoms. $\vec{a}_{1,2,3}$ are the lattice vectors spanning the unit cell of the bcc grid. The blue and red transparent planes indicate the (110) and (100) planes respectively. b) (110) Surface crystalline structure of elongated hexagons. c) (100) Square surface structure. Darker grey balls indicate the positions of the atoms in the second atomic layer.

Tungsten is a paramagnetic 5d transition metal with atomic number 74 and one of the hardest and densest pure metals and it has the highest melting point (3700 K) among all elemental solids. The tungsten single crystal has body-centered-cubic (bcc) structure, wherein each tungsten atom has 8 nearest neighbours (see figure 43 a). The two different surface geometries investigated within this thesis are the (110) plane, coloured in blue in figure 43, which is also the most closely packed surface plane, and the (100) plane (see figure 43 b,c). The (110) surface has elongated hexagonal structure, which is also visible in the hexagonal LEED pattern depicted in figure 44 a) revealing the hexagonal reciprocal lattice. The (110) surface represents also the most closely packed and thermodynamically stable surface structure of tungsten (see figure 43 b). The (100) surface on the other hand has square geometry with atoms of consecutive layers located in the eightfold coordinated central void between each square of atoms in both neighbouring layers (see figure 43 c). The electronic structure of tungsten single crystals is much more complicated compared to the case of the magnesium experiments discussed in chapter III. The density of states (DOS) of the occupied tungsten valence band is dominated by the partly filled and semi-localized tungsten 5d states with binding energies of $2-4$ eV

[208, 209]. The angle-resolved ultraviolet photoemission from tungsten surfaces was studied in depth by Christensen and Feuerbacher [208, 209].

As mentioned twice, the exceptionally high melting point of the tungsten crystal facilitates the preparation and maintainability of the pristine single crystalline surface in UHV conditions. The single crystal is cut by spark erosion and mechanically and electrochemically polished by MaTeck GmbH. The orientation of the crystallographic axes w.r.t. to the surface plane is specified to be better than $0.5°$. After transfer into vacuum the crystal is outgassed at approximately 1200 K for 5 minutes and subsequently flash annealed twice for 10 seconds to 2400 K using electron bombardment from a tungsten filament. At least every second day of experiments, the crystal is sputtered with Ar^+ ions at 1.2 keV for one hour to remove contaminants and polish the surface. Afterwards the single crystal is flash annealed to 2400 K in order to smooth out the nanometer level roughness induced by the sputtering. The filament is switched of and during the cooling of the crystal the chamber is flooded with oxygen at pressure $3 \cdot 10^{-6}$ mbar for 15 seconds. The oxygen reacts with carbon contaminants on the surface. The valve is closed and 25 seconds later a background pressure of $< 10^{-8}$ mbar is reached. Subsequently, the sample is flash annealed to 2400 K again to remove the carbon oxides along with the thin tungsten oxide layer from the crystal surface. This cycle is repeated for 10-15 times at the beginning of every day of measurements. This method efficiently removes carbon impurities from the tungsten surface [210, 211]. After the last oxidation step, a layer of oxide is retained passivizing the surface against further contamination. Just before the experiment and at least every 90 minutes during the experiments, the sample is flash annealed again to recover the clean surface.

The surface cleanliness is controlled with XPS, and the results are depicted in figure 44 along with the LEED patterns associated with the W(110) and W(110) surfaces. The W(110) surface is the dense surface of the bcc-type lattice of the tungsten crystal and thus is not subject to surface reconstruction and the perpendicular lattice relaxation is minuscule [212]. Indeed the topmost atomic distance is contracted by only 3% w.r.t. the bulk interlayer distance of 2.25 Å [213]. The LEED pattern of the W(110) surface is a compressed hexagon indicative of the elongated hexagonal surface unit cell of the (110) projection of the bcc-type lattice (see figures 43 and 44 b). The LEED pattern of the W(100) surface is square, as is the shape of the surface unit cell (see figures 43 and 44 c).

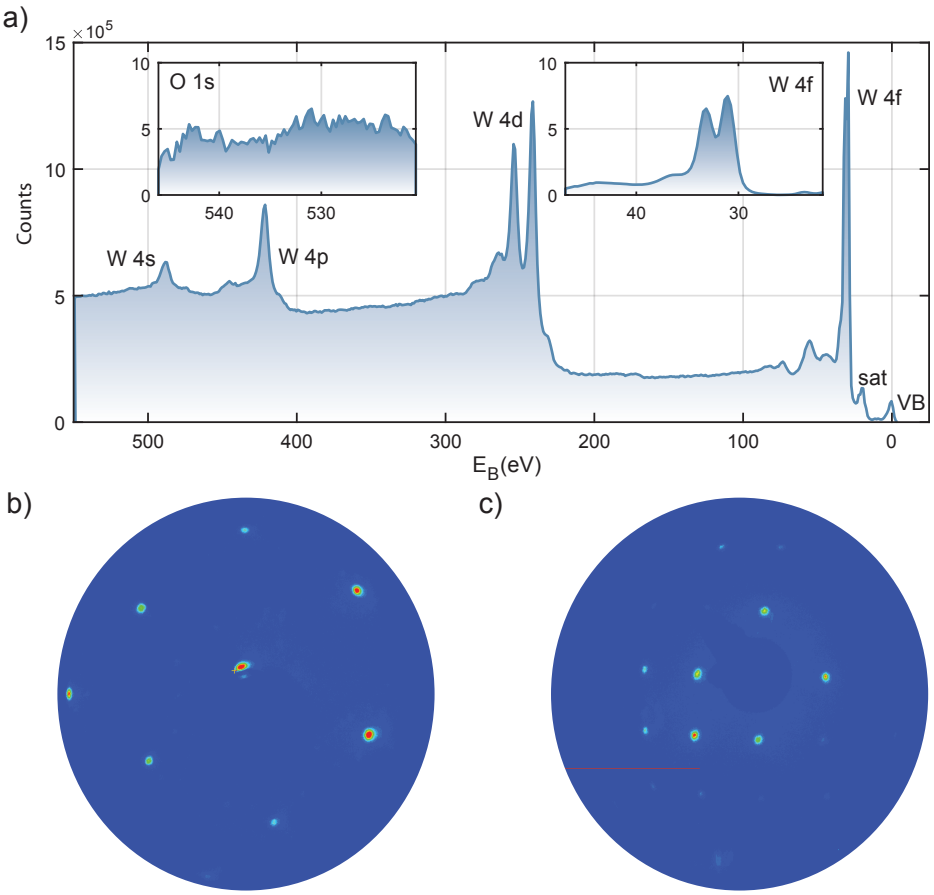

Figure 44 XPS of the W(110) surface with aluminium K_α radiation. Left inset: Zoom into the oxygen 1s spectral region showing no oxygen contamination. Right inset: Zoom into the W 4f spectral region showing the $7/2 - 5/2$ spin-orbit doublet. Insets are measured with increased spectral resolution. b) LEED pattern of W(110) surface measured directly after preparation with electron kinetic energy 130 eV. c) LEED pattern of W(100) surface measured directly after preparation with electron kinetic energy 174 eV. The square LEED pattern is associated with simple cubic geometry of topmost layer of tungsten .

4.3. Time-resolved photoemission from clean tungsten surfaces

In the following section, attosecond chronoscopy and high-resolution photoemission experiments on the W(110) and the W(100) surfaces are presented and described in detail. The motivation behind repeating the whole experimental series with two distinct crystallographic orientations of tungsten is the separation of contributions to the photoemission time delay related to the high-energy band structure and symmetry from intra-atomic scattering and ballistic transport.

4.3.1. W(110)

Despite W(110) being probably the most studied sample in all of condensed matter attosecond chronoscopy, the origin of the large attosecond time delay at 90 eV [12, 214], and its strong variation with photon energy [35], is not yet well understood. Hence, an extended experimental

campaign was conducted, aimed at extending the spectral range and resolution of the attosecond chronoscopy on the W(110) surface, complementing existing measurements at 91.5 eV, 103.1 eV, 110.1 eV and 117.5 eV with further measurements at 124.4 eV, 133.7 eV and 145.0 eV. Additional measurements at 103.1 eV and 117.1 eV were recorded to ensure consistency of the experimental conditions across almost a decade and different operators. The central energy of the AS-3 beamline is set by exchanging the XUV multilayer mirror and the thin metal filter. For photon energies up to 115 eV, a 200 nm zirconium filter is applied to the center of the nitrocellulose pellice. Above 115 eV, 150 nm palladium filters are employed to block low order HHG, which could overlap with the shallow core levels in the kinetic energy spectra and induce systematic errors in the experiments. Static photoemission with attosecond XUV pulses is recorded as a reference and the corresponding spectra are plotted in figure 46. All spectra are recorded without the electrostatic lens in order to avoid saturation of the detection electronics, while limiting the cone-angle of detection to $\pm 2^\circ$. In order to facilitate a quantitative interpretation of the observed attosecond time delays, complementary measurements of the photoemission spectra from W(110) using narrowband synchrotron radiation were performed at the SuperESCA beamline [215] of the Elettra synchrotron in Trieste. Photoelectrons were detected using a hemispherical analyser and the sample was aligned parallel to the plane of the analyser entrance aperture. The XUV radiation impinged on the sample with p-polarization and 70° angle of incidence, almost similar to the geometry in the attosecond experiments. A small setting of the analyser entrance slit was chosen to optimize the kinetic energy resolution of the analyser. The solid angle of detection of the experiment was a narrow strip of size $\pm 0.5^\circ \times 8^\circ$ and the photoemission data is integrated across all angles by the detection electronics. Although this angular acceptance region is significantly smaller than in case of the attosecond experiment using the electrostatic lens, both photoemission experiments are treated as angle-integrated measurement, because the diameter of the first W(110) surface Brillouin zone corresponds only to angles between $\pm 8^\circ$ and $\pm 11^\circ$ for electron kinetic energies between 90 eV and 150 eV.

The photon flux was calibrated from the photocurrent measured on the elliptical refocussing mirror behind the exit slit of the plane wave monochromator, taking into account the energy-dependent quantum yield and reflectivity and transmission of the gold coating [216] at 2° grazing incidence. The energy and flux calibration of the synchrotron experiments is outlined in appendix C. The high-resolution photoemission spectra are convoluted with a 4.5 eV Gaussian function and compared to the results recorded with broadband isolated attosecond pulses (see figure 45).

Despite the mismatch of the angular acceptance profiles of the two experiments, we find good agreement between the two photoemission experiments. In general, the high-resolution photoemission experiment slightly underestimates the relative strength of the background. This is likely related to a small amount of below-cut-off harmonics being transmitted through the attosecond beamline, especially at photon energies 110.1 eV and 133.7 eV, where the filter

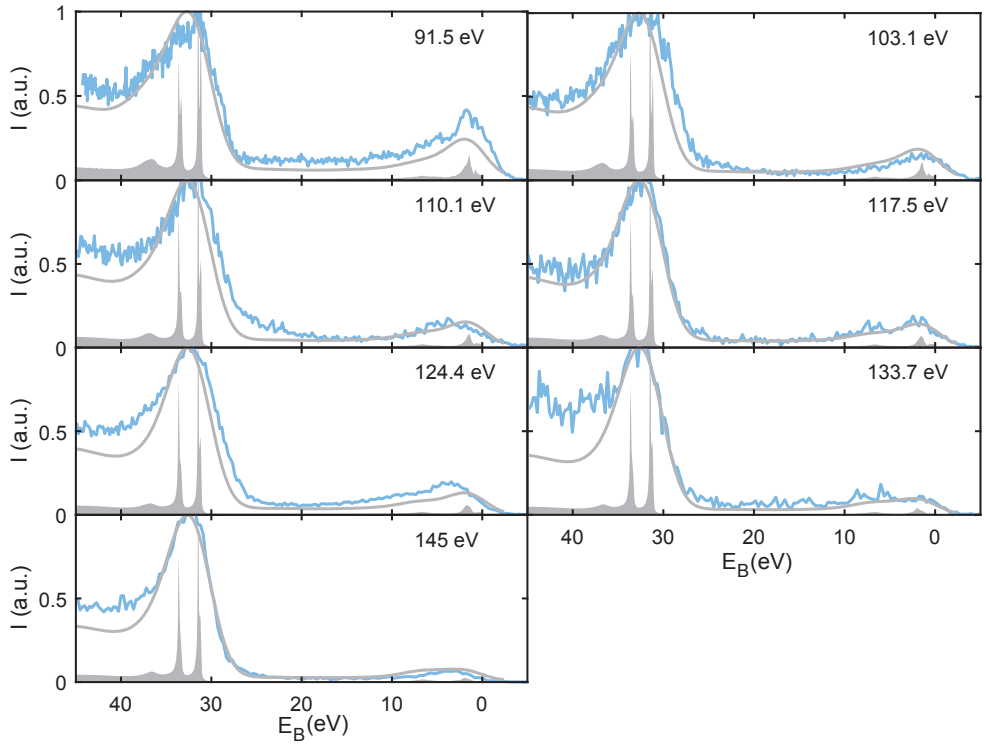

Figure 45 Comparison of static photoemission spectra of W(110) for seven central energies ranging from 91.5 eV to 145 eV recorded with high-resolution photoemission at the Elettra synchrotron (grey area) and with HHG attosecond pulses in the lab (blue). The solid grey line represents a convolution of the high-resolution spectrum with a 4.5 eV Gaussian function, representative of the reflection bandwidth of the XUV multilayer mirror.

transmissions of zirconium and palladium are constant or decreasing with increasing photon energy, contributing to the spectral region identified as inelastic background. The inelastic background is subtracted using the splitted Shirley method and the static TDSE model fit, essentially an incoherent sum of individual Gaussian wavepackets, is plotted in figure 46. These model initial states (orange bars in figure 46) are extracted from [35] to fit the high-resolution photoemission spectrogram at 118 eV and are applied without adjustment as the spectral shape of the valence band photoemission after the convolution with the attosecond pulse bandwidth varies much less dramatically with photon energy compared to the case of magnesium.

The photoelectron spectra are dominated by the strong photoemission from the tungsten 4f core level. The photoemission from the 5d, 6s and 6p orbitals that constitute the delocalized valence band states are not spectrally resolved with isolated attosecond pulses. The relative photoionization cross section σ_{vb}/σ_{4f} is strongly decreasing for increasing photon energies in accordance with the predictions from atomic photoionization calculations using the dipole approximation for the tungsten atomic orbitals [217]. A detailed comparison between different tungsten derived surfaces and their comparison with the high-resolution data, direct and after convolution with a 4.5 eV FWHM Gaussian function, is depicted in figure 63. The photoionization cross sections are directly linked to the so-called inelastic scattering contribution to the attosecond time delay investigated by Lemell et al. [97], which is discussed in more

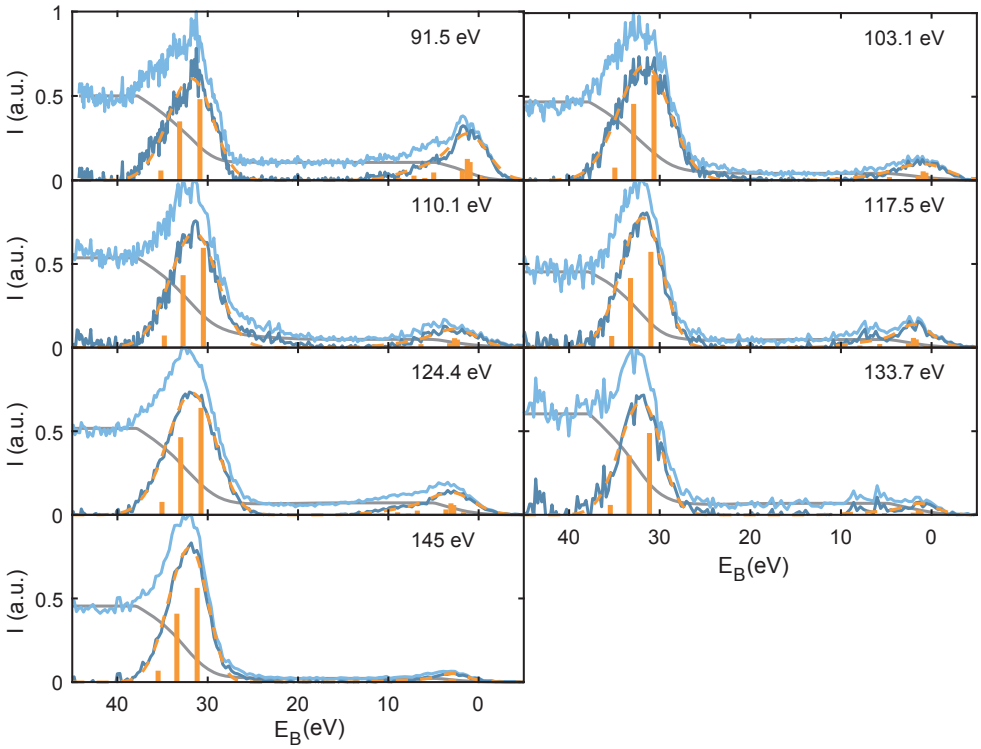

Figure 46 Static photoemission spectra of W(110) irradiated with attosecond pulses at 7 central energies ranging from 91.5 eV to 145 eV. Blue lines denote photoemission intensity before (light) and after (dark) splitted Shirley background (grey) subtraction. Orange bars denote the central energy and intensity of initial states used in the delay retrieval procedure. Orange dashed line represents the fitted Gaussian model.

detail in section 4.5.2. Further analysis and quantitative decomposition of the different electronic states contributing to the valence band photoemission are also deferred to section 4.5.2.

Attosecond streaking spectrograms are recorded with the electrostatic lens activated in order to increase the signal-to-noise ratio and reduce the measurement time to an acceptable fraction of the time between subsequent high-temperature flashes. Typical spectrograms are recorded with $100 - 200$ as equidistant XUV-NIR delay resolution on a $7 - 10$ fs temporal range.

We record the time between each attosecond streaking measurement and the last high-temperature flash anneal and correlate it with the obtained attosecond delay in order to exclude systematic errors from residual surface contamination (see figure 48). Hence, the attosecond time delay of the pristine surface is recovered by extrapolation of the exposure-time after high-temperature flash annealing. The result of the extrapolation is consistent with the findings of [35] for both the first and second beamtimes conducted with the 117.1 eV XUV mirror (see figure 48 a). The contamination of the reactive W(110) surface with O atoms and CO molecules is probable cause of the observed positive slope of ≈ 0.12 as/min. Extrapolation towards zero NIR and UHV exposure recovers the attosecond time delay of the pristine tungsten surface. No presorting of the data according the the shape of the valence band is necessary. Where experimentally possible, a comparison of photoemission time delays from measurements

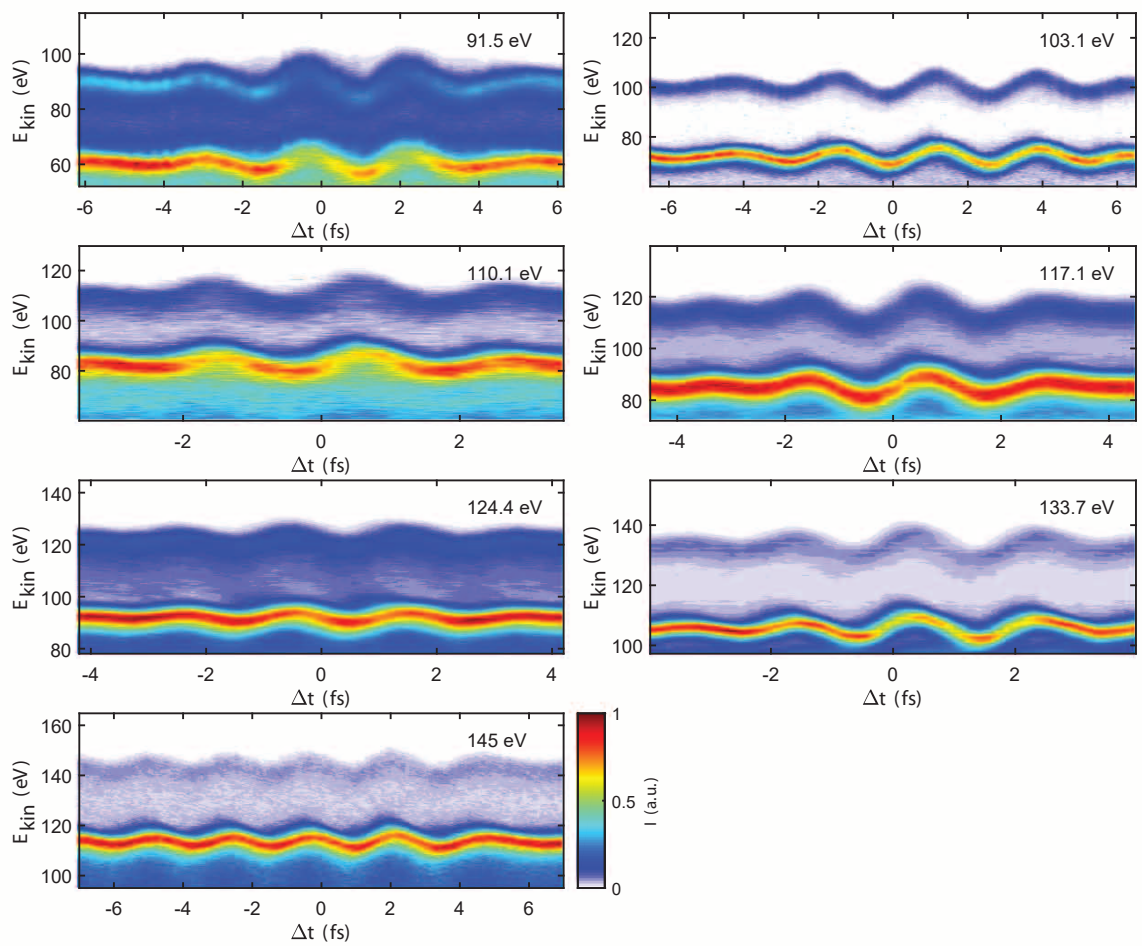

Figure 47 Attosecond streaking spectrograms from W(110) surfaces recorded with 7 different central photon energies from 91.5 eV to 145 eV.

recorded with and without the activation of the electrostatic lens was conducted. No significant influence of the lens activation on the relative attosecond time delays were found. Representative streaking spectrograms for W(110) are depicted in figure 47. Moderate saturation of the detection electronics is accepted in case of the strong W 4f emission, which in principle could introduce systematic errors, because electrons with lower binding energies are preferably detected. However, systematic investigation of the W 4f saturation in both [35] and [218] concluded the introduction of systematic errors to be negligible in case of moderate saturation. The adjusted statistical distributions of retrieved attosecond time delays as well as the photon energy-dependent photoemission time delay of the W 4f orbital w.r.t. the valence band $\Delta\tau$ is depicted in figure 49. Mean values and 95% confidence intervals are printed in table 2.

Analysis of the full data set reveals a strong decrease of the photoemission time delay $\Delta\tau_{vb-4f}$ with increasing photon energy largely irrespective of delay extraction method. This decrease agrees qualitatively with theoretical predictions based on simple classical transport [35], Monte-Carlo simulations of electron transport and scattering [97] and intra-atomic interactions [32]. Notable exception is the PIE retrieval, from which a pronounced local maximum at 133.7 eV is

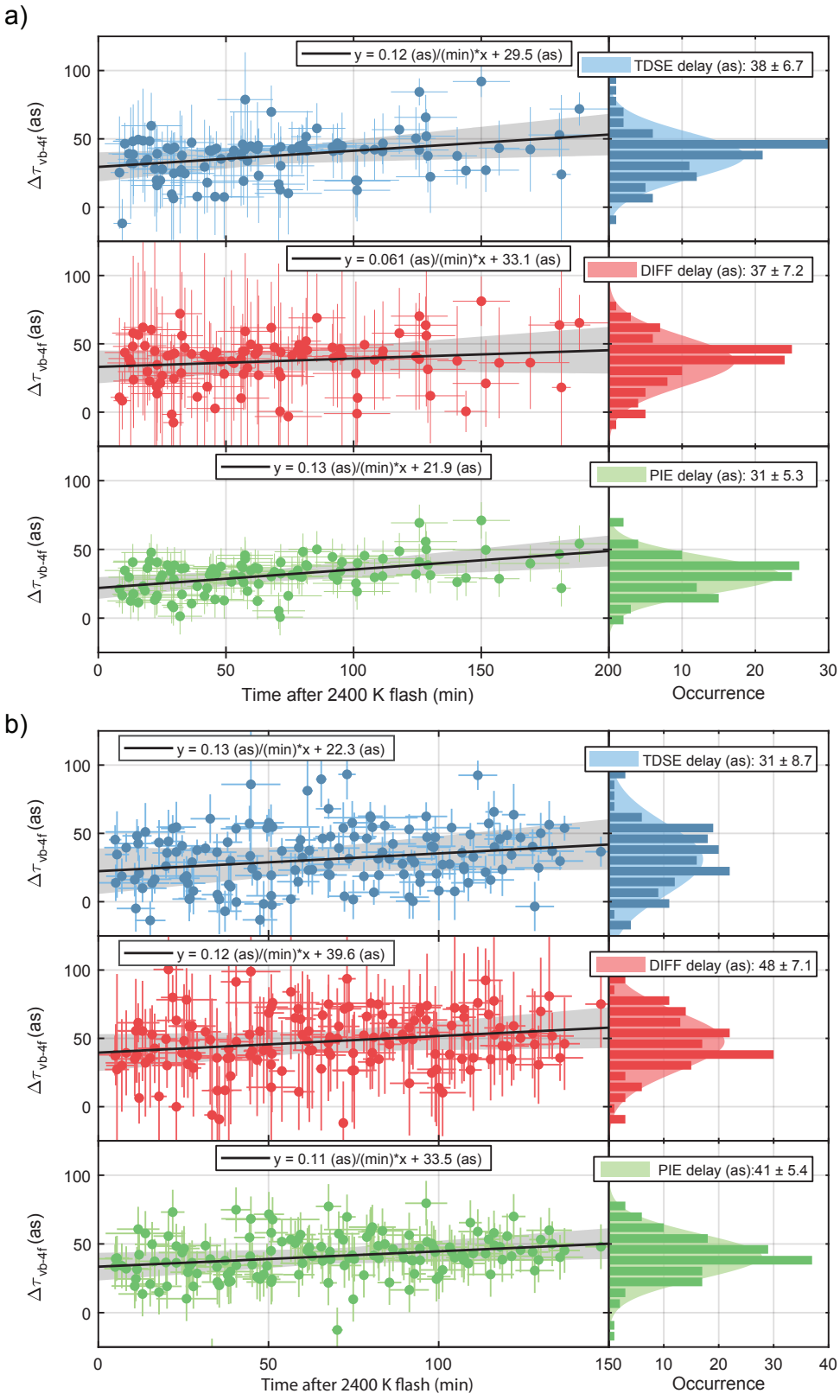

Figure 48 Correlation of time between high-temperature flash annealing and measurement with the retrieved time delays for three methods of delay extraction at central photon energy 117.1 eV (a) and 145 eV (b). The thin vertical and horizontal lines represent the retrieved fitting error of the delay extraction algorithm and the time of beginning and finishing each measurement, respectively.

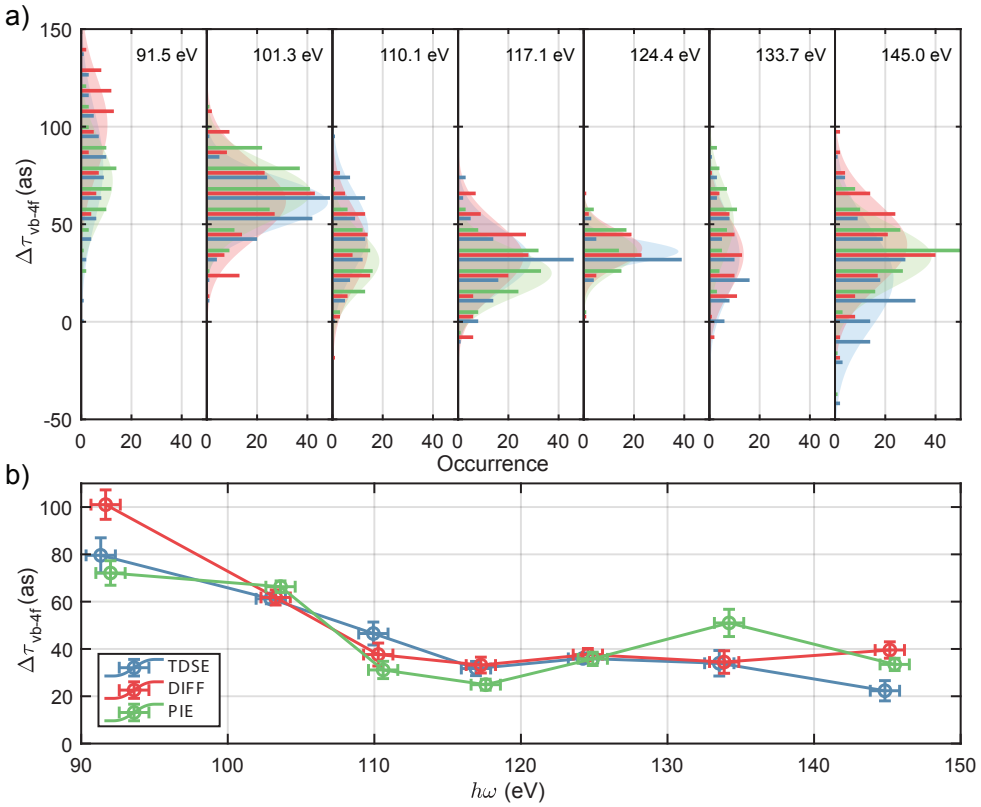

Figure 49 a) Statistical distribution of relative photoemission time delay of W 4f core level w.r.t W(110) valence and conduction bands $\Delta\tau_{vb-4f}$, extracted from repeated attosecond streaking measurements. Colours encode method of evaluation (see appendix E) and central photon energies are marked in the top right of each plot. b) Statistical average of $\Delta\tau_{vb-4f}$ for all delay extraction methods and central photon energies. Error bars denote 95% confidence intervals.

$\hbar\omega$ (eV)	91.5	103.1	110.1	117.1	124.4	133.7	145.0
TDSE (as)	79.6 ± 7.4	61.2 ± 2.1	46.5 ± 4.8	29.5 ± 3.2	36.0 ± 1.6	34.0 ± 5.4	22.3 ± 4.3
DIFF (as)	101.0 ± 6.2	61.8 ± 3.2	37.6 ± 4.9	33.1 ± 3.6	37.6 ± 2.6	34.5 ± 4.8	39.6 ± 3.5
PIE delay (as)	72.1 ± 5.2	66.3 ± 2.4	31.1 ± 3.7	21.9 ± 2.4	35.8 ± 2.8	51.0 ± 5.8	33.5 ± 2.6
$\Delta\tau_{vb-4f}$ (as)	84.2 ± 10.6	63.1 ± 4.0	38.5 ± 7.1	28.2 ± 4.8	36.5 ± 3.6	38.7 ± 8.5	31.8 ± 5.6

Table 2 Mean results and 95% confidence intervals of delay retrieval algorithms for W(110) (see figure 49). The averaged delay $\Delta\tau_{vb-4f,WO}$ is referenced and plotted throughout the discussion of the results.

obtained. A detailed and quantitative discussion involving the results from adsorbate covered W(110) surfaces is deferred to section 4.5.

4.3.2. W(100)

The extension of the experimental study from the W(110) surface to the W(100) surface was motivated by the question whether effects of the final-state band structure would be influential in attosecond solid state chronoscopy experiments and preceded the studies presented in chapter III. The W(100) surface is subject to (2x2) surface reconstruction upon minor hydrogen coverage or low temperatures due to its thermodynamic instability, yet the net change of electronic density

of states upon reconstruction as found from DFT calculations is minor [219].

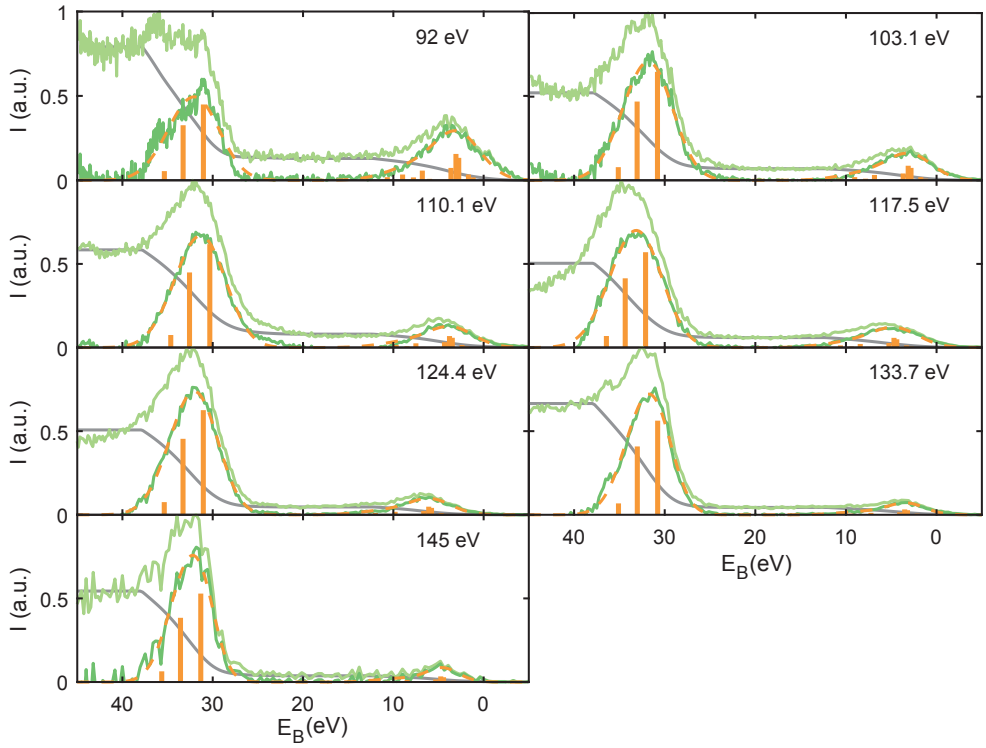

Figure 50 Static photoemission spectra of W(100) irradiated with attosecond pulses at 7 central energies ranging from 91.5 eV to 145 eV. Green lines denote photoemission intensity before (light) and after (dark). splitted Shirley background (grey) subtraction. Orange bars denote the central energy and intensity of initial states used in the delay retrieval procedure. Orange dashed line represents the fitted Gaussian model.

Indeed, we observe only minute differences between the static photoemission spectra recorded with attosecond pulses and depicted in figure 50 and their counterparts recorded on W(110) (see figure 46), hence reinforcing the statement that angle-integrated or normal-emission attosecond chronoscopy is mostly sensitive to the vertical structure of the investigated solid sample. The most striking difference in the spectral shapes of W(110) and W(100) emission are observed at 91.5 eV. This was also reported in [214] along a reduction of $\Delta\tau_{vb-4f}$ by 24 as for the W(100) surface. A set of representative streaking spectrograms for each photon energy is depicted in figure 51. Mean values and 95% confidence intervals are printed in table 3.

The extraction of the retardation of photoemission from the W 4f core level w.r.t the valence and conduction bands $\Delta\tau_{vb-4f}$ from the attosecond streaking spectrograms is performed in the very same manner as in case of W(110) including the extrapolation towards zero NIR and UHV exposure time of the sample. The results of the time delay extraction including the statistical distribution of experimental results are depicted in figure 52.

A most significant deviation between W(110) and W(100) results is observed at photon energy 91.5 eV in agreement with the evaluation result from A. Kim [214]. Furthermore, the local minimum of the relative attosecond time delay around 117 eV is even more pronounced in case

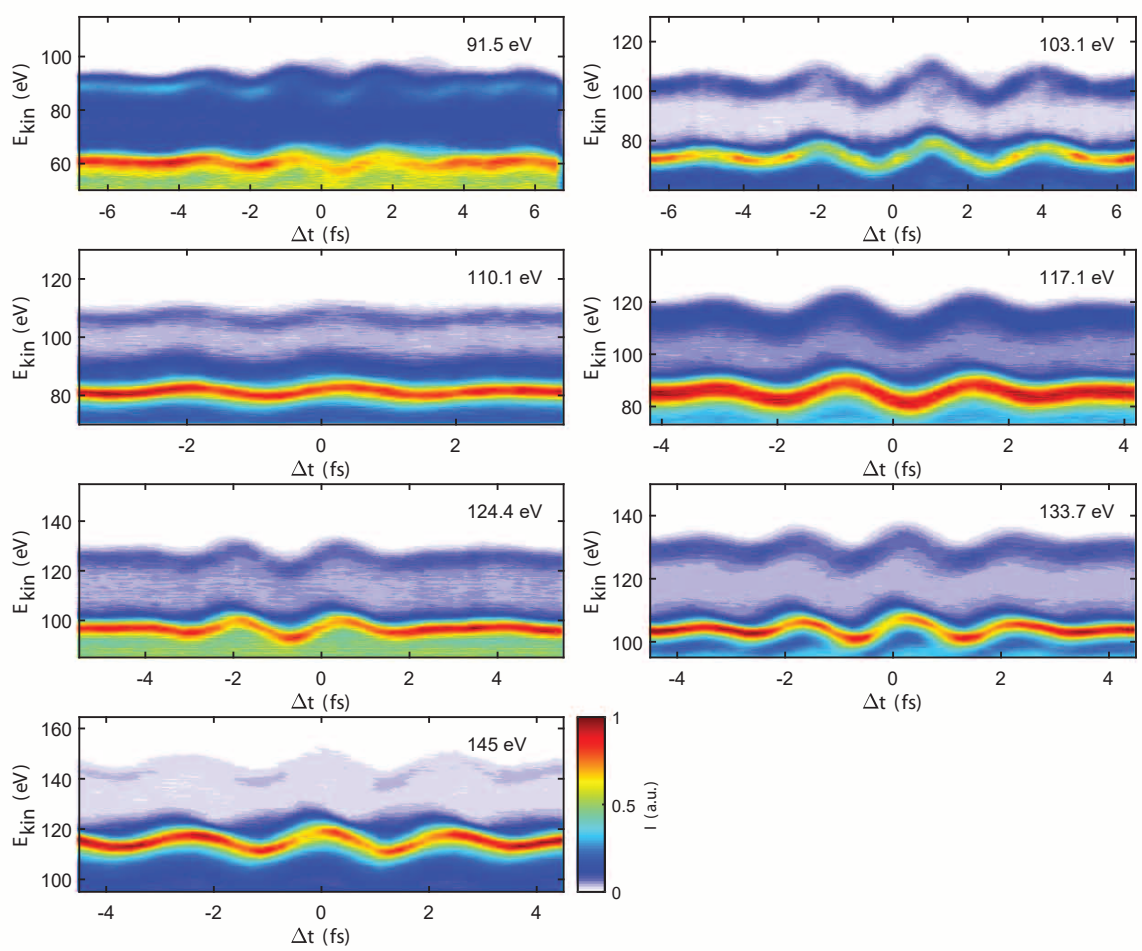

Figure 51 Attosecond streaking spectrograms from W(100) surfaces recorded with 7 different central photon energies from 91.5 eV to 145 eV.

$\hbar\omega$ (eV)	91.5	103.1	110.1	117.1	124.4	133.7	145.0
TDSE (as)	64.0 ± 7.2	70.4 ± 5.8	35.5 ± 4.0	29.4 ± 1.4	39.7 ± 3.8	38.3 ± 2.2	19.8 ± 9.9
DIFF (as)	74.6 ± 3.5	61.1 ± 7.5	47.3 ± 4.5	29.6 ± 1.4	46.9 ± 3.7	40.5 ± 2.6	55.5 ± 6.5
PIE (as)	57.1 ± 5.2	83.2 ± 4.9	35.5 ± 3.5	25.9 ± 1.4	40.1 ± 2.8	49.5 ± 3.3	32.5 ± 9.1
$\Delta\tau_{vb-4f,W(100)}$ (as)	65.3 ± 8.7	71.6 ± 15.3	39.4 ± 6.5	28.3 ± 2.2	42.3 ± 5.3	42.7 ± 4.5	35.9 ± 15.6

Table 3 Mean results and 95% confidence intervals of delay retrieval algorithms for W(100) (see figure 52).

of W(100). This already implies the importance of the electronic band structure of the initial and final states for the resulting photoemission time delays, as effects from energy-dependent inelastic scattering cross sections and intra-atomic interaction should be observed irrespectively of the orientation of the single crystalline sample. Because neither high-resolution photoemission spectra nor DFT calculations are available for the W(100) surface to date, quantitative discussion is limited to clean and adsorbate covered W(110) surfaces.

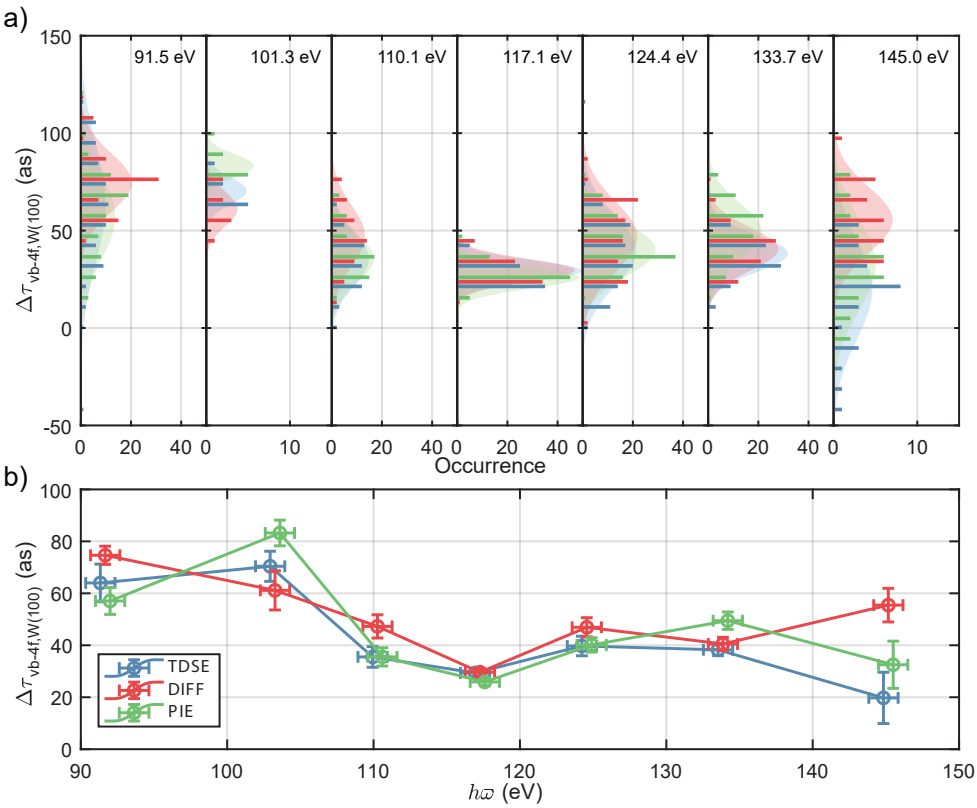

Figure 52 a) Statistical distribution of relative photoemission time delay of W 4f core level w.r.t W(100) valence and conduction bands $\Delta\tau_{vb-4f}$, extracted from repeated attosecond streaking measurements. Colours encode method of evaluation (see appendix E) and central photon energies are marked in the top right of each plot. b) Statistical average of $\Delta\tau_{vb-4f}$ for all delay extraction methods and central photon energies. Error bars denote 95% confidence intervals.

4.4. Time-resolved photoemission from adsorbate covered surfaces

The extensive literature of atomic and molecular adsorption on transition metal surfaces is motivated by their catalytic properties and the extensive industrial applications associated therewith, for which G. Ertl was awarded the Nobel prize in Chemistry 2007. Applying established techniques of preparation and characterization of well-defined atomic surface adsorbate layers allows to extract further information in attosecond chronoscopy in solids [35, 25]. The additional degree of freedom of precisely controlling the vertical structure of the atomic layer-by-layer stack allows us to use adsorbate core-levels and/or valence orbitals as timing reference for the determination of absolute photoemission times, i.e. the time between the absorption of a photon and the ejection of the electron, eliminating the ambiguity of previous experimental results. The concept is visualized in figure 53 for the example of an iodine adlayer on top of a tungsten crystal.

In order to investigate the influence of the electronic band structure of the core levels and valence bands independently, it is necessary to extend energy-resolved attosecond streaking

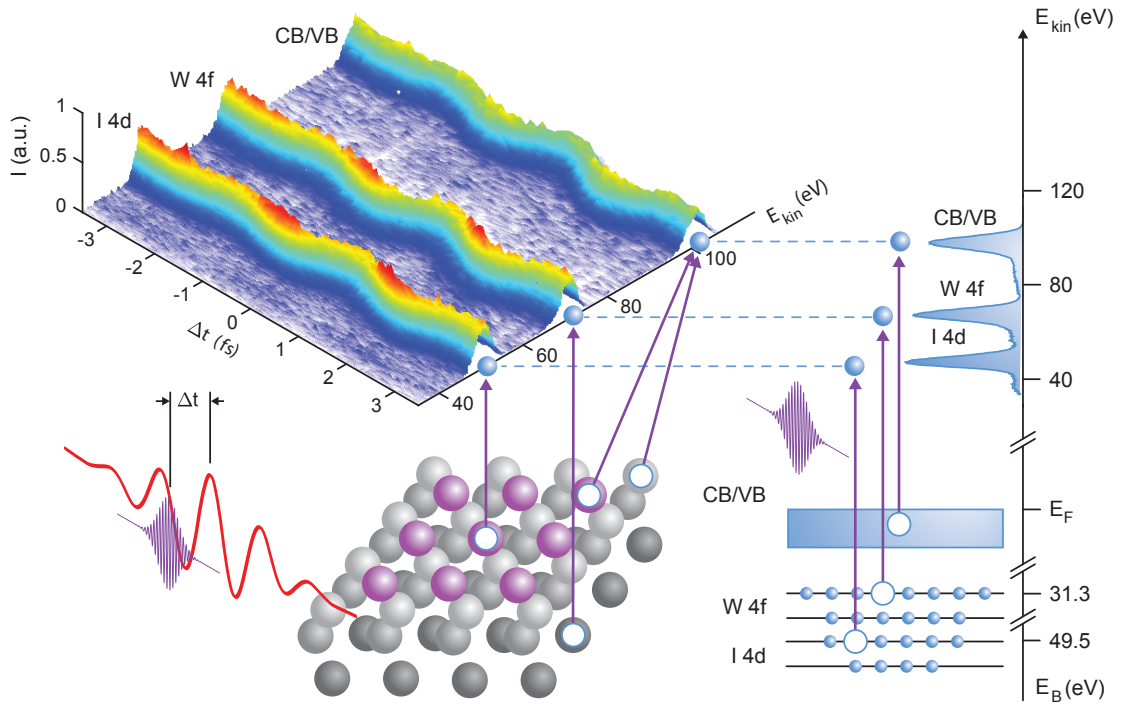

Figure 53 Schematic illustration of attosecond streaking spectroscopy on adsorbate covered surfaces. Top: Attosecond streaking of partially desorbed I/W(110) spectrogram after background subtraction. Bottom: The W(110) crystal (grey spheres) with saturated monolayer of iodine adatoms (purple spheres) is irradiated by XUV (purple) and NIR (red) pulses with controlled time delay Δt. Core level electrons (blue spheres) are emitted from the corresponding element. Valence band electrons from complicated hybridized states. Hole states are indicated as white spheres. Right: Electronic structure of occupied valence band and core states. XUV photoemission is indicated by purple arrows. The static photoemission spectrum corresponding to the depicted attosecond streaking spectrogram is indicated along the kinetic energy axes on the right side.

spectroscopy towards the measurement of absolute photoemission time delays over a large window of photon energies. The adsorption of chemically different atoms does change the shape of the valence band wavefunctions via hybridization of atomic orbitals and the formation of covalent and ionic bonds. In general these processes are associated with (partial) charge transfer and a redistribution of valence band charge density. The core level wavefunctions of surface atoms are only minutely altered, but experience a change in binding energy due to the overall shift in charge density. To this end, two measurement series utilizing iodine and oxygen adsorption have been performed and will be presented in this section.

4.4.1. I/W(110)

Iodine adlayers on W(110) are prepared by exposing the room temperature W(110) surface to $50 - 100$ Langmuir of I_2. The W single crystal is flashed to 2400 K prior to deposition to maintain reproducible surface conditions. The I_2 molecules are dissociated upon adsorption on both W(110) as well as W(100) surfaces [220, 221], because the specific energy of the iodine in the absorption site is lower than in the bound state on top of the clean W surface. If abundant I_2 is provided, as in the case of our experiment, a saturated monolayer (ML) is formed on top of the W(110) surface. Further iodine deposition at room temperature is prevented by the weak

interaction of the I_2 molecule with the I/W(110) surface. Furthermore, dissociation is limited to the first layer and the molecular structure of the higher layers is highly absorptive for visible light. Experiments to this end failed because of the fast evaporation of all iodine atoms above the first monolayer [222]. The saturated monolayer is stable under XUV and NIR irradiation against desorption and contamination for at least 3 hours. It shall be noted that the saturated iodine monolayer only constitutes $7/12$ atoms per unit cell of the W(110) surface [223], but will be referred to in terms of fractional coverage $\theta = 1$. The saturation coverage remained unchanged for I_2 exposures between 20 and 100 Langmuirs.

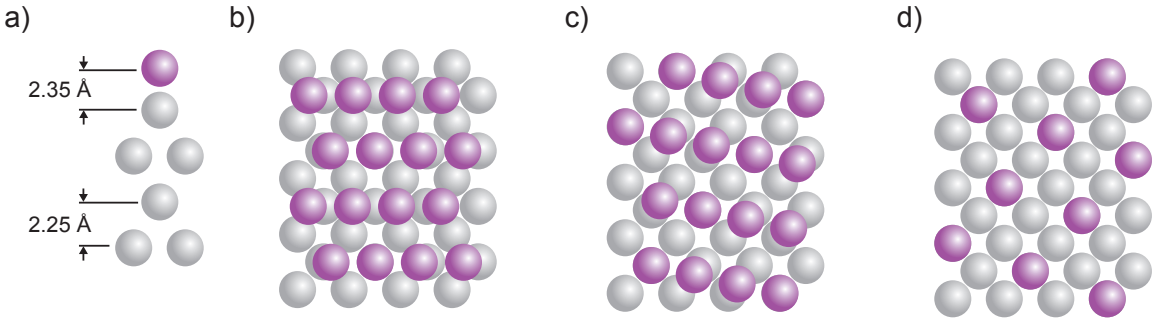

Figure 54 Adsorption geometry of iodine on W(110). a) Vertical adsorption distance determined from DFT calculations [206]. b) Horizontal geometry of saturated monolayer ($\theta = 1$). b) 530 K structure ($\theta = 1$) c) 1010 K structure ($\theta = 0.5$). Partial desorption above 1010 K results in island formation. b,c,d) adapted from [223].

The iodine adsorbate contributes additional spectral intensity both in the valence band as well as in the region of the I 4d core level region at binding energies around -52 eV, which both are separable from the W 4f emission in the photoelectron spectrum and can be analysed w.r.t their attosecond time delays individually. The analysis here will be limited to the relative time delay between the I 4d and W 4f core levels. A much more intricate investigation including the valence band can be found in the thesis of Marcus Ossiander [224]. The charge density of the I 4d orbitals is localized outside the W crystal wholly, and the associated photoelectron wavepacket serves as a time-zero marker for the investigation of absolute photoemission time delays. The iodine adlayer is however expected to change the shape of the infrared field distribution at the interface. Furthermore, the electrons emitted from W atoms experience additional elastic and inelastic scattering on their trajectory leaving the solid and the shape of the surface potential barrier changes upon halogen adsorption. Thus, the influence of the additional contribution of the iodine adlayer on the photoemission time delay of the W 4f level must be investigated systematically, before conclusions about the absolute photoemission time delay can be drawn.

To this end, streaking spectrograms were not only recorded from saturated monolayers, but also from partially desorbed iodine films constituting sub-monolayer coverages ($\theta < 1$). The desorption is accomplished by heating the sample up to about 1400 K for a few seconds. The adsorbate layer undergoes a number of structural phase transitions during heating, which are discussed in detail in [223]. Because the partial desorption of iodine from the W(110) surface opens up potential adsorption sites for CO and O_2 molecules, the sub-monolayers are refreshed after 120 minutes of measurement time. The partial coverage θ is determined by in-situ XUV

photoemission spectroscopy and the results are depicted in figure 55 a,b. The electrostatic lens of the electron TOF spectrometer is deactivated to avoid saturation and the NIR is blocked with a second Zr filter in front of the pellicle. The composite valence band photoemission of I/W(110) consists of the contributions of the clean valence band and the I 5p valence orbital. The normalized photoemission intensities for the I 4d, the W 4f and the composite valence band are fitted with the following model as function of the fractional coverage θ

$$I_{vb}(\theta) = I_{0,vb} \cdot \left(\theta e^{-\frac{d}{\lambda_{vb}}} + 1 - \theta\right) + I_{0,5p} \cdot \theta \cdot e^{-\frac{d}{2\lambda_{vb}}}, \tag{4.1}$$

$$I_{4f}(\theta) = I_{0,4f} \cdot \left(\theta e^{-\frac{d}{\lambda_{4f}}} + 1 - \theta\right),$$

$$I_{4d}(\theta) = I_{0,4d} \cdot \theta \cdot e^{-\frac{d}{2\lambda_{4d}}},$$

$$I_{tot}(\theta) = I_{vb}(\theta) + I_{4f}(\theta) + I_{4d}(\theta), \tag{4.2}$$

wherein $I_{0,x}$ denotes the photoemission intensities neglecting inelastic scattering. The effective thickness of the saturated iodine monolayer is denoted as d and not known a priori. Electrons emerging from iodine emerge from the middle of the iodine adlayer $d/2$ and are subject to reduced scattering. The $I_{0,x}$ are determined by comparison of the relative photoemission intensities of clean W(110) ($\theta = 0$) and saturated monolayers ($\theta = 1$), assuming $d = 3$ Å and inelastic damping according to the universal curve [225]. Subsequently, the coverage of the sub-monolayer spectra is determined by fitting the relative photoemission intensities to the model for each spectrum ($0 < \theta < 1$). The precision of the coverage estimation is controlled by repeating the outlined procedure for $d = 1.5$ Å and $d = 4.5$ Å, which determines the horizontal error bars in figure 55 c,d. The smallest investigated coverages are around 25% of the saturated monolayer, which equates to one iodine atom for every eight tungsten atoms at the surface. At such low coverages, formation of two dimensional islands with local structure similar to figure 54 d is expected according to the extensive literature of halogen adsorption on metal surfaces [223].

Partial desorption of the iodine adlayer only weakly affects the relative photoemission time delay of electrons emerging from the W 4f core level, and the maximum decrease of $\Delta\tau_{4d-4f}$ is limited to 11 as (see table 4) irrespective of the central photon energy of the XUV pulses. The results are compiled in table 4. The success of the submonolayer experiments however rely heavily on the enhancement of the I 4d photoemission cross section due to the so-called giant dipole resonance [226, 227]. This further implies a heavily increased interaction of the outgoing photoelectron wavepacket with the remaining electrons of the 4d subshell. This should lead to an substantial increase in the the absolute photoemission time delay of the I 4d orbital. To this end, further measurements of the attosecond time delay were carried out by Ossiander et al. [206] at the attosecond beamline at TUM on mixtures of helium and low order iodine-substituted alkanes (CH_3I, C_2H_5I), which provide sufficient vapour pressure for gas phase attosecond chronoscopy without additional heating systems at room temperature. The admixing with helium provides a

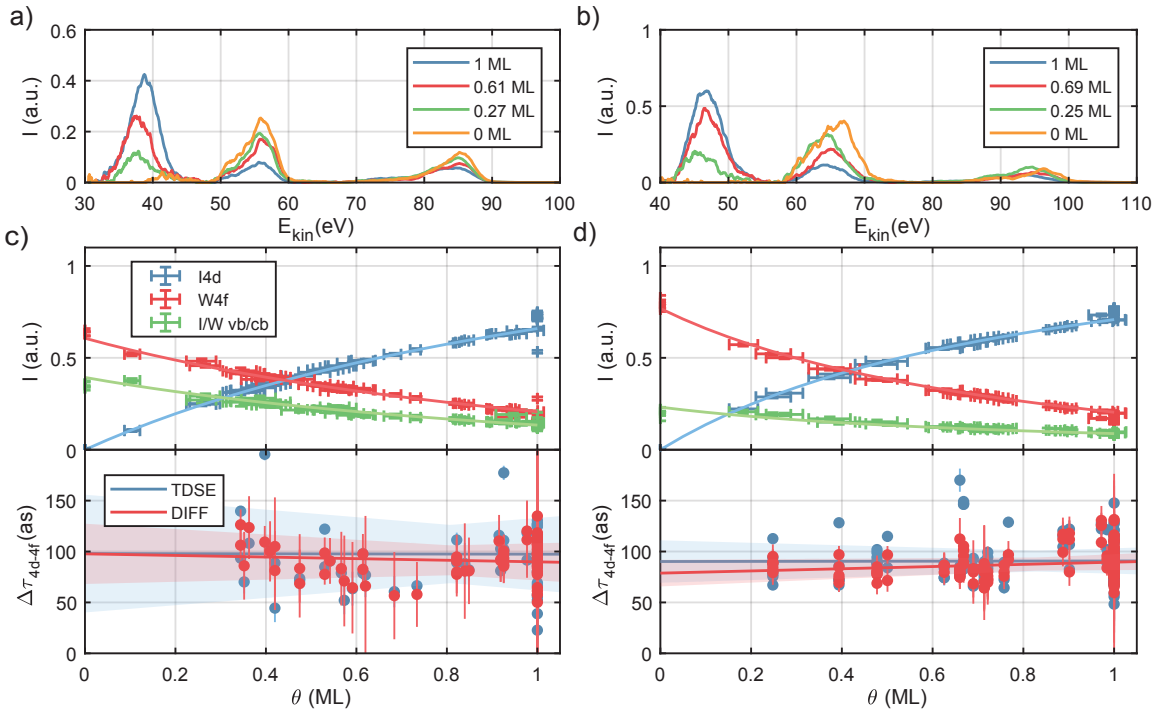

Figure 55 Analysis of iodine coverage on W(110) by means of quantitative XUV photoemission spectroscopy. a) Spectra of I/W(110) at photon energy 91.5 eV for different iodine coverages. The spectra are normalized to the total photocurrent b) Same as a) for photon energy 103.1 eV c) Top: Relative photoemission intensity of I 4d orbital I_{4d}/I_{tot} (blue), W 4f orbital I_{4f}/I_{tot} (red) and the composite valence band I_{vb}/I_{tot} (green) as a function of fractional submonolayer coverage θ. Solid lines represent model fits (see equation 4.2) Bottom: Relative Photoemission time delay $\Delta\tau_{4d-4f}$ as function of fractional iodine coverage θ (see table 4). d) Same as c) for photon energy 103.1 eV

well-defined reference of the absolute photoemission time delay, i.e. the time between arrival of the photon at the position of the atom, with superior accuracy and precision [20]. Indeed, the absolute time delay increases by 25 as between photon energy 103.1 eV and 91.5 eV. Attosecond streaking measurements on the surface and in the gas phase were carried out using the same XUV multilayer mirrors in order to avoid systematic errors.

$\hbar\omega$ (eV)	TDSE (as) $(\theta = 1)$	TDSE (as) $(\theta = 0)$	DIFF (as) $(\theta = 1)$	DIFF (as) $(\theta = 0)$	τ_{I4d} (as)
91.5	97 ± 35	98 ± 57	90 ± 18	98 ± 29	51.5 ± 8.5
103.1	91 ± 12	90 ± 20	90 ± 8	79 ± 13	26.8 ± 3.1

Table 4 Relative photoemission time delay $\Delta\tau_{4d-4f}$ between electron wavepackets emitted from the I 4d and the W 4f orbitals for saturated iodine monolayers and extrapolated to zero coverage. Iodine core level absolute photoemission time delay τ_{4d} as retrieved from gas phase measurements from iodine substituted alkanes and helium.

4.4.2. O/W(110)

Investigations of attosecond time delays from saturated monolayers of oxygen on top of W(110) were initially motivated by questions about the influence of surface contamination on the observed retardation of the W 4f core level photoemission w.r.t to the valence band [12, 35]. Such contamination is mostly associated with the adsorption of CO and O_2 molecules on

the surface, which does contribute to the photocurrent in the valence band. These additional contributions originate wholly outside the tungsten crystal hence appearing much earlier in the NIR streaking field than the electrons originating within the solid, as observed for the case of iodine.

Because the oxygen covered W(110) surface is readily obtained and investigated due to its chemical stability and increased valence band photoemission yields especially at high photon energies, the initial study of contamination induced systematic errors in the attosecond chronoscopy was repeated at every other photon energy. The saturated (1x1) monolayer of oxygen is obtained after exposure to > 1000 L of O_2 at room temperature [228]. The molecule dissociates during the adsorption process. The adsorption geometry of the saturated monolayer of oxygen adsorbed at room temperature onto a W(110) surface is depicted in figure 56 along with the LEED diffraction pattern.

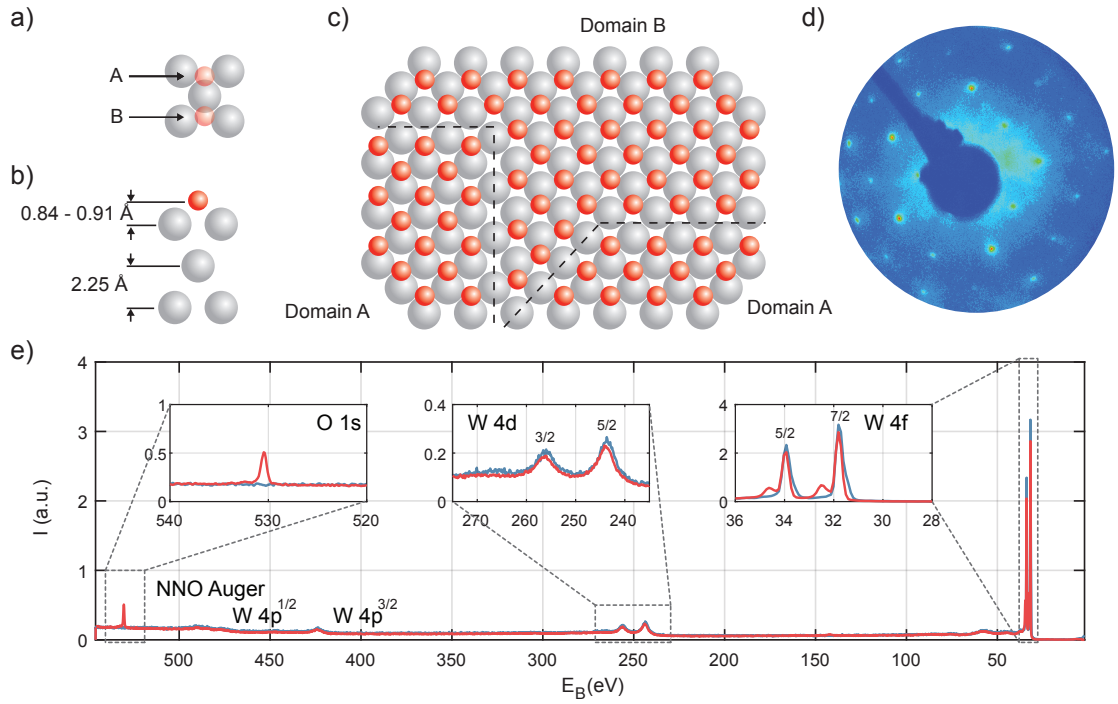

Figure 56 Geometry of oxygen adsorption monolayers on W(110). a) Possible adsorption sites of oxygen in the W(110) surface unit cell. b) Vertical adsorption geometry and interlayer distances. c) Extended O/W(110) surface region for saturated monolayer adsorption at room temperature showing random orientation of A/B adsorption domain boundaries. d) LEED pattern of W(110) surface measured after 10 minutes of oxygen adsorption at room temperature. A saturated monolayer of oxygen atoms is visible through alternating patterns of bright and dark diffraction spots. The increased inelastic background is explained mostly by the increased kinetic energy of the scattering electrons of 450 eV, which is necessary to image multiple diffraction orders. e) XPS spectrum of W(110) (blue) and O/W(110) (red) recorded with synchrotron radiation at photon energy 655 eV. The spectrum around the main photolines are expanded in the insets.

Two distinct and equivalent triply coordinated adsorption sites for oxygen are present on the W(110) surface, which cannot be occupied at the same time due to spatial overlap between the oxygen atoms in adjacent adsorption sites within a single surface unit cell [228, 229]. This implies the formation of distinct domains on the surface, which are randomly orientated in case of room temperature adsorption [230]. For adsorption at elevated temperatures of 1000 K, a (1x12)

superstructure can be observed in LEED [228], which indicates an orientation of the domain boundaries along the $(11\bar{1})$ and $(1\bar{1}\bar{1})$ directions of the crystal [230, 231]. It was however concluded that this additional organization parallel to the surface plane does not influence the attosecond chronoscopy results [35]. The vertical distance between the topmost tungsten atoms and the adsorbed oxygen atoms is between 0.84 Å and 0.91 Å, as determined in full-angle photoelectron diffraction measurements [232, 231].

The spectral shape of the UV valence band photoemission is profoundly changed by the adsorption of oxygen and strong hybridization between the W 5d and the O 2p orbitals [233]. In order to assess these properties at the photon energies accessible to attosecond streaking, we recorded high-resolution photoemission spectra of the saturated O/W(110) surface with narrowband synchrotron radiation at the ELETTRA synchrotron facility. The essential parameters of the photoemission experiment are listed in section 4.3.1 and appendix C. The resulting high-resolution spectra, their convolution with the Gaussian spectrum of the attosecond pulses and the comparison with the photoemission spectra recorded with isolated attosecond pulses are plotted in figure 57.

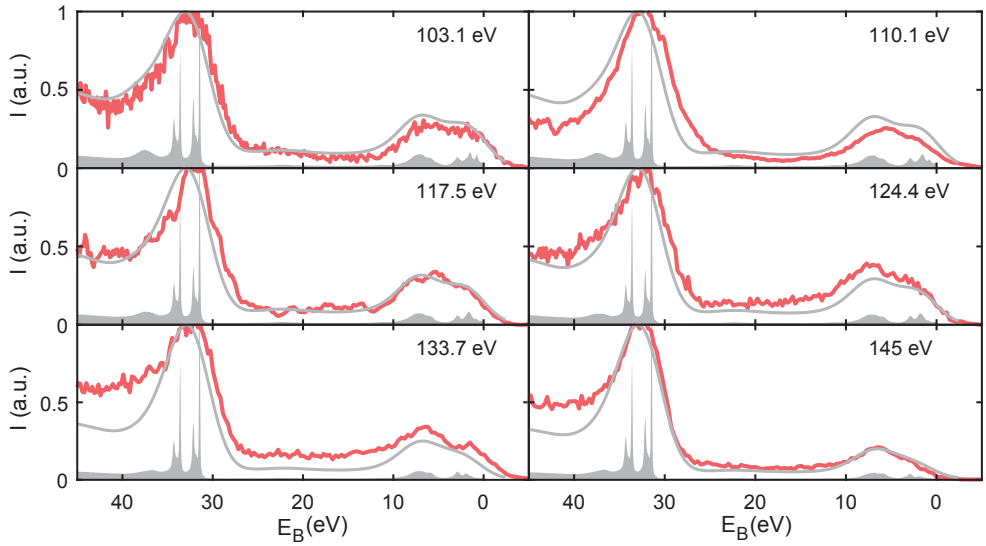

Figure 57 Comparison of static photoemission spectra of O/W(110) for six central energies ranging from 103.1 eV to 145 eV recorded with high-resolution photoemission at the Elettra synchrotron (grey area) and with HHG attosecond pulses in the lab (red). The solid grey line represents a convolution of the high-resolution spectrum with a 4.5 eV Gaussian function, representative of the reflection bandwidth of the XUV multilayer mirror.

The reduction of the background strength at 110.1 eV is likely an effect of partial saturation of the electron detection electronics. The interpretation of increased background signal at the other central photon energies is consistent with the W(110) dataset. Both a shift of the spectral weight away from the Fermi-edge, which is clearly observed in the experimental data, as well as a slight increase of the W(110) work function, unresolved with attosecond pulses, upon oxygen adsorption are expected [233]. The inversion of the asymmetry of the valence band photoelectron spectrum away from the Fermi edge and the strong increase of the combined valence band photoemission is consistent for all photon energies (see figures 46 and 58). The

binding energies and relative amplitudes of the initial states assumed in the fitting algorithm are extracted from [35]. All steady state spectra are again recorded without the electrostatic lens of the TOF spectrometer to avoid saturation of the detection electronics.

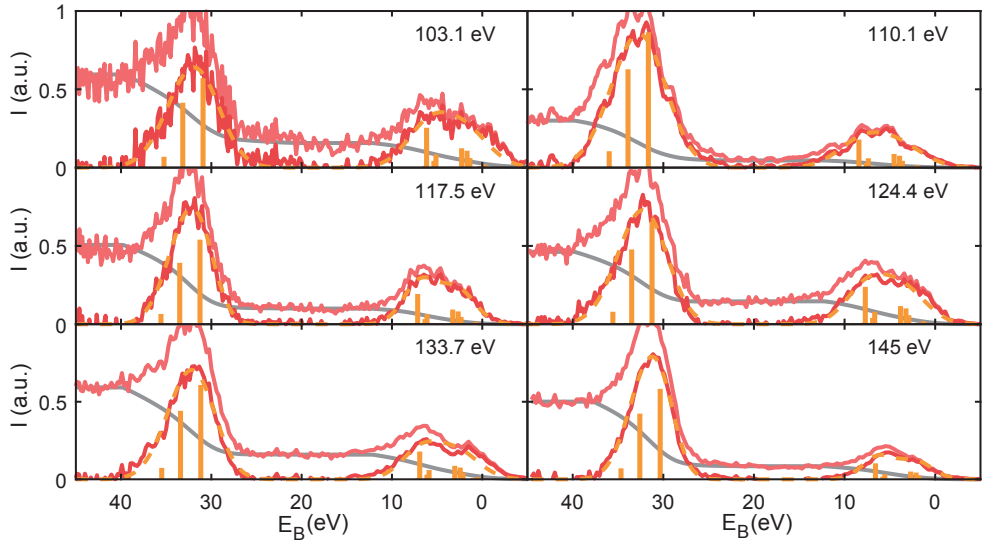

Figure 58 Static photoemission spectra of O/W(110) irradiated with attosecond pulses at 7 central energies ranging from 91.5 eV to 145 eV. Red lines denote photoemission intensity before (light) and after (dark) splitted Shirley background (grey) subtraction. Orange bars denote the central energy and intensity of initial states used in the delay retrieval procedure. Orange dashed line represents the fitted Gaussian model.

For direct comparison of the attosecond photoemission spectra from W(110) and the saturated O/W(110) monolayer, the corresponding spectra at 124.4 eV and 145 eV are plotted in figure 59.

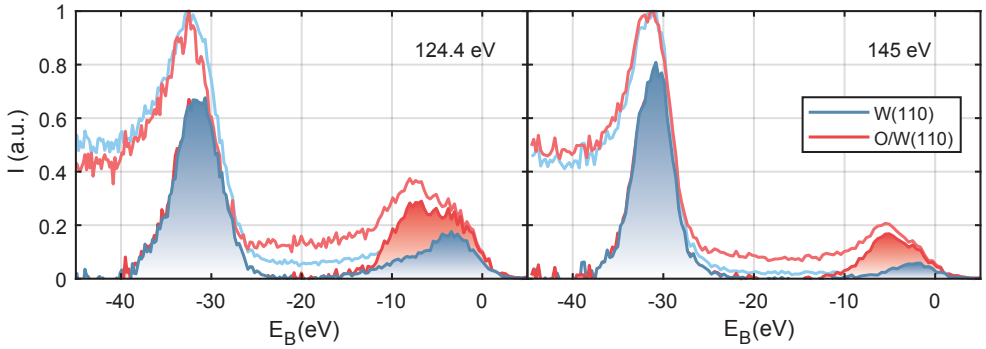

Figure 59 Direct comparison of normalized static photoemission spectra of W(110) (blue) and O/W(110) (red) for central photon energies 124.4 eV (left) and 145 eV (right) both before (light shaded lines) and after splitted Shirley background subtraction.

Streaking spectra are recorded activating the electrostatic lens to speed up measurement times especially at higher photon energies. The comparison of attosecond delay results wherever experimentally possible, with and without the electrostatic lens yielded negligible differences in case of O/W(110), too. Because the oxygen monolayer effectively passivizes the reactive tungsten surface against further oxidation or adsorption [234], no additional precautions about possible surface contamination or extrapolation is necessary during data evaluation, which significantly improves the statistical error in the measurements.

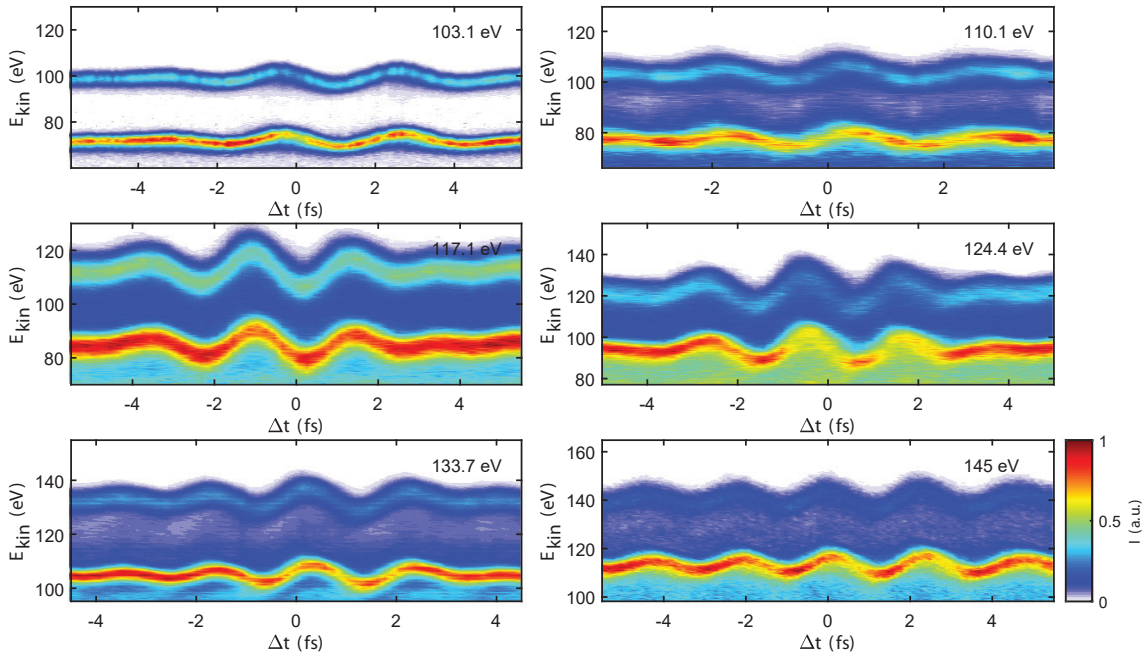

Figure 60 Attosecond streaking spectrograms from oxygen covered W(110) surfaces recorded with 6 different central photon energies from 103.1 eV to 145 eV. At 91.5 eV, W 4f core level of O/W(110) is too weak for reliable attosecond chronoscopy.

In general, results of the relative time delay with the PIE method are about $10 - 20$ as lower compared with the results from the other delay evaluation methods. This is likely related to the different weighting of the individual contribution of the valence band states to the total delay, with the tightly bound oxygen orbitals emerging earlier at all photon energies. The PIE algorithm is evaluated at the maximum of the valence band spectrum (see figure 84), which lies in the oxygen band. The TDSE and DIFF algorithms on the other side do weigh the individual contributions quadratically [20] in the least sqaures algorithm utilized for the determination of the analytic parametrization (see appendix E.2). Both numerically calculated and experimentally measured photoemission spectrograms are however treated in the same manner for delay extraction, which should minimize systematic errors in their mutual comparison.

$\hbar\omega$ (eV)	103.1	110.1	117.1	124.4	133.7	145.0
TDSE (as)	113.0 ± 5.6	81.1 ± 5.7	75.8 ± 2.6	87.2 ± 3.0	106.5 ± 6.0	83.2 ± 4.3
DIFF(as)	122.2 ± 4.4	91.4 ± 4.0	75.0 ± 2.2	95.2 ± 3.4	107.3 ± 4.8	103.3 ± 3.4
PIE (as)	94.4 ± 4.1	72.0 ± 2.8	64.4 ± 4.2	76.8 ± 3.7	89.3 ± 3.3	75.6 ± 3.4
$\Delta\tau_{vb-4f,WO}$ (as)	109.9 ± 9.5	81.5 ± 7.3	71.8 ± 5.5	86.4 ± 6.0	101.0 ± 8.1	87.4 ± 7.8

Table 5 Mean results and 95% confidence intervals of delay retrieval algorithms for O/W(110) (see figure 61). The averaged delay $\Delta\tau_{vb-4f,WO}$ is referenced and plotted throughout the discussion of the results.

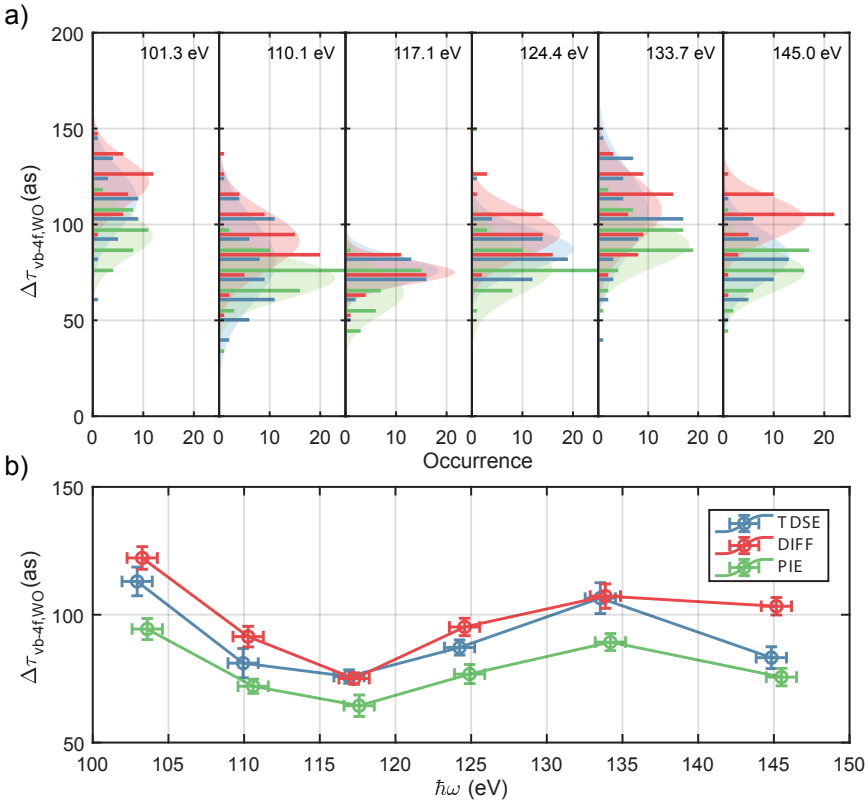

Figure 61 a) Statistical distribution of relative photoemission time delay of W 4f core level w.r.t combined O/W valence band $\Delta\tau_{vb-4f}$, extracted from repeated attosecond streaking measurements. The different colours encode the respective methods of evaluation (see appendix E) and central photon energies are marked in the top right of each plot. b) Statistical average of $\Delta\tau_{vb-4f}$ for all delay extraction methods and central photon energies. Error bars denote 95% confidence intervals.

4.5. Discussion

4.5.1. Intra-atomic scattering phase shifts

The discussion intra-atomic scattering effects follows the same arguments outlined for magnesium in section 3.4.1. For heavy elements like tungsten however, the effects of intra-atomic scattering discussed in detail by Siek et al. for the case of WSe_2 cannot be neglected any more. At XUV to soft X-ray photon energies, the photocurrent originates mostly from initial states derived from the 4f $(l = 3)$ and 5d $(l = 2)$ atomic orbitals. Outgoing photoelectrons are retarded by the centrifugal barrier $U_L = l(l+1)/2r^2$ significantly reducing the kinetic energy of the outgoing electron in the immediate vicinity of the ionic core [32]. The additional time delay experienced by electron wavepackets emitted from W 4f is calculated in the supplementary information of [32] and extrapolated to the higher kinetic energies used in this study. Strong deviation of the extrapolated behaviour would only occur around resonant core level excitations, which modulate the photoemission time delay [133]. However, in the binding energy range between 90 eV and 150 eV, no tungsten states are observed in the XPS spectra. The intra-atomic scattering factors are neglected in the case of the conduction and valence bands as in the case of magnesium similar to [32]. The results for the EWS and CLC delays are depicted in figure 62.

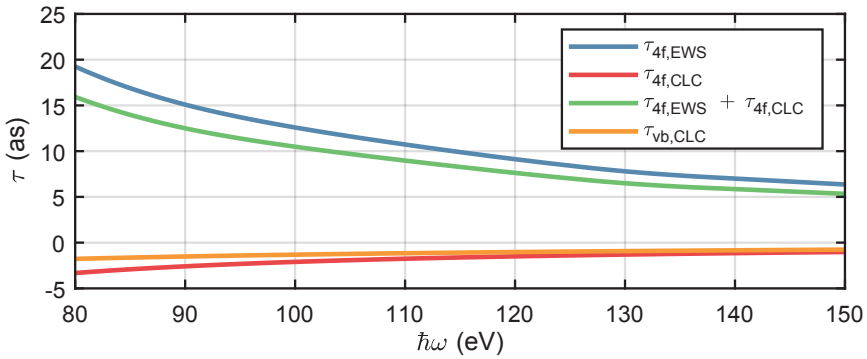

Figure 62 EWS and CLC attosecond time delays for W4f core level and tungsten valence band. The CLC is referenced to the image potential of the W crystal with $Z = 1/4$ (see section 3.4.1). The EWS delay for the delocalized valence band is zero because no localized hole-potential is assumed [32].

While the retardation of the outgoing electron wavepacket cannot be ignored in case of the W 4f core level and has to be accounted for when comparing numerical calculations from one dimensional models and experimental results, the smooth shape of the W 4f curve does not sufficiently explain the two main experimental observations, i.e. the local maxima of the experimental delay at 130 eV and the strong in relative photoemission time delay between the valence band and the 4f core level below photon energies of 110 eV. Resonant intra-atomic processes contribution to the non-monotonic observation of the time delay in tungsten have not been observed in theoretical calculations of the resonant and non-resonant photoionization cross section of the tungsten atom [235].

4.5.2. Classical transport model

Similar to the case of magnesium (see section 3.4.2), it is instructive to calculate the photoemission time delays from ballistic propagation with free electron velocities. Classical transport theory (CTT) [236] in terms of the three-step model of photoemission was successfully used to model the thickness-dependent attosecond time delays between photoemission from different electronic core states in Mg/W adlayer systems [25]. Important parameters such as the elastic and inelastic scattering cross sections and the spatial distribution of photoexcited electrons inside the solid have to be deduced from empirical observations or DFT calculations. The photoexcited high-energy electrons propagating within condensed matter are subject to energy loss by inelastic scattering. Within the one-step theory of photoemission, inelastic scattering is commonly introduced in the form of an imaginary valued optical potential, in essence dampening the inverse-LEED wavefunction inside the solid and confining it to within the first few atomic layers. This approach, while correctly reproducing the primary photoelectron spectrum, i.e. electrons leaving the solid without inelastic scattering, does not include the generation of secondary electrons.

Inelastic scattering delay

The time-dependent investigation of the secondary electron emission is so far limited to CTT [236]. Sophisticated implementations of CTT calculate the elastic and inelastic scattering cross sections from (TD)-DFT or from experimental data [237] and calculate the photoelectron spectrum including secondary electrons with the Monte-Carlo method [97]. This approach allows to draw quantitative conclusions about the secondary electron emission from attosecond streaking spectroscopy [207]. More importantly, Lemell et al. calculated that the photoelectron emission from the W 4f orbital spectrally overlaps with inelastically scattered electrons emitted from valence and conduction band states. These electrons have propagated on average a distance equal to one inelastic mean-free path inside the crystal before scattering and appear delayed w.r.t. primary photoelectrons emitted at the same kinetic energy. This inelastic scattering delay $\Delta\tau_{scatt}$ amounts to 20 as at 105 eV for W(110) [206] and is expected to scale with the relative photoemission intensity of the valence band and the 4f core level in tungsten and the magnitude of the electron energy loss function [195] at the binding energy difference of the valence band and the W 4f core level.

$$\Delta\tau_{scatt}\left(\hbar\omega\right) = 20as \cdot \frac{\sigma_{vb}\left(\hbar\omega\right)}{\sigma_{4f}\left(\hbar\omega\right)} \frac{\sigma_{4f}\left(105\,\text{eV}\right)}{\sigma_{vb}\left(105\,\text{eV}\right)} \tag{4.3}$$

The relative photoemission cross sections for W 4f and W 5p core levels and combined valence and conduction bands are evaluated both depicted in figure 63. Spectra recorded with narrowband synchrotron radiation are convoluted with a FWHM Gaussian of 5 eV to account for the increased spectral bandwidth and fitted using the same algorithm and wavepacket parameters as used for the broadband spectra recorded alongside the attosecond spectra. The scattering time delay $\Delta\tau_{scatt}$ does in fact not contribute to the time delay of the primary W 4f core

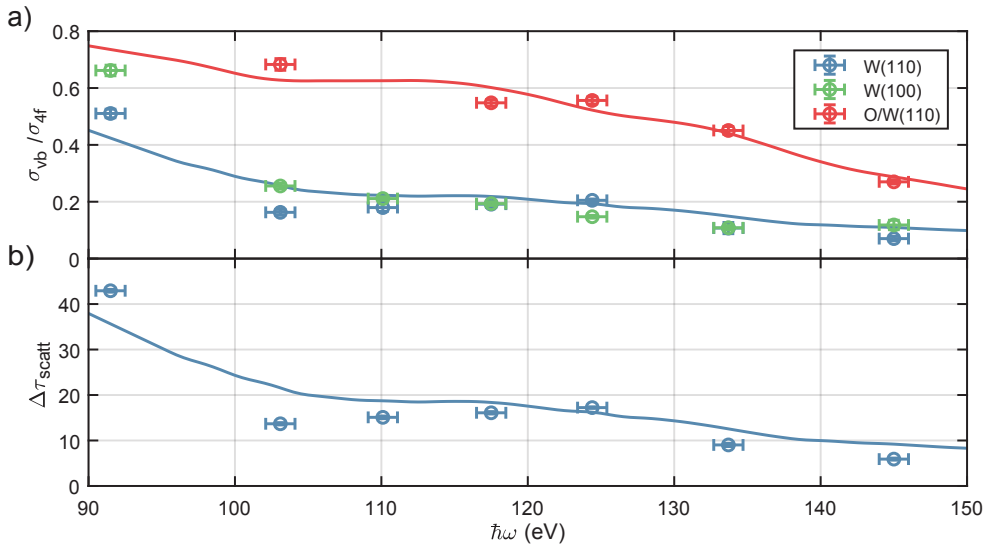

Figure 63 a) Relative subshell photoionization cross sections of the valence band w.r.t the 4f core levels extracted from static photoelectron spectra (see figures 46, 50 and 58). b) Contribution to net time delay of the finite spectral overlap of 4f photoemission with inelastically scattered electrons originating from the valence band extrapolated from the numerical result for W(110) at 105 eV [206].

level photoelectrons, but falsifies the measurement thereof and should be treated as systematic error instead. The true time delay of the photoelectron wavepacket is obtained by subtraction of the scattering delay. This outlines the importance of developing photoemission models beyond the approximation of the imaginary optical potential to correctly gauge, predict and disentangle the individual contributions to the attosecond time-energy distribution of condensed matter photoemission. However, for easier comparison with the experimental results presented above, the scattering delay is added to the attosecond time delays predicted by the classical and semi-classical transport models. Furthermore, it should be noted that the extrapolation of $\Delta\tau_{scatt}$ discussed here serves only as a rough estimation for W(110) and W(100) and cannot easily be applied to O/W(110), because the photoelectrons excited within the oxygen layer are much less likely to scatter inelastically before leaving the surface compared to electrons emitted in the tungsten bulk solid. This however is not a problem for the evaluations and model presented hereunder, because only the W(110) delay enters the comparison between experiments and numerical computations. It shall be noted here quickly that the scattering delay $\Delta\tau_{scatt}$ for Mg(0001) is negligible, because the magnesium electron loss function is small around energy transfers of $45-55$ eV and the photoemission cross section ratio σ_{vb}/σ_{2p} is much larger.

W(110)

In order to model the photoemission time delay it is necessary to assume or determine the depth from which the electrons, which ultimately reach the detector, are excited. We compare the high-resolution photoemission spectrograms recorded from W(110) and O/W(110) and using the rich literature on tungsten photoemission associate the relative contribution of the surface layer of tungsten atoms to different structures in the photoemission spectrogram. The valence band synchrotron photoemission spectrum of W(110) is decomposed into three contributions

with distinct spatial profiles (see figure 64).

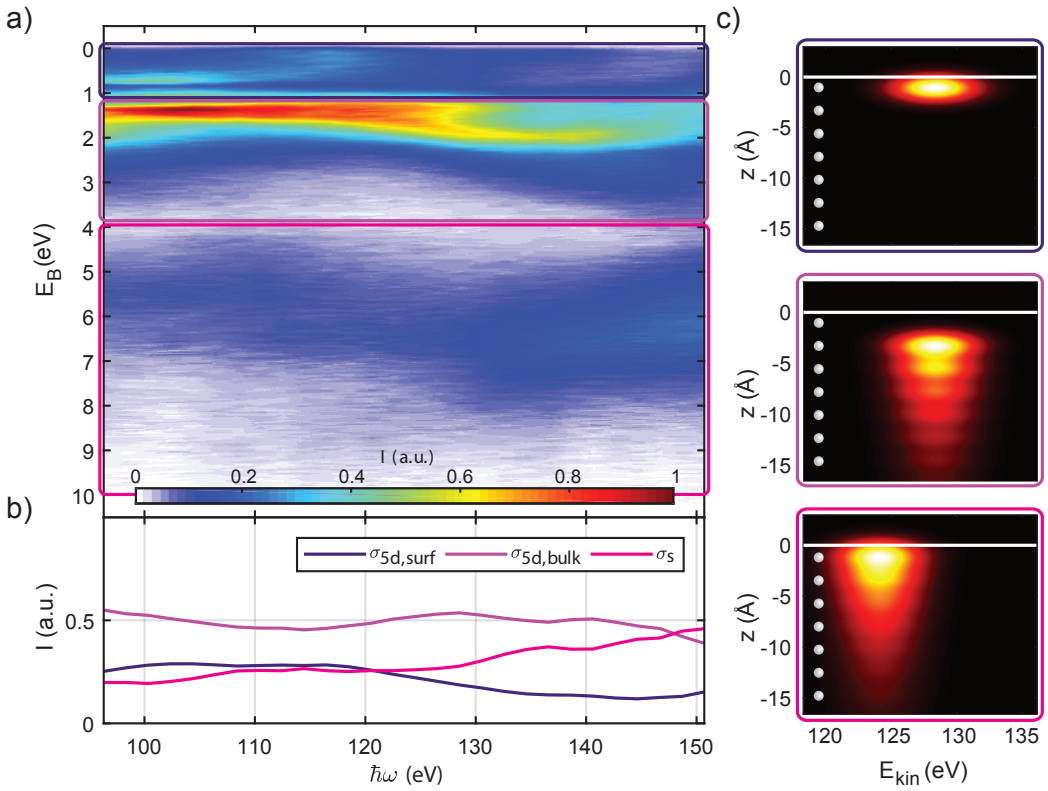

Figure 64 a) High-resolution valence band photoemission spectrogram from W(110). Purple boxes outline the integration region of the different contributions to the total photocurrent. b) Relative contribution of W 5d emission from surface atoms ($\sigma_{5d,surf}$), bulk atoms ($\sigma_{5d,surf}$) and the delocalized W 6s band (σ_{6s}) to the total valence band photocurrent. The assignment of the energy regions is discussed in the text. c) Spatial and kinetic energy distribution of photoexcited electrons reaching the TOF spectrometer immediately after photoabsorption. The inelastic scattering of the photoexcited electrons is introduced via the energy-dependent mean free path λ [205]. Grey balls indicate the position of the tungsten atomic layers. The white line marks the position of the jellium edge of the tungsten crystal.

A striking feature comparing valence band synchrotron energy-dependent photoemission spectrograms from W(110) and O/W(110) is that despite the large change of the surface core level shift (-321 meV $\rightarrow$ 681 meV) upon oxygen adsorption, the 4f binding energy of the second layer does not change [238]. This implies that only the surface atoms are significantly influenced by the partial charge transfer to the oxygen adatom residing in the trifold coordinated adsorption site. Analysis of the valence band photoemission reveals the dominant feature at binding energies between 1.25 eV and 2.5 eV to be very similar in shape for both W(110) and O/W(110) (see figures 64 and 66), which implies this feature to be associated with the W 5d emission from the bulk atoms. However, one study does suggest that also the peak at 1.35 eV binding energy at least in part to originates from a surface state, which shifts to 1.0 eV upon oxygen adsorption [233]. This association is the major source of uncertainty in the overall peak assignment. Photoemission from the region between the Fermi energy and 1.25 eV is known to be associated with surface resonances or surface states [239, 240, 241] and we associate the whole energy region with emission from the first atomic layer. The binding energy region beyond 4.0 eV is associated with the W 6s orbital, which is delocalized among all surface and bulk

tungsten atoms. The W 6p orbitals do not contribute significantly to the electronic structure of the tungsten valence band [97]. The spatial and kinetic energy density of photoexcited electrons reaching the detector without inelastic scattering inside the crystal is modelled according to the equations in section 3.4.2. Knowledge of the extrapolated scattering and EWS delays allows the predictions of the absolute and relative attosecond time delays for W(110) and O/W(110) according to the equations presented in section 3.4.2.

The resulting distributions of the starting positions along the W(110) surface normal and the initial kinetic energies of photoexcited electrons directly after photoabsorption are plotted in figure 64. Electrons with these initial conditions propagate along the surface normal with free-electron velocity accounting for the inner potential but neglecting the finite XUV pulse duration. The time delay is recovered as the instant of the classical electron crossing the jellium edge. It should be noted here that the elastic scattering as investigated in photoelectron diffraction experiments is ignored in the classical simulations, because the elastically scattered electron travels the same total distance within the crystal as in the case ignoring elastic scattering. Furthermore, at such high kinetic energies, elastic scattering takes place predominantly in forward direction with little momentum transfer. Results for both absolute and relative time delays of W(110) are depicted in figure 65.

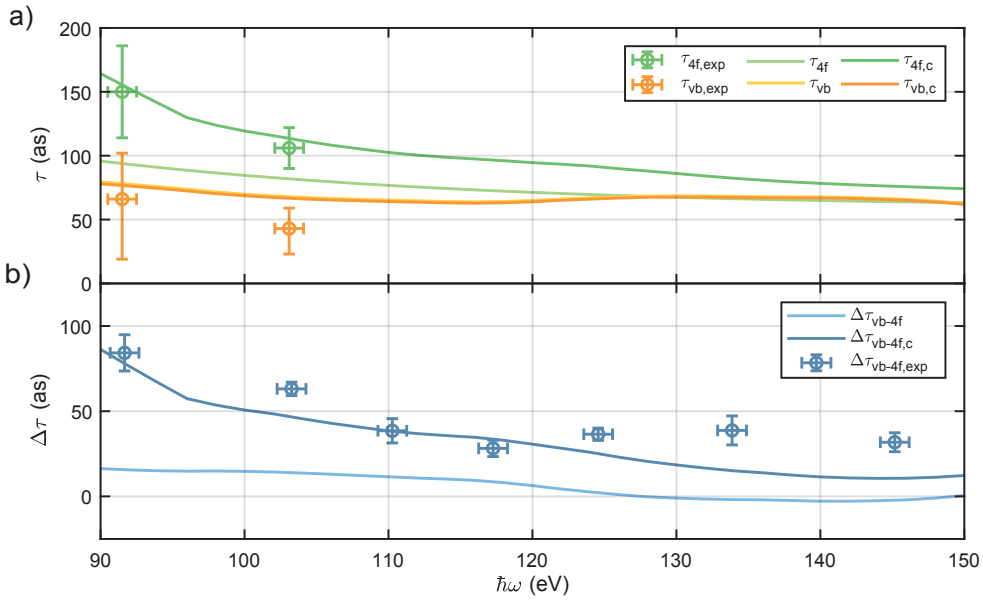

Figure 65 a) Absolute photoemission time delays of W4f core levels and valence band predicted from the classical transport model. The experimental absolute photoemission time delays of the W 4f orbital $\Delta\tau_{4f,exp}$ are transcribed from table 4. The valence band time delay is obtained by subtraction of the relative time delay of the clean surface $\Delta\tau_{4f-vb,exp}$ (see table 2) from the absolute W 4f time delay . Lightly coloured lines represent the pure transport time delay. Dark lines represent the predicted photoemission time delay with corrections from inelastic scattering and EWS delays taken into account. b) Same as a), but for the relative time delay between the W 4f core orbital and the valence and conduction bands.

The absolute time delay of photoemission of the W 4f orbital from the clean W(110) surface is determined from the zero-coverage extrapolation of the I/W(110) and iodine gas phase measurements and are well recovered by the simple calculation. It is noted that literature

results of the IMFP calculation vary considerably between 4.1 Å [205], used here for best agreement with experimental data, and 5.6 Å [97]. Measurements of the mean free path by means of photoelectron diffraction including the elastic scattering term [242, 35] suggest a value around 4 Å for the mean escape depth commensurable with the lower limit of the numerical calculations.

Absolute time delays of the valence band are obtained by subtraction of the relative time delay $\Delta\tau_{vb-4f}$ measured on the clean W(110) surface. The absolute delay of the valence band is lower than predicted by the classical transport model. An underestimation of the group velocity is highly unlikely, as calculations of the complex band structure and inverse LEED state of W(110) show no states at the energy region around 100 eV, which propagate faster than the corresponding free electrons [98]. It is thus much more likely that our spectral decomposition of the 5d band between binding energies 0 and 3 eV does either underestimate the contribution from surface states and resonances or misjudge their spatial distribution. The last point is exemplified by DFT calculations carried out by C. Lemell and F. Libisch, which show that certain surface states of W(110) are located outside the surface atom layer extremely close to the jellium edge and are consequently emitted within 11 as, largely unaffected by inelastic scattering [206].

The relative retardation of the W 4f photoelectron wavepacket is in qualitative agreement with the classical calculations. However, specific features, such as the local maximum at 135 eV, are not adequately reproduced in the calculations, which hints towards further important contributions to the attosecond time delays. The most likely culprit is the energy-dependent group velocity of the photoexcited electron in the high-energy conduction bands. The electron group velocity is defined in terms of the band structure (see equation 2.27). Calculations of the inverse LEED state and its decomposition into partial Bloch and evanescent waves [98] show a pronounced minimum of the group velocity of the outgoing electron wavepacket for final-state energies between 90 eV and 110 eV above the Fermi energy of the W(110) surface. This coincides well with the observed local maximum at 135 eV accounting for the 32 eV binding energy of the W 4f orbital. Then again, reduced group velocities around 100 eV imply longer photoemission delay times of the valence band at these energies, which contradict the experimental finding (see figure 65). The shorter photoemission time of the valence band might be explained by the different behaviour of localized and delocalized states around bandgaps in the final state band structure, which was investigated by E.E. Krasovskii et al. with a quantum mechanical solution to an 1D model potential inspired by the band structure of the tungsten crystal [99].

O/W(110)

Further corroboration of the link between the W 4f electron wavepacket retardation and the gap in the high-energy band structure around final state of 100 eV is found in the experimental trace of the energy-dependent photoemission time delay of O/W(110). The O/W(110) spectrum is

decomposed into bulk and surface contributions in the same manner as in case of the W(110) synchrotron photoemission data, accounting for an additional contribution of the bonding and non-bonding pairs of O 2p electrons and the results are depicted in figure 66.

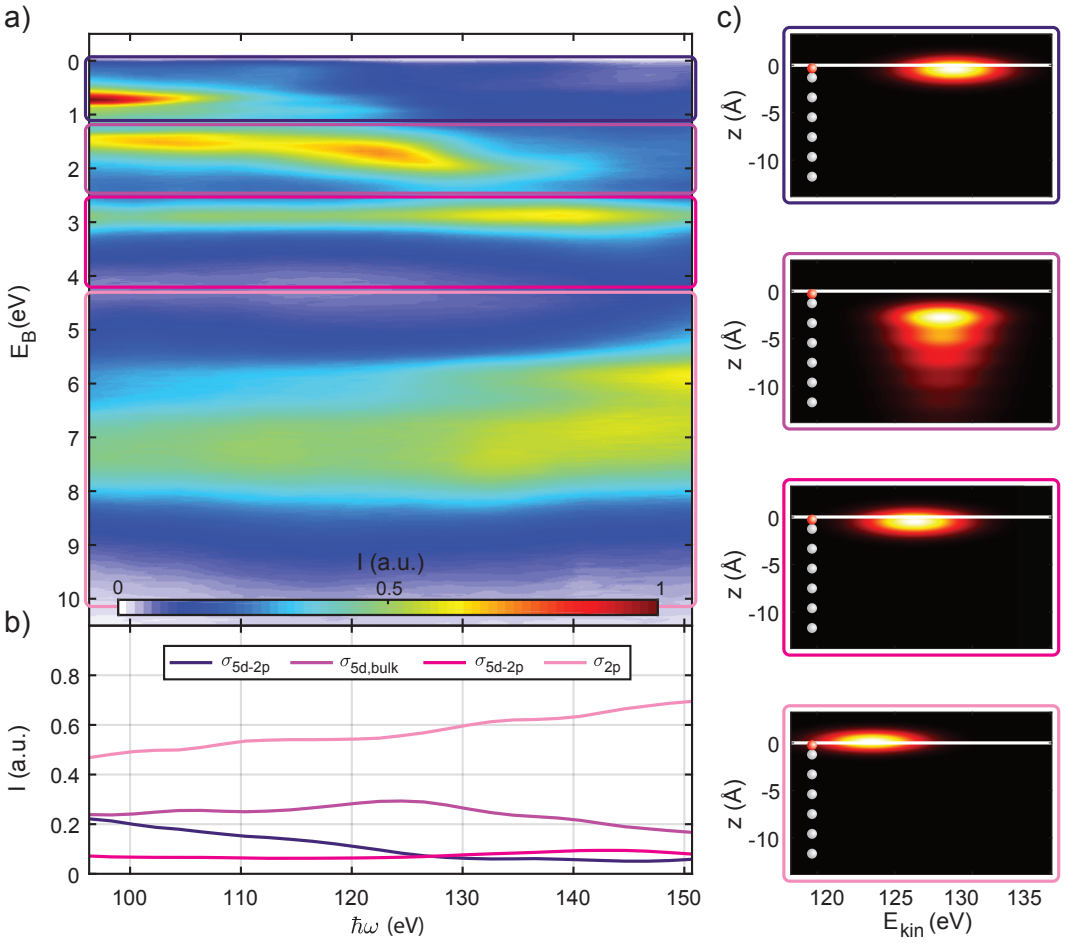

Figure 66 a) High-resolution valence band photoemission spectrogram from O/W(110). Purple boxes outline the integration region of the different contributions to the total photocurrent. b) Relative contribution of corresponding to W 5d emission from WO binding orbitals and W(110) surface resonances ($\sigma_{5d\text{-}2p}$), bulk atoms ($\sigma_{5d,bulk}$) and the delocalized W 6s band (σ_{6s}) to the total valence band photocurrent. c) Spatial and kinetic energy distribution of photoexcited electrons, which reach the TOF spectrometer at the end of their trajectory, immediately after photoabsorption. The inelastic scattering of the photoexcited electrons is introduced via the energy-dependent mean free path λ. Grey balls indicate the position of the tungsten atomic layers. Red balls locate the oxygen adlayer. The white line marks the position of the jellium edge of the tungsten crystal.

The bulk contribution to the W(110) valence band is again observed in the binding energy region between 1.25 eV and 2.5 eV but with about 25% reduced intensity. This is in accordance with increased inelastic scattering of the photoelectron passing through the oxygen adlayer. An additional peak is observed at binding energy 3 eV irrespective of photon energy. This peak is not observed for clean W(110) because the non-relativistic transition matrix element is zero for this part of the band structure due to symmetry [233]. The oxygen adsorption breaks the symmetry and results in a rearrangement of the charge density towards the surface. This type of electronic state is called a split-off band and can be understood as the binding orbital of the WO molecule. In our decomposition this band is located within the oxygen layer and the surface tungsten layer alongside the band between the Fermi edge and binding energy 1.25 eV,

which is enhanced upon oxygen adsorption. It is thus conceivable that the surface resonances mix with the O 2p states to form the chemical bond. The last region of interest are binding energies in excess of 4.25 eV, which are associated with the remaining O 2p orbitals. The weak tungsten 6s orbital is neglected as it contributes less than 10% to the observed photocurrent in this energy region due to the high cross section of the O 2p orbital. The results of the classical transport calculation for the O/W(110) surface are compiled in figure 67. Again, light colouration represents the calculated electron TOF to the jellium edge, and dark colouration represents the total time delay accounting for the EWS delay and the inelastic scattering.

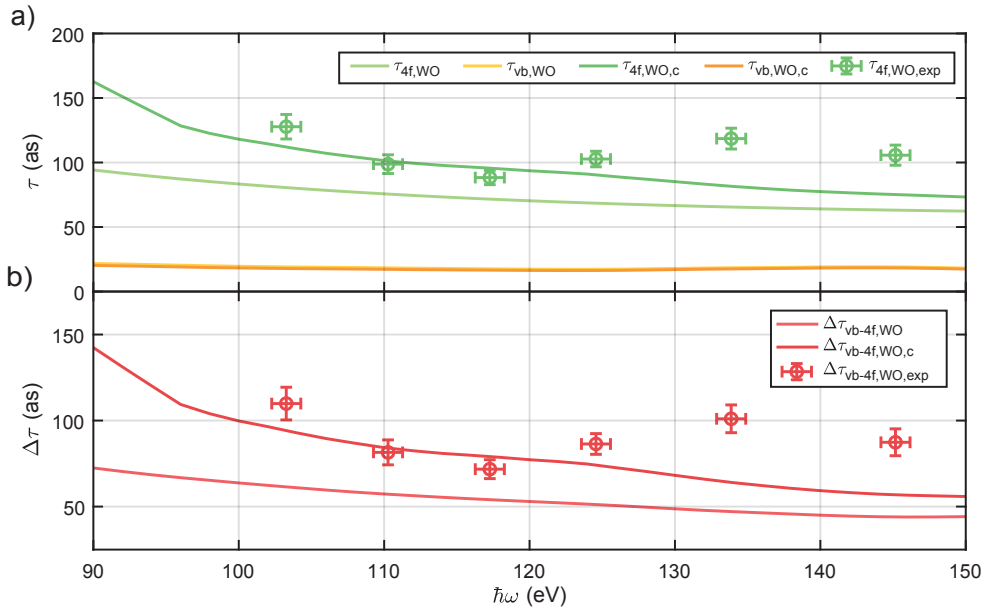

Figure 67 a) Absolute photoemission time delays of W4f and valence band predicted from the classical transport model. The experimental absolute photoemission time delays of the W 4f orbital $\Delta\tau_{4f,WO,exp}$ are obtained from table 5) accounting for the nearly constant time delay of the valence band of about $12-14$ as. Lightly coloured lines represent the pure transport time delay. Dark lines represent the predicted photoemission time delay with corrections from inelastic scattering and EWS delays taken into account. b) Same as a), but for the relative time delay between the W 4f core orbital and the valence and conduction bands.

Again, quantitative agreement between the calculation and the experimental data is found in the photon energy region between 110 eV and 120 eV (see figure 67 b). For measurements outside this interval the classical model underestimates the photoemission time delay similar to the case of W(110). The position of the jellium edge is unchanged w.r.t. the calculations, which is motivated by DFT calculations predicting non-zero density-of-states at the Fermi energy and thus metallic character already within the first layer of tungsten atoms [229, 213]. Surprisingly, within our calculations, the time delay of the combined O/W(110) valence band $\tau_{vb,WO}$ does not change by more than 2 as over the full spectral range. This, along with the small change of W 4f time delay for varying iodine adsorption, motivates the calculation of the absolute time delay of photoelectrons from the W 4f orbital by adding the calculated $\tau_{vb,WO}$ to the experimentally determined relative time delay for O/W(110) $\Delta\tau_{vb-4f,exp}$.

Absolute time delays

Combining the experimental results for I/W(110), O/W(110) and W(110) we can extract the absolute photoemission time delays of both the photoelectron wavepackets originating from the W 4f core level as well as from the W(110) conduction band (see figure 68).

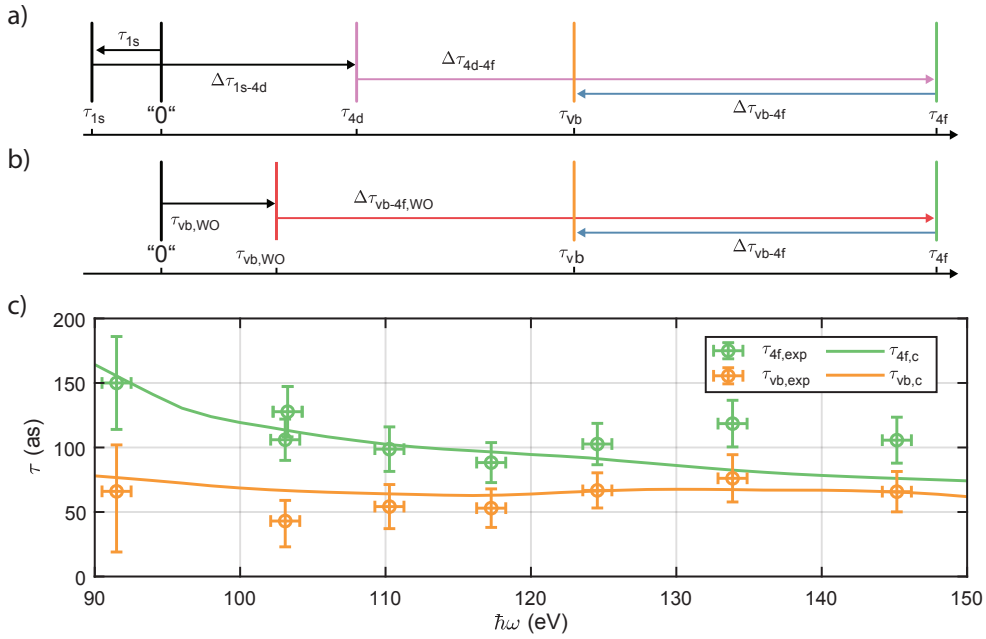

Figure 68 Temporal ordering schematics and experimental values of the absolute photoemission time delays of W 4f core level and valence band of the W(110) surface. a) Time-ordering of the atomic chronoscope method implemented with atomic iodine ($\hbar\omega < 105eV$). The absolute photoemission time delays are linked to the theoretically predicted and experimentally verified time delay of the 1s orbital of atomic helium via a series of attosecond streaking measurements. b) Time-ordering of the absolute time delay calibration using adsorbed oxygen ($\hbar\omega > 105eV$). The time delay absolute time delay of the O/W(110) valence band is dominated by the above surface O 2p contribution and is estimated using classical transport calculations. The absolute time delays of the W 4f τ_{4f} and valence bands τ_{vb} are determined by adding/subtracting the experimentally determined relative time delays for O/W(110) and W(110), respectively. c) Absolute time delays of photoemission of W(110). Predictions from the classical transport model (light color), corrected for the intra-atomic EWS delay and inelastic scattering delay (dark color) are depicted as solid lines.

The error bars in figure 68 are increased by 11 as w.r.t. the experimentally determined relative time delay confidence intervals of O/W(110). This is is equal to the range of the variation of the W 4f time delay upon adsorption of the saturated iodine monolayer. Hence, these increased confidence intervals constitute a conservative estimate of the uncertainty of the oxygen adlayer on the photoemission time delay of the W 4f core level. No core level excitations or other resonant photoemission features are known in the photon energy range between 110 eV and 150 eV for W 5d or O 2p, which could induce strong deviations of the O/W(110) photoemission time delay [235]. The absolute time delay of the valence band is again obtained by subtracting the relative time delay determined on the clean surface from the absolute delay of the W 4f photoemission. The absolute time delays at 91.5 eV and 103.1 eV are directly determined from the I/W(110) and W(110) measurements (see figure 68 a)

$$\tau_{4f,W} = \tau_{4d} + \Delta\tau_{4d-4f}(\theta = 0)\,, \tag{4.4}$$
$$\tau_{vb,W} = \tau_{4f,W} - \Delta\tau_{vb-4f,W}\,.$$

At photon energies above 103.1 eV, the absolute time delays are determined by adding the relative time delay of the oxygen covered W(110) surface to the calculated values for the valence band $\tau_{vb,WO}$. Corrections due to the inelastic scattering are not necessary for conduction band photoemission. The EWS delay of the oxygen 2p orbital is around 1 as, which can be gauged from the calculations for the Mg 2p orbital (see figure 33) by shifting the curve by the difference in binding energy between different 2p core levels (see figure 68 b)

$$\begin{aligned} \tau_{4f,W} &= \tau_{vb,WO} + \Delta\tau_{vb-4f,WO}\,, \\ \tau_{vb,W} &= \tau_{4f,W} - \Delta\tau_{vb-4f,W}\,. \end{aligned} \tag{4.5}$$

The two determination methods disagree by about 20 as at photon energy 103.1 eV, which is a further hint at an overestimation of the valence band photoemission times around the high energy band-gap of the W(110) surface, as already discussed above. The direct determination of the photoemission time delay from the I/W(110) coverage is deemed much more reliable, because no spectral decomposition of the synchrotron spectrogram or assumptions about the high-energy band structure are necessary. For higher-energies the photoemission from O/W(110) is more and more dominated by the oxygen 2p orbital and the reliability of the classical calculation strongly increases. This reduces the overall influence of the uncertainties of the IMFP and the group velocity on the calculated valence band time delay, because a stronger portion of the wavepacket is released already above the jellium edge of the W(110) surface and instantaneously interacts with the NIR streaking field. Riffe et al. report that the W 4f photoelectrons originating from the bulk are diffracted in the oxygen adlayer mainly in forward direction [238, 232], thus experiencing only minute changes of their trajectories, which further corroborates the comparability of core level emission for W(110) and O/W(110). The resulting absolute time delays quantitatively agree with the experiment in the range between 110 eV and 120 eV. The pronounced local maximum around 135 eV is not predicted by the CTT calculation. This suggests a reduced group velocity of the outgoing electron wavepackets around final state energies of 100 eV in agreement with calculations of the inverse LEED state by E.E. Krasovskii [98]. Furthermore, we find that valence band states behave counter-intuitively around the final-state energy region at 100 eV and an advancement of the photoelectron wavepacket is observed instead of the expected retardation, which is also in qualitative agreement with a 1D TDSE calculation with a model potential inspired by the high-energy band structure of W(110) [98, 99]. These hypotheses can be numerically investigated using the semi-classical model of time-resolved photoemission discussed below.

4.5.3. Semi-classical Model

Having established the qualitative connection between the high-energy complex band structure and the observed photoemission time delays for core levels, we further investigate its influence by inserting the z-projected inverse LEED state wavefunction as final state into the semi-classical model (see section 3.4.4). Because of the weak optical potential assumed in the DFT calculation

of the inverse LEED states, the correct inelastic damping of the wavefunctions along the surface normal was empirically applied by multiplication of an energy-dependent exponential damping according to the IMFP [205]. Z-projected final state wavefunctions of W(110) for a few select energies are depicted in figure 69.

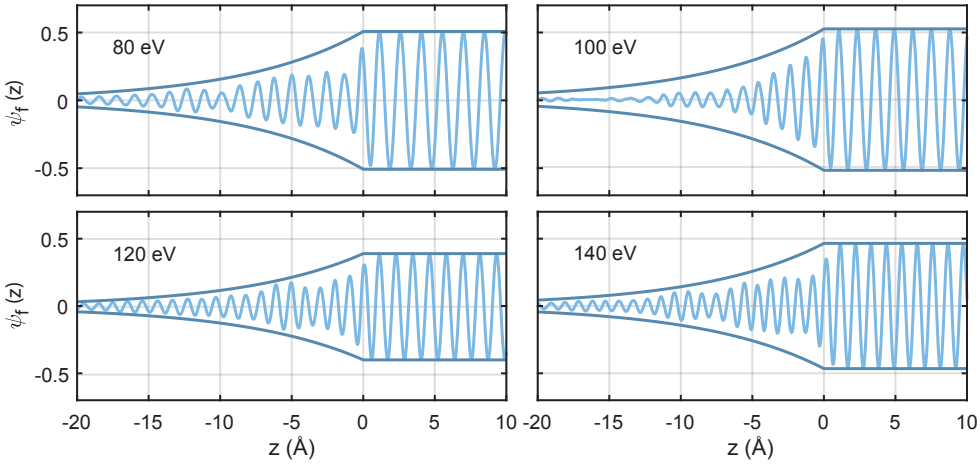

Figure 69 Z-projected inverse LEED wavefunctions of W(110) at select final state energies. The final-state energy is noted in the top left of each panel and referenced to the Fermi energy ($E - E_F$). The dark lines show the energy-dependent exponential damping envelope according to the IMFP [205]. The step-like reduction of the wavefunction amplitudes is indicative of the reflection of the electron wave at the solid-vacuum interface.

The inverse LEED wavefunctions are calculated from the complex band structure of the bulk tungsten crystal and composed of partial evanescent and propagating Bloch waves matched with propagating free-electron waves outside vacuum in a variational ansatz with the $\vec{k} \cdot \vec{A}$ method [123]. The final-state wavefunction at 100 eV is different from the rest as it appears to be uniquely composed of a single evanescent wave damped inside the crystal much more strongly compared to common expectation from IMFP calculations. Indeed this energy range coincides with the pronounced minimum of the group velocity as discussed above. This is indicative of a bandgap along the $\Gamma - N$ symmetry line in reciprocal space. At final-state energies outside of the minimum between 90 eV and 110 eV, the behaviour mimics the expected exponential damping, with a step at $z = 0$ indicative of the reflection/transmission of the outgoing electron wavefunction, which protrudes deep into the crystal bulk.

Initial state wavefunctions for bound valence and conduction band states are generated from a Chulkov-like model potential [200] according to equation 3.20. The parameters of the Yukawa potential used to generate wavefunctions of the 4f core levels are $\zeta = 1.23$ Å and $a_y = 0.159$ Å, instead of the values given by Liao et al. [200], which result in a 3 eV broad, partly delocalized W 4f core level incompatible with the experimental observation of narrowband 4f photoemission spectra. These effective one-electron potentials along the associated highest and lowest-energy initial states of the 4f core and combined valence and conduction bands and their band integrated charge densities are depicted in figure 70.

In our first semi-classical simulation, the electrons propagate towards the jellium edge at

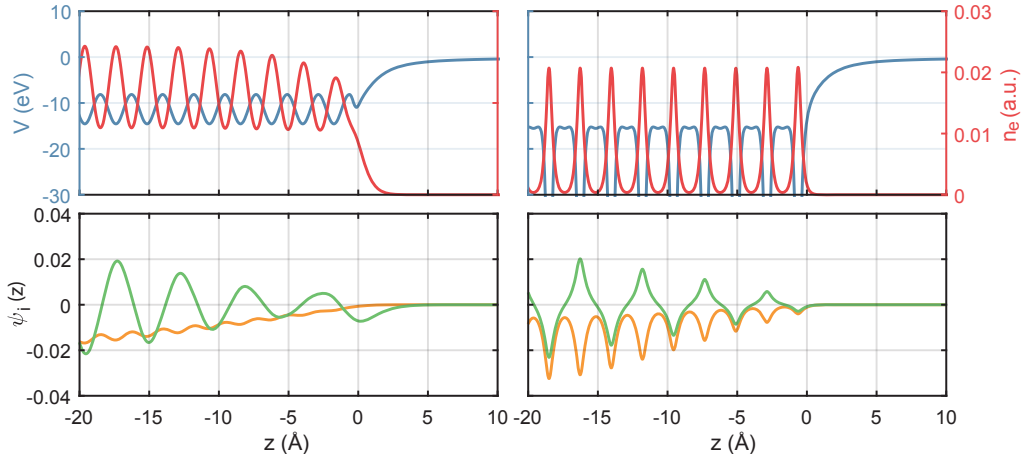

Figure 70 Top: Effective one-electron potential (blue) and integrated charge density of the initial states of the combined valence and conduction band states (left column) and the 4f core level (right column) around the crystal surface. Bottom: Lowest (orange) and highest (green) energy bound state wavefunctions.

free-electron like velocities (see equation 2.28). The spatial dependence of the NIR field on the atomic scale interface is known from TDDFT simulations [25]. The resulting attosecond streaking spectrograms are evaluated with the same methods as the experimental data. The experimental data is convoluted with a 4.5 eV FWHM Gaussian function to mimic the spectral broadening of the final states for realistic optical potentials. Because the NIR streaking field is known a priori in the simulation, absolute time delays can be evaluated straightforwardly by comparing the retrieved optical waveform with the input pulse. The details of the numerical simulation and tests of the numerical convergence are detailed in appendix F. The results of the delay extraction are depicted in figure 71.

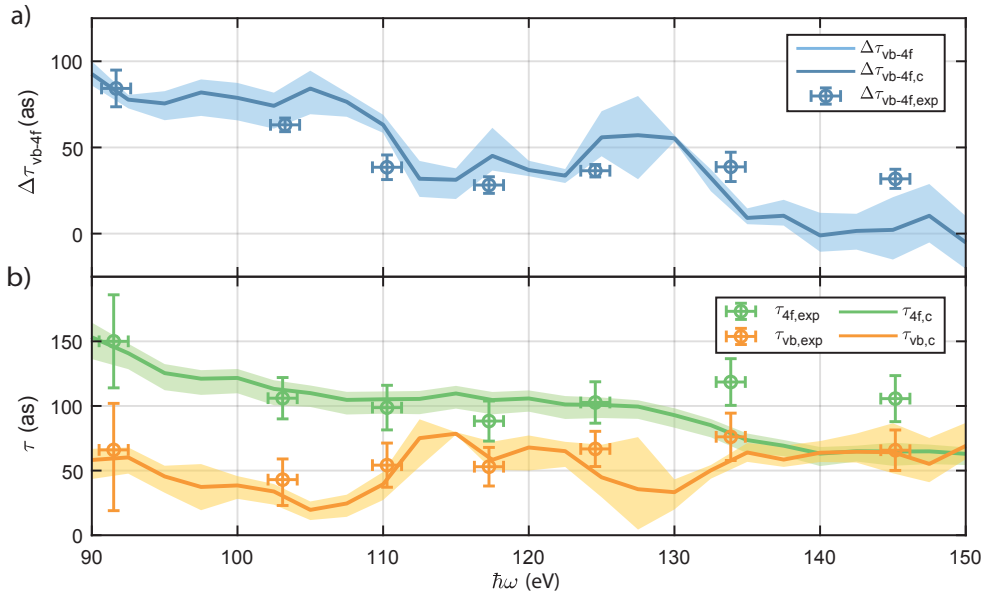

Figure 71 a) Relative photoemission time delay calculated with the semi-classical model (solid line) of photoemission and their comparison with experimental results (markers). The shaded area marks the variation in delay results obtained with different retrieval methods as outlined in the text. b) Same as a), but for absolute photoemission time delays of W 4f core level (green) and W(110) valence band (orange).

Additional retardation of the W 4f photoemission due to the inelastic scattering and the EWS, which are not evaluated within this simple 1D model are added to both the simulated curves of the relative time delay as well as the W 4f absolute photoemission time delay similar to their treatment in the classical transport model. We note that the semi-classical calculation of the relative and absolute time delays does not depend on the specific decompositions of the synchrotron spectrogram as in case of the classical transport model. The advancement of the valence band electron wavepacket around the bandgap is well matched within the experimental and numerical accuracies. The decrease of the penetration depth of the scattering wavefunction of the final-state is thus directly and unambiguously linked to the observed advancement of the photoemission of the delocalized state in agreement with the predictions from [99].

The retardation of the W 4f photoemission at final-state energies in the bandgap, however, is not matched by the simulation. This motivates further investigation of the energy-dependent effective group velocity of the photoelectron wavepacket. Calculating the inverse LEED-wavefunction in terms of a partial wave decomposition based on the complex band structure, i.e. the electron Bloch and evanescent waves, carries the advantage of accessing specific properties, such as the group velocity v_g of the electron wavepacket, directly. The result of the DFT calculation of the inverse-LEED state for a realistic optical potential of 4.0 eV is plotted in figure 72.

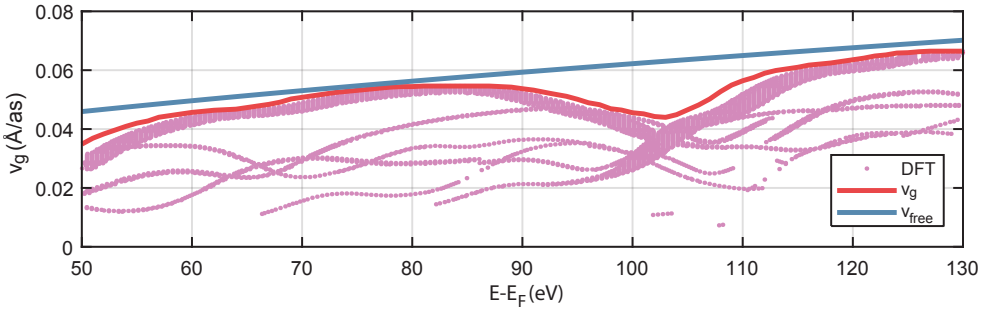

Figure 72 Group velocities of the inverse LEED state. The velocity of free electrons inside the solid is depicted as solid blue line (see equation 2.28). The purple dots mark the group velocity of individual Bloch states. The thickness of the line is proportional to the contribution of the individual partial wave to the total photocurrent. The group velocity of the strongest partial wave is marked in red and introduced into the semi-classical calculations. Electron energies beyond the simulation range are assumed to be free electron-like.

The details of the calculation by E.E. Krasovskii can be found in [122, 123, 98]. The thickness of the purple line is proportional to the contribution of the partial wave to the outgoing photocurrent. The fastest partial waves carry the strongest contribution to the photocurrent, because they are least affected by the elastic and inelastic scattering. The energy axis is referenced to the Fermi level and final state energies outside the calculation window are approximated with the free electron velocity. The results for the adjusted relative and absolute time delays are compiled in figure 73.

Accounting for the energy-dependent group velocity of the final state, we find up to 20 as additional retardation of the W 4f group delay around 135 eV. The retardation of the valence band photoelectrons around 100 eV, however is below 10 as, because of the diminished

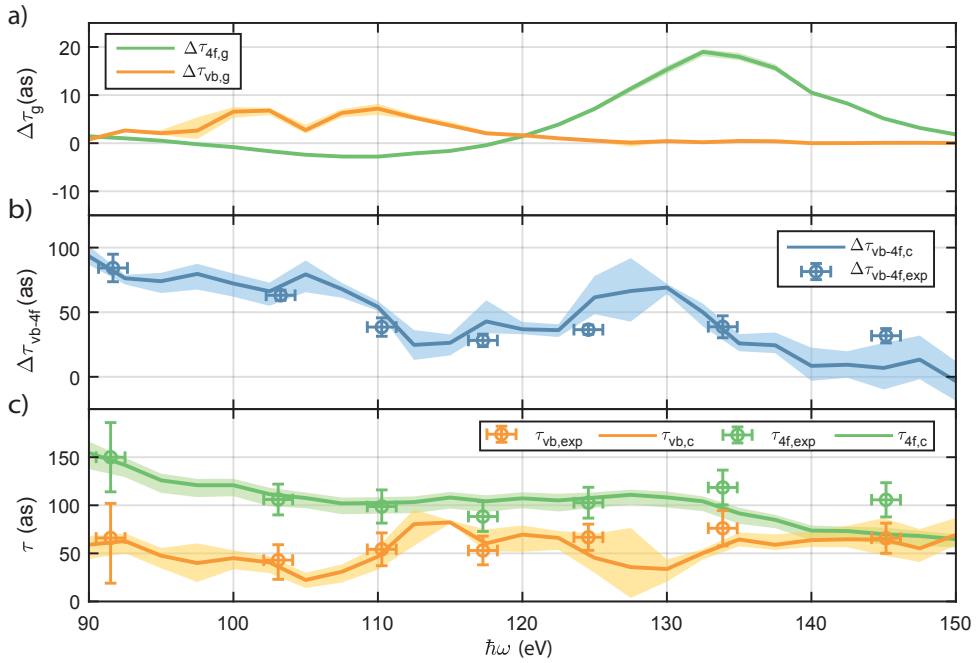

Figure 73 a) Deviation of absolute photoemission time delays accounting for the energy-dependent group velocity of the time-reversed LEED state. b) Relative photoemission time delay calculated with the semi-classical model accounting for the energy-dependent group delay (solid line) of photoemission and their comparison with experimental results (markers). c) Same as b), but for absolute photoemission time delays of W 4f core level (green) and W(110) valence band (orange).

penetration depth of the final state around the high-energy bandgap. The overall agreement improves considerably both in case of the relative and the absolute time delays from which we conclude the importance of calculating and applying the correct group velocity and scattering wave functions in numerical simulations of the attosecond time delay problems. The relative and absolute time delays retrieved from the numerical calculations bear striking quantitative agreement with the experimental data up to photon energies of 135 eV. At photon energies beyond 135 eV, the time delay of the photoemission from W 4f is overestimated by 30 as. One shortcoming of our model, which might be also linked to this observation is the usage of initial states from a model potential and not from proper DFT calculations, which are not orthogonal with the z-projected inverse-LEED final states, thus weakening the applicability of the perturbation approach to the calculation of the photocurrent.

4.6. Conclusion

Summarizing both the experimental efforts on clean and adsorbate covered W(110) we can quantitatively dissect the contribution of the individual microscopic mechanisms that constitute the retardation of the outgoing photoelectron wavepackets w.r.t. to the arrival of the ionizing XUV attosecond pulse at the W(110) surface. The absolute time delay of the 4f core orbital, complied in table 6, is almost constant and the apparent energy-dependent change of the time delay can be mostly traced back to the spectral overlap with inelastically scattered photoelectrons emitted

from the W(110) valence band with energy loss close to the binding energy of the 4f level. The true time delay between the arrival of the XUV pulse and the appearance of the photoelectron in vacuum is found by subtracting $\Delta\tau_{scatt}$ from the measured absolute time delay $\tau_{4f,exp}$.

$\hbar\omega$ (eV)	91.5	103.1	110.1	117.1	124.4	133.7	145.0
$\tau_{4f,exp}$ (as)	150 ± 36	106 ± 16	99 ± 17	88 ± 16	103 ± 16	119 ± 18	106 ± 18
$\tau_{4f,c}$ (as)	147 ± 12	111 ± 9	102 ± 9	105 ± 9	107 ± 8	98 ± 8	70 ± 9
$\Delta\tau_{scatt}$ (as)	50	22	17	16	15	10	7
$\tau_{4f,EWS}$ (as)	15	12	11	10	9	7	7
$\tau_{4f,ball}$ (as)	83	77	74	72	70	69	68
$\tau_{4f,cbs}$ (as)	-1 ± 12	0 ± 9	1 ± 9	7 ± 9	13 ± 8	12 ± 8	-11 ± 9

Table 6 Individual contributions of the different microscopic mechanisms to the absolute photoemission time delay of the W(110) 4f core level.

The situation is quite different for the conduction band, for which a considerable reduction of the absolute time delay is observed in proximity to the high-energy gap in the complex band structure. The results for the absolute time delay of the conduction band are compiled in table 7. The scattering and EWS delay of the high-energy conduction band photoemission and the is neglected in accordance with [97] and [32], respectively.

$\hbar\omega$ (eV)	91.5	103.1	110.1	117.1	124.4	133.7	145.0
$\tau_{vb,exp}$ (as)	66 ± 47	43 ± 20	54 ± 17	53 ± 15	67 ± 14	76 ± 18	66 ± 16
$\tau_{vb,c}$ (as)	61 ± 11	36 ± 9	48 ± 12	64 ± 10	50 ± 18	57 ± 6	64 ± 19
$\tau_{vb,ball}$ (as)	71	66	64	62	61	60	60
$\tau_{vb,cbs}$ (as)	-10 ± 11	-30 ± 9	-16 ± 12	2 ± 10	-11 ± 18	-3 ± 6	5 ± 19

Table 7 Individual contributions of the different microscopic mechanisms to the absolute photoemission time delay of the W(110) valence and conduction bands.

The semiclassical model agrees very well with the experiment with the exception of the data point at 145 eV. The good agreement between the numerical calculations, restricted to the surface normal so far, and the experiments, integrated over the whole first Brillouin zone with the electrostatic lens, is at first surprising and encourages further study and refinement of the employed semiclassical model of photoemission. This could feasibly be achieved by inclusion of true ab-initio initial states obtained from contemporary DFT codes as well as using Monte-Carlo transport integration of the electron trajectories.

Part V

Summary and outlook

Summary and outlook

The observation of the relative time delay between the localized tungsten 4f core level and the delocalized conduction band established a whole new and highly active field of ultrafast metrology of fundamental light-matter interactions. This work aims at establishing a comprehensive understanding of the essential microscopic mechanisms that constitute the resulting time delay between XUV photon absorption and the appearance of the electron in the vacuum. To this end, extensive experimental campaigns were undertaken to extend the existing knowledge and experiments around photoemission timing spectroscopy beyond single energy, relative time delay measurements using the attosecond streaking technique. Herein, the instance in time of the electron traverse over the metal-vacuum interface is measured by recording the modulation of the momentum induced by the Lorentz force of the NIR field, which is precisely synchronized with the isolated attosecond XUV pulse acting on the electron. The instance in time of the photoabsorption is determined by the arrival of the XUV pulse center at the metal-vacuum interface. Relative photoemission time delays are recorded by comparing the time delay of the momentum modulations as function of the XUV-NIR time delay. The absolute time delays of the W 4f core level and the combined valence and conduction band remain unknown. Over the years, a plethora of theoretical models ranging from classical transport theory to semiclassical and quantum-mechanical one-dimensional model systems were implemented, which identified a wide range of microscopic mechanisms for the observed time delays. A comprehensive quantitative modelling of the individual contributions of the attosecond time delay and its comparison with experimental results is lacking so far. Although significant progress has been achieved in the theoretical and numerical modelling of attosecond chronoscopy of solid samples, a time-resolved one step theory, i.e. a direct integration of the time-dependent Schrödinger equation of the attosecond chronoscopy problem in three dimensions is hitherto not computationally not feasible.

The first major result presented in this thesis is the identification of the effect of resonant and non-resonant excitation pathways and their relevance to the photoemission time delays in magnesium. This mechanism was proposed by A.G. Borisov et al. and using their model of time-resolved photoemission, can be related directly to the electronic structure of the initial and final states of photoemission. A key step realized within this thesis is the extension of attosecond streaking from a single frequency measurement towards a broadband energy-dependent spectroscopy. This is realized by utilizing a set of four different XUV multilayer mirrors in the AS-3 beamline and by repeating the measurements to achieve statistical experimental uncertainties in the 10 as range.

Pushing energy-dependent attosecond streaking spectroscopy one step further, extensive measurements of different clean and adsorbate covered tungsten single crystalline surfaces

were undertaken to extend the bandwidth of attosecond chronoscopy on tungsten from 90 eV to 145 eV. In total, measurements with seven different XUV multilayer mirrors were recorded. While such an extensive effort might strike as unreasonable on first glance, it not without this large dataset that quantitative dissection of the results of solid state chronoscopy would be realized for both relative and absolute time delays for the first time. Extending attosecond chronoscopy to absolute time delays is possible by applying well defined adsorbate layers of iodine and oxygen on the W(110) surface. The iodine 4d core level is located entirely outside the metal and serves as an excellent reference of the arrival of the XUV pulse on the sample surface. However, two auxiliary measurements had to be performed in order to demonstrate the ability and accuracy of the determination of the absolute time delay via the surface adsorbate method. First, the effect of the adsorbate overlayer on the tungsten 4f time delay has to be gauged. To this end, partial desorption and in-situ XUV photoemission spectroscopy have been applied to generate well-defined sub-monolayer coverages of iodine atoms on the tungsten substrate down to 1/4th of the saturation coverage. Subsequent, extrapolation towards zero iodine coverage reveals that iodine overlayer only increases the tungsten 4f photoemission time delay by 10 as, owing to the dielectric property of the atomic iodine adlayer and the penetration of the streaking field.

Secondly, strong intra-atomic interactions of the outgoing photoelectron wavepacket with the remaining 4d subshell give rise to the giant dipole resonance. While this enhancement of the photoemission cross section around 100 eV photon energy is crucial in the aforementioned measurements of small coverage iodine adlayers, additional intra-atomic between the arrival of the XUV pulse at the position of the iodine atom and the release of the photoelectron wavepacket is expected due to the increased intra-atomic interaction. Hence, measurements of the absolute time delay were performed using mixtures of helium and small iodine-substituted alkanes by M. Ossiander et al.. Combining all three measurements, we can determine the absolute time delay of the W 4f orbitals and the combined valence and conduction bands on the solid samples. Because of the rapidly diminishing photoemission cross section of I 4d for photon energies beyond 110 eV, this method of absolute delay determination is limited in bandwidth. High-resolution photoemission spectroscopy with energy-tunable narrowband synchrotron radiation was carried out for W(110) and O/W(110). Valence band photoemission is decomposed into bulk and surface contributions, which serve as inputs to a simple classical transport calculation. Strikingly, the valence band delay of the O/W(110) is almost constant. Knowing both the influence of the iodine overlayer and the valence band delay of O/W(110), the absolute time delay of the W 4f orbital can be deduced. The absolute time delay of the valence band follows by subtracting the relative time delay recorded on the clean W(110) surface. Hence, absolute photoemission time delays of the core and valence band states of W(110) from 90 eV to 145 eV have been determined.

Comparing these time delays to our semi-classical model using z-projected inverse LEED states in the calculation, we find widespread quantitative agreement between experiment and

theory. Both the effect of valence band photoemission advancement due to the reduced penetration depth of the scattering final state wavefunction, as well as retardation of the core level photoemission because of reduced group velocities around the high-energy bandgap, are experimentally confirmed. Furthermore, we can quantitatively judge the contributions of the high-energy band structure, inelastic scattering and the Eisenbud-Wigner-Smith scattering phase. To our knowledge, this marks the first study to not only determine a single contribution to the scattering time delay, but quantitatively address the full photoemission process from the intra-atomic interaction within the parent atom, to the contributions of transport, scattering and reflection of the outgoing photoelectron wavepacket within the high-energy complex band structure of the crystal. The semi-classical model presented here guides our steps towards more complete numerical models of time-resolved photoemission using Monte-Carlo simulations to solve the classical transport equations including elastic and inelastic scattering and Kohn-Sham quasiparticle wavefunctions for initial and final states capturing and dissecting all the intricate electronic structure probed by the attosecond chronoscopy techniques.

The time delay of photoemission is complementary to the photoemission cross section as is the quantum-mechanical phase to the probability density. Knowing both, opens up new pathways into photoelectron spectroscopy and the many-body system underlying the physical behaviour of dilute and condensed matter. Fully learning and modelling the absolute attosecond time delays opens up the investigation of more intricate systems, i.e. strongly-correlated systems like topological insulators or superconductors such as cuprates or other low temperature phase transitions.

Part VI

Appendix

A. Calibration of the TOF spectrometer

A typical measurement of attosecond chronoscopy has a total spectral bandwidth exceeding 50 eV at central kinetic energies of around 100 eV. Such large absolute and relative bandwidth can only efficiently be measured with the time-of-flight (TOF) technique, wherein non-relativistic electrons of different kinetic energies are dispersed along a fixed length in field-free propagation. This necessitates the use of a short pulse excitation source, i.e. a picosecond or femtosecond laser or electron gun. For all attosecond measurements presented in this work, a commercial TOF spectrometer from Stefan Kaesdorf, Geräte für Forschung und Industrie (see figure 74), which was custom designed and built to fit into the large experimental chamber, was utilized.

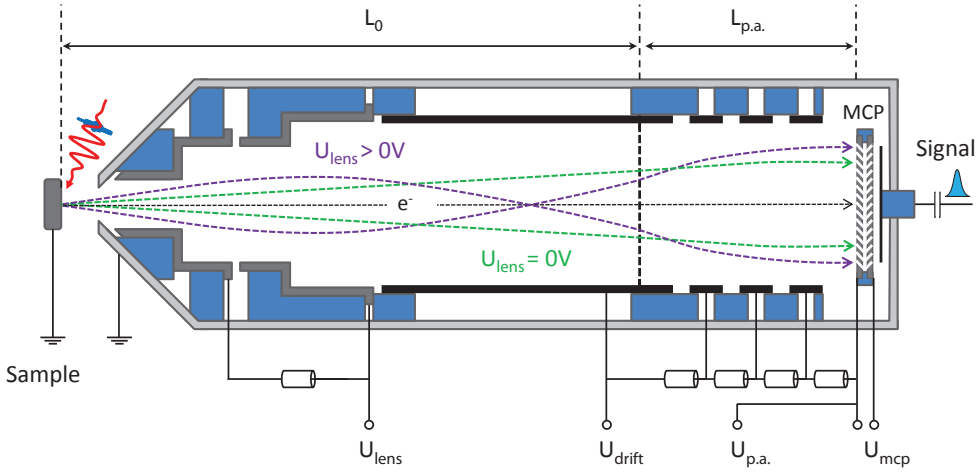

Figure 74 Schematic of the employed time-of-flight (TOF) spectrometer. Depending on the (positive) voltage U_{lens} applied to the electrodes of the electrostatic lens, the collection efficiency can be enhanced for electrons within a certain kinetic energy range by increasing the effective acceptance angle up to $\pm 2.4°$. The regular acceptance angle for $U_{lens} = 0$ is $\approx \pm 2°$ (determined by the diameter of the MCPs and the length of the drift tube). Adapted from [35].

The spectrometer consists of a μ-metal shielded field-free drift section of $L_0 = 425$ mm and a post-acceleration section of length 70 mm. The post-acceleration to 800 V ensures energy independent electron detection efficiency. The first part of the field-free drift section is outfitted with an additional set of cylindrical electrodes constituting an electrostatic Einzel lens, which can be used to increase the cone angle of detection for electrons emitted from the sample from $\pm 2.3°$ up to $\pm 22°$ (see figure 75 c)).

In order to retrieve accurate photoelectron spectra we need to determine to two constants t_0, which is the arrival time of the laser pulse in the interaction region, and the length L_0 of the free flight path of the electrons.

$$E_f = \Delta\Phi + \frac{1}{2} m_e v^2 = \Delta\Phi + \frac{m_e L_0^2}{2(t - t_0)^2}, \tag{A.1}$$

with $\Delta\Phi$ denoting the work function difference between the target and the detector [112]. The

arrival time of photons t_0, sometimes called prompt, can be measured accurately from detection events, which are created from photons scattered from the target into the spectrometer and converted into electrons on the multi-channel-plate (MCP) electron amplifier, accounting for the 1.6 ns photon flight-time along the drift tube. The non-linearity of the time-to-energy conversion necessitates a rescaling of the converted photocurrent spectral distribution $I(E_f)$ using

$$I(E_f) = I(t) \cdot \left| \frac{dt}{dE_f} \right| = \frac{t^3}{m_e L^2}. \tag{A.2}$$

In order to improve the number of electrons detected from the weak XUV excitation, an electrostatic Einzel lens is installed, which improves the angle-of-acceptance of the electron detection. The kinetic energy of the photoelectrons is modified during passage through the electrostatic potential of the lens and thus equation A.1 is not valid any more. Instead the conversion functions are calculated using charged particle trajectory simulations and provided by the manufacturer (see figure 75 a). The signal enhancement of the electrostatic lens has to be corrected for in order to retrieve accurate photoemission time delays from streaking spectrograms. To this end, calibration measurements of the LMM auger photoemission from a silicon crystal around 95 eV, which was selected because of its broadband and largely isotropic emission, have been performed by Stefan Neppl [35] and are applied in all the data evaluations presented in this thesis.

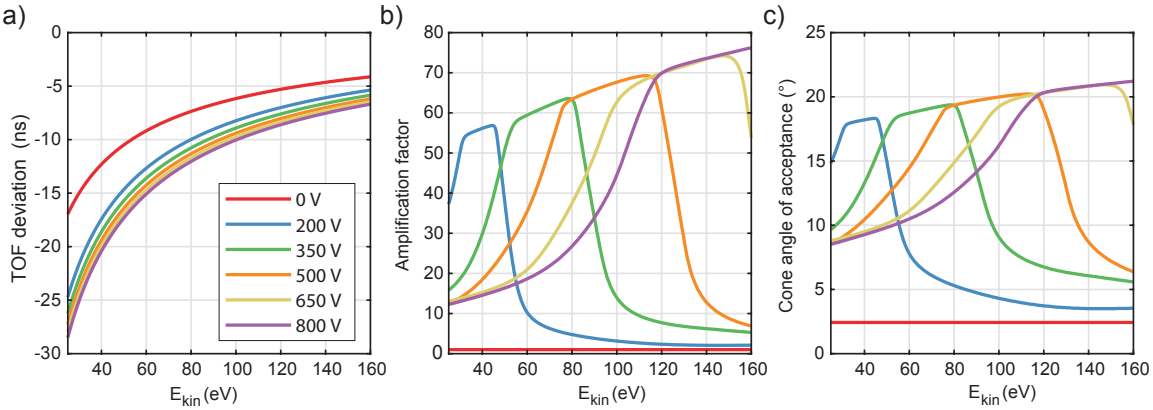

Figure 75 Performance of the electrostatic Einzel lens of the TOF spectrometer as function of the electron kinetic energy. a) Deviation of electron TOF from equation A.1 due to the acceleration in the electrostatic lens and post-acceleration section. b) Signal amplification factor. c) Cone angle of the electron trajectories emitted by the sample and registered on the electron detector.

The photoelectrons are amplified in the MCP electron amplifier and the pulses are out-coupled through a capacitor in vacuum. The timing detection of the electron pulse is performed with a constant-fraction discriminator (Ortec 9307) and a digital multi-scaler card (FAST ComTec P7889) with a time resolution of 100 ps. The spectral resolution ΔE_f follows from the time resolution of the detection electronics Δt as

$$\Delta E_f = \frac{1}{L}\sqrt{\frac{8}{m_e}} E^{3/2} \Delta t, \tag{A.3}$$

which equates to 0.45 eV for electrons with kinetic energy E_f of 150 eV, corresponding to the highest energy electrons detected during the course of the experiments presented in this thesis. The relative geometric trajectory deviation of electrons hitting the center and edge of the MCP active area is negligible. However, a reduction of spectral resolving power of the TOF system is observed if the electrostatic lens is activated.

B. XUV multilayer mirror calibrations

The energy calibration of the time-of-flight spectrometer can be performed by using the narrowband NOO auger electrons emitted from Xenon atoms [113]. Because the time-energy conversion functions are known from charged particle trajectory simulations a priori, we can use the direct photoemission from xenon to determine the XUV spectrum of the isolated attosecond pulse. The mirrors at central energy 145 eV, 117 eV and 92 eV have been characterized with reflectivity measurements using narrowband synchrotron radiation directly [214, 35, 93]. The other multilayer mirrors used for the tungsten and magnesium projects have been calibrated using the known binding energy of the Xenon 4d core level doublet (5/2: 67.5 eV 3/2: 69.5 eV) along with the NOO auger emission (see figure 76).

The prompt t_0 is determined from the spectrum directly. The work function differences $\Delta\Phi$ are adjusted to match the NOO auger spectrum between 8 eV and 36 eV kinetic energy with a precision of typically 0.25 eV. The resulting values of $\Delta\Phi$ are between 0 eV and 1.5 eV depending on the activation of the electrostatic lens, possible space charge build-up at the graphite-coated glass nozzle. These contributions are ignored on solid state spectroscopy measurements, as they do not contribute to the attosecond delay. The photon energy is determined from a least-squares fit of the resulting photoelectron spectrum of the 4d core level photoemission, taking into account the energy-dependent cross section [243] and the spin-orbit doublet of photoemission lines. The resulting central photon energies $\hbar\omega$ and FWHM bandwidths $\Delta_{\hbar\omega}$ are summarized in table 8.

Design	105	112	118	124	135
$\hbar\omega$	103.1	110.1	117.1	124.4	133.7
$\Delta_{\hbar\omega}$	4.6	3.5	4.0	4.8	4.0

Table 8 Results of XUV multilayer calibrations. All values in units of eV.

All central photon energies are within 2 eV of the desired design energy. Although the fit quality suggests an error in determination of $\hbar\omega$ on the order of 20 meV, application of the fitting scheme on different spectra measured with and without the electrostatic lens on different days reveal a fluctuation up to 1 eV, which is marked in the form of error bars throughout this thesis. Furthermore, it should be noted that the intensity of XUV radiation in the cut-off region is most often decreasing towards higher energy and this is expected to result in pulses centered at reduced photon energy w.r.t. the XUV multilayer reflectivity curves. Also the central energy of the reflectivity is shifted towards lower energy for larger angles of incidence of the incoming XUV radiation. The design angle-of-incidence of all multilayer optics was 5°. As a general rule-of-thumb however, it should be noted that the alignment of the attosecond beamline and

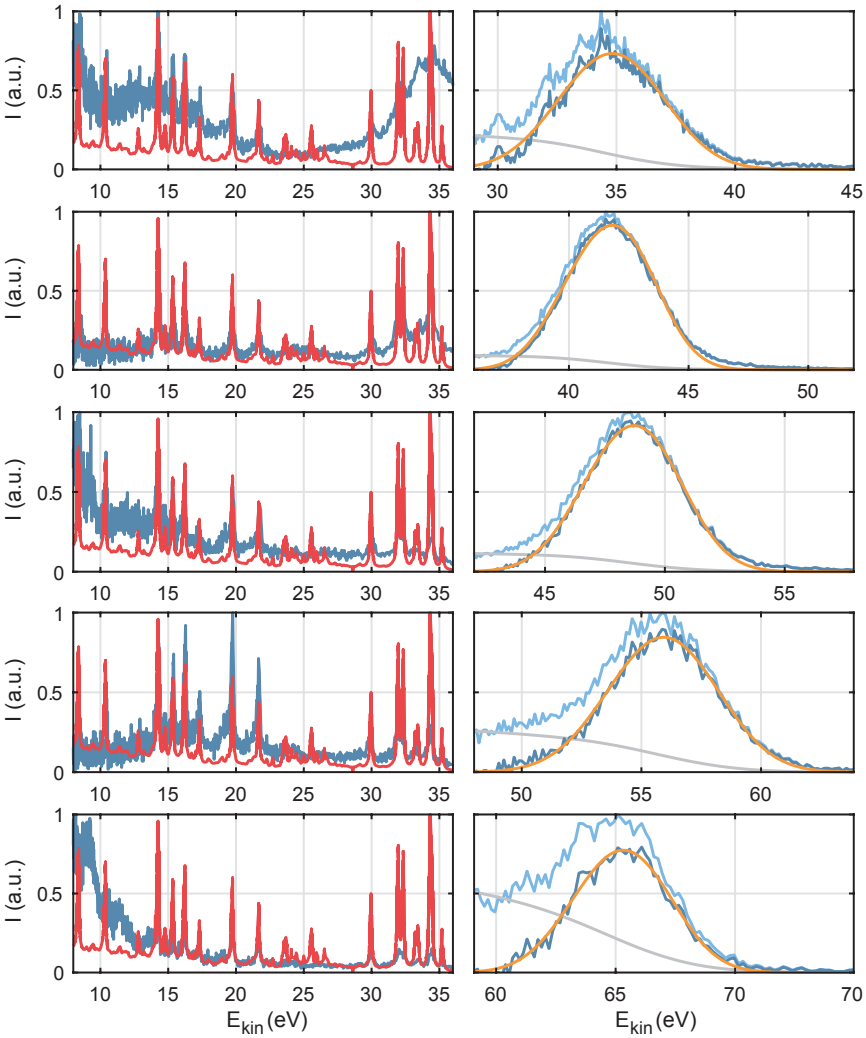

Figure 76 Calibration of central energy and bandwidth of XUV multilayer mirrors, which were not characterized by synchrotron reflectrometry. Design energies from top to bottom: 105 eV, 112 eV, 118 eV, 124 eV, 135 eV. Left side: Xenon NOO auger photoemission spectra confirming the precise calibration of the kinetic energy scale. Spectra measured with attosecond pulses (blue) are compared to high-resolution spectra measured with synchrotron radiation (red) [113]. The weak lines at 25 eV kinetic energy originate from Xe 4d shake-up resonances and are not present in the attosecond XUV spectra, because of the higher photon energy. Right side: Xenon 4d core level photoemission spectra before (light blue) and after background subtraction (dark blue). The Shirley background is indicated in grey. Least-squares fitting (orange) is employed for central energy and bandwidth determination 8.

especially the spatial overlap of XUV and NIR beams is significantly easier, if the angle of incidence on the double mirror is minimized and astigmatism in the imaging system is avoided.

C. Calibration of synchrotron XUV flux and photon energy

High-resolution spectrograms for W(110) and O/W(110) have been measured at the SuperESCA beamline at the Elettra synchrotron in Trieste, Italy. The beamline consists of an 3.6 m undulator, a refocussing plane grating monochromator (SXR-700, Zeiss) and an UHV surface-science end-station equipped with a 200 mm hemisperical analyser (Specs). In order to determine the energy-dependent photoionization cross section and spectral intensities necessary for the implementation of the classical transport model (see section 4.5.2), the energy-dependent photon flux has to be determined. This can be accomplished by direct measurement with a calibrated XUV photodiode or in-situ by continuous measurement of the photocurrent generated on the elliptical refocussing mirror I_{foc}, which was done during our measurements. First the energy-dependent quantum yield Q of the gold coating [91] has to be accounted for (see figure 77 a). Of course, only photons reflected from the gold mirror, which is irradiated at 2° grazing incidence, contribute to the photon flux on target. On the other hand, only photons transmitted through the surface of the gold coating contribute to the measured current. The final calibration formula reads

$$I_{\hbar\omega} = \frac{I_{foc}}{QRT} \tag{C.1}$$

with T and R transmission and reflection coefficients, respectively obtained from [216]. The results of the energy-dependent flux calibration for photon energies between 96 eV and 150 eV are plotted in figure 77. Because the beamtime was allocated after a grating exchange inside the

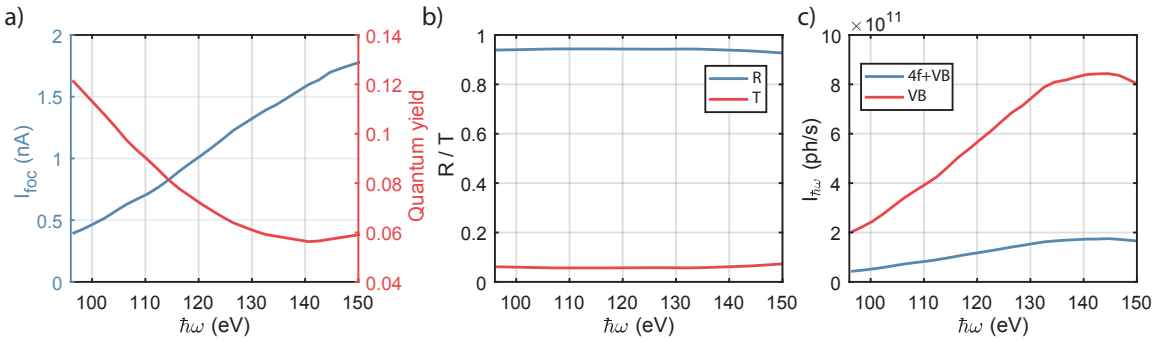

Figure 77 Calibration of synchrotron photon flux from photocurrent measured on the elliptical gold refocussing mirror. a) Measured mirror current (blue) and gold quantum efficiency (red). b) Reflectivity and transmission of thick gold mirror at 2° grazing incidence. c) Calibrated photon flux impinging on the sample for measurements of the full tungsten spectra (blue) and valence band spectra (red).

monochromator, no calibration of the absolute photon energy scale was available. Fortunately, because of the narrow natural linewidth of the W 4f photoelectron peaks, a calibration was easily performed in-situ during the beamtime. The calibration procedure for O/W(110) is depicted in figure 78. After splitted Shirley background subtraction, the W 4f spectral region is fitted

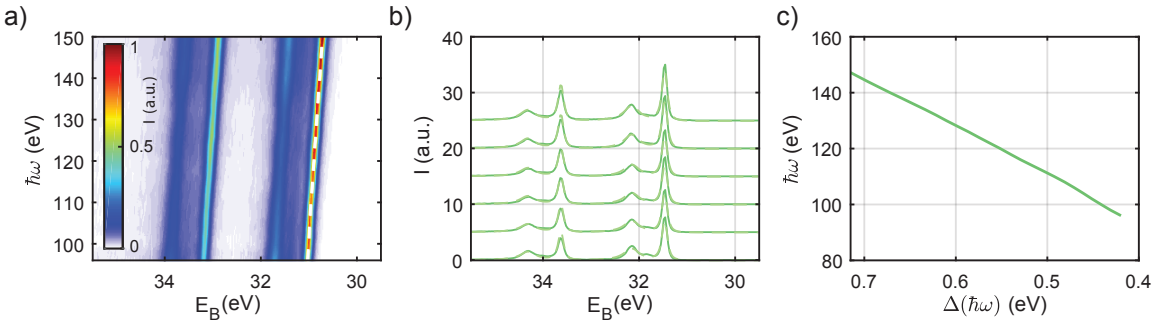

Figure 78 Calibration of the monochromator of the SuperESCA beamline. a) Photon energy scan of W 4f core level of O/W(110). The white line marks the fitted position of the bulk W 4f 7/2 peak with true binding energy 31.45 eV. b) Photoelectron spectra (green) and fit (light green) with Doniach-Sunjic quadruplet for determination of binding energy, surface and spin-orbit splitting for photon energies 100 eV to 150 eV in 10 eV steps. Spectra are vertically offset for clarity. c) Determined deviation between set photon energy and true photon energy.

with at quadruplet of Doniach-Sunjic [244] functions accounting for the splitting due to different chemical environment of oxygen bound surface tungsten atoms and bulk tungsten atoms and the spin-orbit splitting (see figure 78 b). The surface peak of O/W(110) actually consists of three distinct spin-orbit doublets obtained by different loading of the three doubly degenerate but mutually exclusive adsorption sites [238]. For the sake of simplicity, the surface peak is fitted by an increased natural linewidth of 200 meV sufficient for determination of the binding energies. The other peak parameters along with the binding energy of the bulk peak of W 4f 7/2 of 31.45 eV are obtained from the rich literature on tungsten photoemission [245].

Unfortunately a hydrogen background was present during the photoemission experiments in the UHV environment despite the low background pressure of $5 \cdot 10^{-11}$ mbar, which complicates the data evaluation of W(110) photoemission. The surface-core-level shift (SCLS) of the W 4f level is extremely sensitive to small amounts of contaminations and the literature value of -321 meV [246] could only be maintained for few minutes after high-temperature treatment of the tungsten crystal, insufficient to record full photoemission spectrograms. Photoemission from the valence band is much less sensitive towards hydrogen contamination as depicted in figure 79.

Two energy-dependent photoemission spectrograms are recorded 60 minutes and 120 minutes after heating of the tungsten crystal to 2300 K. The difference between these two spectrograms is scaled by the factor 1.5 and subtracted from the 60 minute spectrogram to reveal the spectrogram without contamination. A spectrum 3 minutes after the high-temperature annealing of the sample was recorded at photon energy 110 eV and compared with the corrected spectrum (see figure 79) revealing near perfect subtraction of the adsorbate state at binding energies above 6 eV, which are attributed to low amounts of O atoms and CO molecules on the surface. The photoemission close the Fermi edge is 25% weaker compared with the clean spectrum recorded 3 minutes after high-temperature annealing, which is indicative of the surface resonance nature of the initial states close to the Fermi energy [239].

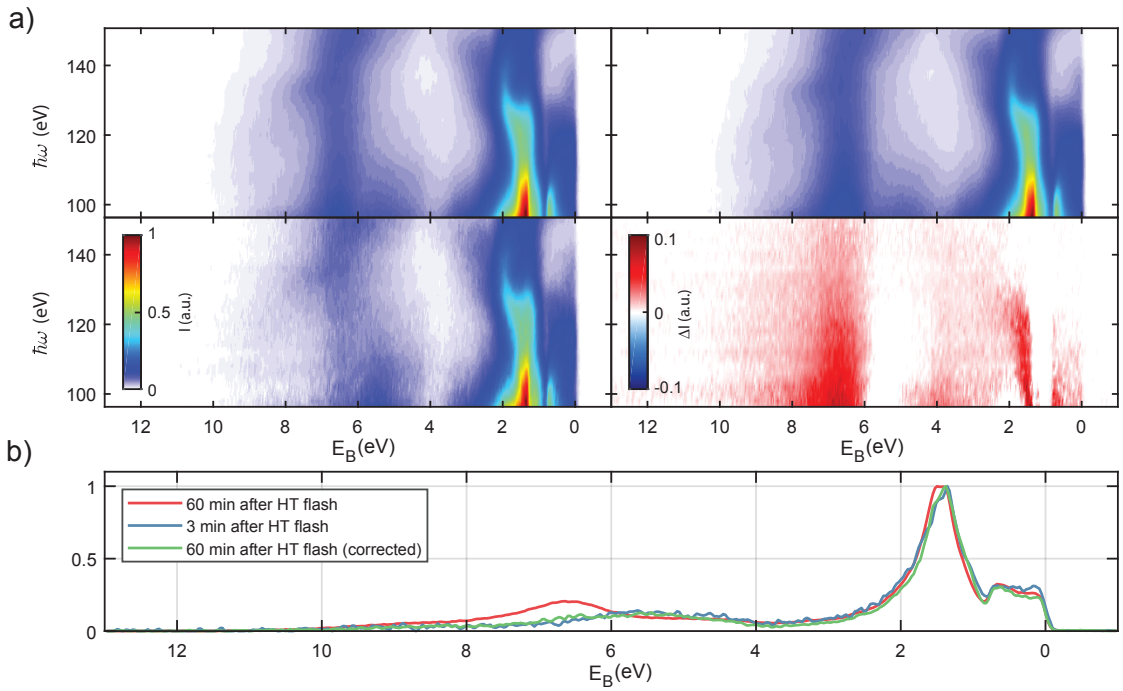

Figure 79 a) Top: Valence band photoemission spectrogram as function of energy taken 60 minutes (left) and 120 minutes (right) after heating of the sample. Bottom: W(110) photoemission decomposed into contributions of the clean surface (left) and accumulated contamination (right) b) Comparison of corrected photoemission spectra before (red) and after correction (green) with photoemission from clean W(110) substrate measured 3 minutes after sample heating. All spectra are normalized to maximum value. Additional photocurrent contribution of adsorbate states is almost exclusively located at binding energies larger than 6 eV and almost completely removed by the correction procedure.

D. Ultrashort optical pulse characterization

As laser pulses of increasingly shorter duration are created with modern lasers, so rises the necessity for accurate temporal characterization [247]. Because femtosecond pulses elude direct measurement with conventional electronics, a pump-probe measurement with equally short laser pulses is necessary. In attosecond physics, record time resolution for characterization of optical light fields is obtained with the attoscond streaking technique [248]. However, the experimental complexity of the attosecond streaking apparatus and its limitation to the characterization of sub-two cycle laser pulses necessitates the utilization of different pulse characterization techniques.

D.1. Frequency-resolved optical gating

The most widespread contemporary femtosecond pulse characterization technique is the frequency-resolved optical gating (FROG) technique introduced by Kane and Trebino [249]. Herein, the output spectrum $P(\omega, \tau)$ of a nonlinear interaction of the probe pulse with either a known reference gate pulse (XFROG) or with itself (FROG) is recorded for a series of time delays τ.

The output of the Ti:Sa CPA systems used throughout this work has been characterized with second harmonic generation (SHG) FROG. The output of the nonlinear hollow-core fiber compression has been characterized using transient-grating (TG) FROG.

D.2. Ptychographic iterative engine

A new development of ultrashort pulse measurement is the use of ptychographic phase-retrieval algorithms in time domain [250]. Whilst originally developed by Walter Hoppe [251] to extract phase information without ambiguity from the combination of several electron diffraction patterns from a spatially shifted sample, it has found widespread use in X-ray microscopy with synchrotron [252] and HHG [253] radiation due to the fact that it can be used to achieve lens-less diffraction limited resolution.

Its application to the time domain is surprisingly straightforward, as the formula of the FROG spectrograms resemble far-field diffraction patterns [250]. A special treat is the so-called extended ptychographic iterative engine (PIE), which allows to use both unknown pulse and gate and retrieve both from the strongly overdetermined spectrogram.

SHG-FROG

The input pulse is split in a Michelson-type interferometer and the two replica of the pulse are superimposed under a finite angle in a $20\ \mu$m Beta-Barium Borate (BBO) crystal [254]. The sum-frequency component of the nonlinear interaction appears in between the two input beams and is isolated with an iris aperture and directed onto an UV-VIS spectrometer. Variation of the pulse delay in the interferometer yields the SHG-FROG spectrogram $P_{SHG}(\omega,\tau)$ of the input pulse $E(t)$ under investigation

$$P_{SHG}(\omega,\tau) \propto \left| \int dt E(t) \cdot E(t-\tau) \cdot e^{i\omega t} \right|^2 . \tag{D.1}$$

Because the symmetry of the resulting spectrogram w.r.t. the pulse-gate delay τ, the time direction of the pulse retrieval is ambiguous and can only be determined in a second measurement placing a known amount of dispersive material into the beam path [254].

The PIE algorithm in the case of SHG-FROG is described in much detail in [255] and reviewed here quickly. The exit field $S_n(t;\tau)$ corresponds to the spectrum measured at delay τ_m in the n-th cycle of the reconstruction algorithm

$$S_{n,m}(t;\tau_m) = E_n(t) \cdot E_n(t-\tau_m). \tag{D.2}$$

A precise calculation of the time-shifted electric field is obtained via the Fourier-shift theorem

$$E_{n,m}(t-\tau_m) = \mathcal{F}^{-1}\left\{ \mathcal{F}\left\{ E_{n,m}(t) \right\} \cdot e^{i\omega\tau^m} \right\}. \tag{D.3}$$

The Fourier transform of the output spectrum $\tilde{S}_{n,m}(\omega,\tau_m) = \mathcal{F}\left\{S_{n+1,m}(t;\tau_m)\right\}$ is calculated in every step (n,m) and its amplitude is replaced by the measured spectrum

$$\tilde{S}_{n+1,m}(\omega;\tau_m) = \sqrt{P_{SHG}(\omega;\tau_m)} \cdot \frac{\tilde{S}_{n,m}(\omega;\tau_m)}{\left|\tilde{S}_{n+1,m}(\omega;\tau_m)\right|}. \tag{D.4}$$

And after inverse Fourier transform $S_{n+1,m}(t;\tau_m) = \mathcal{F}^{-1}\left\{\tilde{S}_{n+1,m}(\omega;\tau_m)\right\}$, the difference is applied to the electric field via the regularized error function [256]

$$E_{n+1,m}(t) = E_{n,m}(t) + \beta \cdot U \cdot \left(S_{n+1,m}(t;\tau_m) - S_{n,m}(t;\tau_m)\right), \tag{D.5}$$

with

$$U = \frac{E^{\dagger}_{n,m}(t-\tau_m)}{(1-\beta)\cdot\left|E_{n,m}(t-\tau_m)\right|^2 + \beta \cdot max\left\{\left|E_{n,m}(t-\tau_m)\right|^2\right\}}. \tag{D.6}$$

One full cycle over all measured delay steps τ_m completes one iteration n of the PIE. Both the order of the delay steps as well as the parameter β is randomized in every iteration n of the iPIE,

which decreases the likelihood for the algorithm to regress into local minima [255]. The algorithm can be started from a random input for $E(t)$ however significant improvement of convergence and reliability is achieved if the initial guess is either produced from the delay-integrated spectrum or frequency-integrated temporal envelope of the measured spectrogram. The result of the ePIE algorithm of the compressed Ti:Sa amplifier output is depicted in figure 17.

TG-FROG

Because of the limited phase-matching bandwidth of SHG in BBO crystals a different nonlinear interaction has to applied to pulse characterization of the sub-two cycle pulses [257]. One such method is dispersionless TG-FROG [258], where three replica beams are generated in the so-called BOXCARS geometry with an appropriate mask and superimposed inside a thin glass plate by reflection from a split focussing mirror. Two of the beams generate a transient refractive index grating via the Kerr-nonlinearity (see eq. 2.37) from which the third beam is diffracted along the direction of the fourth corner of the BOXCARS configuration. This beam is isolated with an iris aperture and detected in a commercial grating spectrograph as function of the delay between the first and second pulses and the third pulse. The spectrum of the refracted radiation is recorded as a function of the delay of the third pulse replica generating a FROG spectrogram

$$P_{TG}(\omega,\tau) \propto \left| \int dt E(t) \cdot |E(t-\tau)|^2 \cdot e^{i\omega t} \right|^2 . \tag{D.7}$$

Because of the finite crossing angle of the beams in the nonlinear medium significant temporal smearing of the FROG signal is observed, which results in instability of the PIE algorithm due to the increased time-bandwidth product. This can be avoided by substitution of the pulse intensity envelope with an independent intensity-gate function $|E(t-\tau)|^2 \rightarrow |G(t-\tau)|$. The ePIE iteration procedure presented above now is applied twice during each iteration (n,m) and updates both the pulse and gate functions according to

$$\begin{aligned} E_{n+1,m}(t) &= E_{n,m}(t) + \beta_E \cdot U_E \cdot (S_{n+1,m}(t;\tau_m) - S_{n,m}(t;\tau_m)) \\ G_{n+1,m}(t) &= G_{n,m}(t) + \beta_G \cdot U_G \cdot (S_{n+1,m}(t;\tau_m) - S_{n,m}(t;\tau_m)) , \end{aligned} \tag{D.8}$$

with

$$\begin{aligned} U_E &= \frac{G^{\dagger}_{n,m}(t-\tau_m)}{(1-\beta_E) \cdot |G_{n,m}(t-\tau_m)|^2 + \beta_E \cdot max\left\{|G_{n,m}(t-\tau_m)|^2\right\}} \\ U_G &= \frac{E^{\dagger}_{n,m}(t+\tau_m)}{(1-\beta_G) \cdot |E_{n,m}(t+\tau_m)|^2 + \beta_G \cdot max\left\{|E_{n,m}(t+\tau_m)|^2\right\}} . \end{aligned} \tag{D.9}$$

The intensity constraint $G_{n+1,m}(t) = |G_{n+1,m}(t)|$, which is applied after each iteration ensures the correct application of the TG-FROG spectrogram function (see equation D.7). The result of the ePIE algorithm of the sub-two cycle laser pulse used for HHG is depicted in figure 19.

E. Photoemission time delay extraction algorithms

Extraction of minute attosecond photoemission time delays from attosecond streaking spectrograms is a challenging task, especially when considering photoemission from condensed matter targets, because of the significant background from inelastically scattered electrons and the spectral overlap of photoelectrons released from different initial states and bands, the coherence properties of which on the attosecond timescale are in general unknown. The focus of this appendix is to present the delay retrieval algorithms utilized throughout this work in a compact and concise manner.

The first class of delay extraction algorithms, called center-of-energy (COE), relies on the inversion of the classical solution to the streaking trajectory by calculating the delay-dependent spectral shift of the ejected photoelectrons (see equation 2.33), from which the photoemission time delay and further parameters of the NIR field are extracted using least-squares fitting. All other algorithms rely on the quantum mechanical formalism 2.5.2, solution of the time-dependent Schrödinger equation in the strong-field approximation (see equation 2.35) with the central momentum approximation (CMA). The photoemission time delay can either be extracted from Gaussian parametrizations of the XUV and NIR fields (TDSE,DIFF) or by direct solution of the phase inversion problem (FROG,PIE). Furthermore a plethora of methods for delay extraction has been developed over the last twelve years both applying the CMA [127, 259] and more recently beyond the CMA [260, 261, 262].

E.1. Center-of-energy algorithms

The relative photoemission time delay can be extracted from an attosecond streaking measurement by separating the streaking spectrogram into separate regions and calculating the mean kinetic energy for each delay τ of either from the first-moment of the spectrum after background subtraction

$$E_{kin}^{(q)}(\tau) = \frac{\int_{E_{q,min}}^{E_{q,max}} dE\, E \cdot P(E,\tau)}{\int_{E_{q,min}}^{E_{q,max}} dE\, P(E,\tau)}, \tag{E.1}$$
$$\Delta E_q(\tau) = E_{kin}^{(q)}(\tau) - \overline{E_{kin}^{(q)}}.$$

The mean first-moment kinetic energy $\overline{E_{kin}^{(q)}}$ is subtracted to yield the delay-dependent streaking energy shift, which is linked to the laser intensity according to 2.33.

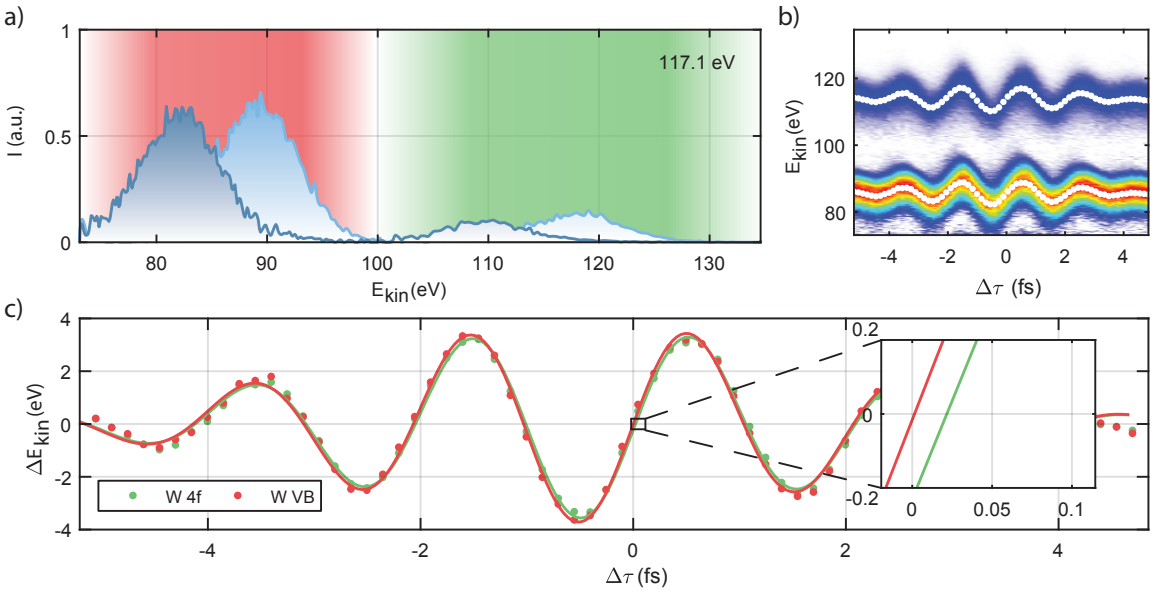

Figure 80 Implementation of the COE algorithm with first-moments for W(100) measured at photon energy 117.1 eV in August 2016. a) Kinetic energy spectra for delay corresponding to maximum negative streaking shift (dark blue) and maximum positive streaking shift (light blue). Colour shaded regions indicate integration regions of first-moment determination. b) Measured attosecond streaking spectrogram. First moments marked in white. c) Streaking shift ΔE_q of the photoelectron kinetic energy for each delay slice of the spectrogram alongside the streaking shift resulting from the fitted vector potential. The photoemission time delay $\Delta\tau$ can be directly extracted from the time delay of the zero-crossing of both kinetic energy shift curves visible in the inset.

Dropping the quadratic term, which is motivated by the small NIR intensities utilized on solid state targets, the streaking energy shifts are fitted with the linear form of equation 2.33

$$\Delta E_q(\tau) = \Delta E_{q0} \cdot e^{-4\ln 2(\tau-\Delta\tau_q)^2/\tau_L^2} \cdot sin\left(\omega_L\left(\tau-\Delta\tau_q\right)+\frac{1}{2}\beta_2\left(\tau-\Delta\tau_q\right)^2+\Phi_{CE}\right). \quad \text{(E.2)}$$

The vector potential of the laser field is parametrized as Gaussian pulse with FWHM duration τ_L, central frequency ω_L with linear chirp β_2. The fitting parameters τ_q denote the time delay of the various photoemission bands (2p,4f,VB) under investigation. Because of the difficulties arising from fitting multiple parameters inside a periodic function, the Levenberg-Marquardt algorithm implemented in MATLAB fails in general to converge to the correct physical solution of the pulse, if not provided with a sufficient range of temporal delays and very good starting values. To ensure convergence, the central frequency w_L is determined through Fourier transform prior to the fit and the CEP and the linear chirp are sequentially fitted with a wide range of starting values. The best fit is chosen for photoemission time delay determination.

Furthermore, the streaking energy shift can be obtained from least-squares fitting of a sum of Gaussian functions chosen to reproduce the unstreaked photoemission spectrum [32]. The FWHM width of the Gaussian functions ΔE_{FWHM} is defined globally in order to reproduce the XUV bandwidth and shape of the photoemission spectrum in absence of the NIR field. The fit is

performed for each delay slice of the spectrogram independently

$$\min_{\Delta E_q(\tau), a_q(\tau)} ||P(E_{kin},\tau) - P_{fit}(E_{kin},\tau)||^2 , \tag{E.3}$$
$$P_{fit}(E,\tau) = \sum_q^Q a_q \sum_{i_q}^{N_q} a_{i_q} \cdot e^{-4ln2\left(E_{B,i_q}-\Delta E_q(\tau)-E\right)^2/E_{FWHM}^2},$$

wherein each photoemission band q is represented by a set of N_q Gaussian functions with amplitudes a_{i_q} and kinetic energies $E_{i,q}$ in absence of the NIR field. The total amplitude of each band a_q and streaking energy shift ΔE_q are fitted for each delay slice of the spectrogram using the Levenberg-Marquardt algorithm. The initial states and Gaussian fits are depicted in figures 46, 50, 58 and 30.

E.2. Time-dependent Schrödinger equation algorithms

More sophisticated methods of analysis of attosecond streaking spectrograms rely on the quantum-mechanical formalism 2.5.2. The numerical effort in calculation of streaking spectrograms can be greatly reduced by implementation of the central-momentum approximation (CMA)

$$\langle p - eA_L(t)|\,\hat{x}\,|i\rangle = \langle p_c|\,\hat{x}\,|i\rangle\,, \tag{E.4}$$
$$\Phi_V(p, A(t)) = \Phi_V(p_c, A(t)),$$

i.e. the replacement of the time-dependent photoemission matrix element by its mean value over the bandwidth of the XUV pulse. The numerical integration can be implemented via inverse Fourier transform. This is necessary to implement efficient delay-extraction algorithms and for handling large data sets. In this work a Gaussian parametrization of the NIR vector potential $A_L(t)$ and XUV pulse $E_{X,i_q}(t)$

$$E_{X,i_q}(t) = \mathcal{F}^{-1}\left\{a_{i_q} \cdot e^{-4ln(2)\left(w-w_X-E_{B,i_q}\right)^2/\Delta w_X^2} \cdot e^{-i\frac{i}{2}\beta_X\left(w-w_X-E_{B,i_q}\right)^2}\right\} \tag{E.5}$$
$$A_L(t) = A_0 \cdot e^{-4ln(2)t^2/t_L^2} \cdot sin\left(\omega_L t + \frac{1}{2}\beta_L t^2\right) \tag{E.6}$$

is fitted to the measured streaking spectrograms using a least-squares algorithm [13, 24]. As first introduced in [20], the XUV pulse is parametrized in the spectral domain and calculated in the time domain via inverse Fourier transform. Hence, the spectral bandwidth of the XUV pulse and its chirp are decoupled, in contrast to the pulse definition in the time domain. The inverse Fourier transform is usually performed analytically, however numerical implementation additionally allows to account for energy-dependent photoemission dipole matrix elements to be

inserted directly into the evaluation. The additional numerical effort is in most cases negligible. The convergence reliability and speed can be greatly enhanced by predetermining the NIR laser field using the COE algorithms and inserting the solution as starting parameters into $A_L(t)$. A set of initial states i_q with binding energies E_{B,i_q} and cross sections $a_{i_q}^2$ are defined to match the spectral envelope of the photoelectron spectrum in absence of the NIR field. These initial states and Gaussian fits are depicted in figures 46, 50, 58 and 30 and are generated from the high-resolution photoemission spectra.

TDSE

The photoemission spectrogram is calculated and the least-squares error function is minimized with the Levenberg-Marquardt method

$$\min_{\omega_X,\beta_X,a_q,A_0,t_L,\omega_L,\beta_L,\Phi_{CE}} ||P(E_{kin},\tau) - P_{fit}(E_{kin},\tau)||^2 , \tag{E.7}$$

$$P_{fit}(E_{kin},\tau) = \sum_q^Q a_q \sum_{i_q}^{N_q} \left| a_{i_q} \int_{-\infty}^{\infty} dt\, E_{X,i_q}(t+\tau) \cdot e^{-i\Phi_V(t;p_{i_q})} \right|^2 ,$$

$$\Phi_V\left(t;p_{i_q}\right) = \int_t^{\infty} dt' \, \left(p_{i_q} \cdot eA_L(t')\right)^2 .$$

The background is calculated with the splitted Shirley method from the reference spectrum and applied to all delays (see figure 81). This background model assumes fully incoherent background emission spanning few-fs time scales. This approximation is reasonable for multiple electron-hole excitation and deep-multiple plasmon contributions. Electrons only subject to a single scattering event traverse the crystal surface within 100 as of the direct photoemission. In the case of the Mg(0001) photoemission, the singly scattered electrons are all located in the narrowband single plasmon peak. Because of the large number of plasmon peaks, no timing information can be obtained about the timescale of the plasmon scattering in the W(110) and W(100) measurements.

DIFF

The second method of background subtraction, featured prominently in gas-phase streaking experiments [13, 20], is deemed the differential method. Herein, the derivative along the delay axis of the spectrogram is used as minimization target of the least-squares algorithm

$$\min_{\omega_X,\beta_X,a_q,A_0,t_L,\omega_L,\beta_L,\Phi_{CE}} \left|\left| \frac{\partial}{\partial\tau} P(E_{kin},\tau) - \frac{\partial}{\partial\tau} P_{fit}(E_{kin},\tau) \right|\right|^2 . \tag{E.8}$$

This has the distinct advantage not to introduce additional free parameters into the data evaluation process. Furthermore, additional weight is given to the delay region of maximal streaking shifts [13] (see figure 82 c,d). The DIFF method necessitates a strong streaking NIR field to generate significant intensity contrast along the delay axis for evaluation, which proves

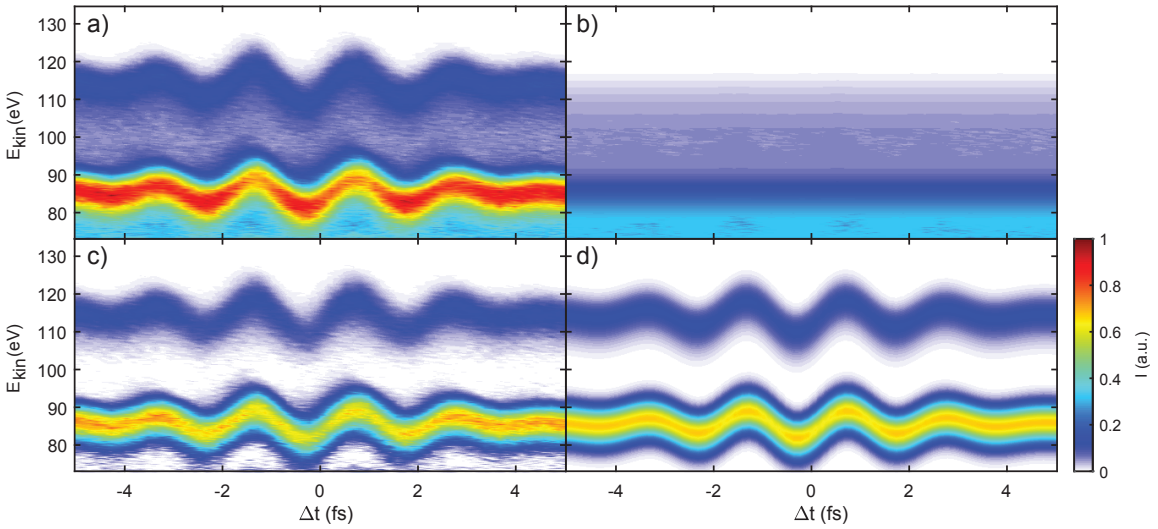

Figure 81 a) Measured attosecond streaking spectrogram of W(100) photoemission measured at photon energy 117.1 eV. b) Background calculated from with the splitted Shirley algorithm. c) Measured spectrum after background subtraction $P(E_{kin}, \tau)$. d) Reconstructed spectrogram $P_{fit}(E_{kin}, \tau)$ generated with the Gaussian parametrization of the quantum-mechanical formalism.

problematic if multiple narrow spaced photoemission lines or satellites are to be investigated.

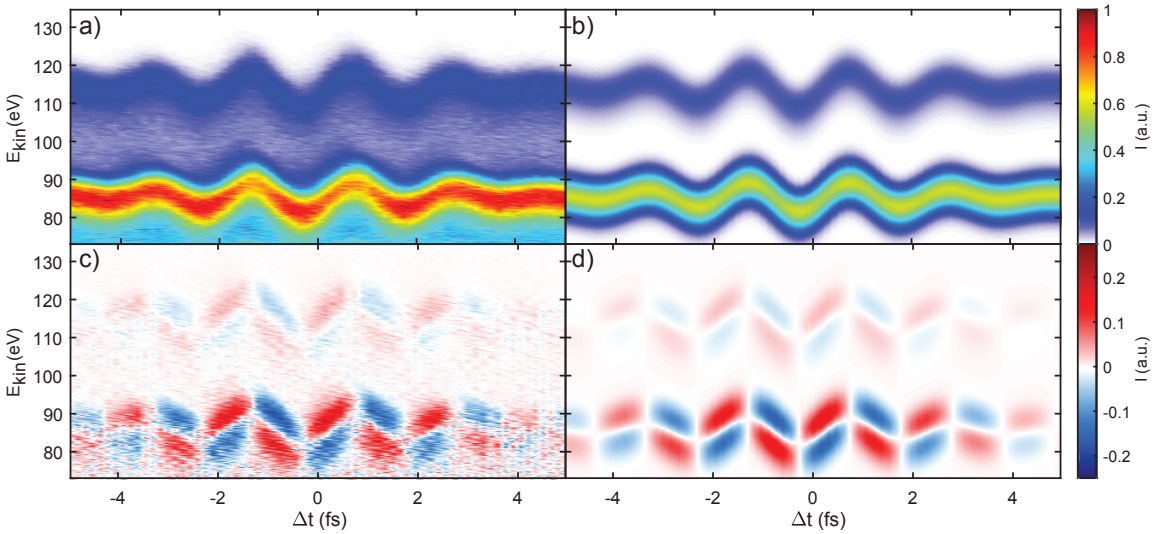

Figure 82 a) Measured attosecond streaking spectrogram of W(100) photoemission measured at photon energy 117.1 eV. b) Reconstructed spectrogram generated with the Gaussian parametrization of the quantum-mechanical formalism. c) Delay differential of attosecond streaking spectrogram for background removal. d) Reconstruction of delay differential. Valence band spectral region amplified by factor 16 for visual clarity.

E.3. Ptychographic algorithm (PIE)

The evaluation of attosecond streaking spectrograms is an incarnation of the 2D phase retrieval problem commonly encountered in ultrashort pulse characterization problems called frequency-resolved optical gating (FROG). Hence, it was recognized early on that algorithms used for femtosecond pulse characterization based on generalized projection [249] could be extended into the attosecond realm [127, 128]. When the ptychographic iterative engine (PIE) was first applied

to ultrafast pulse reconstruction [250], its application to attosecond streaking spectroscopy was straightforward [263]. The PIE is explained in detail in appendix D for TG FROG, which is equivalent to the algorithm for attosecond streaking spectroscopy, with the one notable difference being the replacement of the intensity gate constraint with a pure phase gate constraint

$$G_{n+1,m}(t) = \frac{G_{n+1,m}(t)}{|G_{n+1,m}(t)|}. \tag{E.9}$$

The results of the converged PIE algorithm for a single measurement are depicted in figure 83.

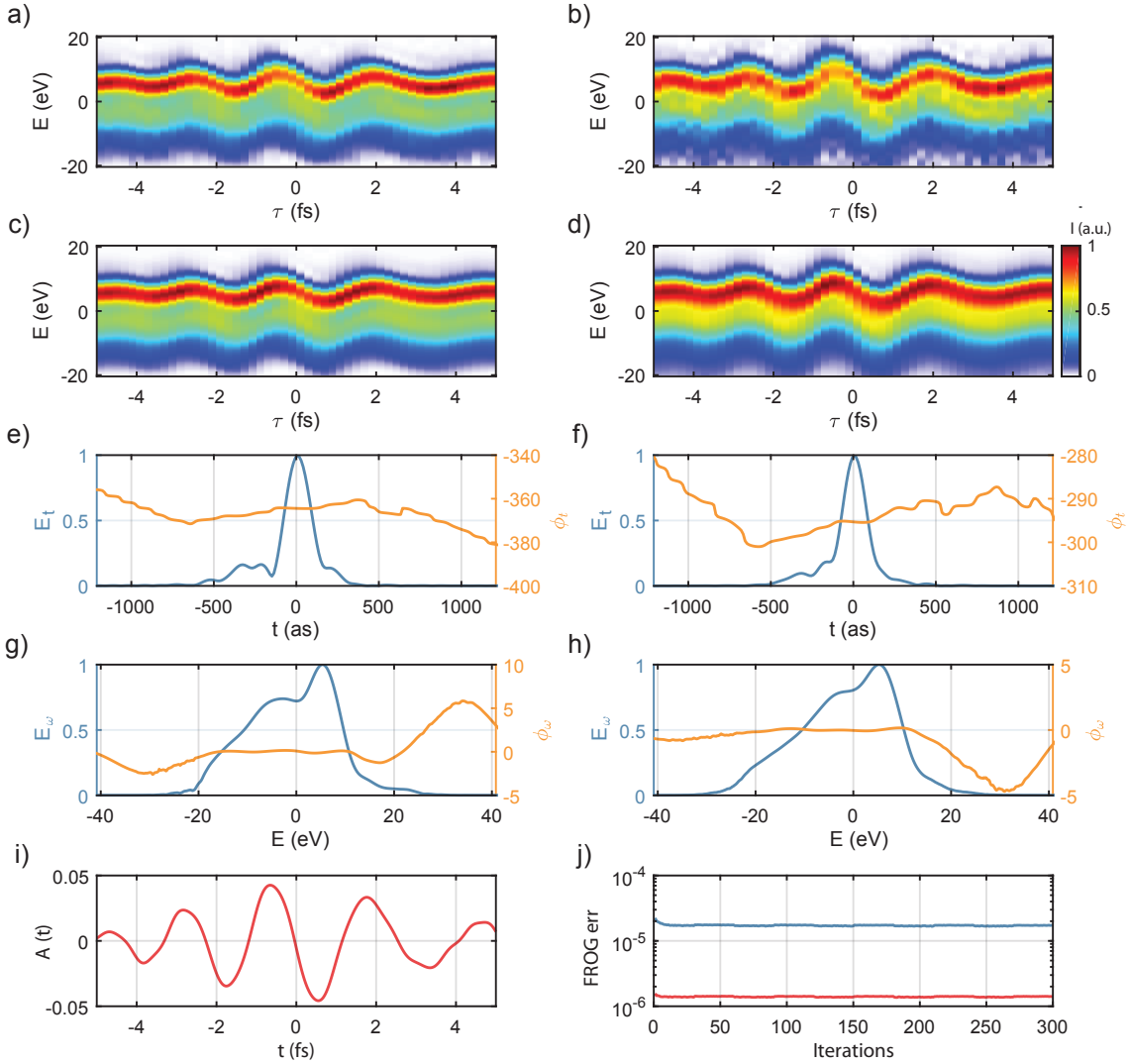

Figure 83 a) Streaking spectrogram of Mg 2p level and associated plasmon loss satellites. b) Streaking spectrogram of Mg valence band states and associated plasmon loss satellites. c,d) Streaking spectrograms reconstructed with the PIE algorithm. e,f) Temporal amplitude and phase of reconstructed XUV fields $E_X(t)$. g,h) Spectral amplitude and phase of reconstructed XUV fields $\tilde{E}_\omega(t)$. i) Vector potential of infrared field calculated form both spectrograms in each iteration. j) Frog error of reconstruction for Mg 2p (red) and valence band (blue) photoelectron wavepackets.

The PIE evaluation relies on the applicability of the CMA, which is in general invalid for attosecond chronoscopy, because the relevant information is spread out over a large bandwidth, i.e. 70 eV

in case of the Mg experiments at kinetic energies as low as 45 eV. The stringent requirement can be relaxed by separating out the spectral regions of interest and applying the CMA independently for each section [20]. Suitable start values for XUV pulses are generated by Fourier transform of the reference spectra recorded 300 fs after the NIR pulse. The delay-dependent first moment (see appendix E.1) is used to generate a suitable starting vector potential A_L. After each iteration of the delay-loop of the ePIE, the vector potentials are extracted from both gate pulses and equally mixed to generate a new vector potential reinserted into the loop. A nonlinear spectral filter is implemented to dampen any frequency components unphysical to the broadened Ti:Sa laser. The update of the phase gate is omitted in several sections of the PIE loop, in particular during the last set of iterations. This constraint ensures the relative photoemission time delay not to be hidden in the time delay between the vector potentials of the two phase gates, but forcibly introduced into the XUV pulses instead. The algorithm converges from the Fourier limited guess pulse within few tens of iterations (see figure 83 j), which correspond to few seconds of calculation time on a 4-core Intel I7 laptop CPU in an non-optimized MATLAB implementation.

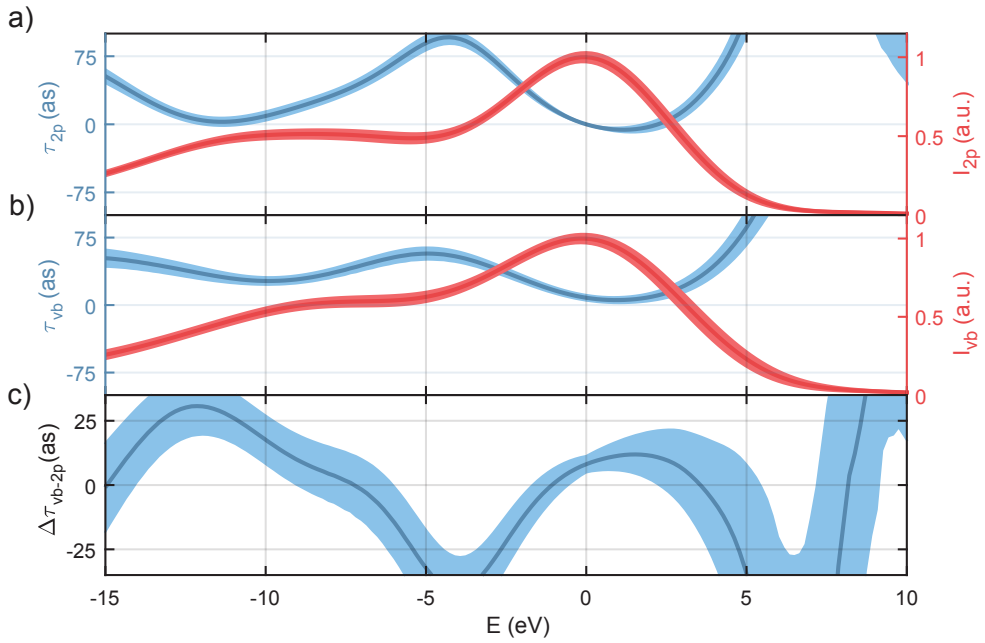

Figure 84 a) Results of PIE retrieval for Mg 2p spectral region and 124.4 eV excitation. Spectral intensity marked in red. Group delay marked in blue. Shaded areas mark 95% confidence area. b) Same as a), but for valence band photoemission. c) Relative group delay $\tau_{g,vb-2p}$.

It should be noted that the obtained XUV pulse FWHM duration of 180 as strongly underestimates the real XUV pulse duration of 450 as obtained from the TDSE and DIFF algorithms, because of the assumed full coherence between direct photoemission and plasmon satellites. Still, relative photoemission time delays can be extracted from the spectral representation of the pulse $\tilde{E}_\omega(\omega)$. The photoemission time delay is extracted from the group delay τ_g yielded by derivative d/dw of

the spectral phase θ_w

$$\theta_w = arg\left(\mathcal{F}\left\{E_X(t)\right\}\right) \tag{E.10}$$
$$\tau_g = -\frac{d}{dw}\theta_w.$$

Repeated measurements are aligned to match their maximum intensity of photoemission, i.e. Mg 2p or W 4f peak, and the free choice of the constant offset of the group delay is set to zero at this point. The mean delay and statistical error of the PIE retrieval data set is evaluated by averaging the results of all individual measurements and evaluated at the maximum of the retrieved spectral amplitude (see figure 84).

F. Details of the numerical calculations

The semiclassical simulations are performed on a spatial grid of size 106 Å divided among 2048 points and a temporal grid of size 9.6 fs comprised of 8192 points. The inverse LEED states are interpolated on the same spatial grid. The 31 layer magnesium or tungsten slab is placed in the center of the simulation field. Simulations are carried out assuming Gaussian Fourier-limited FHWM pulse durations of 480 as and 3.6 fs for the XUV and NIR fields, respectively. The central energy of the XUV field is varied from 90 to 150 eV in steps of 2.5 eV. Because the classical propagation step is carried out per final state and not per photon energy as in case of direct integration of the TDSE, achieving good spectral resolution of the photon energy is computationally quite cheap. The convergence of the numerical simulations is by reducing either number of spatial grid points or temporal grid points by a factor of two. The difference between both sets of computations and the full grid computation is depicted in figure 85.

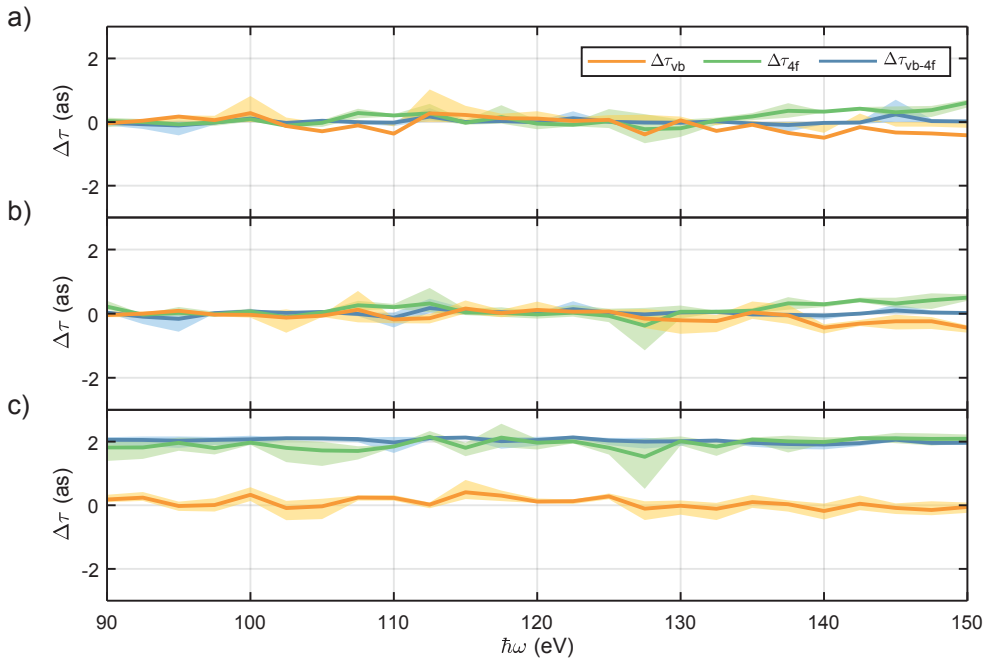

Figure 85 Analysis of numerical convergence of attosecond time delays obtained with the semiclassical model for W(110). a) Change of relative and absolute time delays upon reducing temporal grid resolution by a factor of two. b) Same as a) but for spatial grid resolution. c) Same as a) but for classical trajectory integration step.

Halving the spatial or temporal grid size (see figure 85 a,b) does not change the observed time delays by more than one attosecond, demonstrating the overall convergence of the numerical calculations. Reducing the temporal integration step of the classical trajectory only changes the time delay of the core level by 2 as, which is considerably lower than the experimental and numerical confidence intervals.

Bibliography

[1] H. Hertz. Ueber einen Einfluss des ultravioletten Lichtes auf die electrische Entladung. *Annalen der Physik und Chemie*, 267(8):983–1000, 1887.

[2] W. Hallwachs. Ueber den Einfluss des Lichtes auf electrostatisch geladene Körper. *Annalen der Physik und Chemie*, 269(2):301–312, 1888.

[3] P. Lenard. Erzeugung von Kathodenstrahlen durch ultraviolettes Licht. *Annalen der Physik*, 307(6):359–375, 1900.

[4] A. Einstein. Über einen die Erzeugung und Verwandlung des Lichtes betreffenden heuristischen Gesichtspunkt. *Annalen der Physik*, 322(6):132–148, 1905.

[5] M. Planck. Ueber das Gesetz der Energieverteilung im Normalspectrum. *Annalen der Physik*, 309(3):553–563, 1901.

[6] M. Aeschlimann, C. A. Schmuttenmaer, H. E. Elsayed-Ali, R. J. D. Miller, J. Cao, Y. Gao, and D. A. Mantell. Observation of surface enhanced multiphoton photoemission from metal surfaces in the short pulse limit. *The Journal of Chemical Physics*, 102(21):8606–8613, 1995.

[7] U. Höfer, I. L. Schumay, Ch. Reuß, U. Thomann, W. Wallauer, and Th. Fauster. Time-resolved coherent photoelectron spectroscopy of quantized electronic states on metal surfaces. *Science*, 277(5331):1480–1482, 1997.

[8] P. M. Paul, E. S. Toma, P. Breger, G. Mullot, F. Augë, Ph. Balcou, Muller H. G., and P. Agostini. Observation of a train of attosecond pulses from high harmonic generation. *Science*, 292(5522):1689–1692, 2001.

[9] M. Hentschel, R. Kienberger, Ch. Spielmann, G. A. Reider, N. Milosevic, T. Brabec, P. B. Corkum, U. Heinzmann, M. Drescher, and F. Krausz. Attosecond metrology. *Nature*, 414(6863):509–513, 2001.

[10] R. Kienberger, M. Hentschel, C. Spielmann, G. A. Reider, N. Milosevic, U. Heinzmann, M. Drescher, and F. Krausz. Sub-femtosecond X-ray pulse generation and measurement. *Applied Physics B: Lasers and Optics*, 74(SUPPL.):3–9, 2002.

[11] R. Kienberger, E. Goulielmakis, M. Uiberacker, A. Baltuška, V. Yakovlev, F. Bammer,

A. Scrinzi, Th. Westerwalbesloh, U. Kleineberg, U. Heinzmann, M. Drescher, and F. Krausz. Atomic transient recorder. *Nature*, 427(6977):817–821, 2004.

[12] A. L. Cavalieri, N. Müller, Th. Uphues, V. S. Yakovlev, A. Baltuška, B. Horvath, B. Schmidt, L. Blümel, R. Holzwarth, S. H., M. Drescher, U. Kleineberg, P. M. Echenique, R. Kienberger, F. Krausz, and U. Heinzmann. Attosecond spectroscopy in condensed matter. *Nature*, 449(7165):1029–1032, 2007.

[13] M. Schultze, M. Fieß, N. Karpowicz, J. Gagnon, M. Korbman, M. Hofstetter, S. Neppl, A. L. Cavalieri, Y. Komninos, Th. Mercouris, C. A. Nicolaides, R. Pazourek, S. Nagele, J. Feist, J. Burgdörfer, A. M. Azzeer, R. Ernstorfer, R. Kienberger, U. Kleineberg, E. Goulielmakis, F. Krausz, and V. S. Yakovlev. Delay in photoemission. *Science*, 328(5986):1658–1662, 2010.

[14] R. Pazourek, S. Nagele, and J. Burgdörfer. Attosecond chronoscopy of photoemission. *Reviews of Modern Physics*, 87(3):765–802, 2015.

[15] E. Goulielmakis, Z.-H. Loh, A. Wirth, R. Santra, N. Rohringer, V. S. Yakovlev, S. Zherebtsov, T. Pfeifer, A. M. Azzeer, M. F. Kling, S. R. Leone, and F. Krausz. Real-time observation of valence electron motion. *Nature*, 466(7307):739–743, 2010.

[16] M. Schultze, E. M. Bothschafter, A. Sommer, S. Holzner, W. Schweinberger, M. Fiess, M. Hofstetter, R. Kienberger, V. Apalkov, V. S. Yakovlev, M. I. Stockman, and F. Krausz. Controlling dielectrics with the electric field of light. *Nature*, 493(7430):75–78, 2012.

[17] C. Ott, A. Kaldun, L. Argenti, P. Raith, K. Meyer, M. Laux, Y. Zhang, A. Blättermann, S. Hagstotz, T. Ding, R. Heck, J. Madroñero, F. Martín, and T. Pfeifer. Reconstruction and control of a time-dependent two-electron wave packet. *Nature*, 516(7531):374–378, 2014.

[18] M. Uiberacker, Th. Uphues, M. Schultze, A. J. Verhoef, V. S. Yakovlev, M. F. Kling, J. Rauschenberger, N. M. Kabachnik, H. Schröder, M. Lezius, K. L. Kompa, H.-G. Muller, M. J. J. Vrakking, S. Hendel, U. Kleineberg, U. Heinzmann, M. Drescher, and F. Krausz. Attosecond real-time observation of electron tunnelling in atoms. *Nature*, 446(7136):627–632, 2007.

[19] F. Calegari, D. Ayuso, A. Trabattoni, L. Belshaw, S. De Camillis, S. Anumula, F. Frassetto, L. Poletto, A. Palacios, P. Decleva, J. B. Greenwood, F. Martín, and M. Nisoli. Ultrafast electron dynamics in phenylalanine initiated by attosecond pulses. *Science*, 346:336–339, 2014.

[20] M. Ossiander, F. Siegrist, V. Shirvanyan, R. Pazourek, A. Sommer, T. Latka, A. Guggenmos, S. Nagele, J. Feist, J. Burgdörfer, R. Kienberger, and M. Schultze. Attosecond correlation dynamics. *Nature Physics*, 1(November):10.1038/nphys3941, 2016.

[21] K. Klünder, J. M. Dahlström, M. Gisselbrecht, T. Fordell, M. Swoboda, D. Guénot, P. Johnsson, J. Caillat, J. Mauritsson, A. Maquet, R. Taïeb, and A. L'Huillier. Probing single-photon ionization on the attosecond time scale. *Physical Review Letters*, 106(14):143002, 2011.

[22] I. Jordan, M. Huppert, M. A. Brown, J. A. van Bokhoven, and H. J. Wörner. Photoelectron spectrometer for attosecond spectroscopy of liquids and gases. *Review of Scientific Instruments*, 86(12):123905, 2015.

[23] M. Huppert, I. Jordan, and H. J. Wörner. Attosecond beamline with actively stabilized and spatially separated beam paths. 123106, 2015.

[24] S. Neppl, R. Ernstorfer, E. M. Bothschafter, A. L. Cavalieri, D. Menzel, J. V. Barth, F. Krausz, R. Kienberger, and P. Feulner. Attosecond time-resolved photoemission from core and valence states of magnesium. *Physical Review Letters*, 109(8):22–26, 2012.

[25] S. Neppl, Ralph Ernstorfer, Adrian L Cavalieri, C. Lemell, G. Wachter, E. Magerl, E. M. Bothschafter, M. Jobst, M. Hofstetter, U. Kleineberg, Johannes V Barth, D. Menzel, J. Burgdörfer, P. Feulner, F. Krausz, and R. Kienberger. Direct observation of electron propagation and dielectric screening on the atomic length scale. *Nature*, 517(7534):342–346, 2015.

[26] R. Locher, L. Castiglioni, M. Lucchini, M. Greif, L. Gallmann, J. Osterwalder, M. Hengsberger, and U. Keller. Energy-dependent photoemission delays from noble metal surfaces by attosecond interferometry. *Optica*, 2(5):405, 2015.

[27] W. A. Okell, T. Witting, D. Fabris, C. A. Arrell, J. Hengster, S. Ibrahimkutty, A. Seiler, M. Barthelmess, S. Stankov, D. Y. Lei, Y. Sonnefraud, M. Rahmani, T. Uphues, S. A. Maier, J. P. Marangos, and J. W. G. Tisch. Temporal broadening of attosecond photoelectron wavepackets from solid surfaces. *Optica*, 2(4):383, 2015.

[28] Z. Tao, C. Chen, T. Szilvasi, M. Keller, M. Mavrikakis, H. C. Kapteyn, and M. M. Murnane. Direct time-domain observation of attosecond final-state lifetimes in photoemission from solids. *Science*, 353(6294):62–67, 2016.

[29] C. Chen, Z. Tao, A. Carr, P. Matyba, T. Szilvási, S. Emmerich, M. Piecuch, M. Keller, D. Zusin, S. Eich, M. Rollinger, W. You, S. Mathias, U. Thumm, M. Mavrikakis, M. Aeschlimann, P. M. Oppeneer, H. C. Kapteyn, and M. M. Murnane. Distinguishing attosecond electron-electron scattering and screening in transition metals. *Proceedings of the National Academy of Sciences of the United States of America*, page 201706466, 2017.

[30] N. D. Lang and W. Kohn. Theory of metal surfaces: Induced surface charge and image potential. *Physical Review B*, 7(8):3541–3550, 1973.

[31] A. Liebisch. Electronic screening at metal surfaces and the connection with physical phenomena. *Physica Scripta*, 35:354, 1986.

[32] F. Siek, S. Neb, P. Bartz, M. Hensen, C. Strüber, S. Fiechter, M. Torrent-Sucarrat, V. M. Silkin, E. E. Krasovskii, N. M. Kabachnik, S. Fritzsche, R. D. Muiño, P. M. Echenique, A. K. Kazansky, N. Müller, W. Pfeiffer, and U. Heinzmann. Angular momentum-induced delays in solid-state photoemission enhanced by intra-atomic interactions. *Science*, 357(6357):1274–1277, 2017.

[33] L. Kasmi, M. Lucchini, L. Castiglioni, P. Kliuiev, J. Osterwalder, M. Hengsberger, L. Gallmann, P. Krüger, and U. Keller. Effective mass effect in attosecond electron transport. *Optica*, 4(12):1492, 2017.

[34] M. Lucchini, L. Castiglioni, L. Kasmi, P. Kliuiev, A. Ludwig, M. Greif, J. Osterwalder, M. Hengsberger, L. Gallmann, and U. Keller. Light-matter interaction at surfaces in the spatiotemporal limit of macroscopic models. *Physical Review Letters*, 115(13):137401, 2015.

[35] S. Neppl. *Attosecond Time-Resolved Photoemission from Surfaces and Interfaces*. PhD thesis, Technische Universität München, 2012.

[36] F. Krausz and M. Y. Ivanov. Attosecond physics. *Reviews of Modern Physics*, 81(1):163–234, 2009.

[37] L. V. Keldysh. Ionization in the field of a strong electromagnetic wave. *Soviet Physics JETP*, 20(5):1307–1314, 1965.

[38] M. Protopapas, C. H. Keitel, and P. L. Knight. Atomic physics with super-high intensity lasers. *Reports on Progress in Physics*, 60(4):389–486, 1997.

[39] AM Perelomov, VS Popov, and MV Terent'ev. Ionization of atoms in an alternating electric field. *Sov. Phys. JETP*, 23(5):924–934, 1966.

[40] M. V. Ammosov, N. B. Delone, and V. P. Krainov. Tunnel ionization of complex atoms and of atomic ions in an alternating electromagnetic field. *Sov. Phys. JETP*, 64(December 1986):138–141, 1986.

[41] G. L. Yudin and M. Y. Ivanov. Nonadiabatic tunnel ionization: Looking inside a laser cycle. *Physical Review A*, 64(1):013409, 2001.

[42] T. Popmintchev, M.-C. Chen, D. Popmintchev, P. Arpin, S. Brown, S. Alisauskas, G. Andriukaitis, T. Balciunas, O. D. Mucke, A. Pugzlys, A. Baltuška, B. Shim, S. E. Schrauth, A. Gaeta, C. Hernandez-Garcia, L. Plaja, A. Becker, A. A. Jaroń-Becker, M. M. Murnane, and H. C. Kapteyn. Bright coherent ultrahigh harmonics in the keV X-ray regime from mid-infrared femtosecond lasers. *Science*, 336(6086):1287–1291, 2012.

[43] N. H. Burnett, H. A. Baldis, M. C. Richardson, and G. D. Enright. Harmonic generation in CO2 laser target interaction. *Applied Physics Letters*, 31(3):172–174, 1977.

[44] A. McPherson, G. Gibson, H. Jara, U. Johann, T. S. Luk, I. A. McIntyre, K. Boyer, and C. K. Rhodes. Studies of multiphoton production of vacuum-ultraviolet radiation in the rare gases. *Journal of the Optical Society of America B*, 4(4):595, 1987.

[45] M. Ferray, A. L'Huillier, X. F. Li, L. A. Lompre, G. Mainfray, and C. Manus. Multiple-harmonic conversion of 1064 nm radiation in rare gases. *Journal of Physics B: Atomic, Molecular and Optical Physics*, 21(3):L31–L35, 1988.

[46] X. F. Li, A. L'Huillier, M. Ferray, L. A. Lompré, and G. Mainfray. Multiple-harmonic generation in rare gases at high laser intensity. *Physical Review A*, 39(11):5751–5761, 1989.

[47] A. L'Huillier, K. J. Schafer, and K. C. Kulander. Theoretical aspects of intense field harmonic generation. *Journal of Physics B: Atomic, Molecular and Optical Physics*, 24(15):3315–3341, 1991.

[48] A. L'Huillier, P. Balcou, S. Candel, K. J. Schafer, and K. C. Kulander. Calculations of high-order harmonic-generation processes in xenon at 1064 nm. *Physical Review A*, 46(5):2778–2790, 1992.

[49] P. B. Corkum. Plasma perspective on strong field multiphoton ionization. *Physical Review Letters*, 71(13):1994–1997, 1993.

[50] M. Lewenstein, Ph. Balcou, M. Y.. Ivanov, A. L'Huillier, and P. B. Corkum. Theory of high-harmonic generation by low-frequency laser fields. *Physical Review A*, 49(3):2117–2132, 1994.

[51] A. D. Shiner, C. Trallero-Herrero, N. Kajumba, H. C. Bandulet, D. Comtois, François Légaré, M. Giguère, J. C. Kieffer, P. B. Corkum, and D. M. Villeneuve. Wavelength scaling of high harmonic generation efficiency. *Physical Review Letters*, 103(7):1–4, 2009.

[52] A. D. Shiner, B. E. Schmidt, C. Trallero-Herrero, H. J. Wörner, S. Patchkovskii, P. B. Corkum, J-C. Kieffer, François Légaré, and D. M. Villeneuve. Probing collective multi-electron dynamics in xenon with high-harmonic spectroscopy. *Nature Physics*, 7(6):464–467, 2011.

[53] K. S. Budil, P. Salières, A. L'Huillier, T. Ditmire, and M. D. Perry. Influence of ellipticity on harmonic generation. *Physical Review A*, 48(5):R3437–R3440, 1993.

[54] P. Dietrich, N. H. Burnett, M. Yu. Ivanov, and P. B. Corkum. High-harmonic generation and correlated two-electron multiphoton ionization with elliptically polarized light. *Physical Review A*, 50(5):R3585–R3588, 1994.

[55] P. Antoine, A. L'Huillier, M. Lewenstein, P. Salières, and B. Carré. Theory of high-order harmonic generation by an elliptically polarized laser field. *Physical Review A*, 53(3):1725–1745, 1996.

[56] G. Sansone, E. Benedetti, F. Calegari, C. Vozzi, L. Avaldi, R. Flammini, L. Poletto, P. Villoresi, C. Altucci, R. Velotta, S. Stagira, S. De Silvestri, and M. Nisoli. Isolated single-cycle attosecond pulses. *Science*, 314(5798):443–446, 2006.

[57] H. Mashiko, S. Gilbertson, C. Li, S. D. Khan, M. M. Shakya, E. Moon, and Z. Chang. Double optical gating of high-order harmonic generation with carrier-envelope phase stabilized lasers. *Physical Review Letters*, 100(10):103906, 2008.

[58] T. Fan, P. Grychtol, R. Knut, C. Hernández-García, D. D. Hickstein, D. Zusin, C. Gentry, F. J. Dollar, C. A. Mancuso, C. W. Hogle, O. Kfir, D. Legut, K. Carva, J. L. Ellis, K. M. Dorney, C. Chen, O. G. Shpyrko, E. E. Fullerton, O. Cohen, P. M. Oppeneer, D. B. Milošević, A. Becker, A. A. Jaroń-Becker, T. Popmintchev, M. M. Murnane, and H. C. Kapteyn.

Bright circularly polarized soft X-ray high harmonics for X-ray magnetic circular dichroism. *Proceedings of the National Academy of Sciences*, 112(46):14206–14211, 2015.

[59] W. Becker, S. Long, and J. K. McIver. Modeling harmonic generation by a zero-range potential. *Physical Review A*, 50(2):1540–1560, 1994.

[60] J. Tate, T. Auguste, H. G. Muller, P. Salières, P. Agostini, and L. F. DiMauro. Scaling of wave-packet dynamics in an intense midinfrared field. *Physical Review Letters*, 98(1):013901, 2007.

[61] G. Farkas and C. Tóth. Proposal for attosecond light pulse generation using laser induced multiple-harmonic conversion processes in rare gases. *Physics Letters A*, 168(5-6):447–450, 1992.

[62] N. Dudovich, J. Levesque, O. Smirnova, D. Zeidler, D. Comtois, M. Yu. Ivanov, D. M. Villeneuve, and P. B. Corkum. Attosecond temporal gating with elliptically polarized light. *Physical Review Letters*, 97(25):1–4, 2006.

[63] D. Shafir, H. Soifer, B. D. Bruner, M. Dagan, Y. Mairesse, S. Patchkovskii, M. Y.. Ivanov, O. Smirnova, and N. Dudovich. Resolving the time when an electron exits a tunnelling barrier. *Nature*, 485(7398):343–346, 2012.

[64] N. Dudovich, O. Smirnova, J. Levesque, Y. Mairesse, M. Yu. Ivanov, D. M. Villeneuve, and P. B. Corkum. Measuring and controlling the birth of attosecond XUV pulses. *Nature Physics*, 2(November):781–786, 2006.

[65] P. Balcou, A. S. Dederichs, M. B. Gaarde, and A. L'Huillier. Quantum-path analysis and phase matching of high-order harmonic generation and high-order frequency mixing processes in strong laser fields. *Journal of Physics B: Atomic, Molecular and Optical Physics*, 32(12):2973–2989, 1999.

[66] Ph. Balcou and A. L'Huillier. Phase-matching effects in strong-field harmonic generation. *Physical Review A*, 47(2):1447–1459, 1993.

[67] P. Balcou, P. Salières, A. L'Huillier, and M. Lewenstein. Generalized phase-matching conditions for high harmonics: The role of field-gradient forces. *Physical Review A*, 55(4):3204–3210, 1997.

[68] C. Heyl, J. Güdde, A. L'Huillier, and U. Höfer. High-order harmonic generation with μJ

laser pulses at high repetition rates. *Journal of Physics B: Atomic, Molecular and Optical Physics*, 45(7):074020, 2012.

[69] T. Popmintchev, M.-C. Chen, A. Bahabad, M. Gerrity, P. Sidorenko, O. Cohen, I. P. Christov, M. M. Murnane, and H. C. Kapteyn. Phase matching of high harmonic generation in the soft and hard X-ray regions of the spectrum. *Proceedings of the National Academy of Sciences*, 106(26):10516–10521, 2009.

[70] L. G. Gouy. Sur une propriété nouvelle des ondes lumineuses. *C. R. Acad. Sci. Paris*, 110:1251–1253, 1890.

[71] A. B. Ruffin, J. F. Whitaker, S. Feng, H. G. Winful, and J. V. Rudd. Direct observation of the Gouy phase shift with single-cycle terahertz pulses. In *Quantum Electronics and Laser Science Conference*, volume JTHB3, page 190, 1992.

[72] D. Hoff, M. Krüger, L. Maisenbacher, A. M. Sayler, G. G. Paulus, and P. Hommelhoff. Tracing the phase of focused broadband laser pulses. *Nature Physics*, 13(10):947–951, 2017.

[73] M. Lewenstein, P. Salières, and A. L'Huillier. Phase of the atomic polarization in high-order harmonic generation. *Physical Review A*, 52(6):4747–4754, 1995.

[74] E. Goulielmakis, M. Schultze, M. Hofstetter, V. S. Yakovlev, J. Gagnon, M. Uiberacker, A. L. Aquila, E. M. Gullikson, D. T. Attwood, R. Kienberger, F. Krausz, and U. Kleineberg. Single-cycle nonlinear optics. *Science*, 320(5883):1614–1617, 2008.

[75] I. P. Christov, M. M. Murnane, and H. C. Kapteyn. High-harmonic generation of attosecond pulses in the single-cycle regime. *Physical Review Letters*, 78(7):1251–1254, 1997.

[76] Y. Tamaki, J. Itatani, Y. Nagata, M. Obara, and K. Midorikawa. Highly efficient, phase-matched high-harmonic generation by a self-guided laser beam. *Physical Review Letters*, 82(7):1422–1425, 1999.

[77] C. G. Durfee III, A. R. Rundquist, S. Backus, C. Herne, M. M. Murnane, and H. C. Kapteyn. Phase matching of high-order harmonics in hollow waveguides. *Physical Review Letters*, 83(11):2187–2190, 1999.

[78] V. S. Yakovlev, M. Y.. Ivanov, and F. Krausz. Enhanced phase-matching for generation of soft X-ray harmonics and attosecond pulses in atomic gases. *Optics express*, 15(23):15351–64, 2007.

[79] C. Heyl, H. Coudert-Alteirac, M. Miranda, M. Louisy, K. Kovacs, V. Tosa, E. Balogh, K. Varjú, A. L'Huillier, A. Couairon, and C. L. Arnold. Scale-invariant nonlinear optics in gases. *Optica*, 3(1):75, 2016.

[80] F. Ferrari, F. Calegari, M. Lucchini, C. Vozzi, S. Stagira, G. Sansone, and M. Nisoli. High-energy isolated attosecond pulses generated by above-saturation few-cycle fields. *Nature Photonics*, 4(12):875–879, 2010.

[81] M.-C. Chen, C. A. Mancuso, C. Hernandez-Garcia, F. Dollar, B. Galloway, D. Popmintchev, P.-C. Huang, B. Walker, L. Plaja, A. A. Jaroń-Becker, A. Becker, M. M. Murnane, H. C. Kapteyn, and T. Popmintchev. Generation of bright isolated attosecond soft X-ray pulses driven by multicycle midinfrared lasers. *Proceedings of the National Academy of Sciences*, 111(23):E2361–E2367, 2014.

[82] M. Nisoli, S. De Silvestri, and O. Svelto. Generation of high energy 10 fs pulses by a new pulse compression technique. *Applied Physics Letters*, 68(20):2793–2795, 1996.

[83] M Nisoli, S De Silvestri, O Svelto, R Szipöcs, K. Ferencz, Ch. Spielmann, S. Sartania, and F. Krausz. Compression of high-energy laser pulses below 5 fs. *Optics Letters*, 22(8):522, 1997.

[84] A. Baltuška, M. Uiberacker, E. Goulielmakis, R. Kienberger, V. Sv Yakovlev, Th. Udem, T.W. Hansch, and F. Krausz. Phase-controlled amplification of few-cycle laser pulses. *IEEE Journal of Selected Topics in Quantum Electronics*, 9(4):972–989, 2003.

[85] Th. Udem, J. Reichert, R. Holzwarth, and T. W. Hänsch. Absolute optical frequency measurement of the cesium D_1 line with a mode-locked laser. *Physical Review Letters*, 82(18):3568–3571, 1999.

[86] S. A. Diddams, D. J. Jones, J. Ye, S. T. Cundiff, J. L. Hall, J. Ranka, R. Windeler, R. Holzwarth, T. Udem, and T. W. Hänsch. Direct link between microwave and optical frequencies with a 300 THz femtosecond laser comb. *Physical Review Letters*, 84(22):5102–5105, 2000.

[87] Th. Udem, R. Holzwarth, and T. W. Hänsch. Optical frequency metrology. *Nature*, 416(6877):233–237, 2002.

[88] M. Fieß. *Advancing attosecond metrology*. PhD thesis, Technische Universität München, 2010.

[89] A. Wirth. *Attosecond Transient Absorption Spectroscopy*. PhD thesis, Technische Universität München, 2011.

[90] M. Th. Hassan, T. T. Luu, A. Moulet, O. Raskazovskaya, P. Zhokhov, M. Garg, N. Karpowicz, A. M. Zheltikov, V. Pervak, F. Krausz, and E. Goulielmakis. Optical attosecond pulses and tracking the nonlinear response of bound electrons. *Nature*, 530(7588):66–70, 2016.

[91] B. L. Henke, J. P. Knauer, and K. Premaratne. The characterization of X-ray photocathodes in the 0.1-10 keV photon energy region. *Journal of Applied Physics*, 52(3):1509–1520, 1981.

[92] A. Guggenmos. Private conversation. Technical report, 2018.

[93] A. Guggenmos, M. Jobst, M. Ossiander, S. Radünz, J. Riemensberger, M. Schäffer, A. Akil, C. Jakubeit, P. Böhm, S. Noever, B. Nickel, R. Kienberger, and U. Kleineberg. Chromium/scandium multilayer mirrors for isolated attosecond pulses at 145 eV. *Optics Letters*, 40(12):2846, 2015.

[94] M. Hofstetter, M. Schultze, M. Fieß, B. Dennhardt, A. Guggenmos, J. Gagnon, V. S. Yakovlev, E. Goulielmakis, R. Kienberger, E. M. Gullikson, F. Krausz, and U. Kleineberg. Attosecond dispersion control by extreme ultraviolet multilayer mirrors. *Optics Express*, 19(3):1767, 2011.

[95] C. A. Schmuttenmaer, M. Aeschlimann, H. E. Elsayed-Ali, R. J. D. Miller, D. A. Mantell, J. Cao, and Y. Gao. Time-resolved two-photon photoemission from Cu(100): Energy dependence of electron relaxation. *Physical Review B*, 50(12):8957–8960, 1994.

[96] J. C. Baggesen and L. B. Madsen. Secondary-electron cascade in attosecond photoelectron spectroscopy from metals. *Physical Review A*, 80(3):1–4, 2009.

[97] C. Lemell, B. Solleder, K. Tkési, and J. Burgdörfer. Simulation of attosecond streaking of electrons emitted from a tungsten surface. *Physical Review A*, 79(6):062901, 2009.

[98] E. E. Krasovskii. Attosecond spectroscopy of solids: Streaking phase shift due to lattice scattering. *Physical Review B*, 84(19):195106, 2011.

[99] E. E. Krasovskii, C. Friedrich, W. Schattke, and P. M. Echenique. Rapid propagation of a bloch wave packet excited by a femtosecond ultraviolet pulse. *Physical Review B*, 94(19):195434, 2016.

[100] A. G. Borisov, D. Sánchez-Portal, A. K. Kazansky, and P. M. Echenique. Resonant and nonresonant processes in attosecond streaking from metals. *Physical Review B*, 87(12):2–5, 2013.

[101] Q. Liao and U. Thumm. Attosecond time-resolved photoelectron dispersion and photoemission time delays. *Physical Review Letters*, 112(2):1–5, 2014.

[102] G. D. Mahan. Theory of photoemission in simple metals. *Physical Review B*, 2(11):4334–4350, 1970.

[103] J. B. Pendry. Theory of photoemission. *Surface Science*, 57(2):679–705, 1976.

[104] A. Jain, R. Heider, M. Wagner, A. Duensing, T. Gaumnitz, I. Jordan, J. Ma, J. Riemensberger, M. Mittermair, W. Helml, R. Kienberger, and H. J. Wörner. Attosecond-streaking spectroscopy on a liquid-water microjet. *in preperation*, 2018.

[105] B. Winter, R. Weber, W. Widdra, M. Dittmar, M. Faubel, and I. V. Hertel. Full valence band photoemission from liquid water using EUV synchrotron radiation. *Journal of Physical Chemistry A*, 108(14):2625–2632, 2004.

[106] B. Winter and M. Faubel. Photoemission from liquid aqueous solutions. *Chemical Reviews*, 106(4):1176–1211, 2006.

[107] Niklas Ottosson, Manfred Faubel, Stephen E. Bradforth, Pavel Jungwirth, and Bernd Winter. Photoelectron spectroscopy of liquid water and aqueous solution: Electron effective attenuation lengths and emission-angle anisotropy. *Journal of Electron Spectroscopy and Related Phenomena*, 177(2-3):60–70, 2010.

[108] S. Thürmer, R. Seidel, M. Faubel, W. Eberhardt, J. C. Hemminger, S. E. Bradforth, and B. Winter. Photoelectron angular distributions from liquid water: Effects of electron scattering. *Physical Review Letters*, 111(17):173005, 2013.

[109] Stefan Hüfner. *Photoelectron Spectroscopy*. Advanced Texts in Physics. Springer Berlin Heidelberg, Berlin, Heidelberg, 2003 edition, 2003.

[110] A. Damascelli. Probing the electronic structure of complex systems by ARPES. *Physica Scripta*, T109:61, 2004.

[111] A. Damascelli. Angle-resolved photoemission studies of the cuprate superconductors. *Review of Modern Physics*, 75(April):473, 2003.

[112] R. Schlaf. Calibration of photoemission spectra and work function determination, 2017.

[113] T. X. Carroll, J. D. Bozek, E. Kukk, V. Myrseth, L. J. Sæthre, T. D. Thomas, and K. Wiesner. Xenon N4,5OO auger spectruma useful calibration source. *Journal of Electron Spectroscopy and Related Phenomena*, 125(2):127–132, 2002.

[114] M. P. Seah and W. A. Dench. Quantitative electron spectroscopy of surfaces: A standard data base for electron inelastic mean free paths in solids. *Surface and Interface Analysis*, 1(1):2–11, 1979.

[115] S. Tanuma, C. J. Powell, and D. R. Penn. Calculations of electron inelastic mean free paths. V. Data for 14 organic compounds over the 50-2000 eV range. *Surface and Interface Analysis*, 21(3):165–176, 1994.

[116] S. Tanuma, C. J. Powell, and D. R. Penn. Calculations of electron inelastic mean free paths. *Surface and Interface Analysis*, 37(1):1–14, 2005.

[117] S. Tanuma, C. J. Powell, and D. R. Penn. Calculations of electron inelastic mean free paths. IX. Data for 41 elemental solids over the 50 eV to 30 keV range. *Surface and Interface Analysis*, 43(3):689–713, 2011.

[118] R. A. Bartynski, R. H. Gaylord, T. Gustafsson, and E. W. Plummer. Angle-resolved photoemission study of the surface and bulk electronic structure of Mg(0001) and Mg(1120). *Physical Review B*, 33(6):3644–3656, 1986.

[119] W. Schattke and M. A. Van Hove, editors. *Solid-State Photoemission and Related Methods*. Wiley-VCH Verlag GmbH, Weinheim, Germany, 2003.

[120] C. N. Berglund and W. E. Spicer. Photoemission studies of copper and silver: Experiment. *Physical Review*, 136(1953):A1044–A1064, 1964.

[121] C. N. Berglund and W. E. Spicer. Photoemission studies of copper and silver: Theory. *Physical Review*, 136(4A), 1964.

[122] E. E. Krasovskii and W. Schattke. Surface electronic structure with the linear methods of band theory. *Physical Review B*, 56(20):12874–12883, 1997.

[123] E. E. Krasovskii and W. Schattke. Calculation of the wave functions for semi-infinite crystals with linear methods of band theory. *Physical Review B*, 59(24):R15609–R15612, 1999.

[124] J. Itatani, F. Quéré, G. L. Yudin, M. Y. Ivanov, F. Krausz, and P. B. Corkum. Attosecond streak camera. *Physical Review Letters*, 88(17):173903, 2002.

[125] M. Drescher, M. Hentschel, R. Kienberger, G. Tempea, C. Spielmann, Corkum P. B. Reider, G. A., and F. Krausz. X-ray pulses approaching the attosecond frontier. *Science*, 291(5510):1923–1927, 2001.

[126] M. Kitzler, N. Milosevic, A. Scrinzi, F. Krausz, and T. Brabec. Quantum theory of attosecond XUV pulse measurement by laser dressed photoionization. *Physical Review Letters*, 88(17):88–91, 2002.

[127] Y. Mairesse and F. Quéré. Frequency-resolved optical gating for complete reconstruction of attosecond bursts. *Physical Review A*, 71(1):1–4, 2005.

[128] F. Quéré, Y. Mairesse, and J. Itatani. Temporal characterization of attosecond XUV fields. *Journal of Modern Optics*, 52(2-3):339–360, 2005.

[129] H. G. Muller. Reconstruction of attosecond harmonic beating by interference of two-photon transitions. *Applied Physics B: Lasers and Optics*, 74(SUPPL.):17–21, 2002.

[130] R. López-Martens, K. Varjú, P. Johnsson, J. Mauritsson, Y. Mairesse, P. Salières, M. B. Gaarde, K. J. Schafer, A. Persson, S. Svanberg, C. G. Wahlström, and A. L'Huillier. Amplitude and phase control of attosecond light pulses. *Physical Review Letters*, 94(3):0–4, 2005.

[131] J. M. Dahlström, A. L'Huillier, and A. Maquet. Introduction to attosecond delays in photoionization. *Journal of Physics B: Atomic, Molecular and Optical Physics*, 45(18):183001, 2012.

[132] C. Chen, Z. Tao, C. Hernandez-Garcia, P. Matyba, A. Carr, R. Knut, O. Kfir, D. Zusin, C. Gentry, P. Grychtol, O. Cohen, L. Plaja, A. Becker, A. Jaron-Becker, H. Kapteyn, and M. Murnane. Tomographic reconstruction of circularly polarized high-harmonic fields: 3D attosecond metrology. *Science Advances*, 2(2):e1501333–e1501333, 2016.

[133] V. Gruson, L. Barreau, Á. Jiménez-Galan, F. Risoud, J. Caillat, A. Maquet, B. Carré, F. Lepetit, J.-F. Hergott, T. Ruchon, L. Argenti, R. Taïeb, F. Martín, and P. Salières. Attosecond dynamics through a fano resonance: Monitoring the birth of a photoelectron. *Science*, 354(6313):734–738, 2016.

[134] D. M. Villeneuve, P. Hockett, M. J. J. Vrakking, and H. Niikura. Coherent imaging of an attosecond electron wave packet. *Science*, 356(6343):1150–1153, 2017.

[135] M. Isinger, R. J. Squibb, D. Busto, S. Zhong, A. Harth, D. Kroon, S. Nandi, C. L. Arnold, M. Miranda, J. M. Dahlström, E. Lindroth, R. Feifel, M. Gisselbrecht, and A. L'Huillier. Photoionization in the time and frequency domain. *Science*, 358(6365):893–896, 2017.

[136] D. Strickland and G. Mourou. Compression of amplified chirped optical pulses. *Optics Communications*, 56(3):219–221, 1985.

[137] A Stingl, R. Szipöcs, M. Lenzner, C. Spielmann, and F. Krausz. Sub-10-fs mirror-dispersion-controlled Ti:sapphire laser. *Optics Letters*, 20(6):602, 1995.

[138] A. Stingl, R. Szipöcs, C. Spielmann, and F. Krausz. Generation of 11-fs pulses from a Ti:sapphire laser without the use of prisms. *Optics Letters*, 19(3):204, 1994.

[139] Z. Cheng, F. Krausz, and Ch Spielmann. Compression of 2 mJ kilohertz laser pulses to 17.5 fs by pairing double-prism compressor: Analysis and performance. *Optics Communications*, 201(1-3):145–155, 2002.

[140] P. Tournois. Acousto-optic programmable dispersive filter for adaptive compensation of group delay time dispersion in laser systems. *Optics Communications*, 140(4-6):245–249, 1997.

[141] M. Lenzner, Ch. Spielmann, E. Wintner, F. Krausz, and A. J. Schmidt. Sub-20-fs, kilohertz-repetition-rate Ti:sapphire amplifier. *Optics Letters*, 20(12):1397, 1995.

[142] S. Sartania, Z. Cheng, M. Lenzner, G. Tempea, C. Spielmann, F. Krausz, and K. Ferencz. Generation of 0.1-TW 5-fs optical pulses at a 1-kHz repetition rate. *Optics Letters*, 22(20):1562, 1997.

[143] D. F. Hotz. Gain narrowing in a laser amplifier. *Applied Optics*, 4(5):527, 1965.

[144] C. Spielmann, M. Lenzner, F. Krausz, and R. Szipöcs. Compact, high-throughput expansion-compression scheme for chirped pulse amplification in the 10 fs range. *Optics Communications*, 120(5-6):321–324, 1995.

[145] L. Canova, X. Chen, A. Trisorio, A. Jullien, A. Assion, G. Tempea, N. Forget, T. Oksenhendler, and R. Lopez-Martens. Carrier-envelope phase stabilization and control

using a transmission grating compressor and an AOPDF. *Optics Letters*, 34(9):1333, 2009.

[146] W. Schweinberger, A. Sommer, E. Bothschafter, J. Li, F. Krausz, R. Kienberger, and M. Schultze. Waveform-controlled near-single-cycle milli-joule laser pulses generate sub-10 nm extreme ultraviolet continua. *Optics Letters*, 37(17):3573, 2012.

[147] R. L. Fork, O. E. Martinez, and J. P. Gordon. Negative dispersion using pairs of prisms. *Optics Letters*, 9(5):150, 1984.

[148] E. Treacy. Optical pulse compression with diffraction gratings. *IEEE Journal of Quantum Electronics*, 5(9):454–458, 1969.

[149] Á. Börzsönyi, Z. Heiner, A. P. Kovács, M. P. Kalashnikov, and K. Osvay. Measurement of pressure dependent nonlinear refractive index of inert gases. *Optics Express*, 18(25):25847, 2010.

[150] E. A. J. Marcatili and R. A. Schmeltzer. Hollow metallic and dielectric waveguides for long distance optical transmission and lasers. *Bell System Technical Journal*, 43(4):1783–1809, 1964.

[151] S. T. Cundiff and J Ye. Colloquium: Femtosecond optical frequency combs. *Reviews of Modern Physics*, 75(1):325–342, 2003.

[152] F. W. Helbing, G. Steinmeyer, J. Stenger, H. R. Telle, and U. Keller. Carrier-envelope-offset dynamics and stabilization of femtosecond pulses. *Applied Physics B: Lasers and Optics*, 74(SUPPL.):35–42, 2002.

[153] R. Holzwarth. *Measuring the Frequency of Light using Femtosecond Laser Pulses*. PhD thesis, Ludwigs-Maximilian Universiät München, 2000.

[154] J. Reichert, R. Holzwarth, T. Udem, and T. W. Hänsch. Measuring the frequency of light with mode-locked lasers. *Optics Communications*, 172(1):59–68, 1999.

[155] T. Fuji, J. Rauschenberger, A. Apolonski, V. S. Yakovlev, G. Tempea, Th. Udem, C. Gohle, T. W. Hänsch, W. Lehnert, M. Scherer, and F. Krausz. Monolithic carrier-envelope phase-stabilization scheme. *Optics letters*, 30(3):332–334, 2005.

[156] G. G. Paulus, F. Grasbon, H. Walther, P. Villoresi, M. Nisoli, S. Stagira, E. Priori, and

S. De Silvestri. Absolute-phase phenomena in photoionization with few-cycle laser pulses. *Nature*, 414(6860):182–184, 2001.

[157] T. Wittmann, B. Horvath, W. Helml, M. G. Schaetzel, X. Gu, A. L. Cavalieri, G. G. Paulus, and R. Kienberger. Single-shot carrier-envelope phase measurement of few-cycle laser pulses. *Nature Physics*, 5(5):357–362, 2009.

[158] A. Apolonski, P. Dombi, G. G. Paulus, M. Kakehata, R. Holzwarth, Th. Udem, Ch. Lemell, K. Torizuka, J. Burgdörfer, T. W. Hänsch, and F. Krausz. Observation of light-phase-sensitive photoemission from a metal. *Physical Review Letters*, 92(7):73902, 2004.

[159] T. Paasch-Colberg, A. Schiffrin, N. Karpowicz, S. Kruchinin, Ö. Salam, S. Keiber, O. Razskazovskaya, S. Mühlbrandt, A. Alnaser, M. Kübel, V. Apalkov, D. Gerster, J. Reichert, T. Wittmann, J. V. Barth, M. I. Stockman, R. Ernstorfer, V. S.. Yakovlev, R. Kienberger, and F. Krausz. Solid-state light-phase detector. *Nature Photonics*, 8(3):214–218, 2014.

[160] D. J. Jones, S. A. Diddams, J. K. Ranka, A. Stentz, R. S. Wineder, J. L. Hall, and T. C. Cundiff. Carrier-envelope phase control of femtosecond mode-locked lasers and direct optical frequency synthesis. *Science*, 288(5466):635–639, 2000.

[161] M. Zimmermann, C. Gohle, R. Holzwarth, T. Udem, and T. W. Hänsch. Optical clockwork with an offset-free difference-frequency comb: Accuracy of sum- and difference-frequency generation. *Optics Letters*, 29(3):310, 2004.

[162] S. Koke, C. Grebing, H. Frei, A. Anderson, A. Assion, and G. Steinmeyer. Direct frequency comb synthesis with arbitrary offset and shot-noise-limited phase noise. *Nature Photonics*, 4(7):462–465, 2010.

[163] F. Lücking, A. Assion, A. Apolonski, F. Krausz, and G. Steinmeyer. Long-term carrier-envelope-phase-stable few-cycle pulses by use of the feed-forward method. *Optics Letters*, 37(11):2076, 2012.

[164] A. Baltuška, Th. Udem, M. Uiberacker, M. Hentschel, E. Goulielmakis, Ch. Gohle, R. Holzwarth, V. S. Yakovlev, A. Scrinzi, T. W. Hänsch, and F. Krausz. Attosecond control of electronic processes by intense light fields. *Nature*, 421(6923):611–615, 2003.

[165] M. Schultze. *Attosecond real time observation of ionization and electron-electron interactions*. PhD thesis, Ludwigs-Maximilian Universiät München, 2010.

[166] E. Magerl, S. Neppl, A. L. Cavalieri, E. M. Bothschafter, M. Stanislawski, Th. Uphues, M. Hofstetter, U. Kleineberg, J. V. Barth, D. Menzel, F. Krausz, R. Ernstorfer, R. Kienberger, and P. Feulner. A flexible apparatus for attosecond photoelectron spectroscopy of solids and surfaces. *Review of Scientific Instruments*, 82(6):063104, 2011.

[167] E. Magerl. *Attosecond Photoelectron Spectroscopy of Electron Tunneling*. PhD thesis, Ludwig Maximilians Universität, 2011.

[168] E. Goulielmakis, V. S. Yakovlev, A. L. Cavalieri, M. Uiberacker, V Pervak, A. Apolonski, R. Kienberger, U. Kleineberg, and F. Krausz. Attosecond control and measurement: Lightwave electronics. *Science*, 317(5839):769–775, 2007.

[169] Michael Jobst. *Attosecond Dynamics in Molecules and on Interfaces*. PhD thesis, Technische Universität München, 2015.

[170] E. M. Bothschafter, A. Schiffrin, V. S. Yakovlev, A. M. Azzeer, F. Krausz, R. Ernstorfer, and R. Kienberger. Collinear generation of ultrashort UV and XUV pulses. *Optics express*, 18(9):9173–80, 2010.

[171] K. Zhao, Q. Zhang, M. Chini, Y. Wu, X. Wang, and Z. Chang. Tailoring a 67 attosecond pulse through advantageous phase mismatch. *Optics Letters*, 37(18):3891–3893, 2012.

[172] T. Kita, T. Harada, N. Nakano, and H. Kuroda. Mechanically ruled aberration-corrected concave gratings for a flat-field grazing-incidence spectrograph. *Applied Optics*, 22(4):512, 1983.

[173] N. Nakano, H. Kuroda, T. Kita, and T. Harada. Development of a flat-field grazing-incidence XUV spectrometer and its application in picosecond XUV spectroscopy. *Applied Optics*, 23(14):2386, 1984.

[174] A. Guggenmos, A. Akil, M. Ossiander, M. Schäffer, A. M. Azzeer, G. Boehm, M.-C. Amann, R. Kienberger, M. Schultze, and U. Kleineberg. Attosecond photoelectron streaking with enhanced energy resolution for small-bandgap materials. *Optics Letters*, 41(16):3714, 2016.

[175] C.-H. Zhang and U. Thumm. Attosecond photoelectron spectroscopy of metal surfaces. *Physical Review Letters*, 102(12):1–4, 2009.

[176] C.-H. Zhang and U. Thumm. Effect of wave-function localization on the time delay in photoemission from surfaces. *Physical Review A*, 84(6):065403, 2011.

[177] Q. Liao and U. Thumm. Initial-state, mean-free-path, and skin-depth dependence of attosecond time-resolved IR-streaked XUV photoemission from single-crystalline magnesium. *Physical Review A*, 89(3):1–11, 2014.

[178] A. K. Kazansky and P. M. Echenique. One-electron model for the electronic response of metal surfaces to subfemtosecond photoexcitation. *Physical Review Letters*, 102(17):1–4, 2009.

[179] R. G. Musket, W. McLean, C. A. Colmenares, D. M. Makowiecki, and W. J. Siekhaus. Preparation of atomically clean surfaces of selected elements: A review. *Applications of Surface Science*, 10(2):143–207, 1982.

[180] F. Schiller, M. Heber, V. D. P. Servedio, and C. Laubschat. Electronic structure of Mg : From monolayers to bulk. *Physical Review B*, 70(12):125106, 2004.

[181] L. Aballe, A. Barinov, A. Locatelli, T. O. Mentes, and M. Kiskinova. Initial stages of heteroepitaxial Mg growth on W(110): Early condensation, anisotropic strain, and self-organized patterns. *Physical Review B - Condensed Matter and Materials Physics*, 75(11):1–9, 2007.

[182] L. M. Falicov. The band structure and fermi surface of magnesium. *Philosophical Transactions of the Royal Society A: Mathematical, Physical and Engineering Sciences*, 255(1051):55–83, 1962.

[183] J. C. Kimball, R. W. Stark, and F. M. Mueller. The fermi surface of magnesium III: Local and nonlocal pseudopotential band structure models for magnesium. *Physical Review*, 162(3):600–608, 1967.

[184] E. V. Chulkov, V. M. Silkin, and E. N. Shirykalov. Surface electronic structure of Be(0001) and Mg(0001). *Surface Science*, 188(1-2):287–300, 1987.

[185] P. Hofmann, Ch. Søndergaard, S. Agergaard, S. V. Hoffmann, J. E. Gayone, G. Zampieri, S. Lizzit, and A. Baraldi. Unexpected surface sensitivity at high energies in angle-resolved photoemission. *Physical Review B*, 66(24):245422, 2002.

[186] H. Timmers, M. Sabbar, J. Hellwagner, Y. Kobayashi, D. M. Neumark, and S. R. Leone. Polarization-assisted amplitude gating as a route to tunable, high-contrast attosecond pulses. *Optica*, 3(7):707, 2016.

[187] R. Scheuerer. *Polarisations- und winkelaufgelöste Photodesorptionsmessungen aus*

molekularen Kondensaten nach Rumpfanregung. PhD thesis, Technische Universität München, 1996.

[188] E. E. Krasovskii, W. Schattke, P. Jiíček, M. Vondráček, O. V. Krasovska, V. N. Antonov, A. P. Shpak, and I. Bartoš. Photoemission from Al(100) and (111): Experiment and ab initio theory. *Physical Review B - Condensed Matter and Materials Physics*, 78(16):165406, 2008.

[189] R. Kammerer, J. Barth, F. Gerken, C. Kunz, S. A. Flodstrøm, and L. I. Johansson. Surface-binding-energy shifts for sodium, magnesium, and aluminum metals. *Physical Review B*, 26(6):3491–3494, 1982.

[190] F. A. Gianturco, R. R. Lucchese, and N. Sanna. Calculation of low-energy elastic cross sections for electron-CF4 scattering. *The Journal of Chemical Physics*, 100(9):6464–6471, 1994.

[191] A. P. P. Natalense. Cross section and asymmetry parameter calculation for sulfur 1s photoionization of SF6. *Journal of Chemical Physics*, 111(12):5344–5348, 1999.

[192] J. Rundgren and G. Malmstrom. Transmission and reflection of low-energy electrons at the surface barrier of a metal. *Journal of Physics C: Solid State Physics*, 10(23):4671–4687, 1977.

[193] E. V. Chulkov, V. M. Silkin, and P. M. Echenique. Image potential states on metal surfaces: Binding energies and wave functions. *Surface Science*, 437(3):330–352, 1999.

[194] David R. Penn. Electron mean-free-path calculations using a model dielectric function. *Physical Review B*, 35(2):482–486, 1987.

[195] J. H. Weaver, C. G. Olson, and D. W. Lynch. Optical properties of crystalline tungsten. *Physical Review B*, 12(4):1293–1297, 1975.

[196] W. S. M. Werner, K. Glantschnig, and C. Ambrosch-Draxl. Optical constants and inelastic electron-scattering data for 17 elemental metals. *Journal of Physical and Chemical Reference Data*, 38(4):1013–1092, 2009.

[197] A. K. Kazansky and N. M. Kabachnik. Theoretical description of atomic photoionization by attosecond XUV pulses in a strong laser field: The case of p-shell ionization. *Journal of Physics B: Atomic, Molecular and Optical Physics*, 40(17):3413–3424, 2007.

[198] E. E. Krasovskii and M. Bonitz. Spectral line shape variations in time-resolved photoemission from a solid. *Physical Review Letters*, 99(24):1–4, 2007.

[199] L. Zhang, Y. Yan, Y. Yue, Q. Lin, O. Painter, R. G. Beausoleil, and A. E. Willner. On-chip two-octave supercontinuum generation by enhancing self-steepening of optical pulses. *Optics express*, 19(12):11584–11590, 2011.

[200] Q. Liao and U. Thumm. Attosecond time-resolved streaked photoemission from Mg-covered W(110) surfaces. *Physical Review A*, 92(3):031401, 2015.

[201] L. Verlet. Computer "experiments" on classical fluids. I. Thermodynamical properties of lennard-jones molecules. *Physical Review*, 159(1):98–103, 1967.

[202] W. C. Swope, H. C. Andersen, P. H. Berens, and K. R. Wilson. A computer simulation method for the calculation of equilibrium constants for the formation of physical clusters of molecules: Application to small water clusters. *The Journal of Chemical Physics*, 76(1):637–649, 1982.

[203] J Lindhard. On the properites of a gas of charged particles. *Kgl. Danske Videnskab. Selskab, Mat-fys. Medd.*, 28:8, 1954.

[204] N. D. Mermin. Lindhard dielectric function in the relaxation-time approximation. *Physical Review B*, 1(5):2362–2363, 1970.

[205] S. Tanuma, C. J. Powell, and D. R. Penn. Calculations of electron inelastic mean free paths for 31 materials. *Surface and Interface Analysis*, 11(11):577–589, 1988.

[206] M. Ossiander, J. Riemensberger, S. Neppl, M. Mittermair, M. Schäffer, A. Duensing, M. Wagner, R. Heider, M. Wurzer, M. Gerl, M. Schnitzenbaumer, J. V. Barth, F. Libisch, C. Lemell, J. Burgdörfer, P. Feulner, and R. Kienberger. Absolute timing of electron emission from crystal, surface and adsorbate states. *in preperation*, 2018.

[207] C. Lemell, S. Neppl, G. Wachter, K. Tkési, R. Ernstorfer, P. Feulner, R. Kienberger, and J. Burgdörfer. Real-time observation of collective excitations in photoemission. *Physical Review B*, 91(24):241101, 2015.

[208] N.E. Christensen and B Feuerbacher. Volume and surface photoemission from tungsten. I. Calculation of band structure and emission spectra, 1974.

[209] N. E. E. Christensen and B. Feuerbacher. Volume and surface photoemission from

tungsten. I. Calculation of band structure and emission spectra. *Physical Review B*, 10(6):2349, 1974.

[210] J. A. Becker, E. J. Becker, and R. G. Brandes. Reactions of oxygen with pure tungsten and tungsten containing carbon. *Journal of Applied Physics*, 32(3):411–423, 1961.

[211] K. Zakeri, T. R. F. Peixoto, Y. Zhang, J. Prokop, and J. Kirschner. On the preparation of clean tungsten single crystals. *Surface Science*, 604(2):L1–L3, 2010.

[212] M. Stöhr, R. Podloucky, M. Gabl, N. Memmel, and E. Bertel. Combined ab initio and LEED I V study of submonolayer adsorption of In on W(110). *Physical Review B*, 76(19):195449, 2007.

[213] M. Stöhr. *First Principles Investigations of Adsorption on a Transition Metal Surface: Oxygen and Indium on the (110) Surface of Tungsten*. PhD thesis, Universität Wien, 2009.

[214] A. Kim. *Attosecond time-resolved photoemission from solid samples*. PhD thesis, Technische Universität München, 2015.

[215] A. Abrami, M. Barnaba, L. Battistello, A. Bianco, B. Brena, G. Cautero, Q. H. Chen, D. Cocco, G. Comelli, S. Contrino, F. DeBona, S. Di Fonzo, C. Fava, P. Finetti, P. Furlan, A. Galimberti, A. Gambitta, D. Giuressi, R. Godnig, W. Jark, S. Lizzit, F. Mazzolini, P. Melpignano, L. Olivi, G. Paolucci, R. Pugliese, S. N. Qian, R. Rosei, G. Sandrin, A. Savoia, R. Sergo, G. Sostero, R. Tommasini, M. Tudor, D. Vivoda, F.Q. Wei, and F. Zanini. Super ESCA: First beamline operating at ELETTRA. *Review of Scientific Instruments*, 66(2):1618–1620, 1995.

[216] B. L. Henke, E. M. Gullikson, and J. C. Davis. X-ray interactions: Photoabsorption, scattering, transmission, and reflection at E = 50-30,000 eV, Z = 1-92. *Atomic Data and Nuclear Data Tables*, 54(2):181–342, 1993.

[217] J.J. Yeh and I. Lindau. Atomic subshell photoionization cross sections and asymmetry parameters: 1 < Z < 103. *Atomic Data and Nuclear Data Tables*, 32(1):1–155, 1985.

[218] M. Gerl. Time-resolved investigation of photoelectron dynamics by attosecond streaking spectroscopy on solids. Master's thesis, Technische Universität München, 2013.

[219] D. Singh, S.-H. Wei, and H. Krakauer. Instability of the ideal tungsten (001) surface. *Physical Review Letters*, 57(26):3292–3295, 1986.

[220] N. R. Avery. LEED, Auger and work function study of iodine adsorbed on W(110). *Surface Science*, 43(1):101–122, 1974.

[221] K. J. Rawlings, G. G. Price, and B. J. Hopkins. A LEED and AES study of the adsorption of iodine on W(100) at room temperature. *Surface Science*, 95(1):245–256, 1980.

[222] M. Ossiander. On the expansion of attosecond streaking spectroscopy towards ultrafast surface dynamics. Master's thesis, Technische Universität München, 2014.

[223] R. G. Jones. Halogen adsorption on solid surfaces. *Progress in Surface Science*, 27(1-2):25–160, 1988.

[224] Marcus Ossiander. *Absolute Photoemission Timing*. PhD thesis, Technische Universität München, 2018.

[225] A. Zangwill. *Physics at Surfaces*. Cambridge University Press.

[226] G. Wendin. Collective resonance in the 4d10 shell in atomic Xe. *Physics Letters A*, 37(5):445–446, 1971.

[227] M. Ya Amusia, V. K. Ivanov, and L. V. Chernysheva. Photoionization cross section of 4d10 Xe, Cs and Ba subshells with account of electron shell rearrangement. *Physics Letters A*, 59(3):191–193, 1976.

[228] L. H. Germer and J. W. May. Diffraction study of oxygen adsorption on a (110) tungsten face. *Surface Science*, 4(4):452–470, 1966.

[229] M. Stöhr, R. Podloucky, and S. Müller. Ab initio phase diagram of oxygen adsorption on W(110). *Journal of Physics: Condensed Matter*, 21(13):134017, 2009.

[230] K. E. Johnson, R. J. Wilson, and S. Chiang. Effects of adsorption site and surface stress on ordered structures of oxygen adsorbed on W(110). *Physical Review Letters*, 71(7):1055–1058, 1993.

[231] R.X. Ynzunza, R. Denecke, F.J. Palomares, J. Morais, E.D. Tober, Z. Wang, F.J. Garca de Abajo, J. Liesegang, Z. Hussain, M.A. Van Hove, and C.S. Fadley. Kinetics and atomic structure of o adsorption on W(110) from time- and state-resolved photoelectron spectroscopy and full-solid-angle photoelectron diffraction. *Surface Science*, 459(1-2):69–92, 2000.

[232] H. Daimon, R. Ynzunza, J. Palomares, H. Takabi, and C. S. Fadley. Direct structure analysis of W(110)-(1x1)-O by full solid-angle X-ray photoelectron diffraction with chemical-state resolution. *Surface Science*, 408(1-3):260–267, 1998.

[233] J. Feydt, A. Elbe, H. Engelhard, G. Meister, and A. Goldmann. Normal-emission photoelectron studies of the W(110)-(1x1)O surface. *Surface Science*, 440(1-2):213–220, 1999.

[234] B. McCarroll. Chemisorption and oxidation: Oxygen on tungsten. *The Journal of Chemical Physics*, 46(3):863, 1967.

[235] J. J. Boyle, Z. Altun, and H. P. Kelly. Photoionization cross-section calculation of atomic tungsten. *Physical Review A*, 47(6):4811–4830, 1993.

[236] J. Burgdörfer and J. Gibbons. Electron transport in the presence of a coulomb field. *Physical Review A*, 42(3):1206–1221, 1990.

[237] B. Solleder, C. Lemell, K. Tkési, N. Hatcher, and J. Burgdörfer. Spin-dependent low-energy electron transport in metals. *Physical Review B*, 76(7):075115, 2007.

[238] D. M. Riffe and G. K. Wertheim. Submonolayer oxidation of W(110): A high-resolution core-level photoemission study. *Surface Science*, 399(2-3):248–263, 1998.

[239] G. B. Blanchet, P. J. Estrup, and P. J. Stiles. Surface-reflectance-spectroscopy studies of H on W(110): Surface band structure and adsorbate geometry. *Physical Review Letters*, 44(3):171–174, 1980.

[240] R. H. Gaylord and S. D. Kevan. Electronic contributions to the hydrogen-induced reconstruction of W(110). *Physical Review B*, 37(14):8491–8494, 1988.

[241] Tun-wen Pi, Ie-hong Hong, and Chiu-ping Cheng. Synchrotron-radiation photoemission study of Ba on W(110). *Physical Review B*, 58(7):4149–4155, 1998.

[242] B. Kim, J. Chen, J. L. Erskine, W. N. Mei, and C. M. Wei. Surface and bulk photoelectron diffraction from W(110) 4f core levels. *Physical Review B*, 48(7):4735–4740, 1993.

[243] U. Becker, D. Szostak, H. G. Kerkhoff, M. Kupsch, B. Langer, R. Wehlitz, A. Yagishita, and T. Hayaishi. Subshell photoionization of Xe between 40 and 1000 eV. *Physical Review A*, 39(8):3902–3911, 1989.

[244] S. Doniach and M. Sunjic. Many-electron singularity in X-ray photoemission and X-ray line spectra from metals. *Journal of Physics C: Solid State Physics*, 3(2):285–291, 1970.

[245] D. M. Riffe, G. K. Wertheim, P. H. Citrin, and D. N. E. Buchanan. Core-hole lifetime and screening are different in the surface of W(110). *Physica Scripta*, 41(6):1009–1013, 1990.

[246] D. M. Riffe, G. K. Wertheim, and P. H. Citrin. Different core-hole lifetime and screening in the surface of W(110). *Physical Review Letters*, 63(18):1976–1979, 1989.

[247] R. Trebino, K. W. DeLong, D. N. Fittinghoff, J. N. Sweetser, M. A. Krumbügel, B. A. Richman, and D. J. Kane. Measuring ultrashort laser pulses in the time-frequency domain using frequency-resolved optical gating. *Review of Scientific Instruments*, 68(9):3277–3295, 1997.

[248] E. Goulielmakis. *Complete characterization of light waves using Attosecond pulses*. PhD thesis, Technische Universität Wien, 2005.

[249] D. J. Kane and R. Trebino. Characterization of arbitrary femtosecond pulses using frequency-resolved optical gating. *Ieee Journal of Quantum Electronics*, 29(2):571–579, 1993.

[250] D. Spangenberg, P. Neethling, E. Rohwer, M. H. Brügmann, and T. Feurer. Time-domain ptychography. *Physical Review A*, 91(2):021803, 2015.

[251] W. Hoppe. Beugung im inhomogenen Primärstrahlwellenfeld. I. Prinzip einer Phasenmessung von Elektronenbeungungsinterferenzen. *Acta Crystallographica Section A*, 25(4):495–501, 1969.

[252] P. Thibault, M. Dierolf, A. Menzel, O. Bunk, C. David, and F. Pfeiffer. High-resolution scanning X-ray diffraction microscopy. *Science*, 321(5887):379–382, 2008.

[253] D. F. Gardner, M. Tanksalvala, E. R. Shanblatt, X. Zhang, B. R. Galloway, C. L. Porter, R. Karl Jr, C. Bevis, D. E. Adams, H. C. Kapteyn, M. M. Murnane, and G. F. Mancini. Subwavelength coherent imaging of periodic samples using a 13.5nm tabletop high-harmonic light source. *Nature Photonics*, 11(4):259–263, 2017.

[254] K. W. DeLong, R. Trebino, J. Hunter, and W. E. White. Frequency-resolved optical gating with the use of second-harmonic generation. *Journal of the Optical Society of America B*, 11(11):2206, 1994.

[255] P. Sidorenko, O. Lahav, Z. Avnat, and O. Cohen. Ptychographic reconstruction algorithm for frequency-resolved optical gating: Super-resolution and supreme robustness. *Optica*, 3(12):1320, 2016.

[256] A. Maiden, D. Johnson, and P. Li. Further improvements to the ptychographical iterative engine. *Optica*, 4(7):736, 2017.

[257] J. N. Sweetser, D. N. Fittinghoff, and R. Trebino. Transient-grating frequency-resolved optical gating. *Optics Letters*, 22(8):519, 1997.

[258] M. Li, J. P. Nibarger, C. Guo, and G. N. Gibson. Dispersion-free transient-grating frequency-resolved optical gating. *Applied Optics*, 38(24):5250, 1999.

[259] J. Gagnon, E. Goulielmakis, and V. S. Yakovlev. The accurate FROG characterization of attosecond pulses from streaking measurements. *Applied Physics B: Lasers and Optics*, 92(1):25–32, 2008.

[260] M. Chini, S. Gilbertson, S. D. Khan, and Z. Chang. Characterizing ultrabroadband attosecond lasers. *Optics Express*, 18(12):13006, 2010.

[261] P. D. Keathley, S. Bhardwaj, J. Moses, G. Laurent, and F. X. Kärtner. Volkov transform generalized projection algorithm for attosecond pulse characterization. *New Journal of Physics*, 18(7):073009, 2016.

[262] X. Zhao, H. Wei, Y. Wu, and C. D. Lin. Phase-retrieval algorithm for the characterization of broadband single attosecond pulses. *Physical Review A*, 95(4):2–9, 2017.

[263] M. Lucchini, M. H. Brügmann, A. Ludwig, L. Gallmann, U. Keller, and T. Feurer. Ptychographic reconstruction of attosecond pulses. *Optics Express*, 23(23):29502, 2015.

Acknowledgements

Many persons contributed to the quantity and quality of the results presented in this thesis and to my enjoyment and success in conducting the experiments and (p)repairing lab equipment.

First, I would like to thank **Prof. Reinhard Kienberger** for the opportunity to conduct my doctoral studies in his group at the Max-Plank Institute for Quantum Optics and TUM. I enjoyed plenty of space to pursue ideas beyond the set paths and interpretations and venture into numerical and interdisciplinary aspects of photoemission and surface science. He always supported me and I am thankful for the opportunities of joining multiple international conferences. Far beyond the weekly group meeting I was privileged to receive his guidance and camaraderie and I feel grateful to be a part of the "three founding PHD students" of the Chair of Laser and X-ray Physics at TUM.

I would like to thank **Prof. Peter Feulner** for his guidance into surface science and photoemission and his cheerful attitude to the solution of highly sophisticated challenges of surface and ultra-high vacuum science. Many of the works presented in this thesis are founded on his ideas and knowledge of surface adsorption and its application. I especially enjoyed our beamtime at the Elletra synchrotron.

Furthermore, I would like to further thank **Prof. Johannes Barth**, **Dr. Francesco Allegretti** and the team of E20 for their helpfulness and our productive collaborations, as well as **Prof. Eberhardt Riedle** and his team at BMO for their support and teaching me a lot about optics and ultrashort lasers.

I am grateful to **Prof. Eugene Krasovskii** and **Prof. Andrey Kazansky** for sharing their knowledge and deep understanding of solid-state and atomic and physics and photoemission and for providing valuable numerical calculations.

I feel grateful to all students and postdocs working at the AS-3 beamline previous to my arrival in 2013. The tungsten project is an accumulation of experimental work, where the whole truly excels its parts and I would like to thank **Dr. Stefan Neppl**, **Dr. Andreas Kim**, **Dr. Michael Jobst** and **Michael Gerl** for providing unpublished data, which I used to extend the spectral range of the energy-dependent tungsten measurements. Without them such comprehensive understanding and interpretation of the 12 year old question about the time delay of the tungsten core level could have not been reached. Furthermore, great thanks for their camaraderie and support is to all other members of the AS-3 team, **Dr. Martin Schäffer**, **Michael Gerl**, **Sebastian Jarosch**, **Christian Schröder**, also the creator of our AS-3 Full-Penn and Monte-Carlo CTT codes, **Pascal Scigalla**, **Johannes Mahl**, **Michael Haimerl**, **Dr. Elisabeth Bothschafter**, **Dr.**

Ayman Akil, **Dr. Michael Jobst** and especially **Marcus Ossiander**, with whom spending 100 hours a week in the lab is not as miserable as it may sound.

I would like to thank **Prof. Ferencz Krausz** for the access to the lasers and experimental facilities at MPQ. To this end I would also like to thank **Dr. Nicholas Karpowicz**, **Dr. Martin Schultze** and the rest of the AS team at MPQ for the great work environment in the labs at MPQ and for teaching and assistance in laser alignment and maintenance.

Special thanks is due to **Dr. Silvano Lizzit**, **Dr. Daniel Lizzit** and **Dr. Luca Bignardi**, who provided us with non-official instrument beamtime at the SuperESCA beamline at Elletra. Working with them was a truly pleasant experience and a great contribution to the presented work.

An invaluable ingredient to our experiments are the custom designed XUV multilayer coatings. After all each data point is a different XUV mirror. Without the great and often shockingly fast work of **Dr. Alexander Guggenmos** and **Prof. Ulf Kleineberg**, we could not have done energy dependent streaking spectroscopy.

I would also like to thank all members and alumni of the E11 chair for their support and all the fun we had on the ski and hiking trips. Especially I would like to thank **Priv. Doz. Hristo Iglev**, **Katrin Oberhofer**, **Dr. Oliver Schalk**, **Felix Horstbrink**, **Konrad Hütten**, **Birgitta Bernhardt**, **Marinus Mayerbacher**, **Dr. Tobias Latka**, **Vage Shirvanian** and the whole team of the liquid phase streaking project for their collaboration and/or the fun of sharing an (messy) office.

Furthermore, I would like to thank all the administrative staff of E11, **Susanne Würzinger**, **Stefanie Völkl** and **Viktoria Blaschek**, and the E11 and E20 workshop crew, **Wolfgang Dürichen**, **Lukas Loibl** and **Karl Kölbl**, all of whom I hope are truly enjoying their retirements. Also I would like to thank **Michael Rogg**, **Martin Gruber** and the full team of the MPQ workshop, and **Reinhold Schneider** and **Karl Eberle** for their assistance with all the specialized and custom electronic/vacuum equipment.

Lastly, I want to thank my parents **Maria** and **Josef** and my siblings **Maximilian**, **Josef** and **Maria Anna** for their example and their support during my extensive studies both at home and abroad. I'd like to thank my girlfriend **Katrin** for all of the above and also for proof-reading of my thesis.